Quantum Vibrational Dynamics in Complex Environments: From Vibrational Strong Coupling in Molecular Cavity QED to Phonon-Induced Adsorbate Relaxation

Dissertation zur Erlangung des akademischen Grades
> doctor rerum naturalium < (Dr. rer. nat.)
in der Wissenschaftsdisziplin Theoretische Chemie

vorgelegt von

Eric Wolfgang Fischer, M.Sc.

aus Karlsruhe

an der
Mathematisch-Naturwissenschaftlichen Fakultät
der Universität Potsdam

Potsdam, Juni 2022

Diese Arbeit ist zwischen April 2018 und Juni 2022 in der Arbeitsgruppe von Prof. Dr. Peter Saalfrank am Institut für Chemie der Universität Potsdam entstanden.

Potsdam, Juni 2022

Erstgutachter: Prof. Dr. Peter Saalfrank
Zweitgutachter: Prof. Dr. Oriol Vendrell
Drittgutachter: Prof. Dr. Oliver Kühn

Published online on the
Publication Server of the University of Potsdam:
https://doi.org/10.25932/publishup-56721
https://nbn-resolving.org/urn:nbn:de:kobv:517-opus4-567214

"*There's Plenty of Room at the Bottom*"

Richard P. Feynman

Abstract

Molecules are often naturally embedded in a complex environment. As a consequence, characteristic properties of a molecular subsystem can be substantially altered or new properties emerge due to interactions between molecular and environmental degrees of freedom. The present thesis is concerned with the numerical study of quantum dynamical and stationary properties of molecular vibrational systems embedded in selected complex environments.
In the first part, we discuss "strong-coupling" model scenarios for molecular vibrations interacting with few quantized electromagnetic field modes of an optical Fabry-Pérot cavity. We thoroughly elaborate on properties of emerging "vibrational polariton" light-matter hybrid states and examine the relevance of the dipole self-energy. Further, we identify cavity-induced quantum effects and an emergent dynamical resonance in a cavity-altered thermal isomerization model, which lead to significant suppression of thermal reaction rates. Moreover, for a single rovibrating diatomic molecule in an optical cavity, we observe non-adiabatic signatures in dynamics due to "vibro-polaritonic conical intersections" and discuss spectroscopically accessible "rovibro-polaritonic" light-matter hybrid states.
In the second part, we study a weakly coupled but numerically challenging quantum mechanical adsorbate-surface model system comprising a few thousand surface modes. We introduce an efficient construction scheme for a "hierarchical effective mode" approach to reduce the number of surface modes in a controlled manner. In combination with the multilayer multiconfigurational time-dependent Hartree (ML-MCTDH) method, we examine the vibrational adsorbate relaxation dynamics from different excited adsorbate states by solving the full non-Markovian system-bath dynamics for the characteristic relaxation time scale. We examine half-lifetime scaling laws from vibrational populations and identify prominent non-Markovian signatures as deviations from Markovian reduced system density matrix theory in vibrational coherences, system-bath entanglement and energy transfer dynamics.
In the final part of this thesis, we approach the dynamics and spectroscopy of vibronic model systems at finite temperature by formulating the ML-MCTDH method in the non-stochastic framework of thermofield dynamics. We apply our method to thermally-altered ultrafast internal conversion in the well-known vibronic coupling model of pyrazine. Numerically beneficial representations of multilayer wave functions ("ML-trees") are identified for different temperature regimes, which allow us to access thermal effects on both electronic and vibrational dynamics as well as spectroscopic properties for several pyrazine models.

Kurzfassung

Moleküle sind für gewöhnlich in komplexe Umgebungen eingebettet. In Folge werden charakteristische Eigenschaften des molekularen Subsystems durch Wechselwirkung mit Umgebungsfreitheitsgraden potentiell deutlich verändert. Die vorliegende Dissertation behandelt die numerische Untersuchung von quantendynamischen und stationären Eigenschaften molekularer Schwingungen unter dem Einfluss ausgewählter komplexer Umgebungen. Im ersten Teil werden stark gekoppelte Modelsysteme betrachtet, die durch Wechselwirkung von molekulare Schwingungen mit wenigen quantisierten, elektromagnetischen Feldmoden einer Fabry-Pérot Kavität realisiert werden. Die Eigenschaften von Schwingungspolaritonen und die Relevanz der Dipolselbstenergie werden im Detail untersucht. Weiterhin werden quantenmechanische Effekte sowie ein dynamisches Resonanzphänomen in einem Modelsystem für thermische Isomerisierung unter dem Einfluss einer Kavität identifiziert, die zu signifikant reduzierten thermischen Reaktionsraten führen. Für ein frei rotierendes, schwingendes CO Molekül in einer Kavität finden sich nicht-adiabatische Signaturen in Form von schwingungspolaritonischen konischen Durchschneidungen sowie spektroskopisch identifizierbaren rovibratorischen Licht-Materie-Hybridzustände. Im zweiten Teil wird ein schwach gekoppeltes, numerisch anspruchsvolles Adsorbat-Oberflächen-Model mit einigen tausend Oberflächenmoden diskutiert. Es wird ein numerisch effizientes Verfahren zur Konstruktion einer Hierarchie effektiver Moden vorgestellt, wodurch die Anzahl an Oberflächenmoden kontrolliert reduziert wird. In Kombination mit der *multilayer multiconfigurational time-dependent Hartree* (ML-MCTDH) Methode, wird der Relaxationsprozess der Adsorbatmode für verschiedene Anfangszustände durch Lösung der nicht-Markovschen System-Bad Dynamik auf der charakteristische Relaxationszeitskala untersucht. Skalierungsgesetze von Halbwertszeiten werden aus Schwingungspopulationen erhalten und prominente nicht-markovsche Signaturen in Schwingungskohärenzen, in System-Bad-Verschränkung und in der Energietransferdynamik werden durch Vergleich mit markovscher reduzierter Dichtematrixtheorie identifiziert. Im letzten Teil wird vibronische Dynamik bei endlichen Temperaturen untersucht und die ML-MCTDH Methode im Rahmen der nicht-stochastischen *Thermofield Theory* formuliert. Der thermisch beeinflusste, ultraschnelle interne Konversionsprozess in Pyrazin wird betrachtet. Numerisch effiziente Darstellungen der ML-MCTDH Wellenfunktionen für verschiedene Temperaturen werden vorgestellt und thermische Effekte auf Dynamik und Spektroskopie werden diskutiert.

Contents

Chapter 1

Introduction

Vibrational, free-space rotational and translational motion constitute the nuclear degrees of freedom in molecules. Fully determined by Coulomb interactions of both electrons and nuclei, molecular vibrations are intimately connected to the concept of molecular structure and are accordingly key in understanding chemistry and molecular physics in their many facets. The most basic description of molecular vibrations relies on small amplitude motion of nuclei in the *harmonic approximation*, which provides a powerful but approximate perspective on molecular optical properties as probed by the infrared region of the electromagnetic spectrum. Commonly, every scenario which does not respect restrictions of the harmonic approximation is referred to as involving *anharmonic* effects. Where harmonic *normal modes* are by construction a collection of non-interacting vibrational entities, anharmonicity manifests in interactions between individual modes as well as significantly altered energetic properties of molecular modes.

In chemistry, anharmonic effects naturally play a role in the majority of molecular transformations as for example bond breaking or isomerization reactions, which are tightly related to large amplitude motion of molecular fragments build from individual nuclei. Moreover, molecular vibrations do not only interact anharmonically but naturally couple to both rotational and electronic molecular degrees of freedom. Resulting interactions are essential for understanding both thermal ground state chemistry as well as excited state chemistry involving multiple electronic states. Interactions are particularly relevant for molecules in condensed phase composite systems, as for example molecular reactants in liquid solvents, impurities in crystal lattices or adsorbate molecules on (crystalline) surfaces, to name just a few. Such composite systems are naturally characterized by emerging properties, resulting from the interplay of its different constituents, the molecular "subsystem" and a complex "environment".

Besides the coupling of molecular vibrational modes in matter, their interaction with static and dynamic electromagnetic "light" fields takes a prominent role with relevance ranging from structural spectroscopic studies to light-induced control of chemical reactions. Traditionally, the interaction of electromagnetic radiation with molecules is discussed from a *semiclassical* perspective. Here, molecules interact with one or multiple electromagnetic fields, which are described from the perspective of classical electrodynamics as governed

by Maxwell's equations. In contrast, the molecular system of interest is subject to a fully quantum mechanical description in terms of Schrödinger's equation. The full quantum mechanical description of both electromagnetic radiation and molecular degrees of freedom has been traditionally abandoned to highly specialized topics, which seemed to be rather unrelated to "everyday chemistry". However, this paradigm has changed drastically over the last decade due to seminal experiments in the field of molecular cavity quantum electrodynamics (cQED), which demonstrated the transformative influence of quantized cavity light-fields on both thermal ground state chemistry and photochemistry. As a result, the emerging field of *polaritonic chemistry* was born, which constitutes a highly interdisciplinary scientific "*melting pot*" of concepts from chemistry and quantum optics, eventually reformulating the goal of controlling chemistry by radiation fields.

In this thesis, we are concerned with the numerically study of quantum mechanical stationary and dynamical vibrational properties of molecules interacting with complex environments at zero and finite temperature. Such composite or *system-bath* type problems pose challenging issues due to the nature of the system-bath interaction, the possibly high-dimensional nature of the bath or thermally induced excitations of molecular degrees of freedom. In detail, we present results on three different topics. Firstly, strongly interacting (ro)vibrational light-matter hybrid systems and their role in polaritonic chemistry from the perspective of molecular cavity quantum electrodynamics. Secondly, vibrational relaxation dynamics for a realistic high-dimensional, weakly interacting adsorbate-surface model system and its efficient numerical description. Finally, a promising numerical approach to (non-adiabatic) quantum dynamics at finite temperature combining field theoretical techniques with numerical wave function methods. In order to access those problems successfully, we rely on two different approaches: Powerful numerical techniques to solve the quantum mechanical equation of motion computationally and the power of unitary transformations in quantum mechanics, which provide the freedom of choosing a useful "perspective" on individual problems and render the latter accessible for our purposes.

In Chapter 2, we provide the theoretical framework of this thesis and introduce relevant numerical tools. We first set the stage by presenting the framework for the quantum mechanical description of molecules followed by the central concepts of the Born-Oppenheimer approximation and electronic structure theory, which allow to efficiently approximate the numerical solution of the electronic many-body problem. Further, we introduce the basics for the non-relativistic description of quantized electromagnetic field modes in the setting of molecular cQED, which provides the theoretical framework for polaritonic chemistry and benefits from a cavity Born-Oppenheimer formulation naturally extending concepts from molecular quantum mechanics to cQED. The dynamics of quantum mechanical systems is considered from both a wave function and density operator perspective and the multiconfigurational time-dependent Hartree (MCTDH) method with its variants is introduced, which provides a powerful numerical approach to the time-evolution of quantum mechanical systems. Eventually, we discuss the basics of thermal reaction rate theory for a fully quantum mechanical approach based on the concept of cumulative reaction probabilities as well as the well known approximative framework of Eyring transition state theory.

Turning to the results starting with Chapter 3, we first elaborate on vibrational and rovibra-

tional model systems in the framework of non-relativistic cQED as described by a Pauli-Fierz Hamiltonian in long-wavelength approximation. A particular useful perspective on those problems has been established in terms of the length-gauge representation, which allows to naturally extend basic concepts from quantum chemistry to (ultra)strongly interacting light-matter hybrid systems. In detail, we examine three different aspects of (ro)vibrational light-matter hybrid systems: First, basic properties of vibro-polaritonic ground states and infrared spectroscopic characterization of excited states possibly subject to symmetry constraints of the light-matter hybrid system in dependence of light-matter interaction strength. All aspects are discussed with an emphasize on the role of the dipole self-energy in the effective vibrational Pauli-Fierz Hamiltonian in length-gauge representation. Second, the impact of molecular rotations on energetic, dynamical and infrared spectroscopic properties of a rovibrating diatomic molecule in a fully quantized light-matter interaction model scenario. We identify non-adiabatic signatures in terms of "vibro-polaritonic conical intersections" and "rovibro-polaritonic" light-matter hybrid state exhibiting vibrational, rotational and photonic contributions. Third, the role of light-matter interactions is studied for a thermal isomerization reaction model, which allows us to elaborate on the possible relevance of quantum mechanical effects in (vibro)polaritonic thermal ground state chemistry and reveals an anharmonic dynamical reactant localization effect due to coherent energy exchange between molecular and cavity modes.

In Chapter 4, we change paradigm away from strongly interacting, vibrational light-matter hybrid systems to a realistic high-dimensional, weakly interacting vibrational adsorbate surface model problem. Here, the vibrational relaxation dynamics of an excited adsorbate mode is numerically non-trivial due to the interaction with more than 2000 phonon modes of a semiconductor surface, which renders a straightforward quantum dynamical study prohibitively expensive. We show how to efficiently mitigate this so called "curse of dimensionality" by combining a hierarchical effective mode approach, for which we introduce a numerically efficient construction scheme, with the powerful multilayer multiconfigurational time-dependent Hartree method. Consequently, we are able to extract half-lifetimes of several excited vibrational states and provide a thorough comparison to simplified descriptions in terms of Markovian open system density matrix theory, which reveals intriguing dynamical details of the non-Markovian relaxation process.

Eventually, the third part of the result discussion as presented in Chapter 5, we consider a more general problem opposed to different interaction regimes: The efficient inclusion of finite temperature effects in the quantum dynamical description of vibrational systems. Here, the "curse of dimensionality" is even enhanced due to a density operator description of the thermal quantum system, which lies at heart of quantum statistical mechanics. We approach this issue by extending the multilayer multiconfigurational time-dependent Hartree method to the finite temperature regime by exploiting the originally field theoretical framework of thermofield dynamics. Our approach augments a set of existing methods, which have been developed throughout the last six years in the field of chemical physics, by a numerically powerful alternative in a methodologically well-established setting. We successfully apply our approach to the description of a widely-studied vibronic model system of pyrazine featuring interactions of thermally excited molecular vibrations and electronic states. We thoroughly discuss the efficient numerical inclusion of finite temperature effects

for the thermally-altered ultrafast internal conversion dynamics.
Finally, Chapter 6 closes this thesis by providing a summary and conclusion with respect to herein presented results.

Chapter 2

Theoretical Foundations

Here, we introduce main concepts of the quantum theory of molecules and electronic structure theory in Section 2.1, as well as its extension to non-relativistic cavity quantum electrodynamics including the quanitzed electromagnetic field of an optical Fabry-Pérot cavity in Section 2.2, respectively. Further, we discuss the time-evolution of quantum mechanical systems from both a wave function and a (reduced) density operator perspective, followed by a thorough overview over the multiconfigurational time-depenendent Hartree approach and its variants in Section 2.3. We close by section 2.4, which introduces thermal rate theory from both a fully quantum mechanical perspective based on cumulative reaction probabilities and the traditional but approximative Eyring transition state theoretical formulation.

2.1 Molecular Quantum Mechanics

2.1.1 The Molecular Many-Body Problem

In the non-relativistic limit, the molecular many-body problem for $N_{tot} = N_e + N_k$ particles with N_e electrons and N_k nuclei is fully described by the molecular Hamiltonian

$$\hat{H} = \hat{T}_k + \hat{H}_e + V_{kk} \quad . \tag{2.1}$$

Here, $\hat{T}_k$ is the nuclear kinetic energy operator (KEO)

$$\hat{T}_k = \sum_{a=1}^{N_k} \frac{\hat{\underline{P}}_a^2}{2M_a} \quad , \tag{2.2}$$

with nuclear masses, M_a, and nuclear momentum operators, $\hat{\underline{P}}_a = -\mathrm{i}\hbar\underline{\nabla}_a$, where $\underline{\nabla}_a = \left(\frac{\partial}{\partial X_a}, \frac{\partial}{\partial Y_a}, \frac{\partial}{\partial Z_a}\right)^{\mathrm{T}}$ is the nuclear gradient operator for the a^{th}-nucleus with nuclear Cartesian coordinates X_a, Y_a and Z_a. Further, $\hat{H}_e$ in Eq.(2.1) is the electronic Hamiltonian

$$\hat{H}_e = \hat{T}_e + V_{ee}(\underline{r}) + V_{ek}(\underline{r}, \underline{R}) \quad , \tag{2.3}$$

with electronic KEO, $\hat{T}_e$, electron-electron repulsion, $V_{ee}(\underline{r})$, and electron-nuclear attraction potential, $V_{ek}(\underline{r},\underline{R})$. Here, $\underline{r} = \left(\underline{r}_1,\ldots,\underline{r}_{N_e}\right)^{\mathrm{T}}$ and $\underline{R} = \left(\underline{R}_1,\ldots,\underline{R}_{N_k}\right)^{\mathrm{T}}$ are $3N_e$-dimensional electronic and $3N_k$-dimensional nuclear Cartesian coordinate vectors, respectively. The electronic KEO is explicitly given by

$$\hat{T}_e = \sum_{i=1}^{N_e} \frac{\hat{\underline{p}}_i^2}{2m_e} \quad , \tag{2.4}$$

with electronic momentum operators, $\hat{\underline{p}}_i = -\mathrm{i}\hbar\underline{\nabla}_i$, and electron mass, m_e. The electronic gradient operator reads, $\underline{\nabla}_i = \left(\frac{\partial}{\partial x_i},\frac{\partial}{\partial y_i},\frac{\partial}{\partial z_i}\right)^{\mathrm{T}}$, for the i^{th}-electron with electronic Cartesian coordinates x_i, y_i and z_i, respectively. Further, the nuclear-nuclear repulsion potential, $V_{kk}(\underline{R})$, in Eq.(2.1) provides together with $V_{ee}(\underline{r})$ and $V_{ek}(\underline{r},\underline{R})$ the molecular potential as given by

$$V(\underline{r},\underline{R}) = V_{ee}(\underline{r}) + V_{ek}(\underline{r},\underline{R}) + V_{kk}(\underline{R}) \tag{2.5}$$

$$= \sum_{i>j}^{N_e} \frac{e^2}{4\pi\epsilon_0|\underline{r}_i - \underline{r}_j|} - \sum_{i=1}^{N_e}\sum_{a=1}^{N_k} \frac{Z_a e^2}{4\pi\epsilon_0|\underline{r}_i - \underline{R}_a|} + \sum_{a>b}^{N_k} \frac{Z_a Z_b e^2}{4\pi\epsilon_0|\underline{R}_a - \underline{R}_b|} \quad . \tag{2.6}$$

Here, $\underline{r}_i = (x_i, y_i, z_i)^{\mathrm{T}}$ and $\underline{r}_j = (x_j, y_j, z_j)^{\mathrm{T}}$ are electronic Cartesian coordinate vectors, $\underline{R}_a = (X_a, Y_a, Z_a)^{\mathrm{T}}$ and $\underline{R}_b = (X_b, Y_b, Z_b)^{\mathrm{T}}$, are nuclear Cartesian coordinate vectors, e is the elementary charge, ϵ_0 is the vacuum permittivity and Z_a, Z_b are nuclear charge numbers, respectively. Stationary states, $\Psi(\underline{r},\underline{R})$, of the molecular Hamiltonian satisfy the molecular *time-independent* Schrödinger equation (TISE)

$$\left(\hat{T}_k + \hat{H}_e + V_{kk}\right)\Psi(\underline{r},\underline{R}) = E\,\Psi(\underline{r},\underline{R}) \quad , \tag{2.7}$$

with corresponding molecular energy, E. In this thesis, we consider only bound states and neglect continuum states, which are assumed to be not relevant for the physical processes studied here.

2.1.2 The Born-Oppenheimer Approximation

In order to solve the molecular Schrödinger equation (2.7), a molecular state is commonly written in terms of a *Born-Huang expansion*[1]

$$\Psi(\underline{r},\underline{R}) = \sum_{\nu} \chi_\nu^k(\underline{R})\,\psi_\nu^e(\underline{r};\underline{R}) \quad , \tag{2.8}$$

with nuclear wave functions, $\chi_\nu^k(\underline{R})$, providing the expansion coefficients and adiabatic electronic states, $\psi_\nu^e(\underline{r};\underline{R})$, respectively. The latter only parametrically depend on the nuclear coordinates, $\underline{R}$, and provide a complete orthonormal basis for fixed nuclear configurations. By inserting Eq.(2.8) into the molecular TISE (2.7), two coupled equations are obtained: One for the adiabatic electronic states

$$\hat{H}_e\,\psi_\nu^e(\underline{r};\underline{R}) = E_\nu^e(\underline{R})\,\psi_\nu^e(\underline{r};\underline{R}) \quad , \tag{2.9}$$

with adiabatic electronic energies, $E^e_\nu(\underline{R})$, and a second one satisfied by nuclear states

$$\left(\hat{T}_k + E^e_\nu(\underline{R}) + V_{kk}(\underline{R})\right)\chi^k_\nu(\underline{R}) + \sum_\mu \hat{C}_{\nu\mu}\chi^k_\mu(\underline{R}) = E\,\chi^k_\nu(\underline{R}) \quad , \tag{2.10}$$

with total molecular energy, E. The ν^{th}-adiabatic potential energy surfaces (PES) is defined as

$$V_\nu(\underline{R}) = E^e_\nu(\underline{R}) + V_{kk}(\underline{R}) \quad , \tag{2.11}$$

and provides a potential in Eq.(2.10), which depends on both the electronic quantum number, ν, and nuclear coordinates, $\underline{R}$. Further, $\hat{C}_{\nu\mu}$ in Eq.(2.10) corresponds to the non-adiabatic coupling operator[2]

$$\hat{C}_{\nu\mu} = -\sum_{a=1}^{N_k}\frac{\hbar^2}{2M_a}\left(G_{\nu\mu,a} + 2\underline{F}_{\nu\mu,a}\cdot\underline{\nabla}_a\right) \quad , \tag{2.12}$$

with

$$G_{\nu\mu,a} = \langle\psi^e_\nu(\underline{R})|\underline{\nabla}^2_a|\psi^e_\mu(\underline{R})\rangle_{\underline{r}} \quad , \quad \underline{F}_{\nu\mu,a} = \langle\psi^e_\nu(\underline{R})|\underline{\nabla}_a|\psi^e_\mu(\underline{R})\rangle_{\underline{r}} \quad , \tag{2.13}$$

where integration with respect to electronic coordinates, $\langle\ldots\rangle_{\underline{r}}$, is indicated. In the *Born-Oppenheimer approximation* (BOA)[5, 6], non-adiabatic coupling elements, $\hat{C}_{\nu\mu}$, are set to zero, which effectively decouples the slow nuclear dynamics from the fast electronic dynamics. The underlying idea is, that electronic degrees of freedom (DoF) are assumed to adapt instantaneously to a dynamically changing nuclear configuration. The BOA offers a valid perspective, if relevant adiabatic electronic states are energetically well separated from each other and breaks down for close lying or even crossing electronic states.
Finally, the choice of *adiabatic* electronic states in the Born-Huang expansion Eq.(2.8) is *not unique*. Alternatively, *diabatic* electronic states can be considered, which are not eigenstates of the electronic Hamiltonian and accordingly lead to off-diagonal potential energy couplings. In particular, diabatic electronic states can be chosen such that the nuclear KEO is approximately diagonal and, hence, the non-adiabatic couplings, $\hat{C}_{\nu\mu}$, negligible.[3] In this thesis, we employ the diabatic representation in the framework of vibronic coupling theory in Ch.5.[4]

2.1.3 Electronic Structure Theory

In this thesis, we are mainly concerned with molecular vibrational problems in the BOA, where electrons occupy the respective adiabatic ground state. The latter formally solves the electronic TISE (2.9), however is not exactly accessible for N_e interacting electrons due to the high complexity of the electronic many-body problem. In the following, we briefly review the most important approximative approaches of calculating adiabatic electronic ground states for molecules, which can be conceptually divided into *wave function-based* and *density-based* approaches.

Wave Function Theory

From a wave function perspective[7, 8], the exact non-relativistic N_e-electron ground state in the BOA, $|\psi_0\rangle$, can be expanded in a basis of orthonormal *Slater determinants*, which span the N_e-electron Hilbert space

$$|\psi_0\rangle = C_0\,|\psi_{\mathrm{HF}}\rangle + \sum_{a}^{N_e}\sum_{r}^{N_{virt}} C_a^r\,|\psi_a^r\rangle + \sum_{a<b}^{N_e}\sum_{r<s}^{N_{virt}} C_{ab}^{rs}\,|\psi_{ab}^{rs}\rangle + \dots \quad , \tag{2.14}$$

known as *full configuration interaction* (FCI) ansatz, where N_{virt} is the number of unoccupied, *virtual* orbitals (more details below). Here, $|\psi_{\mathrm{HF}}\rangle$ is the single-reference *Hartree-Fock* (HF) Slater determinant, while $|\psi_a^r\rangle$ and $|\psi_{ab}^{rs}\rangle$ are singly- and doubly-excited Slater determinants, and C_0, C_a^r, C_{ab}^{rs} are corresponding expansion coefficients, respectively. Coefficient indices a, b relate to occupied and r, s to unoccupied or virtual orbitals. The normalized Hartree-Fock Slater determinant is given by

$$\psi_{\mathrm{HF}}(\underline{\mathrm{x}}_1, \dots, \underline{\mathrm{x}}_{N_e}) = \frac{1}{\sqrt{N_e!}} \begin{vmatrix} \chi_1(\underline{\mathrm{x}}_1) & \dots & \chi_{N_e}(\underline{\mathrm{x}}_1) \\ \vdots & & \vdots \\ \chi_1(\underline{\mathrm{x}}_{N_e}) & \dots & \chi_{N_e}(\underline{\mathrm{x}}_{N_e}) \end{vmatrix} \quad . \tag{2.15}$$

It is composed of N_e orthonormal spin-orbitals, $\chi_i(\underline{\mathrm{x}}_j)$, with coordinates $\underline{\mathrm{x}}_j = (\underline{r}_j, \omega_j)$, where $\underline{r}_j$ is the j^{th}-electron's cartesian coordinate vector and ω_j is the corresponding spin coordinate. A Slater determinant naturally accounts for the correct anti-symmetry of a fermionic many-particle wave function and vanishes for two electrons being identical in all quantum numbers, which resembles *Pauli's exclusion principle*.
Furthermore, a single Slater determinant provides the basis of *Hartree-Fock theory*, which is the starting point for single-reference wave function methods in electronic structure theory and resembles a mean-field theory of the electronic many-body problem. In Hartree-Fock theory, the spin-orbitals in Eq.(2.15) are determined variationally by minimizing the corresponding Hartree-Fock energy

$$E_{\mathrm{HF}} = \min_{\{\chi_i\}} \langle\psi_{\mathrm{HF}}|\hat{H}_e|\psi_{\mathrm{HF}}\rangle > E_0 \quad , \tag{2.16}$$

with exact electronic ground state energy, E_0, constituting a lower bound for E_{HF}. The energy difference

$$E_{\mathrm{corr}} = E_0 - E_{\mathrm{HF}} \tag{2.17}$$

resembles the *electronic correlation energy*, E_{corr}, which is by definition not accounted for in Hartree-Fock theory. Variational minimization of the functional in Eq.(2.16) leads to a set of coupled non-linear, integro-differential equations known as Hartree-Fock equations for spin-orbitals, $\chi_i(\underline{\mathrm{x}}_1)$, as given by

$$\left(\hat{h}(\underline{\mathrm{x}}_1) + \sum_{b=1}^{N_e}\left(\hat{\mathcal{J}}_b(\underline{\mathrm{x}}_1) - \hat{\mathcal{K}}_b(\underline{\mathrm{x}}_1)\right)\right)\chi_i(\underline{\mathrm{x}}_1) = \varepsilon_i\,\chi_i(\underline{\mathrm{x}}_1) \quad , \tag{2.18}$$

which are effective single electron equations with orbital energies ε_i, respectively. Spin-orbitals corresponding to the lowest orbital energies, ε_i, determine the Hartree-Fock Slater determinant. In Eq.(2.18), $\hat{h}(\underline{\mathrm{x}}_1)$ is a single-electron operator, which contains a single electron KEO and single electron-nuclear repulsion as

$$\hat{h}(\underline{\mathrm{x}}_1) = -\frac{\hbar^2}{2m_e}\Delta_1 - \sum_{a=1}^{N_k} \frac{Z_a e^2}{4\pi\epsilon_0 |\underline{r}_1 - \underline{R}_a|} \quad , \tag{2.19}$$

with electronic Laplace operator, $\Delta_1 = \underline{\nabla}_1^2 = \frac{\partial^2}{\partial x_1^2} + \frac{\partial^2}{\partial y_1^2} + \frac{\partial^2}{\partial z_1^2}$. Further, $\hat{\mathcal{J}}_b(\underline{\mathrm{x}}_1)$ and $\hat{\mathcal{K}}_b(\underline{\mathrm{x}}_1)$ are Coulomb- and exchange-operators, which account for the interaction of a single electron with a mean-field of $N_e - 1$ electrons and act as

$$\hat{\mathcal{J}}_b(\underline{\mathrm{x}}_1)\chi_a(\underline{\mathrm{x}}_1) = \left[\int \chi_b^\star(\underline{\mathrm{x}}_2)\, \frac{e^2}{4\pi\epsilon_0\, r_{12}}\, \chi_b(\underline{\mathrm{x}}_2)\, \mathrm{d}\underline{\mathrm{x}}_2\right] \chi_a(\underline{\mathrm{x}}_1) \quad , \tag{2.20}$$

$$\hat{\mathcal{K}}_b(\underline{\mathrm{x}}_1)\chi_a(\underline{\mathrm{x}}_1) = \left[\int \chi_b^\star(\underline{\mathrm{x}}_2)\, \frac{e^2}{4\pi\epsilon_0\, r_{12}}\, \chi_a(\underline{\mathrm{x}}_2)\, \mathrm{d}\underline{\mathrm{x}}_2\right] \chi_b(\underline{\mathrm{x}}_1) \quad . \tag{2.21}$$

Both terms result from the electron-electron interaction, $\frac{e^2}{4\pi\epsilon_0\, r_{12}} = \frac{e^2}{4\pi\epsilon_0\, |\underline{r}_1 - \underline{r}_2|}$. Additionally, the exchange term is a consequence of the anti-symmetric nature of the Slater determinant ansatz in Eq.(2.15) and acts exclusively between electrons of identical spin.

Turning back to the FCI expansion in Eq.(2.14), excited Slater determinants are obtained by promoting electrons from occupied to formerly unoccupied, *virtual* orbitals (N_{virt} is the number of virtual orbitals in Eq.(2.14)), *e.g.*, in $|\psi_a^r\rangle$ a single electron was promoted from an initially occupied spin-orbital, $\chi_a(\underline{x}_1)$, to a virtual one, $\chi_r(\underline{x}_1)$, respectively. As noted above, in Eq.(2.14) indices a, b run over occupied and indices r, s run over virtual spin-orbitals.
In general, the FCI approach is only feasible for very small molecules due to the exponential scaling of the electronic Hilbert space with number of particles. Hence, one has to rely on *truncated* configuration interaction (CI) expansions, where one includes for instance only single or both single and double excitations, resulting in configuration interaction singles (CIS) and configuration interaction singles doubles (CISD) approaches, respectively. Although CISD is able to account for a significant portion of electron correlation, it is *not* size-consistent for $N_e > 2$, *i.e.*, the correct energy of two isolated molecular fragments is not reproduced, which prevents a correct description of dissociation reactions. We note for $N_e = 2$, CISD is equivalent to FCI and is therefore size-consistent.

A prominent, size-consistent alternative to truncated CI methods is *coupled cluster* (CC) theory, which has been employed in this thesis. In CC theory, the corresponding wave function, $|\psi_{\mathrm{CC}}\rangle$, is written in terms of an exponential ansatz[8]

$$|\psi_{\mathrm{CC}}\rangle = \exp\Bigg(\underbrace{\sum_{ra} \tau_a^r\, \hat{c}_r^\dagger \hat{c}_a}_{=\hat{T}_1} + \underbrace{\sum_{r>s,a>b} \tau_{ab}^{rs}\, \hat{c}_r^\dagger \hat{c}_s^\dagger \hat{c}_b \hat{c}_a}_{=\hat{T}_2} + \dots\Bigg) |\psi_{\mathrm{HF}}\rangle \quad , \tag{2.22}$$

where the exponent is given by a non-Hermitian cluster operator

$$\hat{T} = \hat{T}_1 + \hat{T}_2 + \dots \quad . \tag{2.23}$$

Here, $\hat{T}_1$ and $\hat{T}_2$ correspond to single- and double-excitation operators, which are given in Eq.(2.22) in terms of (coupled) cluster amplitudes τ_a^r, τ_{ab}^{rs} and electronic creation/annihilation operators $\hat{c}_r^\dagger, \hat{c}_s^\dagger$ and $\hat{c}_a, \hat{c}_b$, respectively.
A hierarchy of CC wave functions is obtained by truncating the cluster operator in Eq.(2.23), which leads at the simplest level to coupled cluster singles (CCS) and coupled cluster singles doubles (CCSD) methods, where one only keeps $\hat{T}_1$ or both $\hat{T}_1$ and $\hat{T}_2$, respectively. In this thesis, we employ the "*gold standard*" of quantum chemistry given by coupled cluster singles doubles with perturbative triples, CCSD(T)[9]. The latter perturbatively includes effects of triple excitations, *i.e.*, the next term $\hat{T}_3$ in Eq.(2.23), and has turned out to be particularly powerful with respect to accuracy relative to numerical costs.

Kohn-Sham Density Functional Theory

A paradigmatically different approach to electronic structure theory is based on the electron density, $\rho(\underline{r}) = \rho(x, y, z)$, which is a function of three spatial coordinates compared to $3N_e$ electronic coordinates in wave function theory. The resulting *density functional theory* (DFT) has developed into a powerful and very versatile approach in electronic structure theory of both molecular and extended systems. Here, we give a brief overview of DFT basics[10].
The formal pillars of DFT are provided by the first and second *Hohenberg-Kohn*-(HK)-Theorems (HK-1 and HK-2). According to HK-1, the electronic ground state energy, E_0, is a *unique* functional of the electron density

$$E_0 = E_0^{\mathrm{HK}} = T[\rho] + V_{ne}[\rho] + J[\rho] + E_{xc}[\rho] \quad . \tag{2.24}$$

Further, HK-2 provides a variational principle for electron densities satisfying

$$E_0 \leq E_0^{\mathrm{HK}}[\rho] \qquad \text{with} \qquad \int \rho(\underline{r})\, \mathrm{d}\underline{r} = N_e \quad , \tag{2.25}$$

where the exact electronic ground state energy, $E_0 = E_0^{\mathrm{HK}}[\rho_0]$, is only obtained if $\rho = \rho_0$ is the exact electronic ground state density. The energy, E_0^{HK}, in Eq.(2.24) is determined by the kinetic energy functional, $T[\rho]$, the electron-nuclei interaction, $V_{ne}[\rho]$, the classical electronic Coulomb interaction, $J[\rho]$, and the exchange-correlation functional, $E_{xc}[\rho]$, which resembles all non-classical, static electron-electron interactions, respectively.
The major advantage of DFT is the reduction of the $3N_e$-dimensional problem as treated in wave function theory to a 3-dimensional problem solely based on electron density. On the other hand, the major drawback emerges from the fact, that neither $T[\rho]$ nor $E_{xc}[\rho]$ in Eq.(2.24) are known exactly for all but the simplest model systems. Here, tremendous ongoing scientific effort has led to a series of approximations with increasing complexity. Starting with the representation of the kinetic energy functional, presumably the most prominent and widespread formulation of practical DFT is given by *Kohn-Sham* DFT (KS-DFT). In KS-DFT, the kinetic energy functional is approximated as, $T[\rho] \approx T^{\mathrm{KS}}[\rho]$, with

$$T^{\mathrm{KS}}[\rho] = -\frac{\hbar^2}{2m_e} \sum_{i=1}^{N_e} \langle \chi_i^{\mathrm{KS}} | \underline{\nabla}^2 | \chi_i^{\mathrm{KS}} \rangle \quad , \tag{2.26}$$

where Kohn-Sham orbitals, $|\chi_i^{\mathrm{KS}}\rangle$, solve the Hartree-Fock like Kohn-Sham equations, which describe a hypothetical system of N_e non-interacting electrons in an external potential. This potential is chosen such, that the orbitals $|\chi_i^{\mathrm{KS}}\rangle$ reproduce the exact electronic ground state density and it can be shown that $T^{\mathrm{KS}}[\rho] < T[\rho]$.
For the exchange-correlation functional, $E_{xc}[\rho]$, a certain hierarchy of approximations with increasing complexity has been developed. The simplest approximation is based on the uniform electron gas and denoted as *local density approximation* (LDA), where $\rho(\underline{r}) = const.$ for all $\underline{r}$. At the next complexity level, the spatial inhomogeneity of molecular electron densities due to the presence of nuclei is taken into account by higher order spatial derivatives, *i.e.*, $E_{xc}[\rho, \underline{\nabla}\rho, \underline{\nabla}^2\rho, \dots]$. This approach leads to the exchange-correlation functionals in *generalized gradient approximation* (GGA) with $E_{xc}[\rho, \underline{\nabla}\rho]$ and meta-GGA functionals, which in addition include higher order derivatives, respectively. In even more involved functionals, the exact exchange interaction of Hartree-Fock theory enters, which provides the class of hybrid functionals. Among others, the latter contains the B3LYP functional[11], which has developed into one of the standard functionals employed in computational chemistry and is relevant for this thesis. Even more sophisticated approaches to $E_{xc}[\rho]$ may subsequently combine elements of previously mentioned classes leading to "hybrid-meta-GGA" functionals, for instance, among others.

2.2 Molecular Cavity Quantum Electrodynamics

2.2.1 The Molecular Pauli-Fierz Hamiltonian

We now consider the theoretical description of molecular systems interacting with quantized electromagnetic field modes of an optical Fabry-Pérot cavity in the framework of cavity quantum electrodynamics (cQED). In the non-relativistic limit, a molecular system composed of $N_{tot} = N_e + N_k$ particles, which interacts with a quantized electromagnetic field is described by the molecular *Pauli-Fierz* Hamiltonian in its *minimal coupling* representation[12, 13]

$$\hat{H} = \sum_{i=1}^{N_e} \frac{\left(\hat{\underline{p}}_i + e\,\hat{\underline{A}}(\underline{r})\right)^2}{2m_e} + \sum_{a=1}^{N_k} \frac{\left(\hat{\underline{P}}_a - Z_a e\hat{\underline{A}}(\underline{r})\right)^2}{2M_a} + V(\underline{r}, \underline{R}) + \hat{H}_C \quad , \tag{2.27}$$

with molecular potential, $V(\underline{r}, \underline{R})$, as introduced in Eq.(2.6). Further, $\hat{H}_C$ is the quantized *transverse* field Hamiltonian and $\hat{\underline{A}}(\underline{r})$ is the corresponding quantized *transverse* vector potential in the Coulomb gauge, *i.e.*, $\underline{\nabla} \cdot \hat{\underline{A}}(\underline{r}) = 0$, which reads[12, 14, 15]

$$\hat{\underline{A}}(\underline{r}) = \sum_{\lambda=1}^{2} \sum_{k=1}^{N_c} \frac{\underline{e}_{\lambda k}}{\omega_k} \sqrt{\frac{\hbar\omega_k}{2\epsilon_0 V_c}} \left(\hat{a}_{\lambda k}\, S_k^{\star}(\underline{r}) + \hat{a}_{\lambda k}^{\dagger}\, S_k(\underline{r})\right) \quad , \tag{2.28}$$

with field mode index, k, and polarization index, λ, for $2N_c$ quantized field modes with harmonic frequencies, ω_k, and polarization vectors, $\underline{e}_{\lambda k}$, respectively. We note, the *longitudinal* contribution of the electric field in the Coulomb gauge enters the Hamiltonian in Eq.(2.27)

via the *instantaneous* Coulomb interaction of the molecular potential, $V(\underline{r}, \underline{R})$.[16] Further, for every mode index, k, in Eq.(2.28), there are two degenerate cavity modes satisfying the orthogonality conditions[12]

$$\underline{e}_{\lambda k} \cdot \underline{e}_{\lambda' k} = \delta_{\lambda\lambda'}, \quad \underline{e}_{\lambda k} \cdot \underline{k}_k = 0 \quad , \tag{2.29}$$

with wave vector, $\underline{k}_k$, of the k^{th}-cavity mode. Moreover, $\hat{a}^\dagger_{\lambda k}$ and $\hat{a}_{\lambda k}$ are photon creation and annihilation operators, which satisfy the canonical commutation relations[12]

$$\left[\hat{a}_{\lambda k}, \hat{a}^\dagger_{\lambda' k'}\right] = \delta_{\lambda\lambda'}\delta_{kk'} \quad . \tag{2.30}$$

Additionally, ϵ_0 is the vacuum permittivity and V_c is the quantization volume of the field, which determines the boundary conditions and accordingly the form of the cavity mode functions, $S_k(\underline{r})$, respectively. Here, we approximately consider $S_k(\underline{r})$ for a free field and invoke the *dipole* or *long-wavelength* approximation[15]

$$S_k(\underline{r}) = e^{-\mathrm{i}\,\underline{k}_k \cdot \underline{r}} = 1 - \mathrm{i}\,(\underline{k}_k \cdot \underline{r}) + \cdots \approx 1 \quad , \tag{2.31}$$

which is justified as the considered cavity mode wavelengths are significantly larger than the spatial extensions of molecular systems in an infrared optical cavity as considered in this thesis. In turn, the transverse vector potential in Eq.(2.28) is approximately spatially uniform, $\hat{\underline{A}}(\underline{r}) \approx \hat{\underline{A}}$. Further, the ensemble of quantized cavity field modes in Eq.(2.27) is described by[12]

$$\hat{H}_C = \sum_{\lambda=1}^{2} \sum_{k=1}^{N_c} \underbrace{\hbar\omega_k \left(\hat{a}^\dagger_{\lambda k}\hat{a}_{\lambda k} + \frac{1}{2}\right)}_{=\hat{h}_{\lambda k}} \quad , \tag{2.32}$$

which resembles a collection of N_C doubly-degenerate, quantized harmonic oscillators with harmonic frequencies, ω_k, and single-mode Hamiltonians, $\hat{h}_{\lambda k}$, respectively. The eigenstates of $\hat{h}_{\lambda k}$ are common harmonic oscillator states, which satisfy in number state representation the relations

$$\hat{a}_{\lambda k}\,|0_{\lambda k}\rangle = 0 \quad , \qquad \frac{\left(\hat{a}^\dagger_{\lambda k}\right)^n}{\sqrt{n!}}\,|0_{\lambda k}\rangle = |n_{\lambda k}\rangle \quad , \qquad \langle n_{\lambda k}|m_{\lambda k}\rangle = \delta_{nm} \quad . \tag{2.33}$$

Here, $|0_{\lambda k}\rangle$ is a single-mode vacuum state and provides with $\{|n_{\lambda k}\rangle\}$ an orthonormal basis, which spans the corresponding single-cavity-mode Hilbert space. Further, $n_{\lambda k}$ is the number of photons in the k^{th}-mode with polarization direction, λ. The eigenstates of $\hat{H}_C$ follow straightforwardly as multi-mode product states constructed from the single-mode states.

2.2.2 The Length-Gauge Representation

Power-Zienau-Woolley Transformation

An appealing form of the Pauli-Fierz Hamiltonian in long-wavelength approximation is given by its *length-gauge* representation[17, 18, 19], equivalently known as dipolar or multipolar

gauge representation[20, 21, 22, 23]. The length-gauge representation is obtained via a unitary transformation mediated by the operator

$$\hat{\mathcal{U}} = \exp\left(\frac{\mathrm{i}}{\hbar}\,\hat{\underline{A}}\cdot\underline{d}(\underline{r},\underline{R})\right) \quad , \tag{2.34}$$

known as *Power-Zienau-Woolley* (PZW) transformation with molecular dipole moment

$$\underline{d}(\underline{r},\underline{R}) = -e\sum_{i=1}^{N_e}\underline{r}_i + e\sum_{a=1}^{N_k} Z_a\underline{R}_a \quad . \tag{2.35}$$

Under the PZW-transformation, the KEO of the minimal-coupling Pauli-Fierz Hamiltonian Eq.(2.27) in long-wavelength approximation turns into

$$\hat{\mathcal{U}}^\dagger\left(\sum_{i=1}^{N_e}\frac{\left(\hat{\underline{p}}_i + e\,\hat{\underline{A}}\right)^2}{2m_e} + \sum_{a=1}^{N_k}\frac{\left(\hat{\underline{P}}_a - Z_a e\hat{\underline{A}}\right)^2}{2M_a}\right)\hat{\mathcal{U}} = \sum_{i=1}^{N_e}\frac{\hat{\underline{p}}_i^2}{2m_e} + \sum_{a=1}^{N_k}\frac{\hat{\underline{P}}_a^2}{2M_a} \quad , \tag{2.36}$$

i.e., the quantized transverse vector potential is removed from the expression on the right-hand side. Details on the PZW-transformation in Eq.(2.36) are provided in Appendix A. Further, the molecular potential energy, $V(\underline{r},\underline{R})$, is invariant under $\hat{\mathcal{U}}$ as it commutes with both $\hat{\underline{A}}$ and $\underline{d}(\underline{r},\underline{R})$. In contrast, the cavity mode Hamiltonian, $\hat{H}_C$, transforms as (*cf.* Appendix A)

$$\begin{aligned}\hat{\mathcal{U}}^\dagger\hat{H}_C\hat{\mathcal{U}} = \sum_{\lambda=1}^{2}\sum_{k=1}^{N_c}\hbar\omega_k\left(\hat{a}_{\lambda k}^\dagger\hat{a}_{\lambda k} + \frac{1}{2}\right) + \sum_{\lambda=1}^{2}\sum_{k=1}^{N_c}\mathrm{i}\,g_k\left(\underline{e}_{\lambda k}\cdot\underline{d}(\underline{r},\underline{R})\right)\left(\hat{a}_{\lambda k}^\dagger - \hat{a}_{\lambda k}\right) \\ + \sum_{\lambda=1}^{2}\sum_{k=1}^{N_c}\frac{g_k^2}{\hbar\omega_k}\left(\underline{e}_{\lambda k}\cdot\underline{d}(\underline{r},\underline{R})\right)^2 \quad .\end{aligned} \tag{2.37}$$

Here, the first term on the right-hand side corresponds to the bare cavity mode Hamiltonian, $\hat{H}_C$, and the second term resembles the imaginary light-matter interaction, $\Delta\hat{H}_{SC}$, which is mediated by the projection of the molecular dipole moment, $\underline{d}(\underline{r},\underline{R})$, on the polarization vector, $\underline{e}_{\lambda k}$, respectively. The term in the second line, quadratic in the molecular dipole moment, is known as *dipole self-energy* (DSE)

$$\hat{H}_{DSE} = \sum_{\lambda=1}^{2}\sum_{k=1}^{N_c}\frac{g_k^2}{\hbar\omega_k}\left(\underline{e}_{\lambda k}\cdot\underline{d}(\underline{r},\underline{R})\right)^2 \quad . \tag{2.38}$$

Further, an additional unitary rotation in the cavity mode subspace, as mediated by[24]

$$\hat{\mathcal{S}} = \exp\left(\mathrm{i}\,\frac{\pi}{2}\sum_{\lambda=1}^{2}\sum_{k=1}^{N_c}\hat{a}_{\lambda k}^\dagger\hat{a}_{\lambda k}\right) \quad , \tag{2.39}$$

leads to a real light-matter interaction term

$$\Delta\hat{H}_{SC} = \sum_{\lambda=1}^{2}\sum_{k=1}^{N_c} g_k \left(\underline{e}_{\lambda k} \cdot \underline{d}(\underline{r}, \underline{R}) \right) \left(\hat{a}^\dagger_{\lambda k} + \hat{a}_{\lambda k} \right) \quad , \tag{2.40}$$

but leaves both the cavity mode Hamiltonian and the DSE-term invariant (*cf.* Appendix A). Hence, with Eqs.(2.34) and (2.39), the minimal-coupling Pauli-Fierz Hamiltonian Eq.(2.27) in dipole-approximation Eq.(2.31) is mapped to

$$\hat{\mathcal{S}}^\dagger \hat{\mathcal{U}}^\dagger \hat{H} \hat{\mathcal{U}} \hat{\mathcal{S}} = \hat{T}_k + \hat{T}_e + V(\underline{r}, \underline{R}) + \hat{H}_C + \hat{H}_{SC} \quad , \tag{2.41}$$

with, $\hat{H}_{SC} \equiv \Delta\hat{H}_{SC} + \hat{H}_{DSE}$. In Eqs.(2.38) and (2.40), g_k is a mode specific light-matter interaction parameter

$$g_k = \sqrt{\frac{\hbar\omega_k}{2\epsilon_0 V_c}} \quad , \tag{2.42}$$

which resembles the vacuum field strength of the respective quantized field mode and is of dimension $[g_k] = V/m \hat{=} E_h/(ea_0)$ (atomic units).
We close by pointing out, that the DSE-term in Eq.(2.38) has been proven central for a correct description of bound light-matter hybrid states in ideal optical cavities with a discrete mode spectrum as described by the Pauli-Fierz Hamiltonian in length-gauge representation.[26, 27] In particular, $\hat{H}_{DSE}$ ensures a bound ground state of the Pauli-Fierz Hamiltonian[26], provides translational invariance and renders the molecular Pauli-Fierz Hamiltonian gauge invariant[27]. Further, as we consider here an idealized closed Fabry-Pérot cavity, which hosts a discrete set of quantized field modes, $\hat{H}_{DSE}$ depends quadratically on g_k in contrast to the multipolar gauge for a mode continuum, where this term is independent of the light-matter coupling strength.[25] Finally, as noted before under the long-wavelength approximation the minimal-coupling representation in Eq.(2.27) and the length-gauge representation in Eq.(2.41) are equivalent due to the unitary character of the PZW-transformation. However, this equivalence is flawed for a Pauli-Fierz Hamiltonian projected on a restricted electronic subspace, which has been subject to some recent discussions[33, 34, 35, 36, 37, 38, 36, 39].

Cavity Mode Coordinate Representation

From a quantum chemist's perspective, a coordinate representation of quantized cavity modes turns out to be tempting as it allows to generalize the concept of potential energy surfaces to molecular cQED.[28] One exploits the well-known identities

$$\hat{p}_{\lambda k} = \mathrm{i}\sqrt{\frac{\hbar\omega_k}{2}} \left(\hat{a}^\dagger_{\lambda k} - \hat{a}_{\lambda k} \right), \quad x_{\lambda k} = \sqrt{\frac{\hbar}{2\omega_k}} \left(\hat{a}^\dagger_{\lambda k} + \hat{a}_{\lambda k} \right) \quad , \tag{2.43}$$

to introduce a "cavity momentum operator", $\hat{p}_{\lambda k} = -\mathrm{i}\hbar\frac{\partial}{\partial x_{\lambda k}}$, and a "cavity displacement coordinate", $x_{\lambda k}$, in mass-weighted harmonic oscillator units, which satisfy the canonical commutation relations

$$[x_{\lambda k}, \hat{p}_{\lambda' k'}] = \mathrm{i}\hbar\, \delta_{\lambda\lambda'}\delta_{kk'} \quad . \tag{2.44}$$

With the identities in Eq.(2.43), the cavity Hamiltonian takes the familiar form

$$\hat{H}_C = \frac{1}{2}\sum_{\lambda=1}^{2}\sum_{k=1}^{N_c}\left(\hat{p}_{\lambda k}^2 + \omega_k^2\, x_{\lambda k}^2\right) \quad . \tag{2.45}$$

By additionally taking into account both the bare light-matter interaction, $\Delta\hat{H}_{SC}$, and the dipole self-energy, $\hat{H}_{DSE}$, one finds

$$\hat{H}_C + \Delta\hat{H}_{SC} + \hat{H}_{DSE} = \frac{1}{2}\sum_{\lambda=1}^{2}\sum_{k=1}^{N_c}\left(\hat{p}_{\lambda k}^2 + \omega_k^2\left(x_{\lambda k} + \sqrt{\frac{2}{\hbar\omega_k^3}}\, g_k\left(\underline{e}_{\lambda k}\cdot\underline{d}(\underline{r},\underline{R})\right)\right)^2\right) \quad , \tag{2.46}$$

which resembles a collection of displaced cavity mode harmonic oscillators depending on the molecular dipole moment, $\underline{d}(\underline{r},\underline{R})$, respectively. Next, by separating-off the cavity mode KEO

$$\hat{T}_c = \frac{1}{2}\sum_{\lambda=1}^{2}\sum_{k=1}^{N_c}\hat{p}_{\lambda k}^2 \quad , \tag{2.47}$$

a cavity potential energy can be introduced as

$$V_c(\underline{r},\underline{R},\underline{x}) = \frac{1}{2}\sum_{\lambda=1}^{2}\sum_{k=1}^{N_c}\omega_k^2\left(x_{\lambda k} + \sqrt{\frac{2}{\hbar\omega_k^3}}\, g_k\left(\underline{e}_{\lambda k}\cdot\underline{d}(\underline{r},\underline{R})\right)\right)^2 \quad , \tag{2.48}$$

with cavity displacement coordinate vector, $\underline{x} = (x_{11}, x_{21}, \ldots, x_{1N_c}, x_{2N_c})$, of length $2N_c$, respectively.

In this thesis, we consider the single-cavity mode limit with $N_c = 1$ in Eq.(2.48) and we denote the remaining harmonic cavity mode frequency as ω_c and the light-matter interaction strength as g. The latter can be related to a Rabi frequency, Ω_R, defined in the Jaynes- and Tavis-Cummings models as[29, 30, 31]

$$\hbar\Omega_R = 2\, g\, |d_{fi}|\sqrt{N_m} \quad , \tag{2.49}$$

with transition dipole moment, d_{fi}, between molecular states f and i of a single molecule, which resonantly interact with a cavity mode of appropriate frequency, and N_m is the number of molecules interacting with the cavity mode. Next, a dimensionless light-matter coupling parameter, η, can be introduced[32]

$$\eta = \frac{g\,|d_{fi}|}{\hbar\omega_c} = \frac{\hbar\Omega_R}{2\hbar\omega_c}\frac{1}{\sqrt{N_m}} \quad , \tag{2.50}$$

where the second equality results from Eq.(2.49). Here, we consider only a single molecule interacting with the cavity mode, *i.e.*, we set $N_m = 1$, respectively. The parameter η then allows for a characterization of the light-matter interaction regimes according to[32]

$$\eta \begin{cases} \leq 0.1 \quad , \quad \text{VSC} \\ > 0.1 \quad , \quad \text{VUSC} \end{cases} \quad . \tag{2.51}$$

where one distinguishes the *vibrational strong coupling* (VSC) regime from the *vibrational ultrastrong coupling* (VUSC) regime. The lower boundary of the VSC regime is at non-zero η and formally determined by the onset of intra-cavity light-matter interaction overcompensating dissipative effects. Then, cavity photons are coherently exchanged between cavity modes and molecular DoF and not preferably emitted to the extra-cavity radiation continuum, which is an ubiquitous process due to non-ideal characteristics of cavity mirrors. The latter is conveniently characterized by a cavity quality factor, $Q = \hbar\omega_c/\kappa$, where κ is an effective cavity decay rate, which resembles spontaneous emission effects.[32, 123, 145]

2.2.3 The Cavity Born-Oppenheimer Approximation

Cavity Born-Huang Expansion

The eigenstates of the Pauli-Fierz Hamiltonian in length-gauge representation and long-wavelength approximation, Eq.(2.41), satisfy the full molecule-photon TISE

$$\left(\hat{T}_k + \hat{T}_c + \hat{H}_{ec} + V_{kk}(\underline{R})\right)\Psi(\underline{r},\underline{R},\underline{x}) = \mathcal{E}\,\Psi(\underline{r},\underline{R},\underline{x}) \quad , \tag{2.52}$$

with light-molecule hybrid states, $\Psi(\underline{r},\underline{R},\underline{x})$, total energy, $\mathcal{E}$, and electron-photon Hamiltonian

$$\hat{H}_{ec} = \hat{T}_e + V_{ee}(\underline{r}) + V_{ek}(\underline{r},\underline{R}) + V_c(\underline{r},\underline{R},\underline{x}) = \hat{H}_e + V_c(\underline{r},\underline{R},\underline{x}) \quad , \tag{2.53}$$

where $V_c(\underline{r},\underline{R},\underline{x})$ is the cavity potential energy as defined in Eq.(2.48). One route to the (approximative) solution of Eq.(2.52) is the *cavity Born-Oppenheimer* (cBO) approach[28], which naturally extends concepts from molecular quantum mechanics to molecular cQED. In the cBO-framework, the full molecule-photon wave function is written in terms of a *cavity Born-Huang expansion*[28]

$$\Psi(\underline{r},\underline{R},\underline{x}) = \sum_\nu \chi_\nu^{kc}(\underline{R},\underline{x})\,\psi_\nu^{ec}(\underline{r};\underline{R},\underline{x}) \quad , \tag{2.54}$$

with adiabatic electron-photon states, $\psi_\nu^{ec}(\underline{r};\underline{R},\underline{x})$, which parametrically depend on both nuclear, $\underline{R}$, and cavity mode displacement coordinates, $\underline{x}$, respectively. Further, $\chi_\nu^{kc}(\underline{R},\underline{x})$, are nuclear-photon wave functions and provide expansion coefficients of the cavity Born-Huang expansion. By inserting Eq.(2.54) into the molecule-photon TISE (2.52), one obtains two coupled equations, one for the adiabatic electron-photon states

$$\hat{H}_{ec}\,\psi_\nu^{ec}(\underline{r};\underline{R},\underline{x}) = E_\nu^{ec}(\underline{R},\underline{x})\,\psi_\nu^{ec}(\underline{r};\underline{R},\underline{x}) \quad , \tag{2.55}$$

with adiabatic electron-photon energies, $E_\nu^{ec}(\underline{R},\underline{x})$, and a second one satisfied by nuclear-photon states

$$\left(\hat{T}_k + \hat{T}_c + E_\nu^{ec}(\underline{R},\underline{x}) + V_{kk}(\underline{R})\right)\chi_\nu^{kc}(\underline{R},\underline{x}) + \sum_\mu \left(\hat{C}_{\nu\mu} + \hat{C}^c_{\nu\mu}\right)\chi_\mu^{kc}(\underline{R},\underline{x}) = \mathcal{E}\,\chi_\nu^{kc}(\underline{R},\underline{x}) \quad . \tag{2.56}$$

In line with Eq.(2.11), one defines the ν^{th}-adiabatic *cavity potential energy surface* (cPES) as

$$V_\nu(\underline{R},\underline{x}) = E^{ec}_\nu(\underline{R},\underline{x}) + V_{kk}(\underline{R}) \quad , \tag{2.57}$$

which now depends on both cavity displacement coordinates, $\underline{x}$, and nuclear coordinates, $\underline{R}$, respectively. The electron-photon TISE (2.55) provides now the counterpart of the electronic TISE (2.9) in the light-molecule hybrid many-body problem. Recent effort lead to a series of approaches to its numerical solution, namely the cQED-extension of DFT denoted as QEDFT[17, 18, 19, 40] and wave function-based approaches as QED-HF, QED-CI and QED-CC theories[41, 42, 43, 44, 45, 46, 47, 48].

Further, Eq.(2.56) generalizes the nuclear TISE (2.10) to the light-matter hybrid scenario and is analogously subject to non-adiabatic derivative couplings, which are now, however, related to both nuclear, $\hat{C}_{\nu\mu}$, and cavity DoF, $\hat{C}^c_{\nu\mu}$, respectively. The latter, cavity non-adiabatic coupling terms stem from the parametric dependence of electron-photon states, $\psi^{ec}_\nu(\underline{r};\underline{R},\underline{x})$, on cavity mode displacement coordinates.[28] In analogy to nuclear non-adiabatic couplings in Eq.(2.12), we introduce

$$\hat{C}^c_{\nu\mu} = -\frac{\hbar^2}{2}\sum_{\lambda=1}^{2}\sum_{l=1}^{N_c}\left(G^c_{\nu\mu,\lambda l} + 2F^c_{\nu\mu,\lambda l}\frac{\partial}{\partial x_{\lambda l}}\right) \quad , \tag{2.58}$$

with

$$G^c_{\nu\mu,\lambda l} = \langle\psi_\nu(\underline{R},\underline{x})|\partial^2_{x_{\lambda l}}|\psi_\mu(\underline{R},\underline{x})\rangle_{\underline{r}} \quad , \quad F^c_{\nu\mu,\lambda l} = \langle\psi_\nu(\underline{R},\underline{x})|\partial_{x_{\lambda l}}|\psi_\mu(\underline{R},\underline{x})\rangle_{\underline{r}} \quad , \tag{2.59}$$

where, $\partial_{x_{\lambda l}} \equiv \frac{\partial}{\partial x_{\lambda l}}$ and $\partial^2_{x_{\lambda l}} \equiv \frac{\partial^2}{\partial x^2_{\lambda l}}$, and integration with respect to electronic coordinates, $\langle\ldots\rangle_{\underline{r}}$, is indicated.

Effective Vibrational Pauli-Fierz Hamiltonian in cBOA

In this thesis, we study vibrational strong coupling problems[49], where molecular vibrations strongly couple to the quantized modes of an infrared cavity. Accordingly, we employ the cavity Born-Oppenheimer approximation (cBOA)[28], by neglecting both types of non-adiabatic coupling contributions in Eq.(2.56), *i.e.*, $\hat{C}_{\nu\mu}$ and $\hat{C}^c_{\nu\mu}$. Under this approximation, the adiabatic electron-photon states and the corresponding cPES are decoupled and we concentrate on the corresponding adiabatic ground state, $\psi^{ec}_0(\underline{r};\underline{R},\underline{x})$. Generally, the cBOA is valid, if (i) the cPES are energetically well separated and (ii) if the cavity momenta $\hat{p}_{\lambda k}$ are sufficiently small, in analogy to the arguments concerning nuclear motion.[28]
Further, due the different energy scales of electronic and vibrational/cavity mode excitation in VSC problems, we assume that the adiabatic electron-photon ground state is in first order well approximated by its purely electronic counterpart

$$\psi^{ec}_0(\underline{r};\underline{R},\underline{x}) \approx \psi^{e}_0(\underline{r};\underline{R}) \quad , \tag{2.60}$$

which is equivalent to effectively neglecting radiative, dipole-induced correlations between electrons and photons. In turn, we obtain an approximated adiabatic ground state cPES

given by

$$V_0(\underline{R},\underline{x}) \approx V_0(\underline{R}) + V_c^0(\underline{R},\underline{x}) = V_0(\underline{R}) + \langle \psi_0^e(\underline{R})|V_c(\underline{r},\underline{R},\underline{x})|\psi_0^e(\underline{R})\rangle_{\underline{r}} \quad , \tag{2.61}$$

with Born-Oppenheimer PES, $V_0(\underline{R})$, as given in Eq.(2.11) and Born-Oppenheimer-ground-state-projected cavity potential energy, $V_c^0(\underline{R},\underline{x})$ (*cf.* Eq.(2.48)). We now introduce the nuclear-photon TISE under cBOA as

$$\left(\hat{T}_k + \hat{T}_c + V_0(\underline{R}) + V_c^0(\underline{R},\underline{x})\right)\chi_n(\underline{R},\underline{x}) = \varepsilon_n \chi_n(\underline{R},\underline{x}) \quad , \tag{2.62}$$

which is satisfied by (ro)vibro-polaritonic states, $\chi_n(\underline{R},\underline{x})$, with energies, ε_n, respectively. The approximated ground state cPES in Eq.(2.62) is then given by

$$V_\eta(\underline{R},\underline{x}) \equiv V_0(\underline{R}) + \underbrace{\sum_{\lambda=1}^{2}\sum_{k=1}^{N_c}\frac{\omega_k^2}{2}\left(x_{\lambda k} + \sqrt{\frac{2}{\hbar\omega_k^3}}\, g_k\left(\underline{\epsilon}_{\lambda k}\cdot\underline{d}_0(\underline{R})\right)\right)^2}_{=V_c^0(\underline{R},\underline{x})} \quad , \tag{2.63}$$

where, $\underline{d}_0(\underline{R})$, is the permanent molecular ground state dipole moment and η characterizes the light-matter interaction as introduced in Eq.(2.50). Hence, the (ro)vibro-polaritonic states, $\chi_n(\underline{R},\underline{x})$, in Eq. (2.62) are eigenstates of an effective vibrational Pauli-Fierz Hamiltonian

$$\hat{H} = \hat{T}_k + \hat{T}_c + V_\eta(\underline{R},\underline{x}) \quad , \tag{2.64}$$

which is given for the molecular electronic ground state in the BOA and neglects correlations between electrons and cavity degrees of freedom. In Ch.3, we discuss different realizations of Eq.(2.64) in the context of polaritonic chemistry and spectroscopy of (ro)vibrational polaritons.

2.3 Quantum Molecular Dynamics

We now turn to the time-evolution of non-relativistic molecular and light-matter hybrid systems. At $T = 0\,\mathrm{K}$, the time-evolution of a quantum mechanical system is determined by the *time-dependent* Schrödinger equation (TDSE)

$$\mathrm{i}\hbar\frac{\partial}{\partial t}\,|\Psi(t)\rangle = \hat{H}\,|\Psi(t)\rangle \quad , \tag{2.65}$$

with initial condition $|\Psi(t_0)\rangle = |\Psi_0\rangle$, where $|\Psi(t)\rangle$ is a general wave packet and $\hat{H}$ is the Hamiltonian of the system, generating the dynamics, respectively. The eigenstates $\{|\Psi_n\rangle\}$ of $\hat{H}$ are characterized by a trivial time-evolution

$$|\Psi_n(t)\rangle = e^{-\mathrm{i}\,E_n t/\hbar}\,|\Psi_n\rangle \quad , \tag{2.66}$$

with energies, E_n, providing a complex time-dependent phase factor. In this thesis, we are mainly concerned with vibrational (vibro-polaritonic) problems in the electronic ground

state. Accordingly, we numerically study the time-evolution of a f-dimensional vibrational wave packet, $|\psi_v(t)\rangle$, by expanding it in an orthonormal, time-independent vibrational basis, $\{|\chi_{i_k}^{(\kappa)}\rangle\}$, spanning the vibrational Hilbert space as

$$|\psi_v(t)\rangle = \sum_{i_1=1}^{N_1} \cdots \sum_{i_f=1}^{N_f} C_{i_1 \ldots i_f}(t) \prod_{\kappa=1}^{f} |\chi_{i_k}^{(\kappa)}\rangle \quad , \tag{2.67}$$

with expansion coefficients, $C_{i_1 \ldots i_f}(t)$, and N_κ vibrational basis functions for the κ^{th}-mode, respectively. This approach is straightforwardly generalized to vibrational strong coupling problems in molecular cQED by including appropriate basis states for cavity modes. Further, an extension to non-adiabatic problems involving several electronic states is analogously straightforward with a vibronic wave function given by

$$|\Psi(t)\rangle = \sum_{i_e=1}^{M_e} |\psi_v^{i_e}(t)\rangle \, |\psi_{i_e}\rangle \quad , \tag{2.68}$$

where M_e is the number of electronic states, $|\psi_{i_e}\rangle$, and the time-dependent vibrational wave packets, $|\psi_v^{i_e}(t)\rangle$, now carry an additional electronic index, i_e, characterizing the corresponding electronic state, $|\psi_{i_e}\rangle$, respectively. A vibronic problem at finite temperature is discussed in Ch.5 of this thesis.

The *standard approach* in Eq.(2.67) can be graphically depicted by means of a diagrammatic representation[51, 52] as shown in Fig.2.1(a), where the rank-f tensor $C_{i_1 \ldots i_f}(t)$ is represented by a single node with f legs holding "physical" indices i_κ and corresponding physical dimension N_κ, respectively.

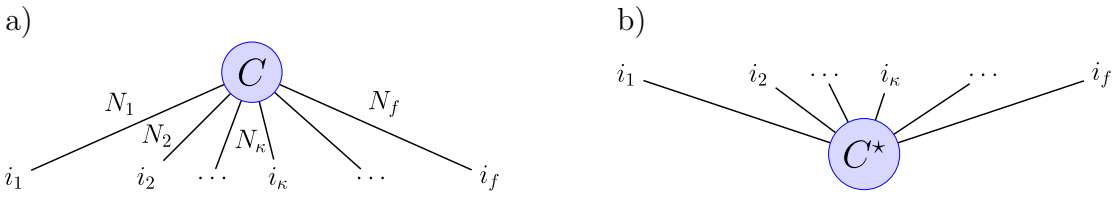

Figure 2.1: Diagrammatic representation of (a) the standard expansion in Eq.(2.67) with physical dimensions, N_κ, equivalent to the number of vibrational basis functions and (b) the corresponding bra-state where physical dimensions, N_κ, are assumed implicitly.

Further, in Fig.2.1(b) we display the bra-state corresponding to the expansion in Eq.(2.67). The problematic aspect of the standard approach to quantum dynamics is related to the exponential scaling of the Hilbert space as $\prod_\kappa^f N_\kappa$ for vibrational problems (or $M_e \prod_\kappa^f N_\kappa$ for vibronic problems), which is known as "*curse of dimensionality*" (CoD) and prohibits the study of quantum systems with many DoF. In order to mitigate the CoD, one has to refer to advanced approaches as for example the *multiconfigurational time-dependent Hartree* (MCTDH) method and its multilayer extension (ML-MCTDH), which have been employed in this thesis and will be introduced below. Beforehand, we turn to the quantum statistical description of quantum dynamics and introduce the concept of a *density operator*.

2.3.1 Density Operator Theory

For temperatures, $T \geq 0\,\mathrm{K}$, a quantum system is in general fully described by its density operator $\hat{\rho}(t)$, which evolves in time according to the *Liouville-von Neumann* (LvN) equation[53, 54, 55]

$$\frac{\partial}{\partial t}\hat{\rho}(t) = -\frac{\mathrm{i}}{\hbar}\left[\hat{H}, \hat{\rho}\right] \quad , \tag{2.69}$$

with commutator, $[\hat{H}, \hat{\rho}] = \hat{H}\hat{\rho} - \hat{\rho}\hat{H}$, and initial state, $\hat{\rho}(t_0) = \hat{\rho}_0$, respectively. In the zero-temperature limit, the LvN equation (2.69) is equivalent to the TDSE (2.65). Further, for a system in thermal equilibrium, the initial state resembles the canonical thermal state

$$\hat{\rho}_0(\beta) = \frac{e^{-\beta\hat{H}}}{Z(\beta)} \quad , \tag{2.70}$$

with inverse temperature $\beta = (k_B T)^{-1}$, Boltzmann constant k_B, temperature T and canonical partition function

$$Z(\beta) = \sum_k e^{-\beta\varepsilon_k} \quad , \tag{2.71}$$

with ε_k being eigenvalues of $\hat{H}$ in Eq.(2.70), respectively. In analogy to Eq.(2.67), the LvN-equation for a f-dimensional vibrational problem can be solved by expanding a vibrational density operator in a basis of vibrational states as

$$\hat{\rho}_v(t) = \sum_{i_1, i_1'=1}^{N_1} \cdots \sum_{i_f, i_f'=1}^{N_f} C_{i_1 \ldots i_f, i_1' \ldots i_f'}(t) \prod_{\kappa=1}^{f} \left|\chi_{i_k}^{(\kappa)}\right\rangle \left\langle\chi_{i_k'}^{(\kappa)}\right| \quad , \tag{2.72}$$

with expansion coefficients, $C_{i_1 \ldots i_f, i_1' \ldots i_f'}(t)$. As for the wave function approach above, a straightforward generalization to vibronic problems (*cf.* Ch.5 for an application) is given by

$$\hat{\rho}(t) = \sum_{i_e, j_e=1}^{M_e} \hat{\rho}_v^{i_e j_e}(t) \left|\psi_{i_e}\right\rangle \left\langle\psi_{j_e}\right| \quad , \tag{2.73}$$

where the vibrational density operator, $\hat{\rho}_v^{i_e j_e}(t)$, is now additionally characterized by electronic indices, i_e, j_e, respectively. Following the diagrammatic notation introduced in Fig.2.1, a pictorial representation of the expansion in Eq.(2.72) is given in Fig.2.2, where the number of vibrational basis functions, N_κ, *i.e.*, the physical dimensions, have been omitted for clarity.

The basis expansion in Eq.(2.72) scales exponentially as $\prod_\kappa^f N_\kappa^2$ (or as $M_e^2 \prod_\kappa^f N_\kappa^2$ for Eq.(2.73)), which is even more severe compared to the wave function approach. Accordingly, the solution of the LvN-equation imposes an intricate numerical problem, which is either only tractable for very small systems or requires powerful numerical methods for larger problems. An approximative but numerically efficient alternative relies on the direct propagation of the *reduced system* density operator, which we introduce in the following.

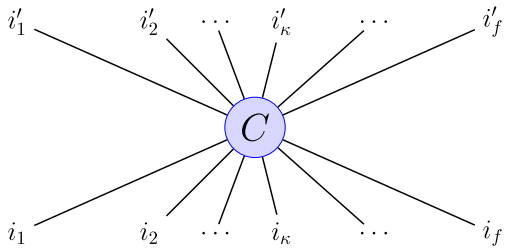

Figure 2.2: Diagrammatic representation of standard expansion for vibrational density operators in Eq.(2.72) where indices i_κ related to ket-states, $|\chi^{(\kappa)}_{i_k}\rangle$, point downwards and indices i'_κ related to bra-states, $\langle\chi^{(\kappa)}_{i'_k}|$, point upwards. Physical dimensions, N_κ, are assumed implicitly.

Reduced System Density Operator Theory

The reduced system density operator is given by

$$\hat{\rho}_S(t) = \mathrm{tr}_B\{\hat{\rho}_v(t)\} \quad , \tag{2.74}$$

where $\hat{\rho}_v(t)$ is the vibrational density operator of the full system and $\mathrm{tr}_B\{\dots\}$ resembles the trace over a set of residual "bath" DoF. The reduced system density operator is equally important at finite and zero temperature and at $T = 0\,\mathrm{K}$, we have $\hat{\rho}_v(t) = |\Psi_v(t)\rangle\langle\Psi_v(t)|$, where $|\Psi_v(t)\rangle$ is the full vibrational wave function of a composite "system-bath" problem. In order to avoid the propagation of $\hat{\rho}_v(t)$ at finite temperature (or propagation of $|\Psi_v(t)\rangle$ at $T = 0\,\mathrm{K}$), one can directly propagate the reduced density operator, $\hat{\rho}_S(t)$, where the effects of the bath on the (vibrational) subsystem are only implicitly taken into account. A prominent approach following this paradigm is given by the open-system LvN-equation in Lindblad form, which provides a *Markovian* quantum master equation by definition, and reads[53]

$$\frac{\partial}{\partial t}\hat{\rho}_S(t) = \mathcal{L}\,\hat{\rho}_S(t) \quad , \tag{2.75}$$

with Lindblad-Liouvillian, $\mathcal{L}$, most generally acting as[56, 57]

$$\mathcal{L}\,\hat{\rho}_S = -\frac{\mathrm{i}}{\hbar}\left[\hat{H}_S, \hat{\rho}_S\right] + \frac{1}{2}\sum_{i,j}\Gamma_{ij}\left(\left[\hat{A}_i, \hat{\rho}_S\hat{A}_j^\dagger\right] + \left[\hat{A}_i\hat{\rho}_S, \hat{A}_j^\dagger\right]\right) \quad . \tag{2.76}$$

where Γ_{ij} constitute elements of a positive semi-definite matrix, $\underline{\underline{\Gamma}}$, which can be diagonalized to yield[53]

$$\mathcal{L}\,\hat{\rho}_S = \underbrace{-\frac{\mathrm{i}}{\hbar}\left[\hat{H}_S, \hat{\rho}_S\right]}_{=\mathcal{L}_0\,\hat{\rho}_S} + \underbrace{\sum_j\left(\hat{A}_j\,\hat{\rho}_S\,\hat{A}_j^\dagger - \frac{1}{2}\left[\hat{A}_j^\dagger\hat{A}_j, \hat{\rho}_S\right]_+\right)}_{=\mathcal{L}_D\,\hat{\rho}_S} \quad , \tag{2.77}$$

with anti-commutator, $\left[\hat{A}_j^\dagger\hat{A}_j, \hat{\rho}_S\right]_+ = \hat{A}_j^\dagger\hat{A}_j\hat{\rho}_S + \hat{\rho}_S\hat{A}_j^\dagger\hat{A}_j$. The first term, $\mathcal{L}_0\,\hat{\rho}_S$, on the right-hand side of Eq.(2.77) constitutes the unitary time-evolution of the reduced system,

which is generated by the system Hamiltonian $\hat{H}_S$. The second term, $\mathcal{L}_D\,\hat{\rho}_S$, relates to the non-unitary dissipator, $\mathcal{L}_D$, which induces dissipation and decoherence in the system. The latter are induced by Lindblad operators, $\hat{A}_j = \sqrt{\gamma_j}\,\hat{C}_j$, with rates, γ_j, and projectors, $\hat{C}_j(\hat{C}_j^\dagger)$, acting on the subsystem Hilbert space, respectively. The Lindblad operators induces transitions between system eigenstates with rates γ_j. Thus, the dissipator implicitly accounts for the action of a (Markovian) bath coupled to the reduced system. Specific examples for reduced system density operator dynamics with rates, γ_j, and projectors, $\hat{C}_j$, are provided in Ch.4 and Appendix C.

The benefit of Eqs.(2.75) to (2.77) manifests in a significantly smaller Hilbert space, *i.e.*, only the system Hilbert space is relevant, which allows to handle the exponential scaling efficiently from a numerical perspective. However, this gain comes at the cost of a series of approximations, which are inherit in the LvN-equation in Lindblad form[53]: The *Born-Markov* approximation and the *secular* approximation, respectively. The former imposes a product structure on the full density operator, $\hat{\rho}(t) = \hat{\rho}_S(t) \otimes \hat{\rho}_B(t)$, for all times t, which is equivalent to a weak system-bath interaction (Born), and assumes the bath correlations to decay significantly faster than a characteristic time-scale of the system dynamics. Hence, "memory" effects in the bath (Markov) are neglected, *i.e.*, Eq.(2.75) with Eq.(2.76) is local in time. Finally, the LvN-equation in Lindblad form respects the secular approximation, which resembles the *rotating-wave-approximation* (RWA)[53], and neglects energy non-conserving contributions in the system-bath interaction. Hence, a unidirectional energy-flow from the system to the bath is provided at $T = 0\,\mathrm{K}$. Notably, at finite temperature there is no unidirectional energy-flow as the system can be thermally excited.

Reduced System Properties

We access properties of the reduced system density operator, in particular purity, von Neumann-entropy and an system energy current. The purity of the reduced system is given by

$$p_s(t) = \mathrm{tr}_S\{\hat{\rho}_S^2(t)\} \leq 1 \quad , \tag{2.78}$$

where the equality holds only, if $\hat{\rho}_S(t)$ corresponds to a *pure* state, *e.g.*, $\hat{\rho}_S = |s\rangle\langle s|$ with some eigenstate $|s\rangle$ of the system. Otherwise the reduced system is referred to being in a *mixed* state. Further, the complementary von Neumann-entropy is defined as[53]

$$S_{\mathrm{vN}}(t) = -k_B\,\mathrm{tr}_S\{\hat{\rho}_S(t)\ln\hat{\rho}_S(t)\} \geq 0 \quad , \tag{2.79}$$

which measures the entanglement between the reduced system and the surrounding bath degrees of freedom. The equality $S_{\mathrm{vN}}(t) = 0$ holds, either if the full system-bath wave function $|\Psi_{\mathrm{SB}}(t)\rangle$ is in a product state, *i.e.*, $|\Psi_{\mathrm{SB}}(t)\rangle = |\Psi_S(t)\rangle\,|\Psi_B(t)\rangle$, which is non-entangled by definition, or if $\hat{\rho}_S(t)$ resembles a pure state. Finally, inspired by Ref.[58], a system energy current is introduced as

$$\mathcal{J}_S(t) = \frac{\partial}{\partial t}\langle\hat{H}_S\rangle(t)\begin{cases} < 0, & S \to B \\ > 0, & S \leftarrow B \end{cases} \quad , \tag{2.80}$$

which allows to quantify both the magnitude and the direction of the energy transfer between system and bath. We use the convention $\mathcal{J}_S(t) < 0$ for an energy-flow directed from the system to the bath ($S \rightarrow B$) and $\mathcal{J}_S(t) > 0$ for the reverse process ($S \leftarrow B$), respectively.

2.3.2 Multiconfigurational Time-Dependent Hartree Theory

In this thesis, we approach the time-evolution of molecular and hybrid light-matter systems for $T \geq 0\,\mathrm{K}$ numerically by means of the multiconfigurational time-dependent Hartree method[59, 60, 61, 62, 63, 64, 65] and its multilayer extension[68, 69, 70, 71, 72]. The MCTDH approach was initially formulated for distinguishable DoF and the zero-temperature regime, but later extended to many-body theory of indistinguishable particles[85, 86, 87, 88, 89, 90, 91, 92, 93] and the finite temperature regime comprising stochastic approaches[95, 96, 97, 98, 99] and density operator theory[105, 106, 107, 108, 109], respectively. In the following, we discuss the basics of the MCTDH ansatz and its extensions as implemented in the Heidelberg MCTDH package[84].

The MCTDH Ansatz

The MCTDH ansatz for a f-dimensional vibrational wave function is given by[61, 63]

$$|\psi_v(t)\rangle = \sum_{j_1=1}^{n_1} \cdots \sum_{j_f=1}^{n_f} A_{j_1 \ldots j_f}(t) \prod_{\kappa=1}^{f} |\varphi_{j_\kappa}^{(\kappa)}(t)\rangle \quad , \tag{2.81}$$

with tensorial coefficients, $A_{j_1 \ldots j_f}(t)$, and time-dependent, orthonormal single-particle functions (SPFs), $|\varphi_{j_\kappa}^{(\kappa)}(t)\rangle$, respectively. The advantage of the MCTDH ansatz manifests in the flexibility of time-dependent SPFs, which mitigates the exponential scaling of the standard approach in Eq.(2.67) as in general $n_\kappa < N_\kappa$.
The time-evolution of coefficients and SPFs is determined by a set of non-linear equations of motion (EoM) derived from the Dirac-Frenkel variational principle (DFVP)[100, 101]

$$\langle \delta\psi(t) | \mathrm{i}\hbar \frac{\partial}{\partial t} - \hat{H} | \psi(t) \rangle = 0 \quad , \tag{2.82}$$

for a wave packet, $|\psi(t)\rangle$, expanded as in Eq.(2.81), which leads to EoM[63, 65]

$$\begin{aligned} \mathrm{i}\hbar \dot{A}_J &= \sum_L \langle \Phi_J | \hat{H} | \Phi_L \rangle \, A_L \\ \mathrm{i}\hbar \, |\dot{\varphi}_j^{(\kappa)}\rangle &= \left(1 - \hat{P}^{(\kappa)}\right) \sum_{k,l=1}^{n_\kappa} \left(\boldsymbol{\rho}^{(\kappa)^{-1}}\right)_{jk} \langle \hat{H} \rangle_{kl}^{(\kappa)} \, |\varphi_l^{(\kappa)}\rangle \end{aligned} \quad , \tag{2.83}$$

which are norm- and energy-conserving for time-independent Hamiltonians.[63] In the first line of Eq.(2.83), J and L are composite indices, *i.e.*, $J = (j_1, \ldots, j_f)$ and $L = (l_1, \ldots, l_f)$, while in the second line, $|\dot{\varphi}_j^{(\kappa)}\rangle$ denotes a time-derivative of a SPF, $\hat{P}^{(\kappa)}$ is a projector on the

κ^{th}-mode's subspace spanned by the SPFs, $\langle \hat{H} \rangle_{kl}^{(\kappa)}$ are the corresponding mean-fields and $\boldsymbol{\rho}^{(\kappa)^{-1}}$ is the inverted density matrix, respectively. In order to numerically solve Eqs.(2.83), the SPFs are regularly expanded in a basis of time-independent, orthonormal primitive basis functions

$$|\varphi_{j_\kappa}^{(\kappa)}(t)\rangle = \sum_{i_\kappa=1}^{N_\kappa} B_{j_\kappa i_\kappa}^{(\kappa)}(t)\, |\chi_{i_\kappa}^{(\kappa)}\rangle \quad , \tag{2.84}$$

with basis size N_κ and time-dependent coefficients, $B_{j_\kappa i_\kappa}^{(\kappa)}(t)$, respectively. In this thesis, we consider basis functions, $|\chi_{i_\kappa}^{(\kappa)}\rangle$, either in terms of a discrete variable representation (DVR) or in terms of bosonic number states, when employing second quantization representation (SQR), respectively.
The MCTDH expansion in Eq.(2.81) can be interpreted as decomposition of the standard approach coefficient tensors, $C_{i_1 \ldots i_f}(t)$, in Eq.(2.67) according to[52, 66]

$$C_{i_1 \ldots i_f}(t) = \sum_{j_1=1}^{n_1} \cdots \sum_{j_f=1}^{n_f} A_{j_1 \ldots j_f}(t) \prod_{\kappa=1}^{f} B_{j_\kappa i_\kappa}^{(\kappa)}(t) \quad , \tag{2.85}$$

which corresponds to a Tucker tensor decomposition[67] of $C_{i_1 \ldots i_f}(t)$ and is diagrammatically depicted in Fig.2.3. Here, the orthonormal tensor $A_{j_1 \ldots j_f}$ constitutes the *root node*,

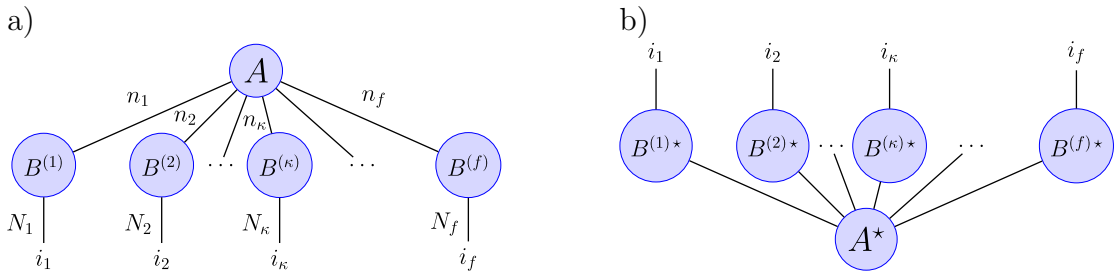

Figure 2.3: Diagrammatic representation of (a) the MCTDH expansion in Eq.(2.81) with "virtual" bond dimensions, n_κ, equivalent to the number of SPFs and physical dimensions, N_κ, equivalent to primitive basis functions and (b) diagrammatic representation of corresponding bra-state where, n_κ and N_κ, are assumed implicitly.

which shares "virtual" bonds characterized by *bond dimensions*, n_κ, resembling the number of SPFs with nodes $B_{j_\kappa i_\kappa}$, respectively. The standard approach Eq.(2.67) is recovered by summing over "virtual" indices j_κ in Eq.(2.85), which corresponds to a *contraction* of virtual bonds in Fig.2.3(a) reproducing Fig.2.1(a) with "physical" indices i_κ, respectively.
An extension of the MCTDH ansatz to vibronic problems is given by the *multi-set formalism*, which straightforwardly follows from Eq.(2.68) by expanding the state-dependent vibrational wave packets, $|\psi_v^{i_e}(t)\rangle$, via the MCTDH ansatz in Eq.(2.81).

Mode-Combination

It is instructive to recognize, that the MCTDH expansion resembles a partitioning of the f-dimensional vibrational Hilbert space as a tensor product of the form[89]

$$\mathcal{H}_v(f) = \mathcal{H}_v^{(1)}(1) \otimes \mathcal{H}_v^{(2)}(1) \otimes \cdots \otimes \mathcal{H}_v^{(f)}(1) \quad , \tag{2.86}$$

where $\mathcal{H}_v^{(\kappa)}(1)$ is the vibrational single-mode subspace of the κ^{th}-mode, respectively. However, this partitioning is not unique and can be generalized by grouping single-mode subspaces into multi-mode subspaces[63, 68, 108]

$$\mathcal{H}_v(f) = \mathcal{H}_v^{(1)}(d_1) \otimes \mathcal{H}_v^{(2)}(d_2) \otimes \cdots \otimes \mathcal{H}_v^{(p)}(d_p) \quad , \tag{2.87}$$

with $\sum_{\kappa=1}^{p} d_\kappa = f$ where $p < f$, such that $\mathcal{H}_v^{(\kappa)}(d_\kappa)$ is a d_κ-dimensional subspace. Accordingly, the MCTDH-expansion in single-mode SPFs (*cf.* Eqs.(2.81) and (2.84)) is also not unique, which leads to the concept of *mode-combination* in terms of multi-mode SPFs as given by

$$|\varphi_{j_\kappa}^{(\kappa)}(t)\rangle = \sum_{i_1=1}^{N_1} \cdots \sum_{i_{d_\kappa}=1}^{N_{d_\kappa}} B_{j_\kappa i_1 \ldots i_{d_\kappa}}^{(\kappa)}(t) \, |\chi_{i_1}^{(\kappa)}\rangle \ldots |\chi_{i_{d_\kappa}}^{(\kappa)}\rangle \quad , \tag{2.88}$$

which span the corresponding d_κ-dimensional multi-mode subspace. A corresponding MCTDH expansion is diagrammatically depicted in Fig.2.4, where an example with two-dimensional SPFs, conveniently denoted as *combined modes*, is considered.

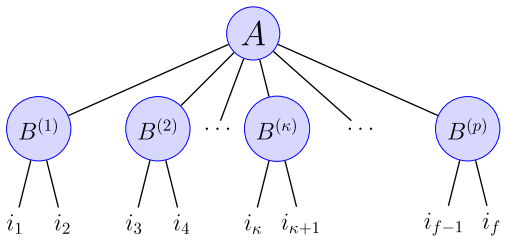

Figure 2.4: Exemplary diagrammatic representation of a MCTDH expansion including combined modes. Number of SPFs, n_κ, and primitive basis functions, N_κ, are assumed implicitly.

The advantage of the mode-combination scheme manifests in a significantly shorter A-vector in Eq.(2.83), which allows for a more efficient study of larger systems. However, this benefit comes at the cost of multidimensional SPFs, which need to be propagated at higher numerical effort, such that only a small number of modes should be combined in order to balance the benefits and disadvantages of mode-combination.[63]

The Multilayer Scheme

The mode-combination scheme leads to the multilayer extension of MCTDH (ML-MCTDH)[68, 69, 70, 71, 72], which has been shown to be a very powerful method for approaching high-dimensional problems[73, 74, 75, 76, 77, 78, 79, 80, 81, 82, 83] and belongs to the more

general family of tree tensor network states (TTNS)[52]. In the ML-MCTDH approach, multi-mode SPFs are not expanded in a basis of time-independent primitive basis functions but rather in a new basis of time-dependent SPFs

$$|\varphi_{j_\kappa}^{(1;\kappa)}(t)\rangle = \sum_{l_1=1}^{m_1} \cdots \sum_{l_{d_\kappa}=1}^{m_{d_\kappa}} A_{l_1 \ldots l_{d_\kappa}}^{(2;\kappa,j_\kappa)}(t) \prod_{\kappa'=1}^{d_\kappa} |\varphi_{l_{\kappa'}}^{(2;\kappa,j_\kappa)}(t)\rangle \quad , \tag{2.89}$$

where SPFs, $|\varphi_{l_{\kappa'}}^{(2;\kappa,j_\kappa)}(t)\rangle$, now form a third layer in the expansion of the f-dimensional vibrational wave packet $|\psi_v(t)\rangle$, respectively. The SPFs of the new layer may subsequently be expanded in yet another set of SPFs constituting a fourth-layer, which underlines the recursive character of this approach. The expansion is truncated by introducing a time-independent primitive basis as in Eqs.(2.84) or (2.88), which results in a tree with L layers, where the primitive one does not count as an individual layer here.[63] The diagrammatic

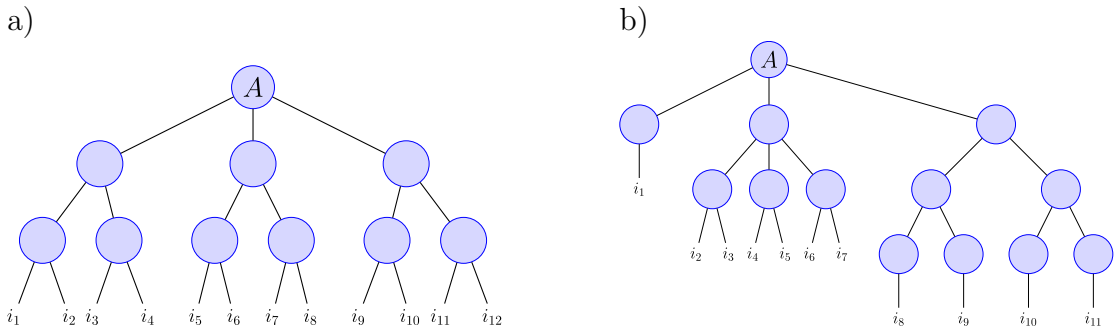

Figure 2.5: Exemplary diagrammatic representations of multilayer expansions for (a) a symmetric three-layer tree and (b) a highly asymmetric tree with three- and four-layer sub-trees. Number of SPFs, n_κ, and primitive basis functions, N_κ, are assumed implicitly.

representation of wave functions is particularly instructive for the ML-MCTDH approach due to its complexity and the resulting diagrams are known as "ML-trees" in the MCTDH community.[69] In Fig.2.5, two different examples for multilayer trees are shown: A symmetric tree with three layers on the left-hand side and a highly asymmetric tree, which has three- and four-layer sub-trees, respectively, on the right-hand side. From the perspective of tensor decomposition, the ML-MCTDH approach corresponds to a hierarchical Tucker decomposition[67] of the rank-f tensor $C_{i_1 \ldots i_f}(t)$ in the standard approach, Eq.(2.67). Notably, the "standard" MCTDH expansion in Eq.(2.81) resembles a two-layer tree in the language of ML-MCTDH.

Improved and Block-Improved Relaxation

The MCTDH approach is not restricted to real-time evolution but applies equivalently to imaginary-time problems, which allows to access the calculation of bound states. The imaginary-time TDSE governing the energy relaxation dynamics reads[102]

$$\hbar \frac{\partial}{\partial \tau} |\psi(\tau)\rangle = \hat{H} |\psi(\tau)\rangle \quad , \tag{2.90}$$

where an initial vibrational wave packet is propagated in imaginary time, $\tau = -\mathrm{i}\,t$, which allows to access the ground state of the system in case the initial state shows a partial overlap with the ground state. In this thesis, we employed the improved relaxation and the block-improved relaxation (BIR) schemes, which allow for a more efficient calculation of the ground state and the calculation of excited states, respectively.[103, 104] For the MCTDH-BIR approach, the A-vector is obtained as eigenvector of the Hamiltonian represented a basis of SPFs, H_{JK}, according to[63]

$$\sum_K H_{JK}\, A_K = E\, A_J \quad , \tag{2.91}$$

whereas the SPFs, $|\varphi_j^{(\kappa)}(\tau)\rangle$, are propagated in negative imaginary time

$$\hbar\, |\dot{\varphi}_j^{(\kappa)}\rangle = -\left(1 - \hat{P}^{(\kappa)}\right) \sum_{k,l=1}^{n_\kappa} \left(\boldsymbol{\rho}^{(\kappa)^{-1}}\right)_{jk} \langle \hat{H} \rangle_{kl}^{(\kappa)}\, |\varphi_l^{(\kappa)}\rangle = 0 \quad . \tag{2.92}$$

Here, $|\dot{\varphi}_j^{(\kappa)}\rangle$ denotes here a derivative with respect to τ, respectively. In this thesis, we employ the improved and block-improved relaxation approaches to calculate ground and excited vibro-polaritonic states of effective vibrational Pauli-Fierz Hamiltonians.

Density Operator MCTDH

The MCTDH approach has been generalized to time-evolution of density operators[105, 106, 107, 108], denoted as ρMCTDH . In the following, we consider the ρMCTDH(2) approach (type-2 density operator), where the vibrational density operator $\hat{\rho}_v(t)$ of a f-dimensional vibrational problem is written as[105]

$$\hat{\rho}_v(t) = \sum_{j_1,l_1=1}^{n_1} \cdots \sum_{j_f,l_f=1}^{n_f} B_{j_1 \ldots j_f, l_1 \ldots l_f}(t) \prod_{\kappa=1}^{f} |\varphi_{j_\kappa}^{(\kappa)}(t)\rangle\, \langle \varphi_{l_\kappa}^{(\kappa)}(t)| \quad , \tag{2.93}$$

with hermitian coefficients, $B_{j_1 \ldots j_f, l_1 \ldots l_f}(t)$, and "ket-bra"-products of SPFs. The latter relate to single-particle density operators (SPDOs), $\hat{\sigma}_{\tau_\kappa}^{(\kappa)}(t)$, via

$$|\varphi_{j_\kappa}^{(\kappa)}(t)\rangle\, \langle \varphi_{l_\kappa}^{(\kappa)}(t)| = \hat{\sigma}_{\tau_\kappa}^{(\kappa)}(t) \quad , \tag{2.94}$$

with composite index $\tau_\kappa = (j_\kappa, l_\kappa)$, where the SPDOs determine the type-1-version of ρMCTDH, *i.e.*, ρMCTDH(1). The SPFs are subsequently represented in a time-independent primitive basis as in Eq.(2.84) and in analogy with Fig.2.3, a diagrammatic representation of Eq.(2.93) can be introduced as shown in Fig.2.6.
The EoM are derived by employing the Dirac-Frenkel/MacLachlan variational principle in combination with the Liouville space formulation of density operator theory[105]

$$\langle\langle \delta\hat{\rho} | \dot{\hat{\rho}} - \mathcal{L}(\hat{\rho}) \rangle\rangle = 0 \quad , \tag{2.95}$$

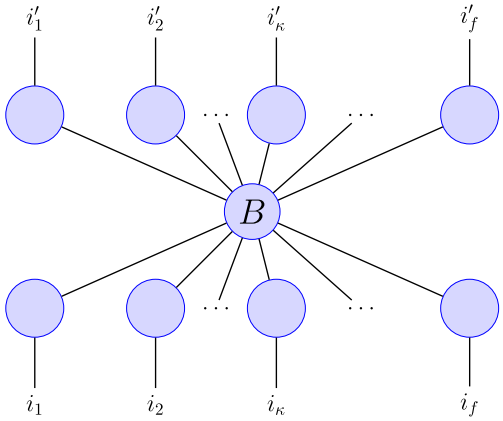

Figure 2.6: Diagrammatic representation of the ρMCTDH expansion in Eq.(2.93) for type-2 density operators. Number of SPFs, n_κ, and primitive basis functions, N_κ, are assumed implicitly.

where $\mathcal{L}$ is the Liouvillian, which has been given for closed systems by $\mathcal{L}_0(\hat{\rho}) = -\frac{\mathrm{i}}{\hbar}[\hat{H}, \rho]$ in Eq.(2.76) and is augmented by $\mathcal{L}_D(\hat{\rho})$ for open systems following Lindblad dynamics (*cf.* Sec.2.3.1). The ρMCTDH approach has been applied to relatively small problems with a couple of vibrational modes and/or electronic states due to the strong exponential scaling of density operator propagation.[105, 106, 110, 111]

2.4 Thermal Reaction Rate Theory

In the last part of this theory section, we turn to the time-independent quantum theory of thermal reaction rates, which is applied to the study of coupled light-matter hybrid systems in molecular cQED.

2.4.1 The Cumulative Reaction Probability Approach

A fully quantum mechanical approach to thermal reaction rates, which takes a scattering-type perspective, defines the thermal rate constant, $k(T, \eta)$, in terms of a cumulative reaction probability (CRP), $N(E, \eta)$, as[112, 113]

$$k(T,\eta) = \frac{1}{2\pi\hbar\, Q_R(T,\eta)} \int_0^\infty N(E,\eta)\, e^{-\beta E}\, \mathrm{d}E \quad , \tag{2.96}$$

which here explicitly depends on η, as introduced in Eq.(2.50), that characterizes the light-matter interaction regime according to Eq.(2.51). Here, $Q_R(T, \eta)$ is the reactant partition function, which in harmonic approximation is given for a collection of f classical oscillators

by

$$Q_R(T,\eta) = \prod_{\kappa=1}^{f} \underbrace{\left(1 - e^{-\beta\hbar\omega_R^{(\kappa)}(\eta)}\right)^{-1}}_{=Q_R^{(\kappa)}(T,\eta)} \quad , \tag{2.97}$$

with single-mode harmonic partition functions, $Q_R^{(\kappa)}(T,\eta)$, and corresponding harmonized reactant frequencies, $\omega_R^{(\kappa)}$, respectively. We note, a different notation for the harmonic partition functions is chosen in this section to distinguish them from the general partition function, $Z(\beta)$, in Eq.(2.71). Further, the CRP accounts for both quantum tunneling and anharmonicites of the transition state region. In order to calculate the CRP, a Green's function approach with absorbing boundary conditions (ABC) formalism is employed in this thesis.[114, 115] Accordingly, the CRP is evaluated as

$$N(E,\eta) = \mathrm{tr}\left\{\hat{\Gamma}_R\,\hat{G}(E,\eta)\,\hat{\Gamma}_P\,\hat{G}^\dagger(E,\eta)\right\} \quad , \tag{2.98}$$

where the trace runs over a basis spanning the vibro-polaritonic Hilbert space. Further, $\hat{G}(E,\eta)$ is the vibro-polaritonic Green's function

$$\hat{G}(E,\eta) = \left(E - \hat{H} + \frac{\mathrm{i}}{2}\hat{\Gamma}\right)^{-1} \quad , \tag{2.99}$$

with vibrational Pauli-Fierz Hamiltonian, $\hat{H}$, as defined in Eq.(2.64) and $\hat{\Gamma}$ is a *complex absorbing potential* (CAP)

$$\hat{\Gamma} = \hat{\Gamma}_R + \hat{\Gamma}_P \quad , \tag{2.100}$$

with contribution located in the reactant region, $\hat{\Gamma}_R$, and the product region, $\hat{\Gamma}_P$, of the cavity potential energy surface. Explicit examples for CRP, $N(E,\eta)$, corresponding rates, $k(T,\eta)$, and complex absorbing potentials, $\hat{\Gamma}_R$ and $\hat{\Gamma}_P$, are given in Ch.3 and Appendix B.

2.4.2 Eyring Transition State Theory

An approximate but well-known framework to thermal reaction rates is provided by Eyring transition state theory (TST). Eyring TST is based on the assumption of an equilibrium between reactants and the activated complex, the absence of barrier-recrossing from the product state and the neglect of quantum tunneling effects, respectively. The corresponding thermal rate constant is written as[117]

$$k^{\mathrm{TST}}(T,\eta) = \frac{1}{2\pi\hbar\beta}\,\frac{Q^\ddagger(T,\eta)}{Q_R(T,\eta)}\,\exp\!\left(-\beta\Delta E_{\mathrm{eff}}^a(\eta)\right) \quad , \tag{2.101}$$

which in molecular cQED additionally depends on the light-matter coupling indicated by η. Here, $Q_R(T,\eta)$ is the classical harmonic reactant partition function as given in Eq.(2.97) and $Q^\ddagger(T,\eta)$ is the classical transition state partition function, here also in harmonic approximation,

$$Q^\ddagger(T,\eta) = \prod_{\kappa=1}^{f-1} \underbrace{\left(1 - e^{-\beta\hbar\bar{\omega}_\kappa^\ddagger(\eta)}\right)^{-1}}_{=Q_\kappa^\ddagger(T,\eta)} \quad , \tag{2.102}$$

with harmonic frequencies, $\bar{\omega}_\kappa^\ddagger$, of f-1 bound modes at the transition state. Further, $\Delta E_{\text{eff}}^a(\eta)$ in Eq.(2.101) is an effective activation energy taking into account quantum corrections, which is defined as

$$\Delta E_{\text{eff}}^a = E_{cl}^a + E_0^\ddagger(\eta) - E_R^0(\eta) \quad , \tag{2.103}$$

with classical activation energy, E_{cl}^a, as well as both harmonic transition state and reactant zero-point energies

$$E_0^\ddagger(\eta) = \sum_{\kappa=1}^{f-1} \frac{\hbar\bar{\omega}_\kappa^\ddagger(\eta)}{2} \quad , \qquad E_R^0(\eta) = \sum_{i=\kappa}^{f} \frac{\hbar\omega_R^{(\kappa)}(\eta)}{2} \quad . \tag{2.104}$$

In general molecular cQED settings, both $E_0^\ddagger(\eta)$ and $E_R^0(\eta)$ are functions of the light-matter interaction as the cPES varies with η. Naturally, $k^{\text{TST}}(T,\eta)$ does not account for quantum tunneling opposed to the fully quantum mechanical rates in Eq.(2.96). An approximative way, to account for tunneling in Eyring TST is given by the Wigner correction

$$\kappa_W(T,\eta) = 1 + \frac{1}{24}\left(\beta\,\hbar|\omega^\ddagger|\right)^2 \quad , \tag{2.105}$$

which depends on the imaginary "barrier" frequency, $|\omega^\ddagger|$, at the transition state, and is used as a prefactor on the right-hand side of Eq.(2.101). In the molecular cQED framework, $|\omega^\ddagger|$ generally depends on the light-matter interaction regimes and so does the Wigner correction factor, $\kappa_W(T,\eta)$, respectively.

2.4.3 Thermodynamic Perspective of Eyring TST

Adopting a thermodynamic perspective, the Eyring rate constant can be rewritten as[116, 118]

$$k^{\text{TST}}(T,\eta) = \frac{1}{2\pi\hbar\beta}\exp\Big(-\beta\Delta G^\ddagger(T,\eta)\Big) \quad , \tag{2.106}$$

where the Gibbs activation free energy, $\Delta G^\ddagger(T,\eta)$, depends on the light-matter coupling and is given by

$$\Delta G^\ddagger(T,\eta) = \Delta H^\ddagger(T,\eta) - T\,\Delta S^\ddagger(T,\eta) \tag{2.107}$$

with activation enthalpy[118]

$$\Delta H^\ddagger(T,\eta) = E_{\text{eff}}^a(\eta) - R\,T \quad , \tag{2.108}$$

and activation entropy, $\Delta S^\ddagger(T,\eta)$, respectively. The thermal rate constant in Eq.(2.106) can now be rewritten as

$$k^{\text{TST}}(T,\eta) = \frac{1}{2\pi\hbar\beta}\exp\left(1 + \frac{\Delta S^\ddagger(T,\eta)}{R}\right)\exp\Big(-\beta\Delta E_{\text{eff}}^a(\eta)\Big) \quad , \tag{2.109}$$

and by comparison with Eq.(2.101), one identifies

$$\exp\left(1 + \frac{\Delta S^\ddagger(T,\eta)}{R}\right) = \frac{Q^\ddagger(T,\eta)}{Q_R(T,\eta)} \quad . \tag{2.110}$$

The latter equation allows to obtain an explicit expression for the activation entropy in terms of classical harmonic partition functions[118]

$$\Delta S^{\ddagger}(T,\eta) = R\left(\ln\left(\frac{Q^{\ddagger}(T,\eta)}{Q_R(T,\eta)}\right) - 1\right) \quad . \tag{2.111}$$

Hence, with $\Delta H^{\ddagger}(T,\eta)$ in Eq.(2.108) a thermodynamic characterization of Eyring TST thermal rates is obtained from the parameters determining Eq.(2.101).

Chapter 3

Vibrational Polaritons in Small Molecules

3.1 Motivation

Traditionally, quantum electrodynamics only played a minor role in molecular sciences as for example in spontaneous emission processes and radiative corrections relevant for high-resolution spectroscopy.[12] This paradigm changed significantly after a series of seminal experiments by Ebbesen and coworkers, who employed optical cavities to reveal the impact of fully quantized light-molecule interactions on chemistry[119, 120, 121, 122] and spectroscopy[123, 124, 125]. Hereafter, the concepts of *electronic strong coupling* (ESC) and *vibrational strong coupling* (VSC) have been established related to whether the cavity field influences photochemistry or thermal ground state chemistry. From a conceptual perspective, strong coupling effects manifest in the rather peculiar concept of light-matter hybrid states, which emerge from the mixing of either electronic or vibrational states with bound states of quantized electromagnetic field modes of optical cavities.[126]
The experimental success induced a significant theoretical effort aiming at a detailed understanding of both ESC and VSC. In combination with experiment, the recently rapidly growing, highly interdisciplinary field of *polaritonic chemistry* was born.[127, 128] The influence of electronic strong coupling on charge transfer processes, photochemistry and electronic spectroscopy, see for example Refs.[129, 130, 131, 132, 133, 134, 135, 136, 137, 138, 24, 139, 140, 141, 142, 143, 144, 145, 146], has been successfully approached by merging concepts from molecular quantum mechanics beyond the BOA and cavity QED. In contrast, the nature of vibrational strong coupling and especially its role in polaritonic chemistry is still under dispute, which recently culminated in a series of articles reviewing the state of the art and pointing at theoretical challenges.[147, 148, 149, 150, 151]
From the broader perspective of system-bath type problems, the vibrational strong coupling scenario can be interpreted as interaction of a molecular system with a "bath" of quantized cavity field modes. However, characteristically the "bath" is here only composed of a few modes and more importantly (ultra)strongly coupled to the molecular vibrations. The latter means that the interaction energy is a significant fraction of characteristic fundamental transition energies in the subsystems. Notably, such a coupling situation renders the system-bath type system to be more accurately described as highly entangled composite

entity, characterized by hybrid states combining properties of both system and bath. A rather contrary scenario characterized by a high-dimensional but only weakly coupled bath, will be discussed in Ch.4.

In the first part of this thesis, we aim at contributing to resolve open questions in VSC polaritonic chemistry by studying the (ultra)strong interactions of molecular vibrations with quantized field modes in an optical Fabry-Pérot cavity for selected model systems. In section 3.2, we will discuss ground and excited state properties for anharmonic vibrational polaritons formed in small molecules via the interaction with a single cavity mode. In particular, we provide a thorough discussion of the influence of the dipole self-energy contribution in the effective vibrational Pauli-Fierz Hamiltonian on different ground and exited state properties of model light-matter hybrid system. In section 3.3, we will lift the restriction of fixed molecular orientation and provide a detailed model study of a rovibrating diatomic and its orientation dependent interaction with doubly degenerate, orthogonally polarized cavity modes. By combining ideas from beyond-BOA quantum mechanics and quantum vibrational dynamics, we identify three-state vibro-polaritonic conical interactions and rovibropolaritonic light-matter hybrid states in corresponding infrared spectra. In the final section 3.4, we will address the influence of VSC on a minimal thermal isomerization model. From a combined analysis based on quantum reaction rate theory and dynamical considerations, we examine the influence of quantum effects on cavity-suppressed inversion rates and identify a dynamical reactant localization manifesting as cavity-molecule resonance effect.

3.2 Ground and Excited State Properties

We discuss ground and excited state properties of anharmonic vibrational polaritons formed in small molecules and thoroughly examine the role of the dipole self-energy term in the effective vibrational Pauli-Fierz Hamiltonian. As model systems, we consider molecular vibrational model systems for anharmonic Morse-type and symmetric double-well potentials, which interact with a single cavity mode. The single-mode limit is realized by aligning the molecular dipole moment with a cavity polarization vector as shown in Fig.3.1. The resulting minimal two-dimensional models systems are discussed with respect to ground and excited state properties. Excited states are accessed by means of autocorrelation-function based vibro-polaritonic infrared spectra. Particularly, we will discuss the dipole self-energy and its impact on both vibro-polaritonic properties and spectra as its relevance has been thoroughly discussed in Refs.[26, 27], but was neglected in recent studies on anharmonic vibrational polaritons[49, 153].

Results discussed in this chapter are reproduced from "E.W. Fischer, P. Saalfrank. Ground state properties and infrared spectra of anharmonic vibrational polaritons of small molecules in cavities. *J. Chem. Phys.* **154**, 104311, (2021)."[152] with permission of AIP Publishing.

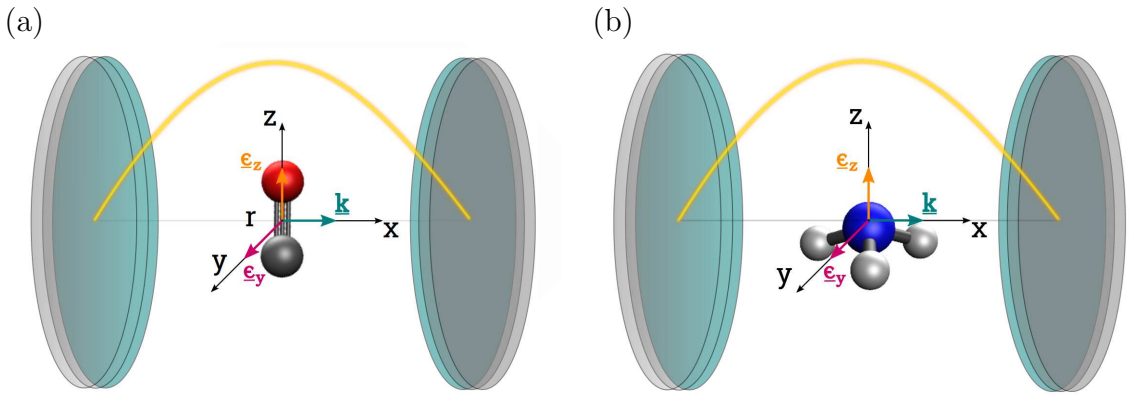

Figure 3.1: Schematic sketch of (a) a diatomic molecule with vibrational coordinate, r, and (b) the ammonia molecule in an optical two-mode cavity with polarization vectors $\underline{\epsilon}_z, \underline{\epsilon}_y$, wavevector, $\underline{k}$, and molecular space-fixed frame with axis x, y, z. In the single-mode limit, both molecules couple exclusively to the z-polarized cavity mode and molecular rotations are neglected.

3.2.1 Molecular Model Systems

We consider the stretching mode in LiH, a localized OH-stretching mode in a deuterated water molecule (HOD) and a one-dimensional model for the ammonia inversion mode, which all couple via their respective nonlinear dipole functions to a single cavity mode. The LiH- and OH-stretching modes provide paradigmatic examples for Morse-type medium and high frequency anharmonic molecular potentials, whereas the NH_3 inversion mode resembles a prototypical symmetric double-well potential. The resulting minimal two-mode problems are described by a two-dimensional effective vibrational Pauli-Fierz Hamiltonian

$$\hat{H} = \hat{H}_S + \hat{H}_C + \hat{H}_{SC} \quad , \tag{3.1}$$

where the first term resembles the molecular "system" Hamiltonian

$$\hat{H}_S = -\frac{\hbar^2}{2\mu}\frac{\partial^2}{\partial q^2} + V(q) \quad , \tag{3.2}$$

with molecular coordinate, q, and reduced mass, μ. The second term in Eq.(3.1) is the single-mode cavity Hamiltonian in coordinate representation

$$\hat{H}_C = -\frac{\hbar^2}{2}\frac{\partial^2}{\partial x_c^2} + \frac{\omega_c^2}{2}x_c^2 \quad , \tag{3.3}$$

with cavity displacement coordinate, x_c, and harmonic cavity mode frequency, ω_c. Finally, the third term, $\hat{H}_{SC}$, combines the bare light-matter interaction, $\Delta\hat{H}_{SC}$, and the dipole self-energy, $\hat{H}_{DSE}$, as

$$\hat{H}_{SC} = \Delta\hat{H}_{SC} + \hat{H}_{DSE} = \sqrt{\frac{2\omega_c}{\hbar}}\, g\, x_c\, d(q) + \frac{g^2}{\hbar\omega_c} d^2(q) \quad , \tag{3.4}$$

with light-matter interaction strength, g, and molecular dipole function, $d(q)$, respectively. We recall, according to Eq.(2.50) the light-matter interaction strength, g, can be expressed in terms of a dimensionless parameter, η, which in turn allows to characterize the VSC and VUSC regimes following Eq.(2.51).
Molecular potentials, $V(q)$, molecular dipole functions, $d(q)$, and energetically lowest lying eigenstates of the vibrational (model) systems considered here are depicted in Fig.3.2.

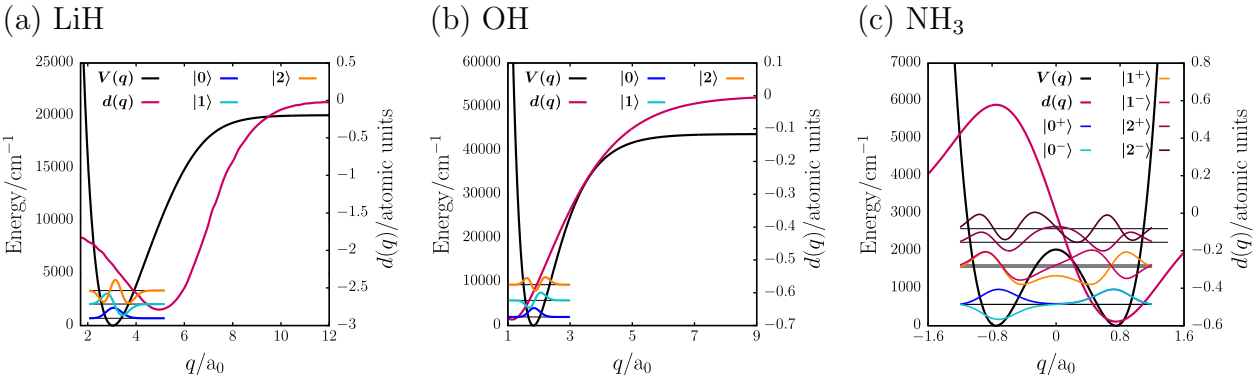

Figure 3.2: Molecular potential functions, $V(q)$, dipole functions, $d(q)$, and lowest lying eigenstates for a stretching modes in (a) LiH, (b) an OH-bond in HOD and (c) the NH_3 inversion mode.

The adiabatic ground state PES of LiH has been calculated on the CCSD(T)/cc-pVQZ level of theory as implemented in GAUSSIAN16[156]. The corresponding dipole function was taken from Ref.[157] and calculated on the FCI/cc-pVQZ level of theory. The OH-stretching mode is modeled by a Morse potential

$$V_{\mathrm{M}}(q) = D_e \left(e^{-a(q-q_e)} - 1\right)^2 \quad , \quad q \in [0.5, 9]\, a_0 \quad , \tag{3.5}$$

and the NH_3 inversion mode is modeled by a symmetric double-well potential

$$V_{\mathrm{DW}}(q) = A_0 + A_2\, q^2 + A_4\, q^4 \quad , \quad q \in [-1.6, 1.6]\, a_0 \quad , \tag{3.6}$$

with either, $V(q) = V_{\mathrm{M}}(q)$, or, $V(q) = V_{\mathrm{DW}}(q)$, in Eq.(3.2). Further, we consider a model dipole function of Mecke type[158, 159] for the OH-Morse oscillator

$$d_{\mathrm{M}}(q) = -\alpha\, q\, e^{-\beta\, q} \quad , \quad q \in [0.5, 9]\, a_0 \quad , \tag{3.7}$$

and an asymmetric model dipole function for the inversion mode

$$d_{\mathrm{DW}}(q) = -\gamma\, q\, e^{-\delta\, q^2} \quad , \quad q \in [-1.6, 1.6]\, a_0 \quad . \tag{3.8}$$

The ammonia inversion potential in Eq.(3.6) is given by a fourth-order polynomial in the inversion coordinate, with a barrier height of $A_0 = 9.249 \cdot 10^{-3}\, E_h = 2030\,\mathrm{cm}$ and a lowest tunneling splitting of $\hbar\omega_{0^+0^-} = 0.92\,\mathrm{cm}^{-1}$ (exp. $0.79\,\mathrm{cm}^{-1}$[160]). The corresponding dipole function in Eq.(3.8) is constructed such, that the maximal value is found at the

two double-well minima with $|d_0| = 1.47\,\mathrm{D} = 0.551\,ea_0$ in agreement with experiment[161], and a sign change occurs at the origin ($q = 0$). We note that both more accurate model potentials (*e.g.*, of Mannig form[162, 163]) and dipole functions[164] exist, however, our approximative treatment here is sufficient for our purposes. All parameters specifying $V_{\mathrm{M}}(q), V_{\mathrm{DW}}(q)$ and $d_{\mathrm{M}}(q), d_{\mathrm{DW}}(q)$ are provided in Tab.3.1, with reduced masses obtained as, $\mu = m_{\mathrm{H}} m_{\mathrm{OD}}/m_{\mathrm{HOD}}$, for the OH-bond and, $\mu = m_{3\mathrm{H}} m_{\mathrm{N}}/m_{\mathrm{NH_3}}$, for the ammonia inversion mode. For LiH, we find a reduced mass of, $\mu = m_{\mathrm{H}} m_{\mathrm{Li}}/m_{\mathrm{LiH}} = 1573.99\,m_e$.

Table 3.1: Parameters for molecular model potentials and dipole functions besides reduced masses for the OH-stretching[158, 159] and NH_3 inversion modes, respectively.

OH	μ/m_e	D_e/E_h	q_e/a_0	a/a_0^{-1}	$\alpha/\lvert e\rvert$	β/a_0^{-1}
	1728.54	0.1994	1.821	1.189	1.634	0.8818
NH_3	μ/m_e	A_0/E_h	$A_2/\mathrm{E}_h\,\mathrm{a}_0^{-2}$	$A_4/\mathrm{E}_h\,\mathrm{a}_0^{-4}$	$\gamma/\lvert e\rvert$	δ/a_0^{-2}
	4533.52	$9.249 \cdot 10^{-3}$	$-3.289 \cdot 10^{-2}$	$2.923 \cdot 10^{-2}$	1.271	0.8887

Here, we study (ultra)strongly coupled vibrational light-matter hybrid model systems for a cavity mode frequency, ω_c, chosen resonant to the fundamental (symmetry allowed) vibrational transition of the molecular mode, with details provided in Tab.3.2. We note, for the ammonia inversion model, the fundamental symmetry allowed transition is between the symmetric ground state $|0^+\rangle$ and the anti-symmetric first excited state, $|1^-\rangle$, due to symmetry reasons as discussed in detail below.

Table 3.2: Transition energies, $\hbar\omega_{fi}$, and transition dipole moments, d_{fi}, for the lowest allowed transitions, starting from the ground state, for all three model systems.

system	$\lvert i\rangle \rightarrow \lvert f\rangle$	$\hbar\omega_{fi}$ / cm^{-1}	d_{fi} / ea_0
LiH	$\lvert 0\rangle \rightarrow \lvert 1\rangle$	1348	0.092
OH	$\lvert 0\rangle \rightarrow \lvert 1\rangle$	3784	0.025
NH_3	$\lvert 0^+\rangle \rightarrow \lvert 1^-\rangle$	1039	0.027

Ground and excited vibro-polaritonic states as well as infrared spectra have been obtained via the MCTDH method as implemented in the Heidelberg MCTDH package[84], employing Block-Improved Relaxation and real-time evolution, respectively. Technical parameters for converged calculations are given in Tab.3.3. Further, we obtain infrared (IR) spectra as

$$\sigma(\omega) = \int_0^T C(t)\, f_W(t)\, e^{+i(\omega-\omega_0)t} e^{-(t/\tau)^2} \mathrm{d}t \quad , \tag{3.9}$$

Table 3.3: Number of SPFs n_s and n_c, Harmonic Oscillator (HO) DVR grid points m_s, m_c and DVR lattice endpoints q_0/q_f and x_{c0}/x_{cf} (given in atomic units) for the molecular system and the cavity mode, respectively, used for MCTDH calculations. Here, "s" stands for system and "c" for cavity mode.

	n_s	n_c	m_s	m_c	q_0/q_f	x_{c0}/x_{cf}
LiH (stretch)	24	24	251	151	$[1.7, 13.3]$	∓ 212.9
OH (stretch)	24	24	151	151	$[0.5, 9.0]$	∓ 127.1
NH_3 (inversion)	28	28	251	251	$[-1.6, +1.6]$	∓ 242.6

with $T = 2\,t_f$, ground-state energy off-set, $\hbar\omega_0$, damping time, $\tau \in \{500, 200, 1000\}$ fs, for LiH, OH and NH_3, respectively, and window function

$$f_W(t) = \left(1 - \frac{t}{T}\right) \cos\left(\frac{\pi}{T}\,t\right) + \frac{1}{\pi} \sin\left(\frac{\pi}{T}\,t\right) \quad . \tag{3.10}$$

The dipole-dipole autocorrelation function is given by[166]

$$C(t) = \int_{q0}^{qf} \int_{xc0}^{xcf} \psi^\star(q, x_c, 0)\, \psi(q, x_c, t)\, \mathrm{d}x_c\, \mathrm{d}q \quad , \tag{3.11}$$

with initial state, $\psi(q, x_c, 0) = d(q)\chi_0(q, x_c)$, where $\chi_0(q, x_c)$ is the vibro-polaritonic ground state of the effective vibrational Pauli-Fierz Hamiltonian and $d(q)$ is the dipole function of the respective molecular system.

3.2.2 Vibro-Polaritonic Ground State Properties

We first discuss properties of vibro-polaritonic ground states as function of η related to the light-matter interaction regime and examine their dependence on the dipole self-energy contribution. Explicitly, we consider the energy difference

$$\Delta\varepsilon_0 = \langle \hat{H} \rangle_0 - \langle \hat{H}_0 \rangle_0 \quad , \tag{3.12}$$

between the interacting vibro-polaritonic ground state energy, $\langle \hat{H} \rangle_0$, and its non-interacting zero-order counterpart, $\langle \hat{H}_0 \rangle_0$, with $\hat{H}_0 = \hat{H}_S + \hat{H}_C$ (*cf.* Eqs.(3.2) and (3.3)), and provide a detailed analysis of individual energetic contributions. Afterwards, we turn to dissociation energies, activation energies as well as equilibrium bond lengths and discuss their dependence on the DSE.

Vibro-Polaritonic Ground State Energy

Starting with the vibro-polaritonic ground state energy, we show $\Delta\varepsilon_0$ in the upper row of Fig.3.3 for all model system as function of η as obtained with and without the DSE contribution.

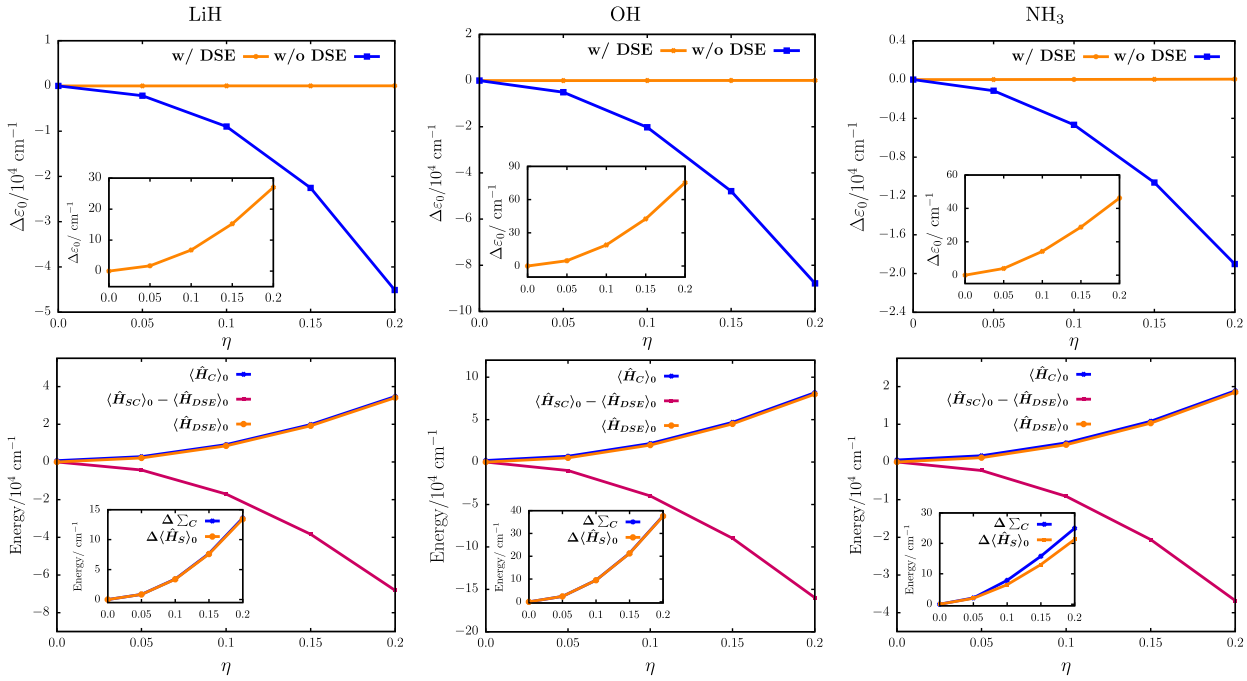

Figure 3.3: Top row: Energy difference, $\Delta\varepsilon_0$, of vibro-polaritonic ground state energy and non-interacting ground state energy. Shown are values obtained with (w/) and without (w/o) dipole self-energy (DSE) contribution, all as a function of the coupling strength parameter, η. Bottom row: Energy decomposition for LiH, OH and NH_3 models obtained with DSE contribution as function of η. Insets show cavity $\Delta\Sigma_C$ and system $\Delta\langle\hat{H}_S\rangle_0$ contributions (see text for definitions) to $\Delta\varepsilon_0$.

In absence of $\hat{H}_{DSE}$, we observe $\Delta\varepsilon_0$ to decrease monotonically by several thousand wavenumbers as η increases. This finding resembles the instability of the vibro-polaritonic ground state as discussed in Refs.[26, 27]. In contrast, in presence of $\hat{H}_{DSE}$ we observe $\Delta\varepsilon_0$ to slightly increase by several tens of wavenumbers as η increases, as depicted in insets of Fig.3.3 top-row. In order to address energetic details, we perform an energy decomposition analysis of $\langle\hat{H}\rangle_0$ in terms of individual contributions

$$\langle\hat{H}\rangle_0 = \langle\hat{H}_S\rangle_0 + \langle\hat{H}_C\rangle_0 + \langle\Delta\hat{H}_{SC}\rangle_0 + \langle\hat{H}_{DSE}\rangle_0 \quad , \tag{3.13}$$

and study their behavior as function of η. First, we discuss the last three contributions, which resemble the cavity mode, $\langle\hat{H}_C\rangle_0$, the bare light-matter interaction, $\langle\Delta\hat{H}_{SC}\rangle_0$, and the dipole self-energy ground state expectation values, $\langle\hat{H}_{DSE}\rangle_0$. We obtain analytic expressions

for the latter contributions, which explicitly reveal the functional dependence on η as

$$\langle \hat{H}_C \rangle_0 = \hbar\omega_c \frac{\eta^2}{d_{fi}^2} \langle d^2 \rangle + \hbar\omega_c \left(\langle \hat{a}^\dagger \hat{a} \rangle + \frac{1}{2} \right) \quad , \tag{3.14}$$

$$\langle \Delta\hat{H}_{SC} \rangle_0 = \langle \hat{H}_{SC} \rangle_0 - \langle \hat{H}_{DSE} \rangle_0 = -2\hbar\omega_c \frac{\eta^2}{d_{fi}^2} \langle d^2 \rangle \quad , \tag{3.15}$$

$$\langle \hat{H}_{DSE} \rangle_0 = \hbar\omega_c \frac{\eta^2}{d_{fi}^2} \langle d^2 \rangle \quad . \tag{3.16}$$

In order to derive the latter, we exploited the second quantization representation for the cavity mode and performed a projected PZW-transformation, which exclusively acts on the electronic ground state subspace[36]. Our results are shown in the lower row of Fig.3.3.
In the non-interacting limit ($\eta = 0$), the bare light-matter interaction and DSE contribution vanish identically, *i.e.*, $\langle \hat{H}_{SC} \rangle_0 = \langle \hat{H}_{DSE} \rangle_0 = 0$, and only the cavity-mode zero point energy contributes, $\langle \hat{H}_C \rangle_0 = \frac{\hbar\omega_c}{2}$. For $\eta > 0$, we find a monotonic increase $\langle \hat{H}_C \rangle_0 \sim \eta^2$ and $\langle \hat{H}_{DSE} \rangle_0 \sim \eta^2$, where the two terms differ by the cavity contribution, $\hbar\omega_c \left(\langle \hat{a}^\dagger \hat{a} \rangle + 1/2 \right)$. Moreover, we find the bare light-matter interaction to decrease as $\langle \Delta\hat{H}_{SC} \rangle_0 \sim -2\eta^2$ for increasing η. Hence, in absence of the DSE one finds for Eq.(3.13), that $\langle \hat{H} \rangle_0 \sim -\eta^2$ as $\eta \to \infty$. This behavior results from the dominant bare light-matter interaction contribution to the ground state energy ($\langle \Delta\hat{H}_{SC} \rangle_0$) in the limit of large η. In contrast, for the complete Pauli-Fierz Hamiltonian the cavity mode and DSE contributions exactly counterbalance $\langle \Delta\hat{H}_{SC} \rangle_0$, which prevents divergence of $\Delta\varepsilon_0$. We note, that identical trends are found for all studied systems with energetic changes in the order of several thousand wavenumbers.
In order to shine some light on the increase of $\Delta\varepsilon_0$ for the scenario with DSE, we compare the zero-point energy corrected system energy, $\Delta \langle \hat{H}_S \rangle_0$, with the total cavity contribution

$$\Delta\Sigma_C = \langle \hat{H}_C \rangle_0 + \langle \Delta\hat{H}_{SC} \rangle_0 + \langle \hat{H}_{DSE} \rangle_0 \quad , \tag{3.17}$$

which sum up to, $\langle \hat{H} \rangle_0 = \Delta \langle \hat{H}_S \rangle_0 + \Delta\Sigma_C$, respectively. As can be observed from the insets in the lower row of Fig.3.3, both $\Delta \langle \hat{H}_S \rangle_0$ and $\Delta\Sigma_C$ increase with η and contribute nearly identically to $\langle \hat{H} \rangle_0$. For the ammonia inversion model, we observe a slightly dominant cavity contribution, $\Delta\Sigma_C$, compared to the system energy, $\Delta \langle \hat{H}_S \rangle_0$. Hence, the increase of $\Delta\varepsilon_0$ with η is traced back to an increase in bare system and cavity mode contributions to the vibro-polaritonic ground state energy.

Dissociation Energies, Activation Energies and Bond Lengths

We now turn to bond dissociation energies for Morse-type model systems and activation energy for the ammonia inversion mode. To proceed, we introduce the cavity potential energy surface for two-dimensional models systems as

$$V_\eta(q, x_c) = V(q) + \frac{\omega_c^2}{2} x_c^2 + \sqrt{\frac{2\omega_c}{\hbar}}\, g\, x_c\, d(q) + \frac{g^2}{\hbar\omega_c} d^2(q) \quad . \tag{3.18}$$

For Morse-type oscillators, we consider a classical dissociation energy as defined by

$$D_{cl} = \lim_{q\to\infty} \min_{x_c} \Big(V_\eta(q, x_c) - V_\eta(q_0, x_{c0}) \Big) \quad , \tag{3.19}$$

with classical cPES minimum, $V_\eta(q_0, x_{c0})$, and a vibro-polaritonic zero-point energy corrected dissociation energy, $D_{qu} = D_{cl} - \varepsilon_0(\eta)$. D_{cl} resembles energy required for dissociation, which minimizes the energy with respect to changes in the cavity displacement coordinate, x_c. Further, we discuss the classical activation energy for the cavity-ammonia inversion model as defined by

$$E^a_{cl} = V_\eta(q^\ddagger, x^\ddagger_c) - V_\eta(q_0, x_{c0}) \quad , \tag{3.20}$$

where $V_\eta(q^\ddagger, x^\ddagger_c)$ is the energy at the cavity transition state with coordinates $\{q^\ddagger, x^\ddagger_c\}$. Additionally, we consider a vibro-polaritonic zero-point energy corrected activation energy, $E^a_{qu} = E^a_{cl} - \varepsilon_0(\eta)$, where we explicitly neglect any corrections due to the transition state, which will be subject of a detailed discussion in Sec.3.4. In Fig.3.4, both classical (top row) and quantum dissociation/activation energies (bottom row) are depicted as function of η. Again, we compare scenarios where we include or exclude the DSE-contribution to the cPES.

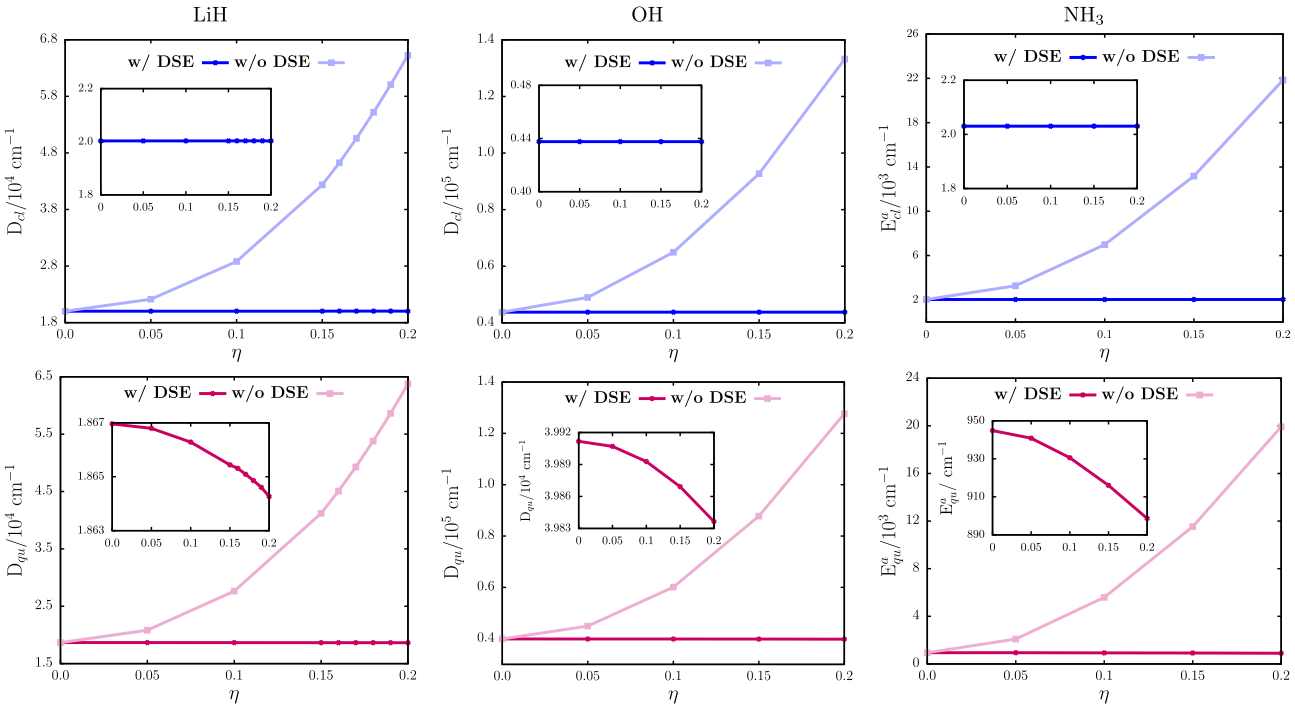

Figure 3.4: Classical $D_{\rm cl}$ (*cf.* Eq.(3.19)) and quantum (initial-state zero-point energy corrected) $D_{\rm qu}$ dissociation energies of LiH and OH, besides classical, $E^{\rm a}_{\rm cl}$, and initial-state zero-point energy corrected activation energies, $E^{\rm a}_{\rm qu}$, of the NH_3 inversion mode, respectively. All as function of η with (w/) and without (w/o) DSE contribution. Insets show curves obtained with DSE on a larger scale.

Beginning with classical dissociation and activation energies, D_{cl} and E^a_{cl}, we observe a strong increase with η when $\hat{H}_{DSE}$ has been neglected. However, we find both D_{cl} and E^a_{cl} to be *independent* of the light-matter interaction in presence of the DSE contribution for all values of η studied here. Results are shown in insets of Fig.3.4, top row.
Further, zero-point energy corrected dissociation, D_{qu}, and activation energies, E^a_{qu}, show a similar behavior as their classical counterparts and increase by several thousand wave numbers in absence of the DSE. In contrast, a decrease of both D_{qu} and E^a_{qu} by several tens of wave numbers with increasing η is found in presence of $\hat{H}_{DSE}$. This trend opposes the classical equivalents, which were found to be independent of the light-matter interaction, and points at the relevance of quantum corrections.

In the following, we shall provide a rigorous justification for the η-independence of classical quantities D_{cl} and E^a_{cl}. To this end, we consider a general cPES, $V_\eta(s, \{q_i\}, \{x_k\})$, with reaction coordinate, s, a set of molecular vibrational coordinates, $\{q_i\}$, and cavity displacement coordinates, $\{x_k\}$, respectively. A path on the cPES, which minimizes the energy along the reaction coordinates, s, satisfies the constraints

$$\frac{\partial}{\partial q_j} V_\eta(s, \{q_i\}, \{x_k\}) = 0 \quad , \tag{3.21}$$

$$\frac{\partial}{\partial x_l} V_\eta(s, \{q_i\}, \{x_k\}) = 0 \quad . \tag{3.22}$$

The second condition allows to determine a set of minimizing cavity displacement coordinates given by

$$x_k^{\min} = -\sqrt{\frac{2}{\hbar\omega_k^3}}\, g_k\, d(s, \{q_i\}) \quad , \tag{3.23}$$

with k^{th}-cavity mode frequency, ω_k, and interaction strength, g_k, which leads with the corresponding minimized cPES, $V_\eta(s, \{q_i\}, \{x_k^{\min}\})$, to

$$\frac{\partial}{\partial q_j} V_\eta(s, \{q_i\}, \{x_k^{\min}\}) = \frac{\partial}{\partial q_j} V(s, \{q_i\}) = 0 \quad . \tag{3.24}$$

The latter equality states, that the minimizing condition with respect to molecular coordinates solely depends on the Born-Oppenheimer PES, $V(s, \{q_i\})$, if the energy is already minimal with respect to changes in cavity displacement coordinates. In particular, the minimizing condition does not depend on the cPES. This property resembles the DSE-induced translational invariance of the Pauli-Fierz Hamiltonian and formally resembles properties of the renormalization term in the *Caldeira-Leggett* Hamiltonian[17, 154, 155].
The consequences of this analysis are three-fold: (i) Extrema on Born-Oppenheimer PES and cPES share the same molecular coordinates, (ii) extremal molecular coordinates are independent of light-matter interaction and (iii) locations of extrema with respect to cavity displacement coordinates depend on the light-matter interaction dependent values of $x_k^{\min}$. Accordingly, under constrained $x_k^{\min}$, the minimum condition of the cPES with respect to molecular coordinates reduces to the minimum condition for the Born-Oppenheimer PES. Hence, there exists no *classical* minimum energy path on a cPES, which is lower in energy

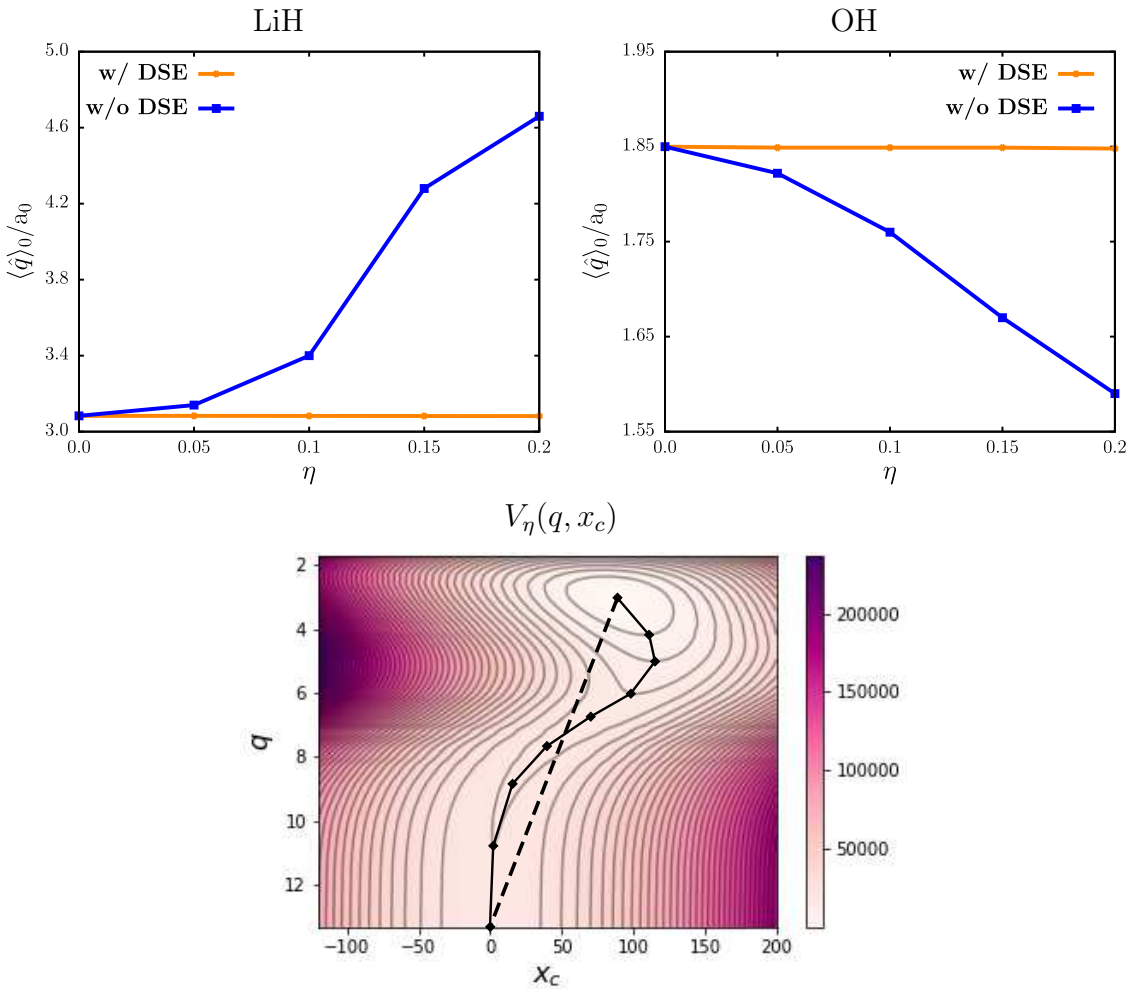

Figure 3.5: Top row: Molecular equilibrium bond length, $\langle\hat{q}\rangle_0$, for LiH and OH obtained with (w/) and without (w/o) DSE contribution. Bottom row: cPES for LiH-cavity hybrid system as function of stretching mode coordinate, q, and cavity displacement coordinate, x_c, in the VUSC regime with $\eta = 0.2$. Minimum energy path (bold) and linear transit pathways from initial to final configurations (dashed).

compared to its analog on the conventional molecular PES. Therefore, a purely classical cPES analysis seems to be inadequate to resolve the details of vibro-polaritonic ground state chemistry and the inclusion of quantum corrections seems mandatory, at least from the time-independent perspective. Another consequence of the latter analysis implies that equilibrium bond lengths, $\langle\hat{q}\rangle_0$, are actually independent of η as shown in Fig.3.5. We note that in absence of the DSE term, we observe an apparent bond stretching (LiH) and shortening (OH), which do not occur for the full Pauli-Fierz Hamiltonian.

Before turning to excited vibro-polaritonic states, we like to stress that our results are independent of the particular form of $V_\eta(s, \{q_i\}, \{x_k\})$, however, they only hold for vibrational strong coupling problems in the limit of vanishing electron-photon correlation (*cf.*

Eq.(2.60)). Here, the latter is a valid simplification, as for cavity modes in the IR regime the contribution of excited electronic states to the ground state cPES is assumed to be small as indicated by recent *ab initio* QED-CC results[47].
We close this section, by pointing out that significantly altered cPES barriers were recently reported for ground state proton-transfer reactions obtained with fully correlated electron-photon approaches[48], which seem to apparently contradict our reasoning. However, the authors of this study considered a cavity mode frequency of $\omega_c = 3\,\mathrm{eV} \approx 24000\,\mathrm{cm}^{-1}$, which is well beyond the energetic range of vibrational strong coupling scenarios. Accordingly, it has to be assumed that this scenario is not covered by arguments given here and presumably bridges VSC and ESC problems, *i.e.*, thermal ground-state chemistry probably changes due to cavity-induced "admixing" of electronically excited state contributions to the ground states cPES.

3.2.3 Vibro-Polaritonic Excited States

We now turn vibro-polaritonic excited states and infrared spectra. As reference states, we consider eigenstates of the zeroth-order non-interacting Hamiltonian, $\hat{H}_0 = \hat{H}_S + \hat{H}_C$, which are exact in the limit, $\eta \to 0$. For the following discussion, we restrict zeroth-order states to ground-state (X_0), single-excitation (X_1) and double-excitation (X_2) manifolds, respectively. The manifolds are characterized by the number of quanta in the zero-order states and are sufficient to properly describe the low-energy properties of our model systems, which are regularly probed in infrared spectroscopic experiments.

Morse-type Oscillators: LiH and OH Stretching Modes

For Morse-type oscillators, we consider zeroth-order reference states, $\{|v_s, n_c\rangle\}$, with

$$\begin{aligned} X_0 = &\quad \{|0_s, 0_c\rangle\} \\ X_1 = &\quad \{|1_s, 0_c\rangle, |0_s, 1_c\rangle\} \\ X_2 = &\quad \{|2_s, 0_c\rangle, |1_s, 1_c\rangle, |0_s, 2_c\rangle\} \end{aligned} \quad . \tag{3.25}$$

The X_1-manifold is doubly degenerate due to the resonance condition, $\omega_c = \omega_{10}$. For the X_2-manifold, two degenerate states $|1_s, 1_c\rangle$ and $|0_s, 2_c\rangle$ are accompanied by $|2_s, 0_c\rangle$, which is slightly lower in energy due to anharmonicity of the molecular stretching mode. In Fig.3.6, we show energy level diagrams for the non-interacting limit and a fully interacting scenario ($\eta = 0.2$), which comprises the lowest six vibro-polaritonic states provided by (3.25) with corresponding densities on the corresponding cPES.
For $\eta > 0$, one finds bright lower and upper vibro-polaritonic states, $|L_1\rangle$ and $|U_1\rangle$, spanning X_1 and bright states $|L_2\rangle, |M_2\rangle$ and $|U_2\rangle$ for the X_2-manifold. In order to make this statement quantitative, we discuss in the following vibro-polaritonic eigenenergies and IR spectra as a function of η. In Fig.3.7 top row, the eigenvalues of vibro-polaritonic states formed in both LiH (left) and OH modes (right) are depicted as function of η relative to the respective ground state energy. Again, we distinguish scenarios where the dipole self-energy term has been taken into account or alternatively neglected. Starting with the full description, one

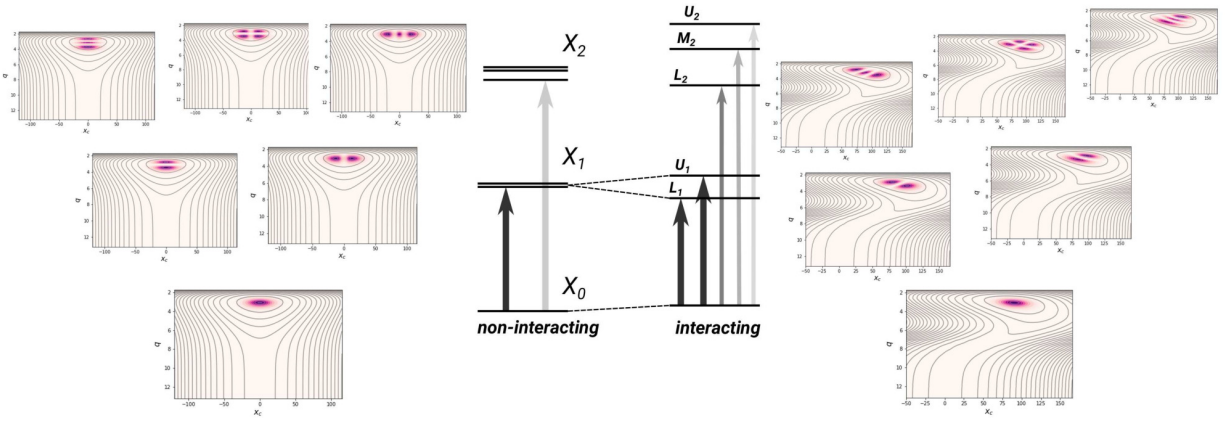

Figure 3.6: Schematic representation of IR active vibro-polaritonic transitions indicated by arrows for Morse-type anharmonic vibrational polaritons in the non-interacting limit (left) and the interacting case (right). Schematic densities shown for non-interacting zeroth-order states and vibro-polaritonic eigenstates, $|L_1\rangle, |U_1\rangle$ and $|L_2\rangle, |M_2\rangle, |U_2\rangle$, for LiH at $\eta = 0.0$ (left) and $\eta = 0.2$ (right) besides contours of the cPES, $V_\eta(q, x_c)$, with DSE.

observes the well-known characteristic formation of two non-degenerate vibro-polaritonic states emerging from the X_1-manifold, *i.e.*, the lower and upper vibrational polaritons $|L_1\rangle$ and $|U_1\rangle$, respectively. Their energetic separation, known as *Rabi splitting*, increases with η. Further, three non-degenerate states $|L_2\rangle, |M_2\rangle$ and $|U_2\rangle$ emerge from the X_2-manifold, with a middle vibrational polariton $|M_2\rangle$. As η increases, $|L_2\rangle$ experiences a red-shift and $|U_2\rangle$ is blue-shifted, while $|M_2\rangle$ does not vary significantly. These findings hold for both Morse-type models due to the similarities in the molecular potential. Notably, this qualitative equivalence is absent, if $\hat{H}_{DSE}$ is neglected. Then, we observe most vibro-polaritonic eigenstates in LiH to decrease in energy with increasing η, passing a minimum around $\eta = 0.13$ and increasing in energy for stronger couplings. In contrast, the OH counterparts all tend to higher energies as η increases.
From a spectroscopic perspective, we observe bright transitions, $X_0 \to X_1$, which allow to identify the two spectroscopically bright vibro-polaritonic states $|L_1\rangle$ and $|U_1\rangle$. Notably, overtone transitions, $X_0 \to X_2$, are found to be significantly weaker in intensity and will therefore not be discussed in what follows. We observe a slightly asymmetric splitting of L_1- and U_1-peaks, which leads to a slightly stronger blue-shift of the upper polariton state relative to the red-shifted lower polariton. For $\eta \leq 0.15$, the two bright states are well described as superposition states

$$\begin{aligned} |L_1\rangle &= \frac{1}{\sqrt{2}}\Big(|1_s, 0_c\rangle - |0_s, 1_c\rangle\Big) \\ |U_1\rangle &= \frac{1}{\sqrt{2}}\Big(|1_s, 0_c\rangle + |0_s, 1_c\rangle\Big) \end{aligned} \quad , \tag{3.26}$$

with some deviations for stronger coupling, where contributions from higher-lying states

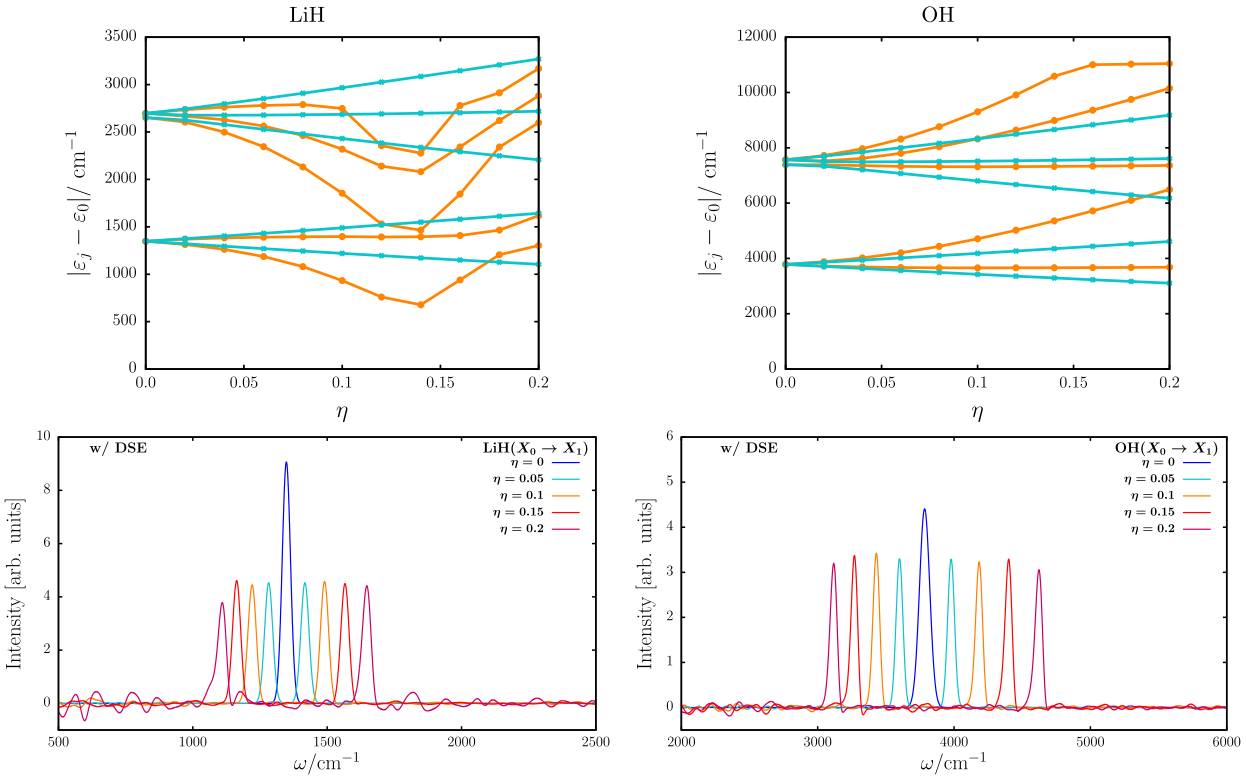

Figure 3.7: Top row: Vibro-polaritonic energy eigenvalues of LiH (left) and OH (right) for X_1- (lower manifold) and X_2-manifolds (upper manifold) as function of the light-matter coupling ratio η with (light blue curves, crosses) and without (orange curves, circles) dipole self-energy contribution included. Bottom row: Vibro-polaritonic IR spectra of LiH (left) and OH (right) for different values of η for transitions $X_0 \to X_1$. In both cases the full Hamiltonian with DSE was considered.

become relevant. As to be expected from the eigenvalues analysis, the spectra change significantly in absence of the DSE contribution as shown in Fig.3.8. Here, we find different peak positions as expected from the analysis of vibro-polaritonic eigenvalues shown in Fig.3.7, but in particular also very different intensities. We can identify two peaks for $\eta \leq 0.1$, with a significantly more intense L_1-transition for LiH in contrast to OH, where the U_1-peak dominates. As η increases, intensities decrease, the U_1-peak experiences as strong blue-shift and the L_1-peak experiences a strong red-shift in both models.

Symmetric Double-Well Potential: NH_3 Inversion Mode

The zero-order basis for the symmetric double-well potential can be characterized by the symmetry of the corresponding vibrational Pauli-Fierz Hamiltonian. For $\eta = 0$, the latter and its eigenstates transform as the irreducible representations of C_{2v}, *i.e.*, A_1, A_2 and B_1, B_2, respectively. We take into account the same manifolds as for the Morse oscillator

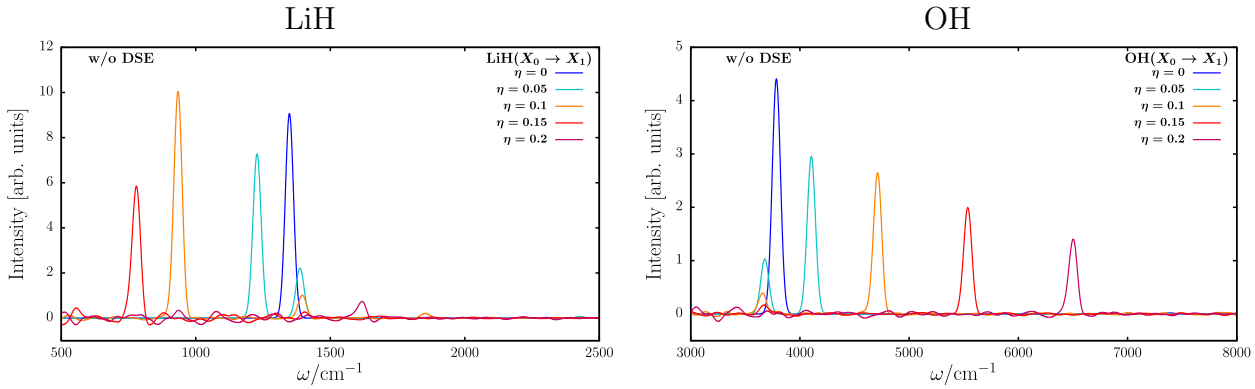

Figure 3.8: Vibro-polaritonic IR spectra of LiH (left) and OH (right) for different values of η for transitions $X_0 \rightarrow X_1$ where the DSE was neglected.

models, here with a total of twelve states given by

$$
\begin{aligned}
X_0 = & \quad \left\{ |0_s^+, 0_c\rangle\,(A_1),\ |0_s^-, 0_c\rangle\,(B_1) \right\} \\
X_1 = & \quad \left\{ |1_s^+, 0_c\rangle\,(A_1),\ \underbrace{|1_s^-, 0_c\rangle\,(B_1),\ |0_s^+, 1_c\rangle\,(B_2)}_{\text{degenerate}},\ |0_s^-, 1_c\rangle\,(A_2) \right\} \\
X_2 = & \quad \left\{ \begin{array}{c} |2_s^+, 0_c\rangle\,(A_1),\ |2_s^-, 0_c\rangle\,(B_2),\ |1_s^+, 1_c\rangle\,(B_1), \\ \underbrace{|0_s^+, 2_c\rangle\,(A_1),\ |1_s^-, 1_c\rangle\,(A_2)}_{\text{degenerate}},\ |0_s^-, 2_c\rangle\,(B_2) \end{array} \right\}
\end{aligned}
\quad , \tag{3.27}
$$

where transformation properties according to irreducible representations of C_{2v} are given in parenthesis. At $\eta > 0$, the symmetry of the vibrational Pauli-Fierz Hamiltonian is reduced, $C_{2v} \rightarrow C_2$, such that $(A_1, A_2) \rightarrow A$ and $(B_1, B_2) \rightarrow B$. Hence, the vibro-polaritonic states can be grouped into two sets, a symmetric and an anti-symmetric one transforming as the corresponding irreducible representations of C_2, *i.e.*, A and B.
In Fig.3.9(a), we depict vibro-polaritonic eigenvalues of states forming X_1- and X_2-manifolds as function of η. In presence of the DSE contribution, we observe the formation of four non-degenerate vibro-polaritonic states in the X_1-manifold, two symmetric (A) and two anti-symmetric (B) ones. With increasing η, the lower two polariton states are red-shifted, while the upper two states experience a blue-shift. In the ultrastrong coupling regime for $\eta = 0.2$, the X_1-manifold resembles a pair of two-fold accidentally degenerate states.
For the energetically higher lying X_2-manifold, we observe a qualitatively similar behavior: The degeneracy of zero-order states is lifted as η increases and six vibro-polaritonic states form, three symmetric and three anti-symmetric ones. Under VUSC, the lowest two states and the intermediate pair become accidentally degenerate. Additionally at $\eta = 0.2$, also the remaining upper two states are degenerate resulting in three pairs of accidentally two-fold degenerate states. Notably, a pair is composed of states with symmetrically inequivalent transformation properties.

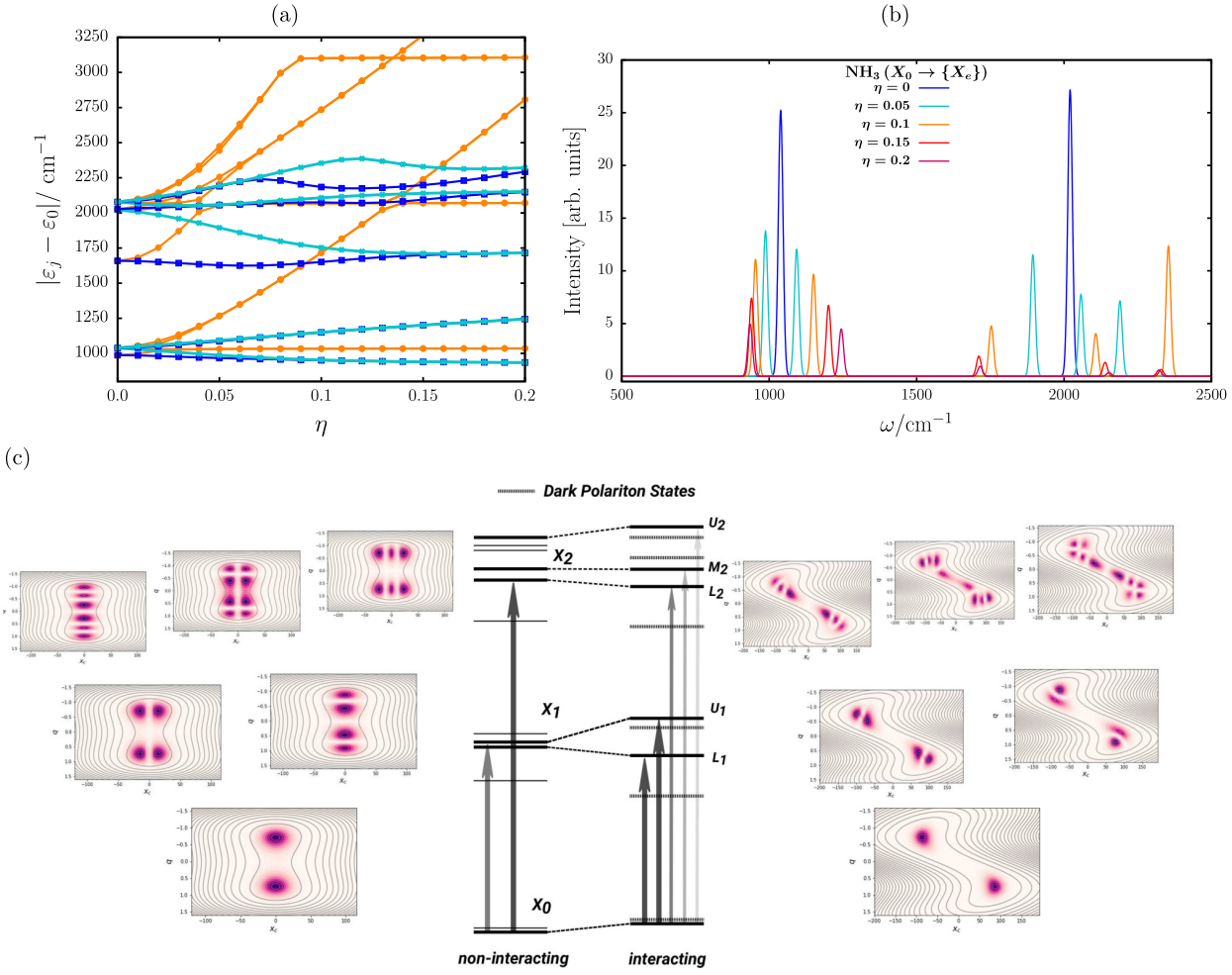

Figure 3.9: (a) Vibro-polaritonic energy eigenvalues for NH_3-cavity problem with (optically bright in light blue/ stars; optically dark in dark blue/squares) and without (orange, circles) DSE contribution resulting from X_1- (lower manifold) and X_2-manifolds (upper manifold), respectively. Energies in dependence of light-matter coupling parameter, η, and relative to the ground state energy. (b) Vibro-polaritonic IR spectrum obtained with DSE contribution for different η values. (c) Schematic representation of IR active vibrational transitions indicated by arrows for double-well-type anharmonic polaritons. Schematic densities of vibro-polaritonic states transforming as anti-symmetric irreducible representations of C_{2v} in the non-interacting limit and as anti-symmetric irreducible representations of C_2 at finite light-matter interaction strength ($\eta = 0.2$, DSE included). Dark vibro-polaritonic states are indicated by dashed lines, bright ones by solid lines. In all cases, the harmonic cavity frequency is chosen as $\omega_c = (\varepsilon_1^- - \varepsilon_0^+)/\hbar$.

In absence of the dipole self-energy contribution, we find a significant blue shift for nearly all vibro-polaritonic eigenstates. In particular, some states from X_1 are strongly shifted to

high energies characteristic for states spanning the X_2-manifold.

We now turn to the corresponding linear IR spectra. Here, it is beneficial to reconsider symmetry arguments: The vibro-polaritonic ground state transforms as A and the molecular dipole function as B. Hence, only vibro-polaritonic states transforming as B are "bright" in the IR spectrum. The latter are contrasted by symmetry-forbidden, symmetric "dark" vibro-polaritonic states transforming as A. Importantly, optical transitions to "dark" vibro-polaritonic states are forbidden by symmetry. This is contrasted by dark or non-interacting states in polaritonic systems, which resemble purely molecular contributions that do not hybridize with cavity mode states.
In Fig.3.9(b) and (c), we show the corresponding IR spectrum obtained with DSE contribution besides an excitation scheme and densities of "bright" vibro-polaritonic states and contours of the corresponding cPES. For $\eta = 0$, we observe a single peak for both X_1- and X_2-manifolds, which correspond to molecular transitions

$$\begin{aligned} |0^+, 0_c\rangle\,(A_1) &\rightarrow |1^-, 0_c\rangle\,(B_2) \\ |0^+, 0_c\rangle\,(A_1) &\rightarrow |2^-, 0_c\rangle\,(B_2) \end{aligned} \quad . \tag{3.28}$$

For $\eta > 0$, two "bright" lower and upper vibro-polaritonic states, $|L_1\rangle$ and $|U_1\rangle$, are formed in the X_1-manifold, which can be understood as linear combinations of zeroth-order states $|1^-, 0_c\rangle$ and $|0^+, 1_c\rangle$, respectively. The slightly higher intensity of the L_1-transition indicates a higher matter contribution to $|L_1\rangle$ opposed to a slightly higher photon character of $|U_1\rangle$. As η increases, intensities of both peaks reduces significantly, which indicates an increase in photonic character of the corresponding states.

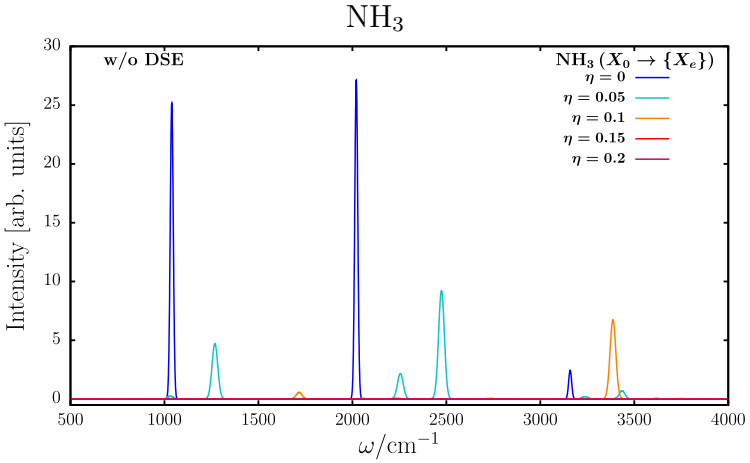

Figure 3.10: Vibro-polaritonic IR spectra of NH_3 for different values of η for transitions $X_0 \rightarrow X_1$ where the DSE was neglected.

In the X_2-manifold, we observe three peaks corresponding to "bright" vibro-polaritonic states, a lower $|L_2\rangle$, a middle $|M_2\rangle$ and an upper vibro-polaritonic state $|U_2\rangle$, respectively. They can be interpreted as linear combinations of zeroth-order states $|2^-, 0_c\rangle\,(B_2)$, $|1^+, 1_c\rangle\,(B_1)$

and $|0^-, 2_c\rangle$ (B_2) as deduced from nodes in densities shown in Fig.3.9(c). Again, we observe an intensity reduction for all X_2-transitions with increasing η, *i.e.*, an increasing photonic contribution to the vibro-polaritonic states, as in case of X_1-transitions. Further, $|L_2\rangle$ experiences a red-shift while $|M_2\rangle$ is gradually blue-shifted. Notably, the U_1-transition is subject to a blue-shift and an intensity gain up to roughly $\eta \approx 1.2$, which turns for even stronger coupling into a slight red-shift accompanied by a drastic intensity reduction (*cf.* Fig.3.9(a)). We finally note, that infrared spectra differ substantially in absence of the DSE (*cf.* Fig.3.10). Here, we observe blue-shifted transitions for increasing η and significantly reduced intensities. In particular, for $\eta > 0.05$ the lowest lying bright states are hardly observable and higher lying transitions seem to be suppressed for even larger values of η.

3.2.4 Summary and Outlook

We studied ground and excited state properties of minimal two-dimensional model systems related to anharmonic molecular modes interacting with a single quantized cavity mode tuned resonant to the fundamental vibrational transition. We considered anharmonic potentials of Morse-type besides a symmetric double-well potential and thoroughly examined the impact of the dipole self-energy term in the effective vibrational Pauli-Fierz Hamiltonian. First, we identified the divergence of the vibro-polaritonic ground state energy in absence of the DSE to behave as $\sim \eta^2$ for $\eta \to \infty$, which is traced back to a diverging bare light-matter interaction contribution. Notably, this divergence is exactly canceled by the bare cavity mode and DSE contributions, when the full Pauli-Fierz Hamiltonian is employed. Second, we found classical dissociation and activation energies for cavity potential energy surfaces to be independent of the light-matter interaction when the DSE is included. Further, we showed that no minimum energy path exists on a cPES, which is lower in energy than its counterpart on molecular PES, and molecular coordinates of extrema on cPES are identical to the values on molecular PES. The latter finding additionally implied that molecular ground state equilibrium bond lengths are also independent of the light-matter interaction as studied here. Our results hold for VSC scenarios in the limit of vanishing electron-photon coupling, which is assumed to be a valid approximation for infrared cavities. Third, excited state energies and vibro-polaritonic infrared spectra reveal well known features as upper and lower vibro-polaritonic states for Morse-type oscillators but also more complex, symmetry characterized light-matter states for the double-well system. In particular, we identified for the latter symmetry-allowed "bright" and symmetry-forbidden "dark" vibro-polaritonic states in corresponding infrared spectra. As observed before, also excited state energies and IR spectra are strongly altered when comparing scenarios with and without the dipole self-energy. In the latter case, we observed irregular and partially divergent behavior of energy eigenvalues as function of the light-matter interaction. Additionally, intensities of infrared transition to vibro-polaritonic excited states are strongly altered.
As an outlook, we point at a possible perturbative treatment of electron-photon correlation in VSC problems as characteristic infrared cavity mode energies differ significantly from electronic excitation energies. This would probably allow for refining our findings by accessing respective correlations in cPES normal mode analysis and vibro-polaritonic infrared spectra, with some relevance as recently pointed out in Ref.[165].

3.3 Dynamics and Spectroscopy of Rovibrational Polaritons

In the previous section, we discussed the properties of vibrational polaritons formed in a diatomic molecule, which interacted only with a single cavity mode and was aligned with the latters polarization direction. In this second part, we lift the alignment restriction and consider a freely rovibrating CO molecule, which now interacts with both degenerate and orthogonally polarized cavity modes as depicted in Fig.3.11(a).

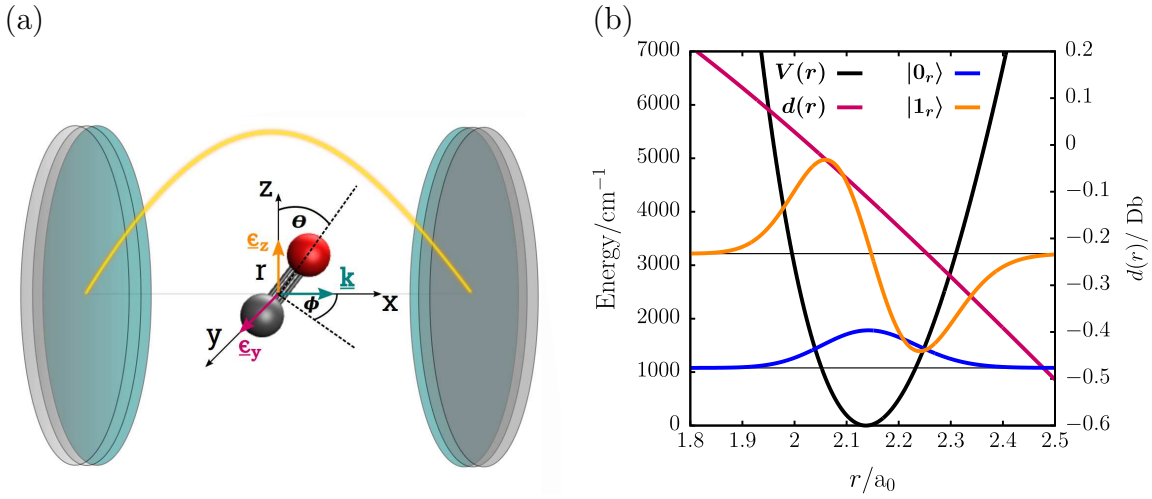

Figure 3.11: (a) Schematic sketch of diatomic molecule with vibrational coordinate r and angular coordinates θ, ϕ in optical two-mode cavity with polarization vectors $\underline{\epsilon}_z, \underline{\epsilon}_y$ and wavevector $\underline{k}$ and molecular space-fixed frame with axes x, y, z. A z-polarized cavity mode is indicated in yellow. (b) Anharmonic potential, $V(r)$, and dipole function, $d(r)$, of CO stretching mode in units of Debye (Db) (interpolated CCSD(T)/aug-cc-pV5Z results) with vibrational ground state $|0_r\rangle$ and first excited state $|1_r\rangle$.

The impact of molecular rotations on (vibrational) polaritons was studied only by few authors recently[167, 168, 169, 170], where the dipole moment was allowed to vary with respect to the polarization direction of a single cavity mode. Here, we extend work in this direction by including the second, orthogonally polarized cavity mode present in the Pauli-Fierz Hamiltonian. In particular, we follow the non-adiabatic perspective of Vibók and coworkers[170], identify previously unknown rotation induced, three-state vibro-polaritonic conical intersections (VPCI) in the X_1-manifold and thoroughly characterize the non-adiabatic system by means of dynamical and spectroscopic studies.

Results presented in this section are reproduced from "E.W. Fischer, P. Saalfrank. Cavity-induced Non-Adiabatic Dynamics and Spectroscopy of Molecular Rovibrational Polaritons studied by Multi-Mode Quantum Models. arXiv:2205.00945, (2022). Under revision at *Journal of Chemical Physics*"[171].

3.3.1 Theory and Model

Rovibrational Pauli-Fierz Hamiltonian

We consider an effective rovibrational Pauli-Fierz Hamiltonian for a single rovibrating diatomic carbon monoxide (CO) molecule, which interacts with two degenerate cavity modes polarized along z- and y-axis of the molecular center of mass frame (*cf.* Fig.3.11)

$$\hat{H} = \hat{H}_S + \sum_{\lambda=z,y} \hbar\omega_c \left(\hat{a}_\lambda^\dagger \hat{a}_\lambda + \frac{1}{2}\right) + \hat{H}_{SC} \quad . \tag{3.29}$$

The second term resembles the cavity mode Hamiltonian in second quantization representation with polarization index, $\lambda = z, y$, and cavity mode frequency, ω_c. Further, the molecular rovibrational "system" Hamiltonian reads

$$\hat{H}_S = \frac{\hat{j}^2}{2I} \underbrace{-\frac{\hbar^2}{2\mu}\frac{\partial^2}{\partial r^2} + V(r)}_{=\hat{H}_{\rm vib}} \quad , \tag{3.30}$$

with moment of inertia, $I = \mu\, r^2$, reduced mass μ, CO-stretching coordinate r, and vibrational Hamiltonian, $\hat{H}_{\rm vib}$, as determined by the adiabatic ground state PES of CO, $V(r)$. The angular momentum operator, $\hat{j}^2$, is given by

$$\hat{j}^2 = -\hbar^2 \left(\frac{1}{\sin\theta}\frac{\partial}{\partial\theta}\, \sin\theta \frac{\partial}{\partial\theta} + \frac{1}{\sin^2\theta}\frac{\partial^2}{\partial\phi^2}\right) \quad , \tag{3.31}$$

with polar angle, $\theta \in [0, \pi]$, and azimuthal angle, $\phi \in [0, 2\pi)$, respectively. The light-matter interaction is mediated by the molecular ground state dipole moment

$$\underline{d}(r, \theta, \phi) = d(r) \begin{pmatrix} \sin\theta\cos\phi \\ \sin\theta\sin\phi \\ \cos\theta \end{pmatrix} \quad , \tag{3.32}$$

where $d(r)$ is the molecular dipole moment along the CO-bonding axis. Further, as before we have in Eq.(3.29), $\hat{H}_{SC} = \Delta\hat{H}_{SC} + \hat{H}_{DSE}$, where the bare light-matter interaction Hamiltonian contains here the projections of $\underline{d}(r, \theta, \phi)$ on both z- and y-polarization vectors of the cavity modes, *i.e.*, $(\underline{e}_\lambda \cdot \underline{d}(r, \theta, \phi))$ with $\lambda = z, y$, and is given by

$$\begin{aligned} \Delta\hat{H}_{SC} &= \sum_{\lambda=z,y} g \left(\underline{e}_\lambda \cdot \underline{d}(r, \theta, \phi)\right) \left(\hat{a}_\lambda^\dagger + \hat{a}_\lambda\right) \quad , \\ &= g\, d(r) \Big(\left(\hat{a}_z^\dagger + \hat{a}_z\right) \cos\theta + \left(\hat{a}_y^\dagger + \hat{a}_y\right) \sin\theta \sin\phi \Big) \quad . \end{aligned} \tag{3.33}$$

The dipole self-energy term is proportional to $(\underline{e}_\lambda \cdot \underline{d}(r, \theta, \phi))^2$ and with the dipole moment in Eq.(3.32) obtained as

$$\hat{H}_{DSE} = \sum_{\lambda=z,y} \frac{g^2}{\hbar\omega_c} \Big(\underline{e}_\lambda \cdot \underline{d}(r, \theta, \phi)\Big)^2 = \frac{g^2}{\hbar\omega_c} d^2(r) \Big(\cos^2\theta + \sin^2\theta \sin^2\phi\Big) \quad . \tag{3.34}$$

Here, we assume that the center of mass of the rovibrating CO is fixed in the cavity, such that the full Hamiltonian is five-dimensional with three molecular coordinates, r, θ and ϕ, and two cavity modes. We note that the center of mass motion would be only relevant for the light-matter interaction in case of a molecular ion. Further, we introduce a mixed basis composed of a grid basis for the angular coordinates and a state-representation for the vibro-polaritonic modes (see below). The latter are characterized by quantum numbers, v_r, for the CO-vibration and, n_z, n_y, for the cavity modes. The dynamics as generated by the rovibrational Pauli-Fierz Hamiltonian is governed by the TDSE

$$\mathrm{i}\hbar \frac{\partial}{\partial t}\Psi(v_r, n_z, n_y, \theta, \phi, t) = \hat{H}\, \Psi(v_r, n_z, n_y, \theta, \phi, t) \quad , \tag{3.35}$$

where, $\Psi(v_r, n_z, n_y, \theta, \phi, t)$, is a five-dimensional rovibro-polaritonic wave packet. Below, we will discuss two different initial states to solve Eq.(3.35), which are given by either an isolated rovibrational excitation of the molecule or a light-matter superposition state, respectively.

Molecular Model

We consider a single CO molecule with reduced mass, $\mu = m_{\mathrm{C}} m_{\mathrm{O}}/m_{\mathrm{CO}} = 12506\, m_e$ (electron mass m_e). The molecular *ab initio* PES, $V(r)$, and molecular dipole function, $d(r)$, were calculated on the CCSD(T)/aug-cc-pV5Z level of theory via the software package Gaussian16[156] as function of the CO-bond-length r (*cf.* Fig.3.11(b)). For the ground state equilibrium bond length, we obtain a value of $r_e = 2.145\, a_0$ and for the rotational constant we find $B = \frac{\hbar}{4\pi c \mu r_e^2} = 1.91\,\mathrm{cm}^{-1}$, which is in close agreement with experiment where $B_{\mathrm{exp}} = 1.92\,\mathrm{cm}^{-1}$[172].
Further, the two lowest vibrational eigenvalues/eigenstates (*cf.* Fig.3.11(b)) of the vibrational Hamiltonian, $\hat{H}_{\mathrm{vib}}$, are otbained numerically via a Colbert-Miller discrete variable representation[173] with $N_r = 1501$ grid points. The corresponding fundamental anharmonic transition frequency is found as, $\hbar\omega_{10} = 2137\,\mathrm{cm}^{-1}$, which compares well with an experimental value of $2143\,\mathrm{cm}^{-1}$[174]. In the following, we set the cavity mode frequency, $\hbar\omega_c = \hbar\omega_{10}$. Further, the fundamental vibrational transition dipole moment is obtained as $d_{10} = 0.066$ ea$_0$, which is in agreement other work[175]. Finally, the molecular dipole function, $d(r)$, which changes roughly linearly in the r-range depicted in Fig.3.11(b), takes an absolute equilibrium value of $|d(r_e)| = 0.12\,\mathrm{Db}$, which is in close agreement with literature[176].

Diabatic Vibro-Polaritonic Basis

We recognize that the rotational constant, B, and the fundamental vibrational transition energy, $\hbar\omega_{10}$, set two different excitation energy scales with $B \ll \hbar\omega_{10}$, which allow for adiabatic separation of vibrational ("fast") and rotational ("slow") degrees of freedom following arguments by Vibók and coworkers[170]. Hence, we introduce a restricted basis of zero-order "vibro-polaritonic" states, $|v_r, n_z, n_y\rangle$, which constitute eigenstates to $\hat{H}_0 = \hat{H}_{\mathrm{vib}} + \hat{H}_C$. In

the following, we concentrate on the low-energy properties of the rovibrational light-matter hybrid system, *i.e.*, X_0- and X_1-manifolds as introduced in Sec. 3.2, which are given by

$$\begin{cases} X_0: & |0_r, 0_z, 0_y\rangle \\ X_1: & |1_r, 0_z, 0_y\rangle, |0_r, 1_z, 0_y\rangle, |0_r, 0_z, 1_y\rangle \end{cases} , \tag{3.36}$$

In the VSC regime, the three-dimensional single-excitation manifold, X_1, properly accounts for the description of the lowest lying excited vibro-polaritonic states. We note, higher-lying excited state manifolds, *e.g.*, X_2 and X_3 are neglected here, as they are energetically well separated from X_1 and not primarily probed in conventional IR experiments. Based on Eq.(3.36), a rovibro-polaritonic wave packet is expanded as

$$\Psi(v_r, n_z, n_y, \theta, \phi, t) = \sum_k \varphi_k(\theta, \phi, t) \, |D_k\rangle \quad , \tag{3.37}$$

where we denote the zero-order basis states generically as $|D_k\rangle$, and $\varphi_k(\theta, \phi, t)$ are time-dependent, rotational wave packets. Further, in the zero-order basis the rovibrational Pauli-Fierz Hamiltonian constitutes a matrix operator in (θ, ϕ)-space, as given by

$$\underline{\underline{H}} = \underline{\underline{T}}(\theta, \phi) + \underline{\underline{V}}(\theta, \phi) \quad . \tag{3.38}$$

Here, $\underline{\underline{T}}(\theta, \phi)$ is a is a 4×4-rotational KEO matrix and $\underline{\underline{V}}(\theta, \phi)$ the corresponding potential energy matrix, respectively. The rotational KEO matrix is given by

$$\underline{\underline{T}}(\theta, \phi) = \frac{\hat{j}^2}{2\mu} \begin{pmatrix} \langle 0_r|\frac{1}{r^2}|0_r\rangle & \langle 0_r|\frac{1}{r^2}|1_r\rangle & 0 & 0 \\ \langle 1_r|\frac{1}{r^2}|0_r\rangle & \langle 1_r|\frac{1}{r^2}|1_r\rangle & 0 & 0 \\ 0 & 0 & \langle 0_r|\frac{1}{r^2}|0_r\rangle & 0 \\ 0 & 0 & 0 & \langle 0_r|\frac{1}{r^2}|0_r\rangle \end{pmatrix} \quad , \tag{3.39}$$

where $\langle \dots \rangle$ indicates integration with respect to the molecular stretching coordinate, r. The zero-point energy shifted potential energy matrix is given by

$$\underline{\underline{V}}(\theta, \phi) = \begin{pmatrix} \frac{g^2}{\hbar\omega_c} f_{\theta\phi} \langle d^2 \rangle_{00} & \frac{g^2}{\hbar\omega_c} f_{\theta\phi} \langle d^2 \rangle_{10} & g \, d_{00} \cos\theta & g \, d_{00} \sin\theta \sin\phi \\ \frac{g^2}{\hbar\omega_c} f_{\theta\phi} \langle d^2 \rangle_{10} & \hbar\omega_{10} + \frac{g^2}{\hbar\omega_c} f_{\theta\phi} \langle d^2 \rangle_{11} & g \, d_{10} \cos\theta & g \, d_{10} \sin\theta \sin\phi \\ g \, d_{00} \cos\theta & g \, d_{10} \cos\theta & \hbar\omega_c + \frac{g^2}{\hbar\omega_c} f_{\theta\phi} \langle d^2 \rangle_{00} & 0 \\ g \, d_{00} \sin\theta \sin\phi & g \, d_{10} \sin\theta \sin\phi & 0 & \hbar\omega_c + \frac{g^2}{\hbar\omega_c} f_{\theta\phi} \langle d^2 \rangle_{00} \end{pmatrix} , \tag{3.40}$$

with dipole self-energy matrix elements, $\langle d^2 \rangle_{v_r v_r'} = \langle v_r | d_z^2(r) | v_r' \rangle$, and rotational potential

$$f_{\theta\phi} = \cos^2\theta + \sin^2\theta \sin^2\phi \quad . \tag{3.41}$$

The first diagonal entry in $\underline{\underline{V}}(\theta, \phi)$, corresponds to the zero-order ground state and the diagonal elements of the lower 3×3-block resemble states forming the X_1-manifold in the

order given by Eq.(3.36). Equivalently, the same assignment holds for the kinetic-energy matrix elements in Eq.(3.39).
The X_0- and X_1-manifolds are energetically well separated by $\hbar\omega_{10} = \hbar\omega_c$ and subject to a weak anharmonic coupling ($g^2 \langle d^2 \rangle_{10}$) induced by the dipole self-energy and comparatively strong light-matter coupling ($g\, d_{00}$). Further, the DSE constitutes a potential in angular coordinates on the diagonal ($g^2 \langle d^2 \rangle_{v_r v_r} f_{\theta\phi}$) and the singly-excited molecular state couples to the two singly-excited cavity mode states ($g\, d_{10}$).
As the rovibrational coupling in the KEO, induced by $\frac{\hat{j}^2}{2\mu} \langle 0_r | \frac{1}{r^2} | 1_r \rangle$, is weak, the Pauli-Fierz Hamiltonian takes a diabatic-like representation in the zero-order basis, Eq.(3.36). We interpret "adiabatic" eigenstates diagonalizing $\underline{\underline{V}}(\theta, \phi)$ as vibro-polaritonic states[170], which resemble the vibro-polaritonic ground state $|G\rangle$, a lower $|L_1\rangle$, a middle $|M_1\rangle$ and an upper $|U_1\rangle$ vibro-polaritonic state, respectively. Further, the corresponding eigenvalues $\varepsilon_G(\theta, \phi), \varepsilon_{L_1}(\theta, \phi), \varepsilon_{M_1}(\theta, \phi)$ and $\varepsilon_{U_1}(\theta, \phi)$, are functions of the angular coordinates, θ and ϕ, and provide vibro-polaritonic PES for the rotational dynamics of the molecule.

3.3.2 Vibro-Polaritonic Conical Intersections

In the first part of this discussion, we consider cavity-induced non-adiabatic effects in the vibro-polaritonic single-excitation manifold resulting from the adiabatic decoupling of rotational and vibro-polaritonic degrees of freedom. Under VSC, the vibro-polaritonic surfaces $\varepsilon_{L_1}(\theta, \phi)$, $\varepsilon_{M_1}(\theta, \phi)$ and $\varepsilon_{U_1}(\theta, \phi)$ are subject to three-state vibro-polaritonic conical intersections (VPCIs) under the conditions

$$\hbar\omega_{10} = \hbar\omega_c \quad , \quad \theta = \frac{\pi}{2} \quad , \quad \phi = 0, \pi \quad . \tag{3.42}$$

The three-state VPCIs, as shown in Fig.3.12a) and b) for $\eta = 0.05$ and $\eta = 0.1$, are located in a two-dimensional branching space spanned by angular coordinates. We identify two

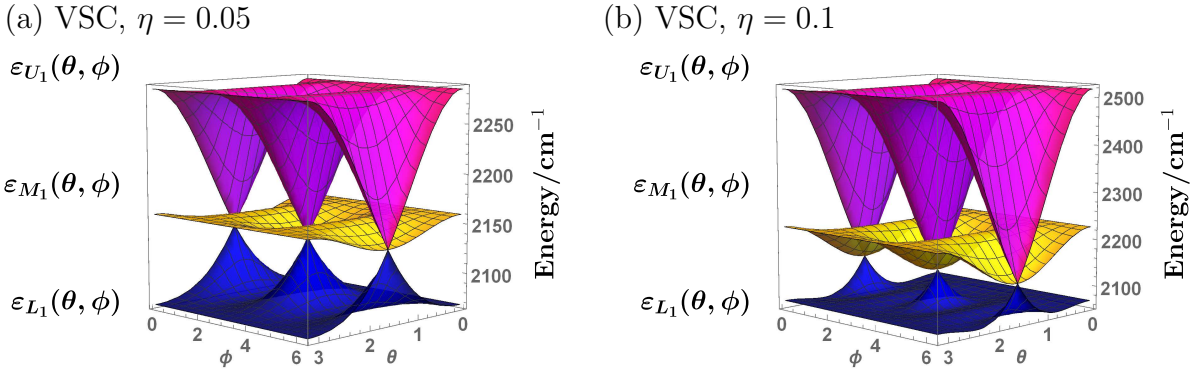

Figure 3.12: Three-state vibro-polaritonic conical intersections (VPCIs) between lower vibro-polaritonic, $\varepsilon_{L_1}(\theta, \phi)$, middle vibro-polaritonic, $\varepsilon_{M_1}(\theta, \phi)$, and upper vibro-polaritonic surfaces, $\varepsilon_{U_1}(\theta, \phi)$, for (a) VSC regime with $\eta = 0.05$ and (b) onset of VUSC regime with $\eta = 0.1$.

distinct intersections located at $(\theta, \phi) = (\frac{\pi}{2}, 0)$ and $(\theta, \phi) = (\frac{\pi}{2}, \pi)$ due to the periodicity of

the azimuthal angle ϕ. The three-state VPCIs exhibit a characteristic double-cone topology formed by the L_1- and U_1-surfaces. Further, they are triple-degenerate at the intersection point due to an additional crossing with the middle vibro-polaritonic surface, $\varepsilon_{M_1}(\theta, \phi)$, which exhibits a local minimum here. In the VSC regime (here with $\eta = 0.05$), the splitting of the L_1- and U_1-surfaces is slightly asymmetric with respect to the M_1-surface as can be seen in Figs.3.12(a) and (c). At the onset of the VUSC regime, the L_1/U_1-splitting turns out to be strongly asymmetric (*cf.* Figs.3.12(b) and (d)), with a dominant inverse cone in $\varepsilon_{U_1}(\theta, \phi)$. The M_1-surface forms more pronounced minima at the intersection points for stronger light-matter interaction and the L_1-surface is subject to mild "mexican-hat"-type potentials close to the intersection coordinate.

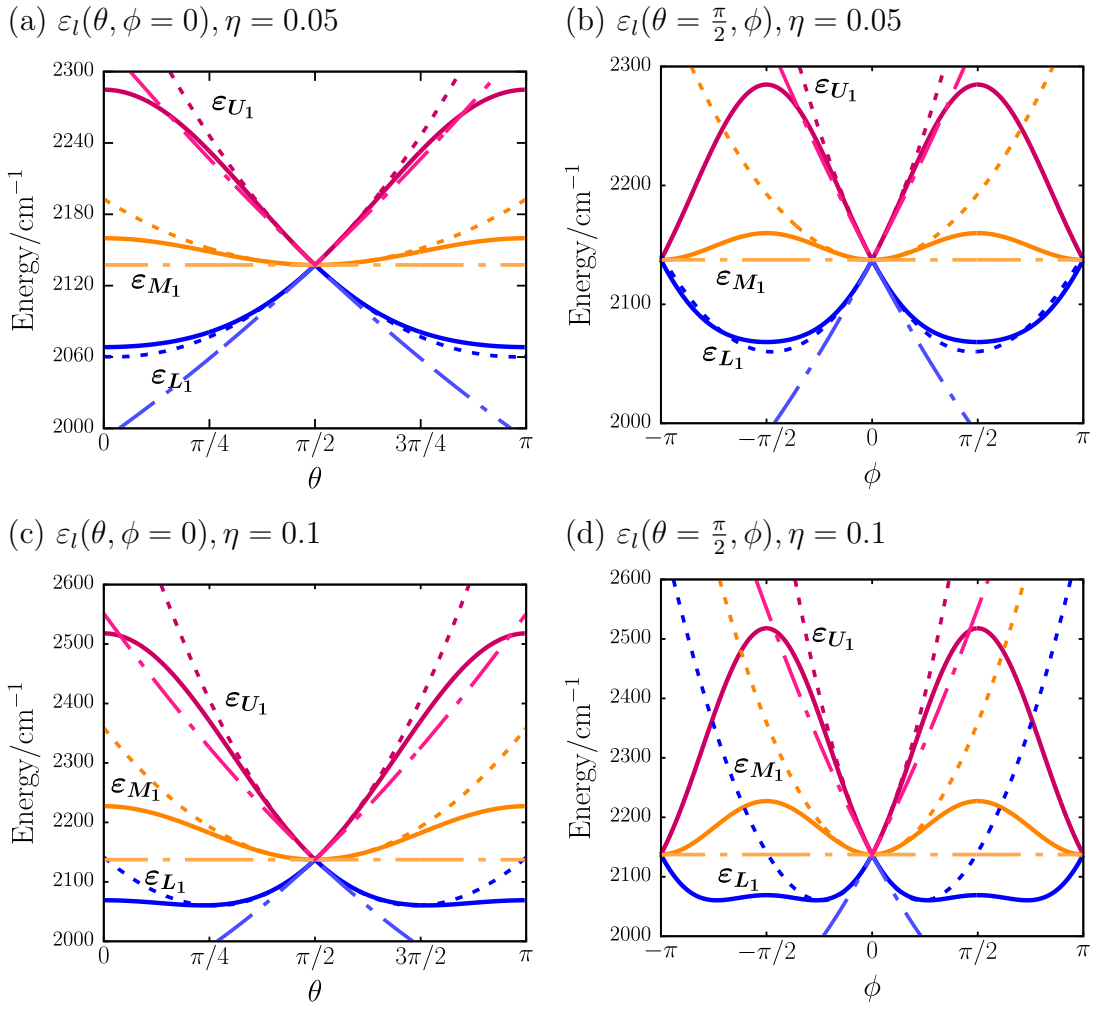

Figure 3.13: One dimensional cuts through vibro-polaritonic surfaces (bold), linear (dotted-dashed) and quadratic approximations (dotted) with $\varepsilon_l(\theta, \phi = 0)$, (a) and (c), and $\varepsilon_l(\theta = \frac{\pi}{2}, \phi)$, (b) and (d), for $\eta = 0.05$ (top row) and $\eta = 0.1$ (bottom row) with, $l = L_1, M_1, U_1$.

In order to reveal the detailed characteristics of a VPCI close to the intersection point, we expand $\underline{\underline{V}}(\theta, \phi)$ up to first order in angular coordinates θ and ϕ around the intersection

point at $(\theta, \phi) = (\frac{\pi}{2}, 0)$. There, we have

$$\cos\theta \approx \theta - \frac{\pi}{2} \quad , \quad \sin\theta \sin\phi \approx \phi \quad , \tag{3.43}$$

and

$$f(\theta, \phi) \approx \phi^2 + \left(\theta - \frac{\pi}{2}\right)^2 = f^{(1)}(\theta, \phi) \quad . \tag{3.44}$$

The corresponding approximate potential energy matrix reads

$$\underline{\underline{V}}^{(1)}(\theta, \phi) = \begin{pmatrix} G_{00}\, f^{(1)}_{\theta\phi} & G_{10}\, f^{(1)}_{\theta\phi} & -g_{00}\left(\theta - \frac{\pi}{2}\right) & g_{00}\,\phi \\ G_{10}\, f^{(1)}_{\theta\phi} & \hbar\omega_{10} + G_{11}\, f^{(1)}_{\theta\phi} & -g_{10}\left(\theta - \frac{\pi}{2}\right) & g_{10}\,\phi \\ -g_{00}\left(\theta - \frac{\pi}{2}\right) & -g_{10}\left(\theta - \frac{\pi}{2}\right) & \hbar\omega_c + G_{00}\, f^{(1)}_{\theta\phi} & 0 \\ g_{00}\,\phi & g_{10}\,\phi & 0 & \hbar\omega_c + G_{00}\, f^{(1)}_{\theta\phi} \end{pmatrix} \tag{3.45}$$

with, $f^{(1)}_{\theta\phi} = f^{(1)}(\theta, \phi)$, $\hbar\omega_{10} = \hbar\omega_c$, $G_{v_r v_r'} = \frac{g^2}{\hbar\omega_c} \langle d^2 \rangle_{v_r v_r'}$ and $g_{v_r v_r'} = g\, d_{v_r v_r'}$ where $v_r, v_r' = 0, 1$. In Figs.3.13, we show cuts through the VPCI along θ and ϕ, with exact surfaces (bold), linear (dotted-dashed) and quadratic (dotted) approximations. The latter are obtained from diagonalizing $\underline{\underline{V}}^{(1)}(\theta, \phi)$ without (linear, $f^{(1)}_{\theta\phi} \approx 0$) and with (quadratic, $f^{(1)}_{\theta\phi} \neq 0$) DSE contribution.

We observe three characteristic features of the VPCI: (i) For small values of both θ and ϕ in $\varepsilon_{L_1}(\theta, \phi)$ and $\varepsilon_{U_1}(\theta, \phi)$, we have $f^{(1)}_{\theta\phi} \approx 0$ and the degeneracy is lifted linearly in angular coordinates, (ii) $\varepsilon_{M_1}(\theta, \phi)$ exhibits a harmonic character at the intersection point, which results from the potential character of the dipole self-energy ($f^{(1)}_{\theta\phi}$ in Eq.(3.45)) and (iii) the mild "mexican-hat"-type nature of $\varepsilon_{L_1}(\theta, \phi)$ at $\eta = 0.1$ also stems from the DSE.

We finally note that the topological motive of a cavity-induced three-state VPCI is similar to *accidental* three-state conical intersections in molecular vibronic coupling theory.[177, 178, 179, 180]

3.3.3 Rovibro-Polaritonic Dynamics

We now turn to the dynamics of different rovibro-polaritonic wave packets, which mimic an externally driven rovibrating light-matter hybrid system subject to a classical z-polarized driving laser field. The latter could be directly included in the rovirational Pauli-Fierz Hamiltonian, however, we assume here simply that the excitation process already happened resulting in appropriately prepared initial states. In order to simulate different laser-polariton coupling scenarios, we consider two different initial states given by

$$\Psi_0^{(r)} = |1_r, 0_z, 0_y\rangle\; Y_0^1(\theta, \phi) \quad , \tag{3.46}$$

$$\Psi_0^{(r,z)} = \frac{1}{\sqrt{2}}\Big(|1_r, 0_z, 0_y\rangle + |0_r, 1_z, 0_y\rangle\Big)\, Y_0^1(\theta, \phi) \quad . \tag{3.47}$$

with singly-excited rotational state, $Y_0^1(\theta, \phi)$. Here, $\Psi_0^{(r)}$ constitutes a rovibrational excitation of the molecule and $\Psi_0^{(r,z)}$ corresponds to a superposition of singly-excited molecular

rovibrational and single-photon cavity mode states. The first state resembles an excitation scenario, where the external laser field couples exclusively to the molecule, whereas the second accounts additionally for a coupling to the z-polarized cavity mode. Both scenarios are accounted for by transition dipole moments

$$\mu^{(r)} = d_{10}^{(r)} \, |1_r, 0_z, 0_y\rangle \langle 0_r, 0_z, 0_y| \cos\theta \quad , \tag{3.48}$$

$$\mu^{(r,z)} = d_{10}^{(r,z)} \left(|1_r, 0_z, 0_y\rangle \langle 0_r, 0_z, 0_y| + |0_r, 1_z, 0_y\rangle \langle 0_r, 0_z, 0_y| \right) \cos\theta \quad . \tag{3.49}$$

The initial states (3.46) and (3.47) follow as, $\Psi_0^{(r)} = \mu^{(r)} \, |0_r, 0_z, 0_y\rangle \, Y_0^0(\theta, \phi)$, and, $\Psi_0^{(r,z)} = \mu^{(r,z)} \, |0_r, 0_z, 0_y\rangle \, Y_0^0(\theta, \phi)$, where we set, $d_{10}^{(r)} = d_{10}^{(r,z)} = 1$ in the following.
We discuss the time-evolution of those initial states from the perspective of zero-order (diabatic) populations

$$P_{\text{dia}}^{(k)}(t) = \int_0^{2\pi} \int_0^{\pi} |\varphi_k(\theta, \phi, t)|^2 \, \sin\theta \, \mathrm{d}\theta \, \mathrm{d}\phi \quad , \tag{3.50}$$

with rotational wave packets, $\varphi_k(\theta, \phi, t)$, introduced in Eq.(3.37) and their vibro-polaritonic (adiabatic) equivalents, $P_{\text{ad}}^{(l)}(t)$, with $l = G, L_1, M_1, U_1$, respectively. The latter result from adiabatic rotational wave packets, $\varphi_l^{\text{ad}}(\theta, \phi, t)$, entering an expansion similar to Eq.(3.37) in terms of adiabatic vibro-polaritonic basis states $|G\rangle, |L_1\rangle, |M_1\rangle$ and $|U_1\rangle$. Moreover, we study the adiabatic rotational dynamics by means of adiabatic reduced rotational densities

$$\rho_l^{\text{ad}}(\theta, t) = \int_0^{2\pi} |\varphi_l^{\text{ad}}(\theta, \phi, t)|^2 \, \mathrm{d}\phi \quad , \tag{3.51}$$

which resemble the reduced dynamics of rotational wave packets, $\varphi_l^{\text{ad}}(\theta, \phi, t)$, on different vibro-polaritonic surfaces as shown in Fig.3.12. We note that the dynamics along the θ-coordinate turns out to be particularly illustrative compared to the ϕ-coordinate. The TDSE (3.35) is solved by means of the MCTDH approach in its multi-set formulation as implemented in the Heidelberg MCTDH package[84]. We obtain converged results for propagation time $t_f = 3000\,\text{fs}$ by employing a two-dimensional Legendre DVR (PLeg) for angular coordinates with grid points, $N_\theta = 51$ and $N_\phi = 37$, and $n_s = 3$ SPFs per vibro-polaritonic state. Vibro-polaritonic populations and reduced rotational densities are equivalently obtained via the MCTDH method.

Vibropolaritonic Population Dynamics

We first access zero-order state contributions to different vibro-polaritonic states, which we extract from vibro-polaritonic populations at $t = 0$ for both initial states $\Psi_0^{(r)}$ and $\Psi_0^{(r,z)}$ as shown in Figs.3.14 and 3.15. For $\Psi_0^{(r)}$, we find both $|L_1\rangle$ and $|U_1\rangle$ to be populated to the same extent at $t = 0$. Additionally, there is no contribution from $|M_1\rangle$, *i.e.*, no molecular excited state contributes to the middle polariton, which identifies $|M_1\rangle$ as purely photonic in nature. Further, for $\Psi_0^{(r,z)}$, we observe contributions from all three vibro-polaritonic states, with equally populated $|L_1\rangle$ and $|U_1\rangle$ and minor contributions of $|M_1\rangle$. Hence, $|L_1\rangle$ and $|U_1\rangle$

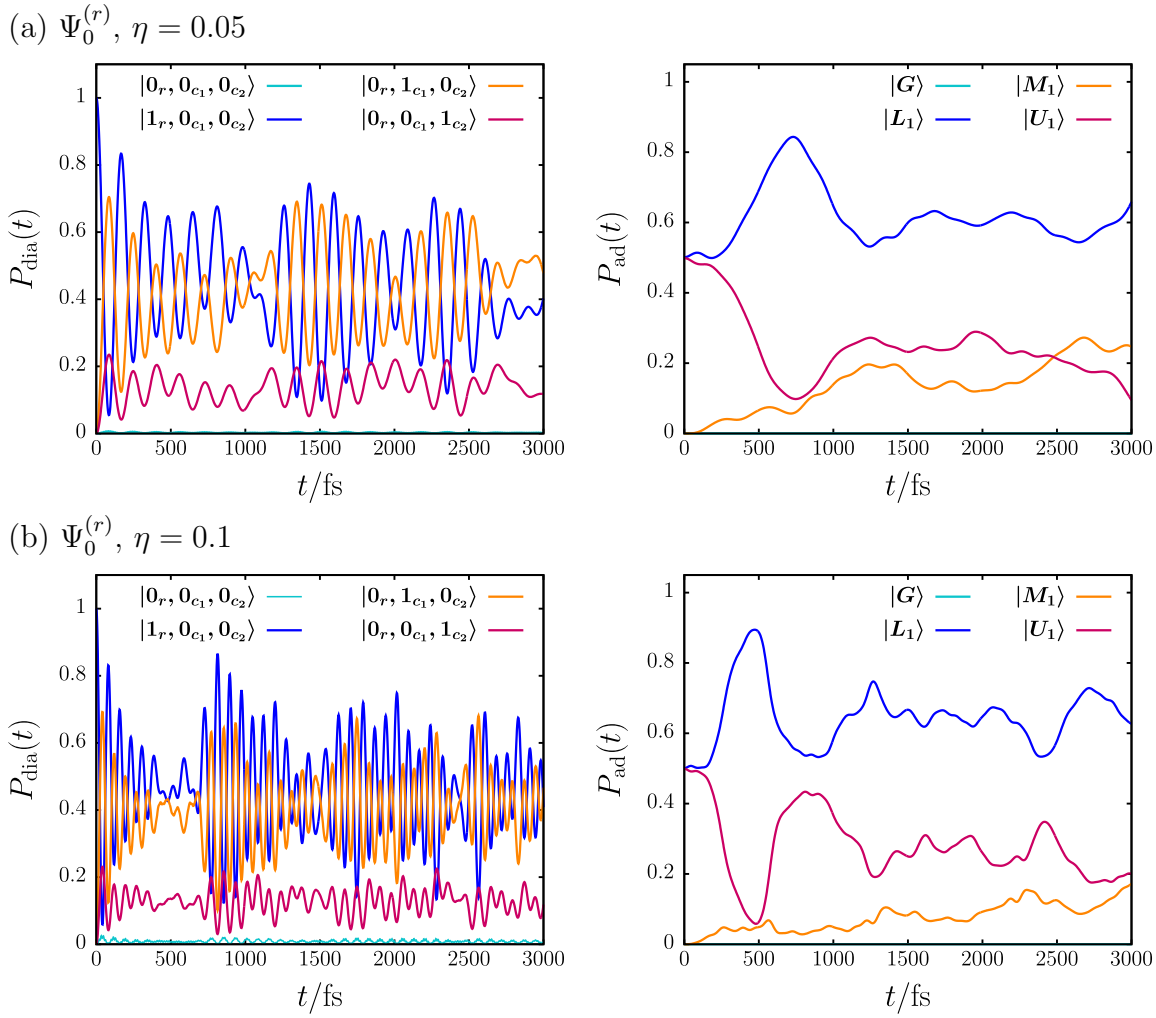

Figure 3.14: Zero-order (diabatic), $P_{\mathrm{dia}}(t)$, (left column) and vibro-polaritonic (adiabatic), $P_{\mathrm{ad}}(t)$, (right column) population dynamics for rovibrational singly-excited initial state, $\Psi_0^{(r)}$, with (a) $\eta = 0.05$ and (b) $\eta = 0.1$ for propagation time, $t_f = 3000\,\mathrm{fs}$.

are identified as light-matter hybrid states containing contributions from both molecular and cavity mode excitations.

As time evolves, we observe a fast initial population transfer to both singly-excited cavity mode states followed by a coherent exchange dynamics, which is dominated by the molecular and the z-polarized excited states and subject to quantum beats with a period of roughly 1000 fs. For an increased light-matter interaction strength ($\eta = 0.1$), the quantum beat period is shortened to roughly 600 fs and the frequency of coherent zero-order population transfer is strongly enhanced. In contrast, vibro-polaritonic dynamics (*cf.* Figs.3.14(a) and (b), right column) is dominated by slow population transfer from $|U_1\rangle$ to $|L_1\rangle$, accompanied by a gradual population of the $|M_1\rangle$. For $\eta = 0.05$, we observe a characteristic maximum in the $|L_1\rangle$-population at around 700 fs, which is shifted to roughly 500 fs for $\eta = 0.1$. Later

times are characterized by several decaying recurrences in $|U_1\rangle$.

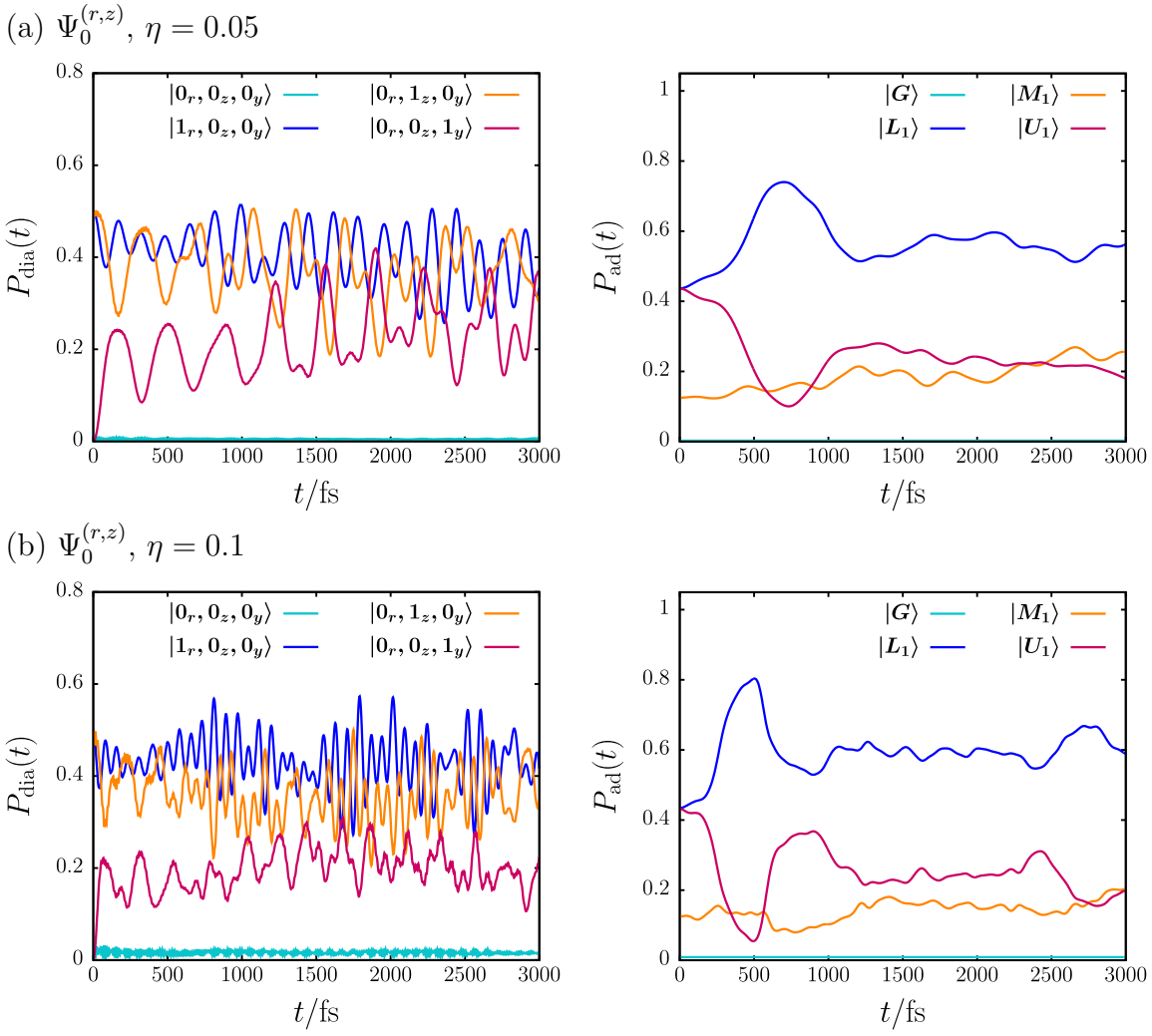

Figure 3.15: Zero-order (diabatic), $P_{\mathrm{dia}}(t)$, (left column) and vibro-polaritonic (adiabatic), $P_{\mathrm{ad}}(t)$, (right column) population dynamics for singly-excited superposition state, $\Psi_0^{(r,z)}$, with (a) $\eta = 0.05$ and (b) $\eta = 0.1$ for propagation time, $t_f = 3000\,\mathrm{fs}$.

For the dynamics initiated by $\Psi_0^{(r,z)}$, we find a significantly slower zero-order population transfer between the molecular and the z-polarized excited mode states for both coupling scenarios (*cf.* Figs.3.15(a) and (b), left column). From the vibro-polaritonic perspective, as depicted in the right column of the same figure, $|U_1\rangle$ is initially depopulated again in favor of $|L_1\rangle$, accompanied by a slight population increase in $|M_1\rangle$. The first maximum in $|L_1\rangle$ appears at same times as observed above and for longer times, the population dynamics is less structured here. We note, for both $\Psi_0^{(r)}$ and $\Psi_0^{(r,z)}$ the zero-order ground state is weakly contributing at $\eta = 0.1$ and exhibits a strongly oscillatory dynamics, which is especially pronounced for $\Psi_0^{(r,z)}$.

From this population-based perspective, we finally conclude that (i) only $|L_1\rangle$ and $|U_1\rangle$ are light-matter hybrid states opposed to the purely photonic $|M_1\rangle$ state and (ii) the inclusion of rotational degrees of freedom provides a cavity-induced transfer channel between vibro-polaritonic excited states. Notably, the latter is absent in purely vibrational problems, where an additional "bath" is required to mediate population transfer between vibro-polaritonic states.

Reduced Rotational Dynamics

We now change perspective and consider reduced dynamics of vibro-polaritonic reduced rotational densities, $\rho_l^{(r)}(\theta,t)$, and, $\rho_l^{(r,z)}(\theta,t)$, for the two different initial states, where l labels the vibro-polaritonic surface. In particular, we focus on non-adiabatic signatures of the three-state VPCI in reduced rotational densities.

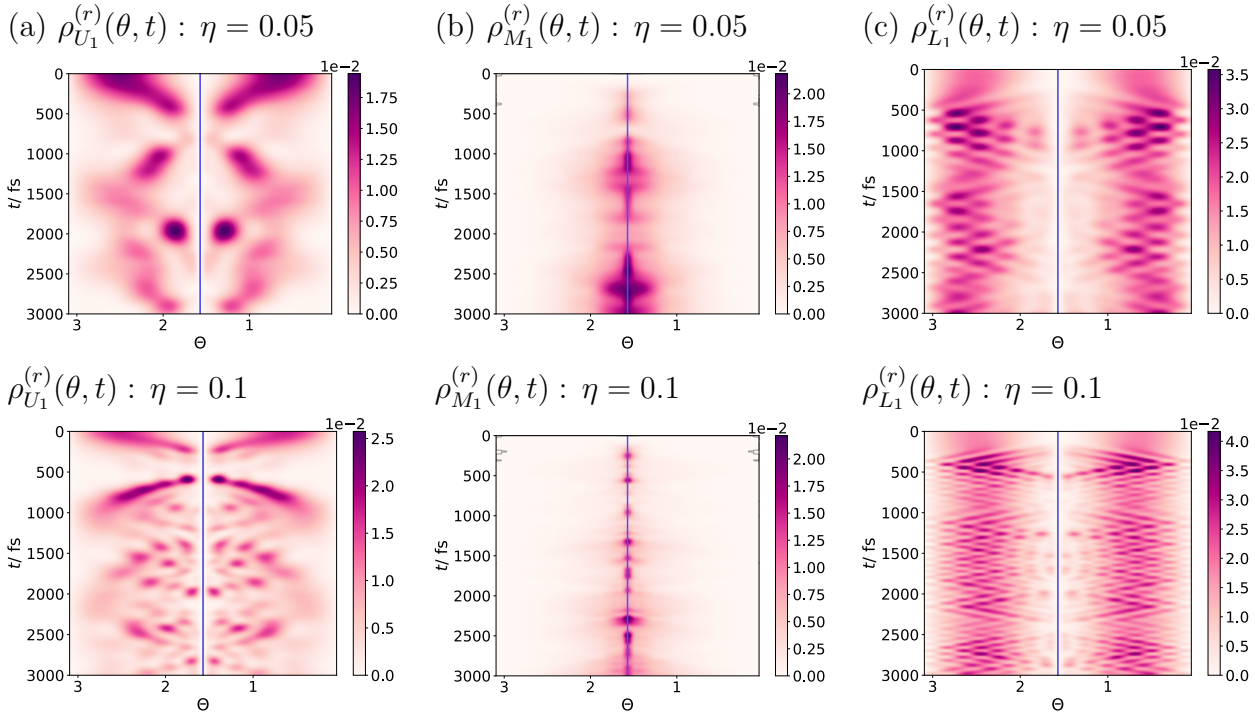

Figure 3.16: Time-evolution of adiabatic reduced rotational densities, $\rho_l^{(r)}(\theta,t)$, for rovibrational singly-excited initial state, $\Psi_0^{(r)}$, with vertical time-axis and horizontal θ-axis on (a) upper vibro-polaritonic surface, $\varepsilon_{U_1}(\theta,\phi)$, (b) middle vibro-polaritonic surface, $\varepsilon_{M_1}(\theta,\phi)$, and (c) lower vibro-polaritonic surface, $\varepsilon_{L_1}(\theta,\phi)$, for $\eta = 0.05$ (top row) and $\eta = 0.1$ (bottom row). Total adiabatic reduced rotational density, $\rho^{(r)}(\theta,t) = \sum_l \rho_l^{(r)}(\theta,t)$, with $l = G, L_1, M_1, U_1$ normalized for fixed time t.

In Figs.3.16 and 3.17, the time-evolution of $\rho_l^{(r)}(\theta,t)$ and $\rho_l^{(r,z)}(\theta,t)$ is shown for the excited-state surfaces $\varepsilon_{U_1}(\theta,\phi)$ (left column), $\varepsilon_{M_1}(\theta,\phi)$ (middle column) and $\varepsilon_{L_1}(\theta,\phi)$ (right column), respectively, with $\eta = 0.05$ (top row) and $\eta = 0.1$ (bottom row). The horizontal axis

covers the θ-coordinate and the vertical time-axis runs from 0 fs to 3000 fs (top to bottom). The position of the interaction point at $\theta = \frac{\pi}{2}$ is marked by a vertical blue line.
Starting with $\rho_l^{(r)}(\theta, t)$, we find density initially symmetrically distributed with respect to the intersection point on both L_1- and U_1-surfaces with larger amplitude for the latter in line with Figs.3.14. Under VSC with $\eta = 0.05$, the density symmetrically approaches the intersection region on ε_{U_1} followed by a transfer to the L_1-surface with minor contributions on M_1. On the lower-polariton surface, the density tends initially away from the VPCI. At around 700 fs, a rich interference pattern can be observed. From the perspective of rotational wave packets, we observe a non-adiabatic transfer between U_1- and L_1-surfaces, where wave packets initially located on different surfaces interfere with each other. As time progresses, $\rho_{L_1}^{(r)}(\theta, t)$ reenters the intersection region and a recurrence on ε_{U_1} is observed, which manifests as second maximum in $\rho_{U_1}^{(r)}(\theta, t)$ occurring around 1300 fs and 2000 fs. Throughout the

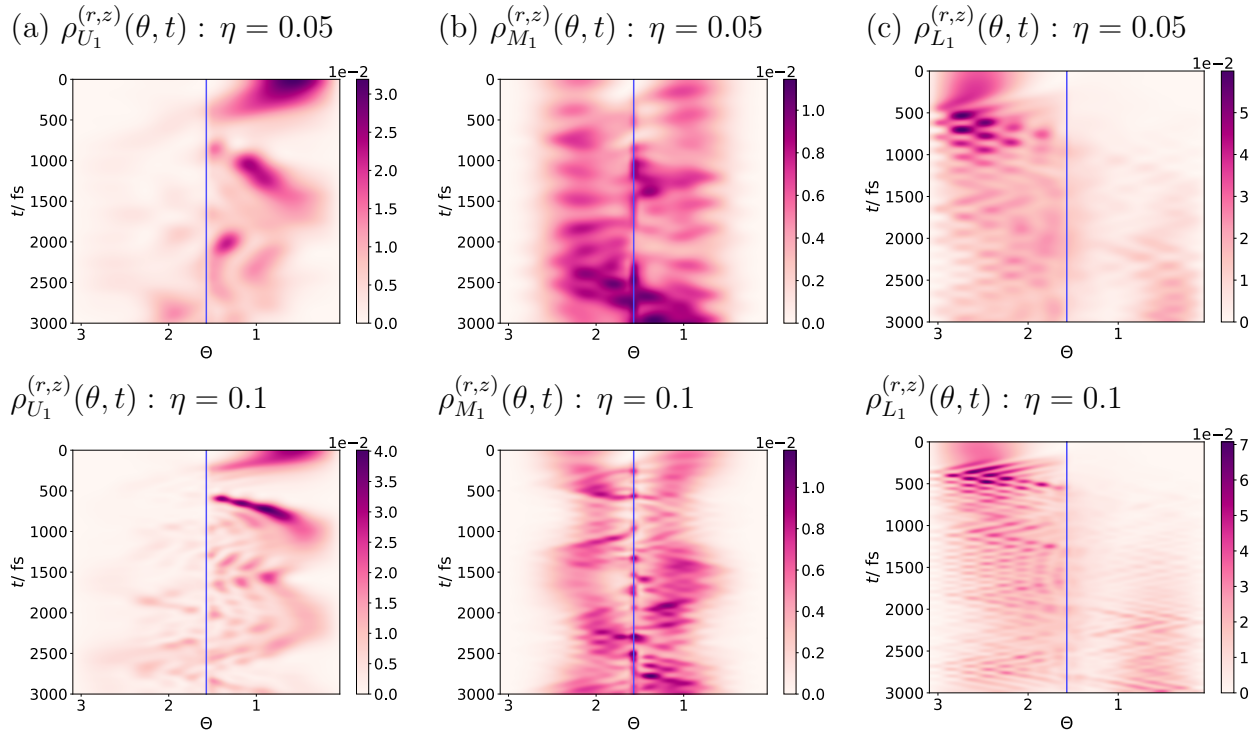

Figure 3.17: Time-evolution of adiabatic reduced rotational densities, $\rho_l^{(r,z)}(\theta, t)$, for singly-excited superposition state, $\Psi_0^{(r,z)}$, with vertical time-axis and horizontal θ-axis on (a) upper vibro-polaritonic surface, $\varepsilon_{U_1}(\theta, \phi)$, (b) middle vibro-polaritonic surface, $\varepsilon_{M_1}(\theta, \phi)$, and (c) lower vibro-polaritonic surface, $\varepsilon_{L_1}(\theta, \phi)$, for $\eta = 0.05$ (top row) and $\eta = 0.1$ (bottom row). Total adiabatic reduced rotational density, $\rho^{(r,z)}(\theta, t) = \sum_l \rho_l^{(r,z)}(\theta, t)$, with $l = G, L_1, M_1, U_1$ normalized for fixed time t.

recurrence event, we observe a stronger population of the M_1-surface, with density restricted to the harmonic vicinity of the intersection region. For $\eta = 0.1$, we observe the transfer process to be faster but qualitatively equivalent to the VSC regime. Interestingly, at the

onset of VUSC the reduced density is severely concentrated in the region close to the intersection point and only sparely explores the M_1-surface. This effect results from the enhanced population transfer between the upper and lower polariton surfaces.
For dynamics resulting from, $\Psi_0^{(r,z)}$, reduced vibro-polaritonic rotational density is initially distributed over all three vibro-polaritonic surfaces (*cf.* Fig.3.17) in line with the population analysis. Further, $\rho_{L_1}^{(r,z)}(\theta,t)$ and $\rho_{U_1}^{(r,z)}(\theta,t)$ show a highly asymmetric distribution relative to the intersection point, whereas $\rho_{M_1}^{(r,z)}(\theta,t)$ is symmetric with respect to the intersection and significantly weaker in magnitude. The time-evolution manifests again as non-adiabatic density transfer between U_1- and L_1-surfaces mediated by the VPCI, which leads to interference of rotational wave packets on the L_1-surface. In contrast to the rovibrationally excited initial state, $\Psi_0^{(r)}$, the M_1-surface is here significantly stronger explored. We attribute this effect to the presence of a finite population at $t = 0$, as the non-adiabatic population transfer from L_1-/U_1-surfaces to the M_1-surface is rather inefficient as seen before. Further, the asymmetric character of the reduced densities on the U_1- and L_1-surfaces dominates the dynamics roughly up to 1500 fs and gradually decreases for latter times. In line with previous arguments, a stronger light-matter interaction enhances the density transfer and interference effects turn out to be more pronounced. Additionally, the M_1-surface is less homogeneously populated and the density is contracted around the intersection coordinate.
In summary, adiabatic rotational densities reveal VPCI-mediated population transfer between vibro-polaritonic surfaces, which is dominated by (i) a funneling effect of the VPCI and (ii) interference of rotational wave packets initially located at different vibro-polaritonic surfaces.

3.3.4 Rovibro-Polaritonic Infrared Spectroscopy

We now discuss infrared spectra of the rovibro-polaritonic system and examine spectral signatures of the three-state VPCI. We calculate infrared spectra, $\sigma(\omega)$, without damping function as

$$\sigma(\omega) = A \int_0^T C(t)\, f_W(t)\, e^{+\mathrm{i}\omega t}\mathrm{d}t \quad , \tag{3.52}$$

with autocorrelation function, $C(t)$, window function, $f_W(t)$, as given in Eq.(3.10) and a constant, which we here set $A = 1$. Further, the dipole-dipole autocorrelation function reads

$$C(t) = \langle\Psi_0|\left(\mu^{(i)}\right)^\dagger \exp\left(-\mathrm{i}\underline{\underline{H}}t/\hbar\right)\mu^{(i)}|\Psi_0\rangle \quad , \tag{3.53}$$

where, $|\Psi_0\rangle = |0_r, 0_z, 0_y\rangle\, Y_0^0$, and, $\mu^{(i)}$, with $i = r, (r,z)$ is given in Eqs.(3.48) and (3.49). We note that the latter is an approximation, as we do not account for an excitation out of the vibro-polaritonic ground state and set the prefactors of the transition dipole moments to unity.
All spectra have been obtained for a total propagation time of $T = 2t_f = 6000$ fs. As a reference, we consider IR spectra obtained for a purely vibro-polaritonic system in the single-mode limit, *i.e.*, a CO molecule solely interacting with the z-polarized cavity-mode, which allows us to address both rotational effects and contributions of the second cavity

mode. In this case, we consider "single-mode limit" initial states

$$\tilde{\psi}_0^{(r)} = |1_r, 0_z\rangle \quad , \quad \tilde{\psi}_0^{(r,z)} = \frac{1}{\sqrt{2}}\Big(|1_r, 0_z\rangle + |0_r, 1_z\rangle\Big) \quad , \tag{3.54}$$

Further spectroscopic details are revealed by identifying contributions of eigenstates, ϕ_i, of the effective Hamiltonian, $\underline{\underline{H}}$, in Eq.(3.38) to initial states via intensities

$$I^{(r)} = \sum_i |\, \langle \Psi_0^{(r)} | \phi_i \rangle \,|^2 \, \delta(\hbar\omega - \varepsilon_i) \quad , \quad I^{(r,z)} = \sum_i |\, \langle \Psi_0^{(r,z)} | \phi_i \rangle \,|^2 \, \delta(\hbar\omega - \varepsilon_i) \quad . \tag{3.55}$$

Eigenvalues, ε_i, and intensities are obtained by diagonalizing $\underline{\underline{H}}$ in Eq.(3.38) via a Lanczos algorithm as implemented in the Heidelberg MCTDH package[84] with the same primitive basis as employed for the dynamics.

Cavity IR Spectra

We begin our discussion with IR spectra in the VSC regime with $\eta = 0.05$ as shown in Fig.3.18(a) and (b) for initial states $\Psi_0^{(r)}$ and $\Psi_0^{(r,z)}$. For both initial states, we observe a series of transitions with a dominant L_1-peak at $2076\,\mathrm{cm}^{-1}$ below the intersection point energy of $2137\,\mathrm{cm}^{-1}$. In the region of the U_1-surface, we find a progression of five peaks between $2207\,\mathrm{cm}^{-1}$ and $2309\,\mathrm{cm}^{-1}$ depending on the initial state with spacing $17 - 33\,\mathrm{cm}^{-1}$. The peak intensity increases with energy with a significantly less intense high-energy peak terminating the progression. For $\Psi_0^{(r,z)}$, we additionally observe a prominent peak at $2171\,\mathrm{cm}^{-1}$, which resembles an excitation of the purely photonic intermediate polariton state and is absent for $\Psi_0^{(r)}$.
The single mode limit reveals the well-known L_1- and U_1-peaks for $\tilde{\psi}_0^{(r)}$ with a Rabi-splitting of $\Omega_R = 214\,\mathrm{cm}^{-1}$ (grey curves). For $\tilde{\psi}_0^{(r,z)}$, the chosen linear combination exactly captures the U_1-state leading to a single peak in the spectrum. Accordingly, the inclusion of rotational effects leads to a much richer excitation spectrum (colored curves) compared to the single-mode limit (grey curves).
By analyzing intensities, $I^{(r)}$ and $I^{(r,z)}$, we extract the detailed character of observed excitations, which are hidden in spectra due to finite peak widths. The latter result from finite propagation times of rovibro-polaritonic wave packets. Both $I^{(r)}$ and $I^{(r,z)}$ show similar dominant contributions to the light-matter hybrid L_1- and U_1-peaks. Only $I^{(r,z)}$ exhibits the purely photonic M_1-peak as expected. Interestingly, $I^{(r,z)}$ shows additional contributions from multiple energetically close lying states with varying intensity to individual peaks. As those contributions are absent for the rovibrationally excited initial state, we attribute them a dominant rotational light-matter hybrid character, *i.e.*, the additional peaks seem to be dominated by photonic contributions.
For IR spectra obtained at the onset of the VUSC regime ($\eta = 0.1$), we find an overall broadening of the spectrum and observe the emergence of additional peaks as shown in Fig.3.18(c) and (d). In the single-mode limit, we obtain a large Rabi-splitting of $\Omega_R = 433\,\mathrm{cm}^{-1}$. Further, the rovibro-polaritonic progression in the U_1-spectral region turns out to be more pronounced with seven peaks showing slightly increased spacing of $29 - 49\,\mathrm{cm}^{-1}$. The latter

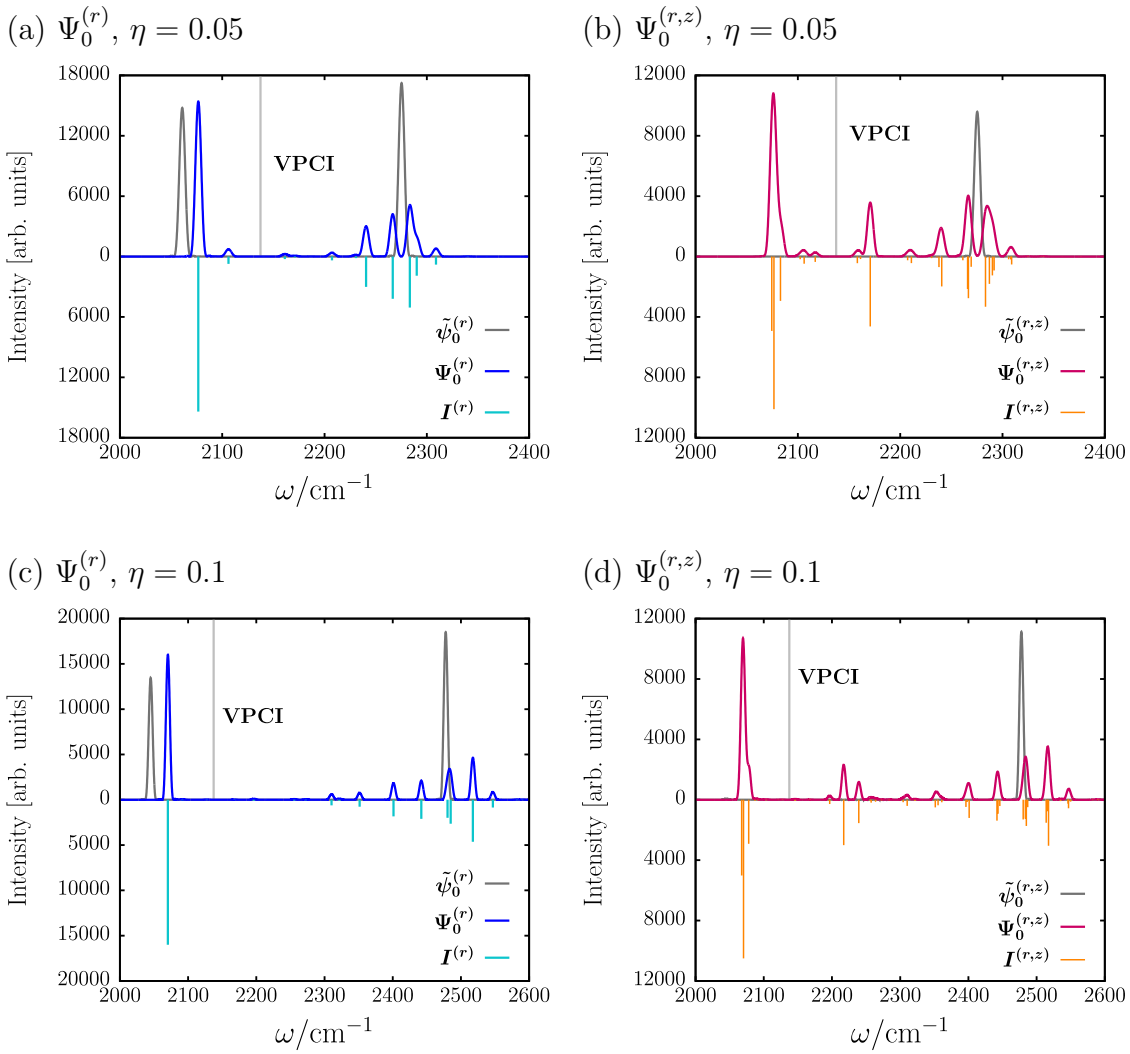

Figure 3.18: Vibro-polaritonic infrared spectra for different initial states and light-matter interaction parameters η with single-mode limit initial states, $\tilde{\psi}_0^{(r)}$ and $\tilde{\psi}_0^{(r,z)}$, (grey curves) in Eq.(3.54) , VPCI energy (grey vertical lines) and intensities, $I^{(r)}$ and $I^{(r,z)}$, in Eq.(3.55). Top row: Infrared-spectra for the vibrational strong coupling (VSC) regime with $\eta = 0.05$ for (a) molecular rovibrationally excited initial state, $\Psi_0^{(r)}$, and (b) light-matter superposition state, $\Psi_0^{(r,z)}$. Bottom row: (c) and (d) analogous to (a) and (b) in top row for onset of vibrational ultrastrong strong coupling (VUSC) regime at $\eta = 0.1$.

again decreases for increasing peak energy. The middle-polariton peak at $2171\,\mathrm{cm}^{-1}$ for the light-matter excited initials state now splits into three peaks at $2116, 2239$ and $2258\,\mathrm{cm}^{-1}$, respectively. As previously for VSC, we observe a number of rovibro-polaritonic hybrid states with lower intensity, which contribute to peaks in the spectrum obtained from $\Psi_0^{(r,z)}$ as indicated by $I^{(r,z)}$ and $I^{(r)}$ and are potentially close in energy.

We conclude that rovibro-polaritonic IR spectra indicate the formation of light-matter hy-

brid states with contributions from both molecular rotations and vibrations as well as cavity mode excitations, *i.e.*, rovibro-polaritonic states, with non-adiabatic signatures prominently manifesting in terms of a rovibro-polaritonic progression in the spectral region of the U_1-inverse cone.

Cavity Loss Effects

Finally, we consider the impact of experimentally ubiquitous spontaneous emission effects from cavity modes on rovibro-polaritonic infrared spectra. Spontaneous emission manifests

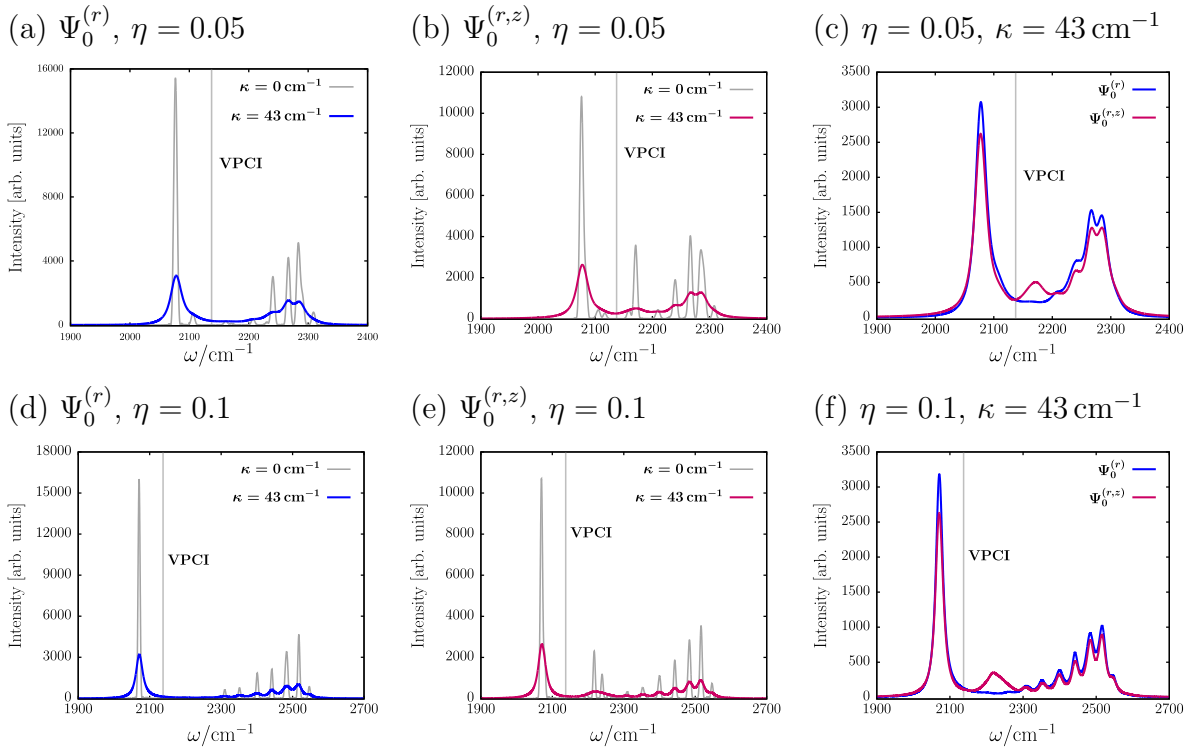

Figure 3.19: Vibro-polaritonic infrared spectra subject to dissipation (colored) with cavity decay rate, κ, for different initial states and light-matter interaction regimes with non-dissipative reference (grey) and VPCI energy (vertical line). Top row: Infrared-spectra for the vibrational strong coupling (VSC) regime with $\eta = 0.05$ for (a) molecular rovibrationally excited initial state $\Psi_0^{(r)}$, (b) light-matter superposition state $\Psi_0^{(r,z)}$ and (c) comparison of both dissipative spectra. Bottom row: (d)-(f) analogous to (a)-(c) in top row for onset of vibrational ultrastrong strong coupling (VUSC) regime at $\eta = 0.1$.

in finite cavity mode excitation lifetimes, which we consider by means of a phenomenological approach recently employed in electronic strong coupling studies[142, 144, 145]. There, the cavity mode Hamiltonian, $\hat{H}_C$, is replaced by a non-Hermitian operator

$$\hat{H}_C^{(\kappa)} = \sum_{\lambda=z,y} \left(\hbar\omega_c - \mathrm{i}\,\frac{\kappa}{2}\right) \hat{a}_\lambda^\dagger \hat{a}_\lambda \quad , \tag{3.56}$$

where the imaginary contribution is determined by an effective cavity decay rate, κ, respectively. Here, we set $\kappa = 43\,\mathrm{cm}^{-1}$ to model a infrared cavity with quality factor $Q = \frac{\hbar\omega_c}{\kappa} = 50$, being slightly lower as in Ref.[123] for example. We note that the zero-point energy contribution is neglected in Eq.3.56 to avoid artificial ground state decay[145].
In Fig.3.19, we compare infrared spectra subject to spontaneous emission induced dissipation with non-dissipative results as already presented in Fig.3.18. Most notably, cavity-loss-effects manifest as significant intensity reduction and peak broadening in addition to a suppression of the purely photonic M_1-peak. For the VSC scenario with $\eta = 0.05$, spectra resulting from $\Psi_0^{(r)}$ and $\Psi_0^{(r,z)}$ only slightly differ in their intensity as observable from Figs.3.19(a)-(c), with slightly more intense L_1-/U_1-transitions for $\Psi_0^{(r)}$. Further, the rovibro-polaritonic progression induced by the VPCI is only weakly observable and resembles a couple of shoulders in the U_1-spectra region. For increased light-matter interaction strength, however, the progression is clearly visible for both initial state although it suffers from the peak broadening effects.

3.3.5 Summary and Outlook

We studied a model for a freely rovibrating diatomic molecule (CO) interacting with two orthogonally polarized degenerate cavity modes tuned resonant to the fundamental vibrational transition of CO. A non-adiabatic perspective as motivated by significantly different energy scales of rotational and vibro-polaritonic degrees of freedom allowed us to identify the formation of three-state vibro-polaritonic conical intersections (VPCI) between three singly-excited vibro-polaritonic surfaces. From a dynamical perspective, the VPCI provide an effective transfer channel between upper and lower polariton states, whereas the purely photonic middle polariton state is only weakly populated. Further, non-adiabatic effects manifest especially in rotational dynamics, where passage of rotational density through the VPCI leads to rich interference patterns between rotational wave packets initially located on different surfaces. Finally, the non-adiabatic properties of the rovibrating light-matter hybrid system manifest in infrared spectra as pronounced multi-peak progression in the spectral region of the upper vibro-polaritonic surface. We assigned the peaks to rovibro-polaritonic hybrid states containing contributions from all degrees of freedom and examined the spontaneous emission induced peak broadening due to finite cavity mode line-widths in experimentally accessible Fabry-Pérot cavities.
For future studies, we point foremost to ensemble effects of multiple rovibrating diatomics interacting with orthogonally polarized cavity modes. Ensemble effects are assumed to alter the character of vibro-polaritonic states and spectra, respectively. Especially the nature of the middle-polariton state in an ensemble of molecules, the emergence of dark molecular states, *i.e.*, states assumed to have no photonic contributions, as well as cavity-induced energy transfer dynamics for interacting and non-interacting ensembles might be of interest under the influence of molecular rotations.

3.4 A Cavity-Altered Thermal Isomerization Model

In this last section of Ch.3, we reconsider the ammonia inversion process in the single-cavity-mode limit from the perspective of a minimal cavity-altered thermal isomerization model. This project has been inspired by celebrated VSC experiments of Thomas *et al.*, who studied cavity-altered, selective cleavage of Si-C and Si-O bonds in silane molecules[122]. Significant theoretical efforts were made contributing to the detailed understanding of reactivity under VSC[181, 182, 183, 184, 185, 186, 187, 188, 189, 190, 191, 192, 193, 194, 195, 196, 197, 198, 199], which is, however, still under dispute.

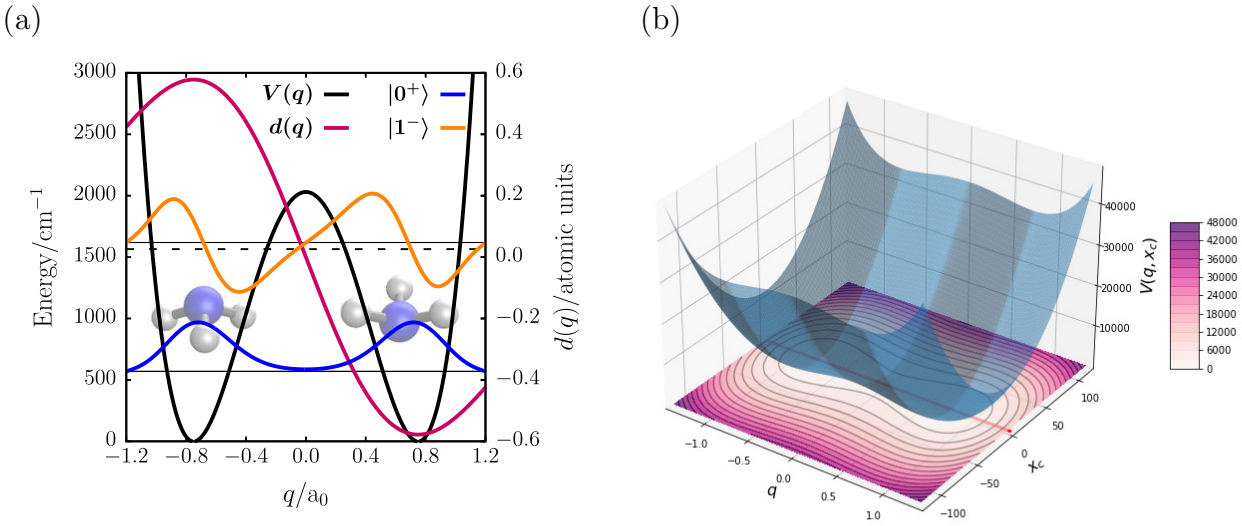

Figure 3.20: (a) Symmetric double-well potential, $V(q)$ (*cf.* Eq.(3.6)), modeling ammonia inversion mode, a model dipole function, $d(q)$ (*cf.* Eq.(3.8)), as well as symmetric ground state, $|0^+\rangle$, and anti-symmetric first excited state, $|1^-\rangle$ (dashed-black line indicates symmetric, first excited state $|1^+\rangle$; close-up of Fig.3.2c)). The inversion coordinate and dipole moment are given in atomic units (a_0 and ea_0 with Bohr radius a_0 and elementary charge e). (b) Two-dimensional cavity potential energy surface, $V_\eta(q, x_c)$, of non-interacting ($\eta = 0$) cavity-plus-ammonia inversion model with minimum energy path (MEP) given in red. Coordinates are given in atomic units (a_0 for q and $\sqrt{m_e}\, a_0$ for x_c), the potential energy in wavenumbers, cm^{-1}.

Here, we study the cavity-altered ammonia-inversion model and discuss effects of VSC on the cPES, thermal reaction kinetics and quantum dynamics. We give a detailed characterization of the model cPES, the corresponding minimum energy path and transition state as function of light-matter interaction regime and cavity mode frequency. Further, we obtain thermal rates characterizing the cavity-altered inversion process from the perspective of Eyring TST and fully quantum mechanical rate theory. In combination with the topological cPES analysis, we identify the crucial role of quantum effects, which lead to both a strong cavity-induced suppression of the inversion process and tunneling. We finally discuss an emergent resonance effect in our minimal model, which manifests as dynamical localiza-

tion of a reactant wave packet for a cavity mode tuned resonant to a harmonized reactant frequency.

Results discussed in this chapter are reproduced from "E.W. Fischer, J. Anders, P. Saalfrank. Cavity-Altered Thermal Isomerization Rates and Dynamical Resonant Localization in Vibropolaritonic Chemistry. *J. Chem. Phys.* **156**, 154305, (2022)."[200] with permission of AIP Publishing.

3.4.1 Cavity Potential Energy Surface Analysis

We start the discussion by examining properties of the cPES, $V_\eta(q, x_c)$, as function of the light-matter interaction strength as parametrized by η. The molecular symmetric double-well potential, the dipole function as well as the two eigenstates with energy difference resonant to the cavity mode ($\hbar\omega_c = \hbar\omega_{1^-0^+} = 1039\,\mathrm{cm}^{-1}$) are shown again in Fig.3.20a. Further, we depict once more the corresponding two-dimensional cPES in Fig.3.20b for the non-interacting limit with $\eta = 0.0$.

In Fig.3.21(a)-(d), $V_\eta(q, x_c)$ is shown for selected values of η. For increasing light-matter interaction, we observe a distortion of the cPES, which leads to a symmetry reduction from the molecular point group C_{2v} in the non-interacting limit to C_2 at finite interaction strength as already discussed in Sec.3.2. Accordingly, the two double-well minima located at $q_0^\pm = \pm 0.75\,a_0$ remain invariant under two-fold rotation and the cavity transition state is located at the origin of the q-x_c-plane for all values of η.

Further, we introduce a cavity minimum energy path (cMEP), $\underline{r}_\eta(Q)$, which provides a geodesic curve on the cPES in the q-x_c-plane.[201] The path-length can be defined as

$$L\left[\underline{r}_\eta(Q)\right] = \int_{Q_0}^{Q_f} \sqrt{\left(\frac{\partial\, r_\eta^{(1)}(Q')}{\partial Q'}\right)^2 + \left(\frac{\partial\, r_\eta^{(2)}(Q')}{\partial Q'}\right)^2}\,\mathrm{d}Q' \quad , \tag{3.57}$$

with mass-weighted molecular coordinate, $Q = \sqrt{\mu}\,q$, and, Q_0 and Q_f, being initial and final points along the path. The cMEP length allows us to introduce a reaction coordinate, s, and the corresponding cavity reaction potential, $V_\eta(s)$. In Fig.3.21(a)-(d), the cMEP is indicated by red lines. As η increases, we observe a transition from a linear to a "s"-shaped path, which comes in hand with an increase of the path length, L. The corresponding $V_\eta(s)$ for different path lengts are shown in Fig.3.22 for selected η. As shown in Sec.3.2, we find the double-well structure of the reaction potential and the classical activation energy to be conserved at finite light-matter interaction. However, for increasing η the double-well potential is "stretched" due to the elongation of the cMEP, which results in a considerable barrier broadening effect. We will quantify the latter observation below.

A quantitative characterization of the cPES is possible by means of harmonic analysis at the stationary points, *i.e.*, at a minimum and at the first-order saddle point resembling the cavity transition state. First, we expand $V(Q, x_c)$ up to second order in Q around the

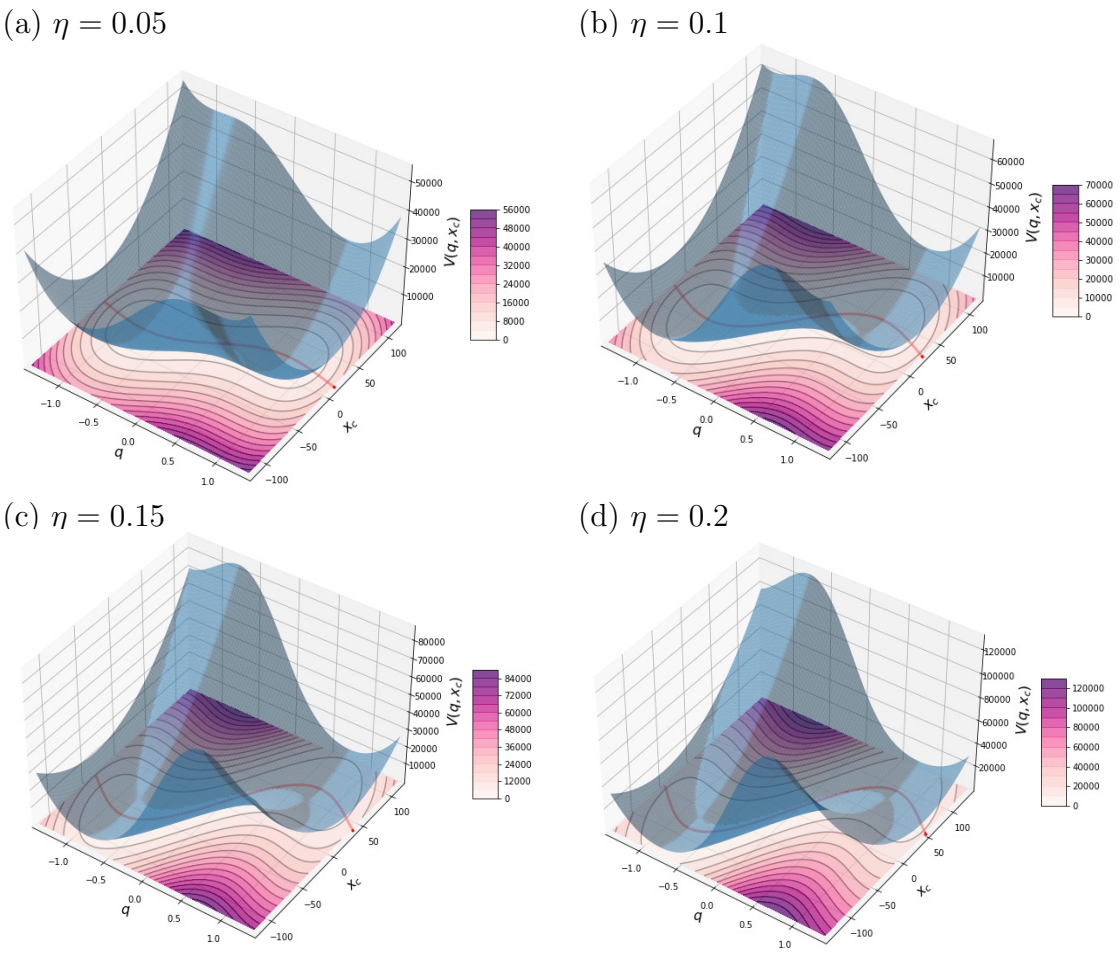

Figure 3.21: Cavity potential energy surfaces, $V_\eta(q, x_c)$, for ammonia inversion model and (a)-(d) selected values of η at resonance ($\omega_c = \omega_{1^-0^+}$), with minimum energy paths indicated by red lines (see text for details). Coordinates, q and x_c, are given in atomic units as in Fig.3.20(a), and energy scale in wavenumbers, cm^{-1}.

"reactant" minimum at $Q_0 = \sqrt{\mu}\, q_0^-$, as

$$V_\eta^0(Q, x_c) = \frac{1}{2} \begin{pmatrix} Q - Q_0 & x_c \end{pmatrix} \begin{pmatrix} \dfrac{2\,(6A_4\,Q_0^2 + A_2\,\mu_s)}{\mu_s^2} & 0 \\ 0 & \omega_c^2 \end{pmatrix} \begin{pmatrix} Q - Q_0 \\ x_c \end{pmatrix} + \sqrt{\frac{2\omega_c}{\hbar}}\, g\, x_c\, d_0(Q_0) + \frac{g^2}{\hbar\omega_c}\, d_0^2(Q_0) \quad , \tag{3.58}$$

where the mass-weighted reactant Hessian reads

$$\underline{\underline{W}}^0 = \begin{pmatrix} \dfrac{2\,(6A_4\,Q_0^2 + A_2\,\mu)}{\mu^2} & 0 \\ 0 & \omega_c^2 \end{pmatrix} \quad . \tag{3.59}$$

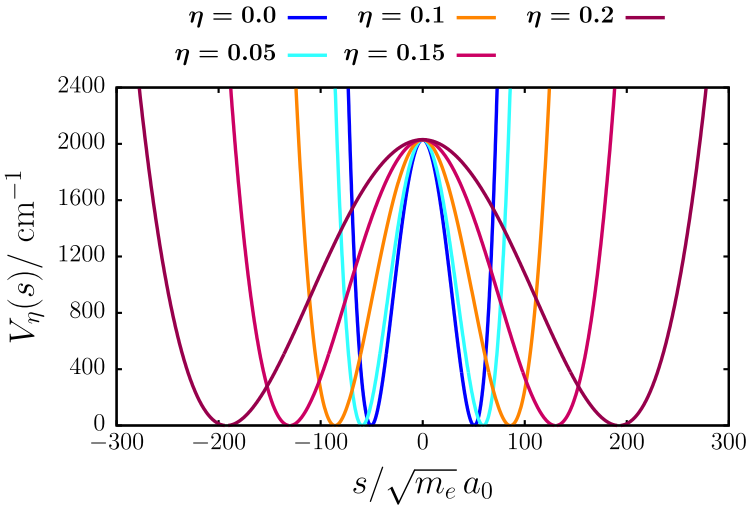

Figure 3.22: Cavity reaction potential, $V_\eta(s)$, along the cavity minimum energy path for selected values of η with mass-weighted atomic units for cavity reaction coordinate, s.

As $\underline{\underline{W}}^0$ is already diagonal, the reactant normal-mode frequencies, $\omega_R^{(1)}$ and $\omega_R^{(2)}$, are directly obtained as

$$\omega_R^{(1)} = \sqrt{\frac{2\,(6A_4\,Q_0^2 + A_2\,\mu)}{\mu^2}} \quad , \tag{3.60}$$

$$\omega_R^{(2)} = \omega_c \quad . \tag{3.61}$$

In our model, both $\hbar\omega_R^{(1)} = 1182\,\mathrm{cm}^{-1}$ and $\hbar\omega_R^{(2)} = 1039\,\mathrm{cm}^{-1}$ are independent of light-matter coupling, which vanishes here in the double-harmonic approximation. The two frequencies resemble the harmonized molecular reactant mode and the cavity mode frequency, respectively. We note that both minima located at $q_0^{\pm}$ are equivalent by symmetry and we could have analogously considered the minimum at q_0^{+} as reactant minimum.
Next, we consider a quadratic approximation to the cPES at the cavity transition state with coordinate $Q^\dagger = 0$, where

$$V_\eta^\ddagger(Q, x_c) = \frac{1}{2}\begin{pmatrix} Q & x_c \end{pmatrix} \underbrace{\begin{pmatrix} \frac{2}{\mu_s}\left(\frac{g^2\,\gamma^2}{\hbar\omega_c} + A_2\right) & -\sqrt{\frac{2\omega_c}{\hbar\,\mu_s}}\,g\,\gamma \\ -\sqrt{\frac{2\omega_c}{\hbar\,\mu_s}}\,g\,\gamma & \omega_c^2 \end{pmatrix}}_{=\underline{\underline{W}}^\ddagger} \begin{pmatrix} Q \\ x_c \end{pmatrix} \quad , \tag{3.62}$$

with mass-weighted Hessian, $\underline{\underline{W}}^\ddagger$, which now explicitly contains off-diagonal coupling elements linear and a diagonal DSE correction quadratic in the light-matter coupling strength, g, appearing in the upper molecular "block". In the non-interacting limit ($\eta = 0.0$), one

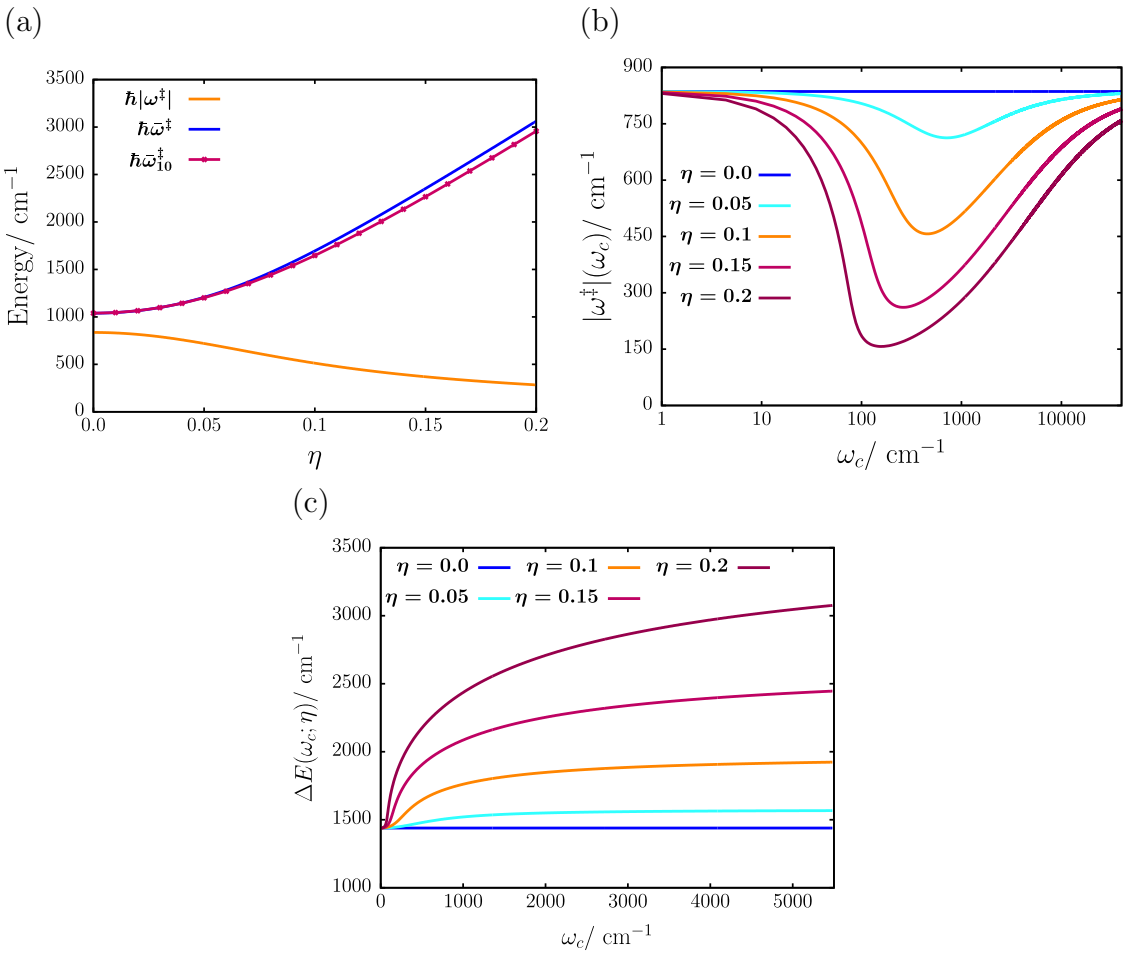

Figure 3.23: (a) Harmonic cTS barrier frequency, $|\omega^\ddagger|$, and "valley" frequency, $\bar{\omega}^\ddagger$, besides anharmonic "valley" frequency, $\bar{\omega}^\ddagger_{10}$, as functions of η with $\omega_c = 1039\,\mathrm{cm}^{-1}$. (b) Harmonic cTS barrier frequency, $|\omega^\ddagger|$, (logarithmic ω_c-axis) and (c) "valley" frequency, $\bar{\omega}^\ddagger$, as function of cavity mode frequency, ω_c, for selected values of η.

obtains two normal modes with frequencies

$$\omega^\ddagger = \mathrm{i}\sqrt{\frac{2\,|A_2|}{\mu}} \equiv \mathrm{i}\,|\omega^\ddagger| \quad , \tag{3.63}$$

$$\bar{\omega}^\ddagger = \omega_c \quad , \tag{3.64}$$

where, $\hbar|\omega^\ddagger| = 836\,\mathrm{cm}^{-1}$, resembles an imaginary barrier frequency characteristic for a first-order saddle point and $\bar{\omega}^\ddagger$ is a "valley" frequency of the corresponding orthogonal normal mode.
In Fig.3.23(a), both frequencies are shown as function of η. We observe a substantial decrease of $\hbar|\omega^\ddagger|$ from 836 to $284\,\mathrm{cm}^{-1}$ ($\eta = 0.2$), which is contrasted by a significant increase of $\hbar\bar{\omega}^\ddagger$ from 1039 to $3062\,\mathrm{cm}^{-1}$ ($\eta = 0.2$). The barrier broadening effect observed

in Fig.3.22 directly translates to the decrease in $\hbar|\omega^\ddagger|$, which determines the curvature of the cPES at the transition state. The second aspect, *i.e.*, the increase in $\hbar\bar{\omega}^\ddagger$ with η, can be interpreted as "narrowing" effect of the valley at the transition state of the cPES. Notably, this "valley-narrowing" effect is very well described in the double harmonic approximation and we find only minor deviations in anharmonically corrected $\hbar\bar{\omega}^\ddagger_{10}$ (*cf.* Fig.3.23(a)).

We now proceed by discussing $|\omega^\ddagger|$ as function of ω_c at fixed η. For $|\omega^\ddagger|$, we observe the formation of a minimum at non-zero η when the cavity frequency is close to the barrier frequency as shown in Fig.3.23(b). As $|\omega^\ddagger|$ relates to the barrier width, this effect corresponds to a barrier broadening maximum and resembles a "barrier resonance effect". We note, a similar effect has been recently identified in a Shin-Metiu model, where it has been interpreted from a classical perspective as caging effect.[194] However, it misses direct connection to experimentally observed resonance phenomena.[121] In particular, we shall show below that the herein observed barrier resonance has no effect on reaction rates in our inversion model when a fully quantum mechanical treatment is considered.

Further, we find the effective activation energy, ΔE^a_{eff}, Eq.(2.103), to exhibit a strongly nonlinear increase with ω_c at fixed η. In detail, the nonlinear behavior restricts to small cavity frequencies for all η and tends to η-dependent constant values as ω_c becomes large. For small cavity mode frequencies, the nonlinear character stems from the dominant contribution of $\bar{\omega}^\ddagger$, which depends on both η and ω_c in contrast to the reactant mode frequencies (*cf.* Eqs.(3.60) and (3.61)), which are independent of η in our model. For large ω_c, both $\bar{\omega}^\ddagger$ and $\omega^{(2)}_R$ increase linearly with ω_c at the same rate, such that $\Delta E^a_{\text{eff}} \propto const.$ at fixed η with respect to variations in ω_c.

In summary, the cPES analysis allows us to deduce two consequences of light-matter interaction, which are relevant for thermal reaction rates to be discussed in the next section. First, the "valley narrowing" effect at the cavity transition state, which is equivalent to a "stiffening" of the valley mode, leads to a decrease of energetically accessible states at the cavity transition state as η increases. Hence, a decrease of thermal reaction rates with increasing η is suggested. Second, the "barrier broadening" effect indicates a cavity induced suppression of tunneling, which further decreases thermal reaction rates especially at low temperatures. We emphasize that both effects are purely quantum mechanical in character and we observe no classical cavity-induced effects on our model cPES.

3.4.2 Cavity-Altered Thermal Isomerization Rates

We now connect our findings of the cPES analysis to cavity-altered thermal reaction rates. In particular, we compare results obtained from a fully quantum mechanical rate theory formulated in terms of cumulative reaction probabilities with harmonic Eyring transition state theory (*cf.* Secs.2.4.1 and 2.4.2). The CRP-based approach allows us to discuss the deep tunneling regime relevant at low temperatures and thus consequences of the barrier broadening effect.

Cavity Eyring TST Thermal Rates

In Fig.3.24(a), we show Arrhenius plots, *i.e.*, $\ln k^{\mathrm{TST}}$ vs. $1/k_BT = \beta$, for Eyring TST thermal rates, k^{TST} (*cf.* Eq.(2.101)), at selected values of η. We consider $\beta \in [0.001, 0.02]\,\mathrm{cm}$, which corresponds to a temperature range of $[1438, 72]\,\mathrm{K}$.

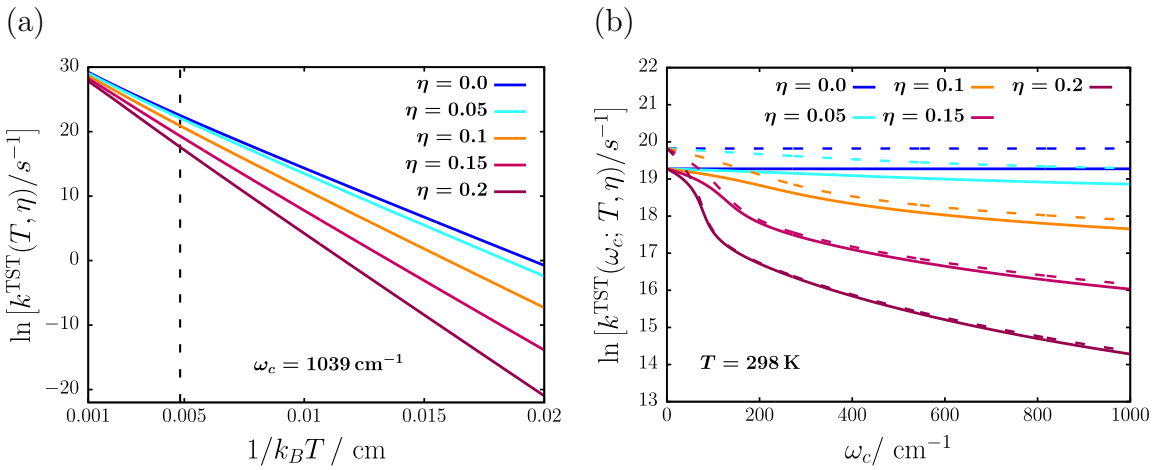

Figure 3.24: (a) Arrhenius plot of logarithmic harmonic Eyring TST rates, $\ln k^{\mathrm{TST}}(T,\eta)$, as function of inverse temperature, $1/k_BT$, at $\omega_c = 1039\ \mathrm{cm}^{-1}$ for selected η (black, dashed-line indicates $T = 298\,\mathrm{K}$). (b) Natural logarithm of harmonic Eyring TST rates, $\ln k^{\mathrm{TST}}(\omega_c;T,\eta)$, as function of cavity frequency, ω_c, with (dashed) and without (bold) Wigner tunneling correction for $T = 298\,\mathrm{K}$.

As a general trend, we observe $\ln k^{\mathrm{TST}}$ to decrease with increasing light-matter coupling strength. In the high-temperature limit, thermal rates for different interaction regimes converge to a similar value, but diverge in the low temperature limit, where a significant rate suppression is observed. By reconsidering the topological analysis of the cPES at the cavity transition state, the decrease in thermal reaction rates can be rationalized by the "valley narrowing" effect related to the increase of $\bar{\omega}^{\ddagger}$ with η (*cf.* Fig.3.23)(a)). Importantly, this effect is purely quantum mechanical in nature and results from the zero-point energy corrections of the light-matter hybrid valley mode to the effective activation energy, $\Delta E^a_{\mathrm{eff}}$. The classical activation energy, E^a_{cl}, is independent of the light-matter interaction regime in the herein studied cPES framework as shown in Sec.3.2.2.
From a thermodynamic perspective, the Eyring TST thermal rate Eq.(2.109) can be written as

$$\ln k^{\mathrm{TST}}(T,\eta) = \ln B(T) - \beta\left(E^a_{cl} - E^0_R + \frac{\hbar\bar{\omega}^{\ddagger}(\eta)}{2}\right) \quad , \tag{3.65}$$

with

$$B(T) = \frac{1}{2\pi\hbar\beta}\exp\left(1 + \Delta S^{\ddagger}(T,\eta)/R\right) \quad , \tag{3.66}$$

where, $B(T)$, turns out here to only weakly depend on both T and η. Hence, $k^{\mathrm{TST}}(T,\eta)$

mainly changes due to the activation enthalpy as given by Eq.(2.108), which is significantly determined by cavity-induced zero-point energy effects.
Further, we consider $\ln k^{\mathrm{TST}}(T,\eta)$ as a function of harmonic cavity mode frequency, ω_c, at constant temperature $T = 298\,\mathrm{K}$ for selected values of η. Here, we additionally consider the Wigner correction (*cf.* Eq.(2.105)), which approximately accounts for tunneling and allows us to additionally access the impact of the "barrier resonance effect" in $|\omega|^{\ddagger}$ (*cf.* Fig.3.23(b)), from the perspective of Eyring TST. With and without Wigner correction, we find $\ln k^{\mathrm{TST}}(T,\eta)$ to monotonically decrease with increasing ω_c for all values of η considered here. The Wigner correction turns out to be small for large ω_c and η, and slightly more important for small ω_c and η. In particular, we do not observe a signature of the barrier resonance in the Wigner corrected rates (note, bare $k^{\mathrm{TST}}(T,\eta)$ are independent of $|\omega|^{\ddagger}$). In contrast, the nonlinear dependence on ω_c for small cavity mode frequencies and a linear η-dependent regime for large ω_c, can be traced back to $\Delta E^a_{\mathrm{eff}}$ as shown in Fig.3.23(c), *i.e.*, this effect is again the result of cavity-induced zero-point energy effects.

Cavity CRP Thermal Rates

We now turn to fully quantum mechanical thermal rates based on cumulative reaction probabilities. CRP thermal rates allow us to address details of tunneling, while fully accounting for anharmonic effects of the cPES. Numerical details are provided in Appendix B.

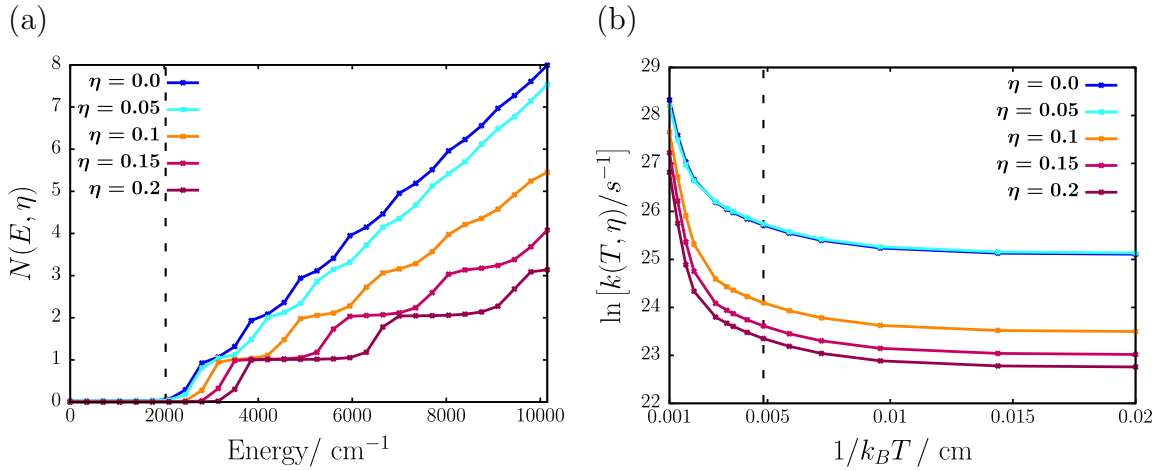

Figure 3.25: (a) Cumulative reaction probability, $N(E,\eta)$, for cavity-altered ammonia inversion model as a function of energy, E, above the reactant well minimum for selected values of η. Classical barrier height, $E^a_{cl} = 2030\,\mathrm{cm}^{-1}$, is indicated by a vertical dashed black line. (b) Arrhenius plot of logarithmic thermal rate constants, $\ln k(T,\eta)$, obtained from CRP as a function of inverse temperature, $1/k_BT$, for selected values of η (here black, dashed-line indicates $T = 298\,\mathrm{K}$). In both plots (a) and (b), the cavity frequency is $\omega_c = 1039\ \mathrm{cm}^{-1}$.

We first discuss the CRP, $N(E,\eta)$, as function of energy for selected values of η (*cf.* Fig.3.25(a)). The energy scale is given with respect to the classical reactant minimum,

where $E = 0$ and the classical activation energy, $E_{cl}^{a} = 2030\,\mathrm{cm}^{-1}$, is indicated by a vertical black-dashed line.
We observe $N(E, \eta)$ to increase in a step-like fashion with an onset in the vicinity of E_{cl}^{a}, which is blue-shifted onset for increasing η. The number of steps in $N(E, \eta)$ and its average slope decreases with increasing η. The step-like increase resembles the successive opening of reactive channels, which correspond to the number of bound states at the cavity transition state. The distance between two steps in the CRP is roughly given by $\hbar\bar{\omega}^{\ddagger}$, which reflects the quantized nature of the related valley mode. Notably, the reduction of reactive channels (steps) with increasing light-matter interaction strength can be directly related to the "valley narrowing" effect and the reduction of energetically accessible states for a given thermal energy. Further, small deviations occurring at larger energies and η, which manifest as shorter step intervals, are related to small anharmonic effects as already noted with respect to Fig.3.23(a).
We now discuss Arrhenius plots for CRP rates as shown in Fig.3.25(b) for the same parameter regimes as discussed in Fig.3.24(a). For the high-temperature regime, we find a similar behavior as for the Eyring TST rates and at ambient temperatures an overall reduction of the thermal reaction rate for increasing light-matter interaction strength is found. At low temperatures the Arrhenius plot deviate substantially from the Eyring TST results. Here, $\ln k(T, \eta)$ is dominated by plateaus, which resemble the (deep) tunneling regime. In particular, we observe a decrease of constant $\ln k(T, \eta)$ with increasing η, which relates to significantly attenuated tunneling rates for increasing light-matter interaction strength.
In summary, we find two key signatures for cavity-induced effects on thermal reaction rate constants in our model, which directly connect to findings of the cPES analysis. First, an overall rate reduction with increasing η, which resembles the "valley narrowing" effect that effectively lowers the number of thermally accessible reaction channels at the cavity transition state. Second, a cavity-induced tunneling attenuation in the (deep) tunneling regime, which relates to a barrier broadening effect of the cPES.

3.4.3 Resonant Dynamical Reactant Localization

In the third part of this discussion, we consider the time-dependent perspective on the cavity-altered ammonia inversion model and identify a *dynamical resonance effect*, which leads to reactant wave packet localization and consequently suppressed inversion probabilities.

A Dynamical Resonance Effect

We solve the time-dependent Schrödinger equation for the cavity-altered ammonia inversion model with initial state

$$\psi_0(q, x_c) = \psi_G(q; q_i)\,\phi_0(x_c) \quad . \tag{3.67}$$

Here, $\psi_G(q; q_i)$ is a molecular Gaussian wave packet, which is obtained by displacing the ground state of the molecular harmonized reactant mode with frequency $\omega_R^{(1)} = 1182\,\mathrm{cm}^{-1}$ to $q_i = -0.9\,a_0$. Further, $\phi_0(x_c)$ is the bare cavity mode ground state wave function, *i.e.*,

we consider a cavity without any photons. We follow the time-evolution of the wave packet by means of an inversion probability defined as

$$P_{\text{inv}}(t) = \int_{-\infty}^{\infty} \mathrm{d}x_c \int_{-\infty}^{\infty} \mathrm{d}q\, \theta(q)\, |\psi(q, x_c, t)|^2 \quad , \tag{3.68}$$

where $\theta(q)$ is the Heaviside step function centered at q_0. $P_{\text{inv}}(t)$ resembles the probability of populating the "product"-well of the two-dimensional cPES, which is specified by molecular coordinates $q > 0$, respectively.

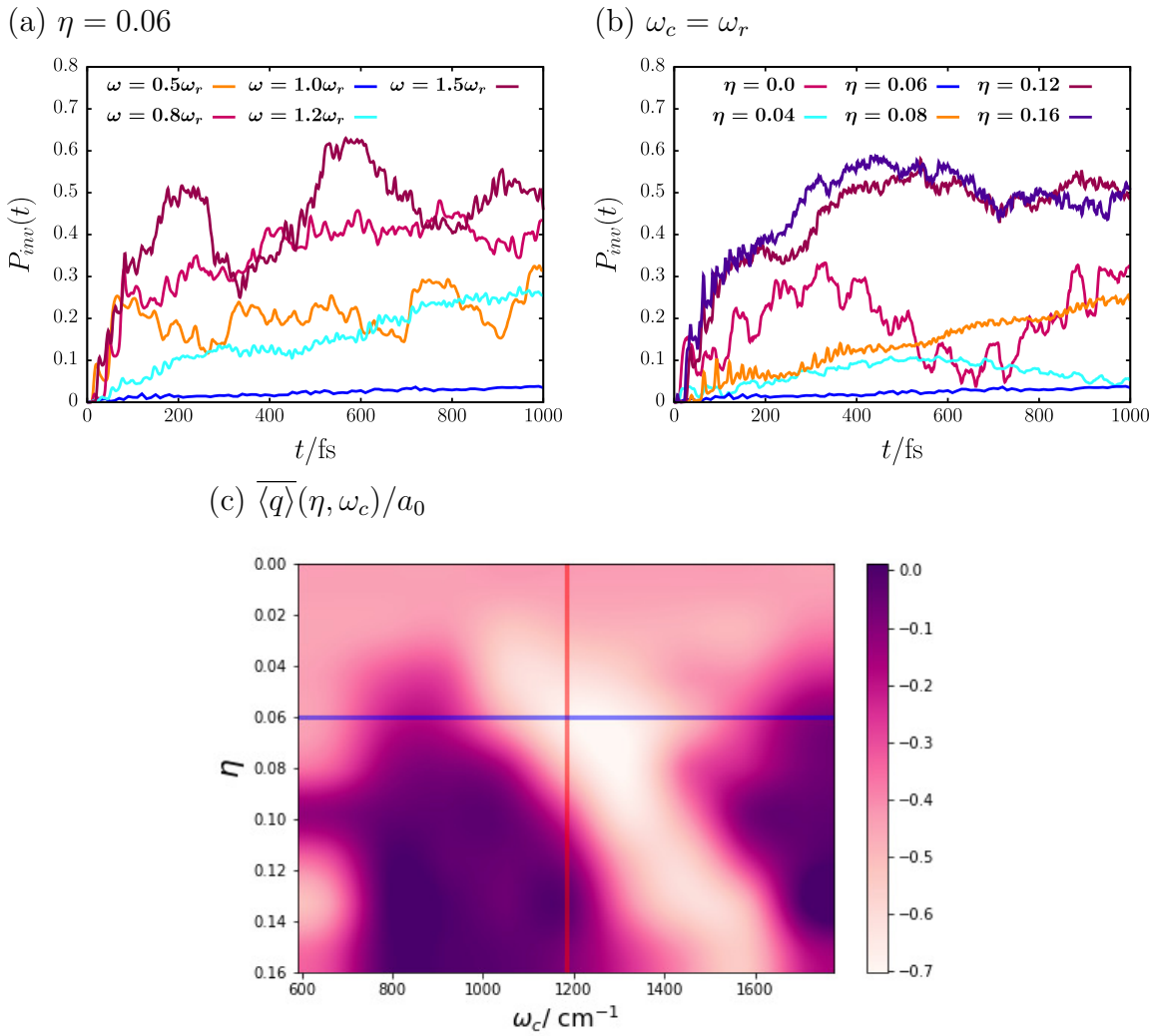

Figure 3.26: (a) Inversion probability, $P_{\text{inv}}(t)$, as function of time for selected values of cavity frequency, ω_c, at $\eta = 0.06$ (blue horizontal line in (c)). (b) Inversion probability, $P_{\text{inv}}(t)$, for selected values of η at $\omega_c = \omega_r = 1182$ cm^{-1} (red vertical line in (c)). (c) Contour plot of interpolated time-averaged position expectation values, $\overline{\langle q \rangle}$ (color bar in atomic units, a_0), as function of η and ω_c obtained from 81 pairs (η, ω_c).

We discuss $P_{\text{inv}}(t)$ for a propagation time of $t_f = 1000\,\text{fs}$ and two scenarios depicted in Fig.3.26: (a) We fix the light-matter interaction regime with $\eta = 0.06$ and vary the cavity frequency as multiples of the harmonized molecular reactant frequency $\omega_r = \omega_R^{(1)} = 1182\,\text{cm}^{-1}$. (b) We fix the cavity frequency $\omega_c = \omega_r$ and vary the light-matter interaction via η. Technical details concerning converged MCTDH calculations are provided in Tab.3.4.

Table 3.4: Number of single particle functions (SPFs) (n_s, n_c), primitive harmonic oscillator DVR basis functions (m_s, m_c) and molecular/cavity grid endpoints q_0/q_f, x_{c0}, x_{cf} for different light-matter interaction regimes (η).

η	n_s	n_c	m_s	m_c	q_0/q_f	x_{c0}/x_{cf}
$0.0 - 0.08$	20	20	251	251	$[-1.6, +1.6]$	∓ 316.39
$0.1 - 0.14$	24	24	301	301	$[-1.6, +1.6]$	∓ 347.61
0.16	26	26	301	301	$[-1.6, +1.6]$	∓ 347.61

Starting with Fig.3.26(a), we observe $P_{\text{inv}}(t)$ to increase with time, if the cavity mode is "off-resonant" to the harmonized molecular reactant mode, *i.e.*, $\omega_r \neq \omega_c$. Further, the inversion probability is characterized by several dynamical revivals and interference events in the reactant well. An increase in $P_{\text{inv}}(t)$, with $P_{\text{inv}}(t_f) > 0.25$, resembles a wave packet passage of the cavity transition state and population of the product well. In contrast, for the resonant case with $\omega_r = \omega_c$, we observe a drastic suppression of $P_{\text{inv}}(t)$, with $P_{\text{inv}}(t_f) \approx 0.035$, *i.e.*, less then 4 % of the wave packet reaches the product-well after 1 ps.
Turning to Fig.3.26(b), we observe a strong dependence of $P_{\text{inv}}(t)$ on the light-matter interaction regime for $\omega_r = \omega_c$. In the VUSC regime with $\eta > 0.1$, $P_{\text{inv}}(t)$ takes larger values for the studied time-interval, while in the VSC regime with $0 < \eta < 0.1$, the inversion yield turns out to be reduced.

The reduction of $P_{\text{inv}}(t)$ suggests a temporary localization of the vibro-polaritonic wave packet in the reactant region for specific parameter combinations (η, ω_c). In order to quantify the localization effect, we consider a time-averaged molecular displacement expectation value[199]

$$\overline{\langle q \rangle}(\eta, \omega_c) = \frac{1}{t_f} \int_0^{t_f} \mathrm{d}t' \int_{-\infty}^{\infty} \mathrm{d}x_c \int_{-\infty}^{\infty} \mathrm{d}q\, q\, |\psi(q, x_c, t')|^2 \quad , \tag{3.69}$$

as function of cavity frequency, ω_c, and light-matter interaction, η. In Fig.3.26(c), we show $\overline{\langle q \rangle}$ as contour plot, where the color-bar indicates the mean displacement with $\overline{\langle q \rangle} \in [-0.7, 0.0]\, a_0$, the vertical axis resembles $\eta \in [0.0, 0.16]$ and the horizontal axis $\omega_c \in [0.5\,\omega_r, 1.5\,\omega_r]\,\text{cm}^{-1}$, respectively. The horizontal blue line and the vertical red line relate to scenarios (a) and (b) as depicted in the corresponding Figs.3.26(a) and (b).
We observe a rather uniform behavior of the mean displacement for small η and all ω_c considered here. For $\eta \geq 0.03$ (VSC), the formation of a global minimum at $\omega_c \approx \omega_r$ is observed, which is blue shifted with increasing η. Further, we find $\overline{\langle q \rangle} \approx -0.7\, a_0$ for $\eta = 0.06$

in resonance, which resembles the suppressed $P_{\text{inv}}(t_f)$ in Fig.3.26. Accordingly, we argue that the vibro-polaritonic wave packet is effectively localized close to the classical reactant well minimum at $q_0 = -0.75\,a_0$ over the time interval studied here. Hence, a population of the product region on the cPES is suppressed, which is equivalent to a suppression of P_{inv}, respectively. Notably, we observe this *dynamical resonant localization* effect to be quite sensitive to changes in both the cavity frequency and the light-matter interaction regime.
Before turning to energetic aspects of the localization mechanism, we like to point out the absence of the herein discussed resonance effect when considering the normal-mode perspective discussed above. This circumstance points at an anharmonic effect, *i.e.*, at least a cubic coupling term, $q^2 x_c$, is required for the coupling between reactant and cavity mode, which is not captured under double-harmonic approximation.

Energy Analysis of Dynamical Localization

We further examine the details of the resonant localization by performing a time-dependent energy analysis of the model system. In particular, we discuss the time-evolution of expectation values $\langle \hat{H}_S \rangle (t)$, $\langle \hat{H}_C \rangle (t)$, $\langle \Delta \hat{H}_{SC} \rangle (t)$ and $\langle \hat{H}_{DSE} \rangle (t)$. We briefly recall, $\Delta \hat{H}_{SC}$, is the bare light-matter interaction. Further, we set $\eta = 0.06$ and consider cavity frequencies $\omega_c = 0.8\,\omega_r$, $\omega_c = \omega_r$ and $\omega_c = 1.5\,\omega_r$ with results shown in Figs.3.27(a)-(c), respectively. We note, the total energy at $t = 0$ is given by $\langle \hat{H} \rangle = \langle \hat{H}_S \rangle + \frac{\hbar \omega_c}{2} + \langle \hat{H}_{DSE} \rangle$ and conserved as we neglect dissipative effects.
For $t > 0$, dominant contributions to $\langle \hat{H} \rangle (t)$ stem from bare cavity mode, $\langle \hat{H}_C \rangle (t)$, and bare light-matter interaction, $\langle \Delta \hat{H}_{SC} \rangle (t)$, respectively. The dipole self-energy $\langle \hat{H}_{\text{DSE}} \rangle (t)$ contributes only weakly. $\langle \hat{H}_C \rangle (t)$ and $\langle \Delta \hat{H}_{SC} \rangle (t)$ show large amplitude oscillations roughly with opposite phase. For $\omega_c = \omega_r$, the dynamics exhibits a coherent character modulated by small quantum beats, which turns into incoherent small-amplitude time-evolution for $\omega_c \neq \omega_r$. Notably, the system contributions oscillates at significantly smaller amplitude but in phase with the bare interaction contribution. The dominant contribution of $\langle \Delta \hat{H}_{SC} \rangle (t)$ in resonance can be rationalized in terms of post-rotating-wave contributions to the bare light-matter interaction, which simultaneously excite both molecular system and cavity mode. Hence, both the bare cavity mode and the system are coherently excited, however, the system only "locally" in the reactant region, which motivates the comparatively lower amplitudes here.
We finally turn to the time-evolution of molecular and cavity displacement coordinate expectation values, $\langle q \rangle (t)$ and $\langle x_c \rangle (t)$. In Figs.3.27(d) and (e), we show the corresponding graphs for η and cavity frequencies as before. As the cPES is twisted for $\eta > 0$, the vibro-polaritonic wave packet needs a significant contribution along both the molecular and the cavity displacement coordinate to effectively traverse the cavity transition state region and populate the product well. This is the case for $\omega_c \neq \omega_r$, where we find the molecular displacement as well as the cavity displacement to approach values close to the transition state in a rather irregular oscillatory fashion. In contrast, the resonance scenario is dominated by coherent oscillations of both expectation values around a mean value of roughly $-0.7\,a_0$ for the molecular coordinate and $-25\,\sqrt{m_e}\,a_0$ for the cavity displacement coordinate. This resembles a coherent excitation of the vibro-polaritonic wave packet perpendicular to the

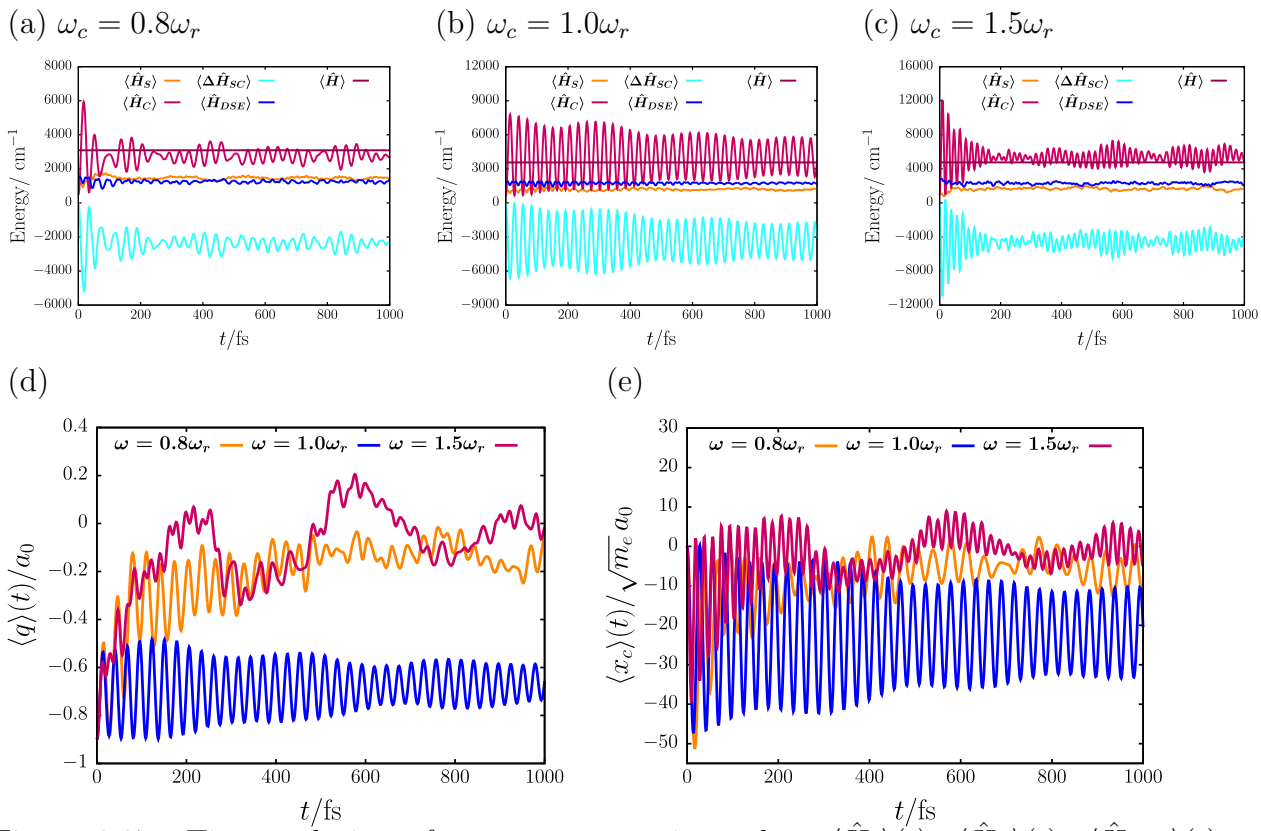

Figure 3.27: Time-evolution of energy expectation values $\langle\hat{H}_{\mathrm{S}}\rangle(t)$, $\langle\hat{H}_{\mathrm{C}}\rangle(t)$, $\langle\hat{H}_{\mathrm{DSE}}\rangle(t)$, $\langle\Delta\hat{H}_{\mathrm{SC}}\rangle(t)$ and $\langle\hat{H}\rangle(t)$ in the VSC regime with $\eta = 0.06$ for cavity frequencies (a) $\omega_c = 0.8\omega_r$, (b) $\omega_c = \omega_r$ and (c) $\omega_c = 1.5\omega_r$. Expectation values of molecular displacement coordinate $\langle q\rangle(t)$ (d) and cavity coordinate $\langle x_c\rangle(t)$ (e) as function of time t for the three cavity frequencies and the VSC regime as considered in (a),(b) and (c).

cavity reaction path, *i.e.*, the wave packet is hindered in efficiently reaching the transition state region as a necessary molecular component is missing in favor of the cavity component. Consequently, the inversion probability is significantly reduced for the studied time-interval as a result of coherent energy transfer between molecular and cavity degrees of freedom.

3.4.4 Summary and Outlook

We studied a cavity-altered thermal isomerization model for the ammonia inversion mode and a single cavity mode from a fully quantum mechanical perspective. Our main findings relate to a cavity-induced reactive slow-down of the isomerization process, which has two quantum mechanical origins: First, the number of thermally accessible states at the cavity transition state decreases for increasing light-matter interaction ("valley-narrowing-effect") and second, tunneling between reactant and product sites is strongly attenuated due to a cavity-induced increase of the reaction barrier's width ("barrier-broadening-effect). Both findings manifest in significantly reduced thermal inversion rates, where the former aspect plays a major role at ambient temperature and the latter takes over in the (deep) tunneling

regime at low temperature. Moreover, we identified an emergent presumably anharmonic dynamical resonance effect, which manifests as localization of a reactant wave packet when the cavity mode is tuned resonant to a harmonized reactant mode frequency. From an energetic analysis, we characterize the resonance to induce a strongly coherent excitation of the vibro-polaritonic wave packet perpendicular to the cavity reaction path, which efficiently suppresses the inversion probability.

Overall, we identify the cavity as having a "negative" decelerating impact on thermal reaction rates in our minimal model, which is at least qualitatively comparable to experimental findings of Ebbesen and coworkers[121, 122]. Notably, the cavity acts as an energy acceptor in the dynamical study and significantly changes the nature of the "ground-state reactivity landscape"[122] when taking the cPES perspective.

In future studies, one might in particular overcome the minimal character of our model taking into account more degrees of freedom, potentially in the framework of a cavity reaction path Hamiltonian formalism. This could allow for approaching still open questions from the experimental side on cavity-related resonance effects[122] and, especially, the possibly "positive" cavity-controlled acceleration of thermal ground state reactions in a quantum mechanical framework as experimentally reported in Ref.[202] for a reactant-solvent system under VSC.

Chapter 4

Phonon-Driven Vibrational Adsorbate Relaxation

4.1 Motivation

We now turn to phonon-driven vibrational relaxation dynamics for a high-dimensional adsorbate-surface model, which we study from a system-bath perspective.[203, 204, 205, 206, 207] Vibrational dynamics of adsorbates near surfaces takes an important role in both (applied) surface science and as a paradigmatic model for an open quantum system. The dissipation of excess vibrational energy and decoherence inherently influences for example spectral line broadening in spectroscopy[208], inelastic scattering processes[209, 210], chemical surface reactivity[211, 212] and protective effects in microelectronic devices[213, 214]. Vibrational relaxation processes at semiconductor surfaces as considered here are dominated by adsorbate vibration-phonon coupling, in contrast to electron-hole excitation relevant for dissipative processes at metal surfaces.[215, 216, 217]

Opposed to previously discussed (ultra)strong vibrational coupling scenarios in light-matter hybrid systems (*cf.* Ch.3), adsorbate-surface type system-bath models usually comprise weak system-bath couplings and a high-dimensional phonon bath. The issue now turns from describing very strongly interacting subsystems to an efficient treatment of the high-dimensional bath Hilbert space suffering from the "*curse of dimensionality*". Specifically, we study here an adsorbate-surface type system-bath model constructed in the Saalfrank group, which describes a low frequency D-Si-Si bending mode on a fully deuterium-covered, reconstructed silicon surface D:Si(100)-(2×1).[205] The bending mode effectively couples to the phonon band of the silicon surface via one-phonon processes. Recent studies of this quantum mechanics/molecular mechanics (QM/MM) system-bath model were restricted to relaxation processes involving the first and second excited vibrational system states with quantum numbers, $v_0 = 1, 2$, due to the high-dimensional harmonic surface-phonon bath comprising more than 2000 modes.[206, 207]

Here, we significantly improve on those results by combining an effective mode approach with the multilayer-MCTDH method allowing for the study of relaxation processes involving higher-lying excited initial states (here up to $v_0 = 5$), which have been inaccessible in

previous studies. Further, we introduce a numerically efficient approach to the construction of "hierarchical" effective modes. Moreover, as the adsorbate-surface system-bath model constitutes a realistic open quantum system, it allows for the study of non-Markovian effects from a fully quantum mechanical perspective. The latter is contrasted by Markovian reduced density matrix dynamics described in terms of the open-system Liouville-von Neumann equation in Lindblad form.

Results discussed in this chapter are reproduced from "E.W. Fischer, M. Werther, F. Bouakline, P. Saalfrank. A hierarchical effective mode approach to phonon-driven multilevel vibrational relaxation dynamics at surfaces. *J. Chem. Phys.* **153**, 064704, (2020)."[218] and "E.W. Fischer, M. Werther, F. Bouakline, F. Grossmann, P. Saalfrank. Non-Markovian Vibrational Relaxation Dynamics at Surfaces. *J. Chem. Phys.* **156**, 214702, (2022)."[219] with permission of AIP Publishing.

4.2 Adsorbate-Surface System-Bath Dynamics

4.2.1 The D:Si(100) Adsorbate-Surface Model

We introduce the main characteristics of the D:Si(100) adsorbate-surface model, which has been constructed in the spirit of a QM/MM embedded cluster model in Ref.[205].

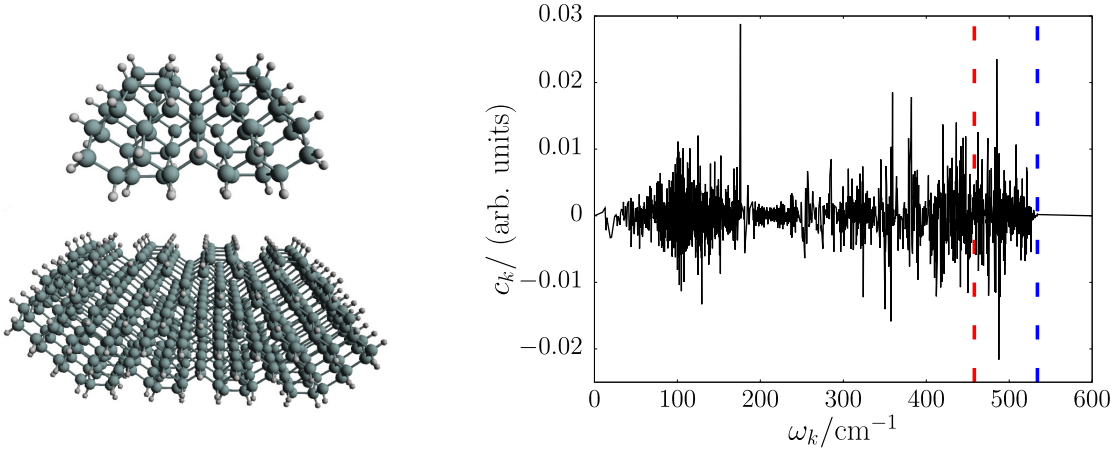

Figure 4.1: Left: Adsorbate-surface clusters modeling D-covered Si(100) surface in spirit of embedded quantum mechanics/molecular mechanics model with small system cluster (DFT/B3LYP, top) and large bath cluster (Brenner-type force-field, bottom). Right: Linear coupling coefficients, c_k, for $N_B = 2259$ modes as function of harmonic bath frequency, ω_k, with fundamental system frequency, $\omega_{10} = 458\,\mathrm{cm}^{-1}$ (red), and bath Debye frequency, $\omega_D = 534\,\mathrm{cm}^{-1}$ (blue).

A single adsorbate D-Si-Si mode has been extracted from a normal mode analysis of a small $Si_{70}D_{54}$ cluster (*cf.* Fig.4.1, left), treated quantum mechanically by means of DFT

via the hybrid functional B3LYP. Subsequently, an anharmonic vibrational potential has been computed along the corresponding system normal mode coordinate q, and the corresponding one-dimensional vibrational TISE has been solved for vibrational energies, $\{\varepsilon_v\}$, and eigenstates, $\{|v\rangle\}$, respectively. The zero-point energy is $228\,\mathrm{cm}^{-1}$ and the vibrational level spacing for the five lowest vibrational states read $\omega_{10} = 458\,\mathrm{cm}^{-1}$, $\omega_{21} = 459\,\mathrm{cm}^{-1}$, $\omega_{32} = 461\,\mathrm{cm}^{-1}$, $\omega_{43} = 463\,\mathrm{cm}^{-1}$ and $\omega_{54} = 466\,\mathrm{cm}^{-1}$, which indicates an overall mild anharmonicity.
The harmonic surface vibrations ("phonons") have been described by means of molecular mechanics employing a Brenner-type force field for a large $Si_{602}D_{230}$ cluster (*cf.* Fig.4.1, left). A constrained normal mode analysis excluding the system vibrations gives $832\times3-7 = 2489$ normal modes. The latter are subsequently reduced to $N_B = 2259$ by neglecting high frequency modes, which do not participate in the vibrational relaxation process of interest. The phonon bath is characterized by harmonic frequencies, $\omega_k \in [9.8, 534]\,\mathrm{cm}^{-1}$, with the Debye frequency of silicon at $\omega_D = 534\,\mathrm{cm}^{-1}$, respectively. The D-Si-Si fundamental transition energy, $\hbar\omega_{10}$, lies in the phonon band (*cf.* Fig.4.1, right), which renders one-phonon processes for energy transfer between system and bath efficient. The interaction is bilinear in the system and bath displacement coordinates, and characterized by a set of linear coupling coefficients, $\{c_k\}$, as shown on the right-hand side of Fig.4.1.

4.2.2 An Adsorbate-Surface System-Bath Hamiltonian

The D:Si(100)-adsorbate-surface model is realized by a system-bath Hamiltonian of the form[205, 206, 207]

$$\hat{H} = \hat{H}_S + \hat{H}_I + \hat{H}_B \quad , \tag{4.1}$$

with vibrational adsorbate system contribution, $\hat{H}_S$, and phonon-bath contribution, $\hat{H}_B$, which we group into a zero-order Hamiltonian[206, 207]

$$\hat{H}_0 = \hat{H}_S + \hat{H}_B = \frac{\hat{p}_s^2}{2} + V(q) + \sum_{k=1}^{N_B} \frac{\hbar\omega_k}{2}\left(\hat{p}_k^2 + x_k^2\right) \quad . \tag{4.2}$$

Here, the first two terms on the right-hand side resemble the system Hamiltonian with system momentum operator, $\hat{p}_s$, coordinate, q, and potential, $V(q)$. The third term resembles N_B non-interacting harmonic oscillators in dimensionless coordinates with harmonic frequencies, ω_k, momenta, $\hat{p}_k$, and displacement coordinates, x_k, respectively. Further, the interaction Hamiltonian, $\hat{H}_I$, has been obtained from an expansion of the full system-bath interaction up to first order in bath coordinates, *i.e.*, considering one-phonon processes only, and reads[206, 207]

$$\hat{H}_I = \sum_{k=1}^{N_B} \lambda_k(q)\, x_k \quad , \tag{4.3}$$

with nonlinear coupling function, $\lambda_k(q)$, in the system coordinate, q, for the k^{th}-bath oscillator. In the following, we employ a spectral representation for the system Hamiltonian based on

$$\hat{H}_S\,|v\rangle = \varepsilon_v\,|v\rangle \quad , \quad \langle v|v'\rangle = \delta_{vv'} \quad , \quad \sum_v |v\rangle\,\langle v| = \hat{1} \quad , \tag{4.4}$$

with eigenvalues, ε_v, and corresponding orthonormal system eigenstates, $|v\rangle$. Further, we consider a second quantization representation of harmonic bath modes with

$$\hat{p}_k = \mathrm{i}\sqrt{\frac{\hbar}{2}}\left(\hat{b}_k^\dagger - \hat{b}_k\right) \quad , \quad x_k = \sqrt{\frac{\hbar}{2}}\left(\hat{b}_k^\dagger + \hat{b}_k\right) \quad , \tag{4.5}$$

where, $[\hat{b}_k, \hat{b}_{k'}^\dagger] = \delta_{kk'}$. Then the zero-order system-bath Hamiltonian can be rewritten as

$$\hat{H}_0 = \sum_{v=0}^{N_S-1} \varepsilon_v \, |v\rangle \langle v| + \sum_{k=1}^{N_B} \hbar\omega_k \left(\hat{b}_k^\dagger \hat{b}_k + \frac{1}{2}\right) \quad . \tag{4.6}$$

Further, the interaction Hamiltonian now takes the form

$$\hat{H}_I = \sum_{v,v'}^{N_S-1} \sum_{k=1}^{N_B} \lambda_{vv'}^k \sqrt{\frac{\hbar}{2}} \, |v\rangle \langle v'| \left(\hat{b}_k^\dagger + \hat{b}_k\right) \quad , \tag{4.7}$$

with coupling matrix elements, $\lambda_{vv'}^k = \langle v|\lambda_k(q)|v'\rangle_q$, where integration with respect to the system coordinate is indicated. In the following, we further simplify the problem by linearizing the coupling functions, $\lambda_k(q) \approx c_k \, q$, with linear system-bath coupling coefficients, c_k, such that, $\lambda_{vv'}^k \approx c_k \, \langle v|q|v'\rangle_q \equiv c_k \, q_{vv'}$. By introducing system raising ($\hat{P}_{vv'}^\dagger$) and lowering ($\hat{P}_{vv'}$) operators as

$$\hat{P}_{vv'}^\dagger \equiv |v\rangle \langle v'| \quad , \quad \hat{P}_{vv'} \equiv |v'\rangle \langle v| \quad , \quad v > v' \quad , \tag{4.8}$$

we can rewrite the full system-bath Hamiltonian now as

$$\hat{H} = \sum_{v=0}^{N_S-1} \varepsilon_v \, |v\rangle \langle v| + \sum_{v>v'}^{N_S-1} q_{vv'} \left(\hat{P}_{vv'}^\dagger + \hat{P}_{vv'}\right) \sum_{k=1}^{N_B} c_k \sqrt{\frac{\hbar}{2}} \left(\hat{b}_k^\dagger + \hat{b}_k\right) + \sum_{k=1}^{N_B} \hbar\omega_k \left(\hat{b}_k^\dagger \hat{b}_k + \frac{1}{2}\right) \quad , \tag{4.9}$$

where we introduced the restriction, $v > v'$, in the second term. The interaction Hamiltonian now factorizes into a system and a bath contribution, *i.e.*, is bilinear in nature, which allows to capture one-phonon processes composed of two types of contributions: (i) Energy conserving one-phonon processes mediated by $\hat{P}_{vv'}^\dagger \, \hat{b}_k$ and $\hat{P}_{vv'} \, b_k^\dagger$, which lead to energy exchange between system and bath, and (ii) energy non-conserving processes induced by $\hat{P}_{vv'}^\dagger \, \hat{b}_k^\dagger$ and $\hat{P}_{vv'} \, \hat{b}_k$, which simultaneously excite system and bath modes due to energy stored in the interaction term. The latter terms are regularly neglected in the rotating wave approximation (RWA), such that we denote them as post-RWA contributions. Here, we do not invoke the RWA but discuss the relevance of post-RWA terms on vibrational relaxation in a weak-coupling, system-bath scenario.

The time-evolution of phonon-driven vibrational system relaxation is fully governed by the system-bath wave function, $|\Psi_{\mathrm{SB}}(t)\rangle$, evolving according to the system-bath TDSE

$$\mathrm{i}\hbar\frac{\partial}{\partial t} \, |\Psi_{\mathrm{SB}}(t)\rangle = \left(\hat{H}_S + \hat{H}_I + \hat{H}_B\right) |\Psi_{\mathrm{SB}}(t)\rangle \quad , \tag{4.10}$$

with initial state given by

$$|\Psi_{\rm SB}(t_0)\rangle = |v_0\rangle\,|0_1,\ldots,0_{N_B}\rangle = |v_0\rangle\,|\underline{0}_B\rangle \quad . \tag{4.11}$$

Here, $|\Psi_{\rm SB}(t_0)\rangle$ resembles an uncorrelated initial system-bath state composed of an initially excited system state, $|v_0\rangle$, with quantum number, $v_0 \geq 1$, and the harmonic multi-mode bath ground state, $|\underline{0}_B\rangle = |0_1,\ldots,0_{N_B}\rangle$, respectively. Vibrational system relaxation is study by means of the reduced system density matrix

$$\hat{\rho}_S(t) = {\rm tr}_B\{|\Psi_{\rm SB}(t)\rangle\,\langle\Psi_{\rm SB}(t)|\} \quad , \tag{4.12}$$

which is obtained from the full system-bath density operator, $|\Psi_{\rm SB}(t)\rangle\,\langle\Psi_{\rm SB}(t)| = \hat{\rho}(t)$, by tracing out the bath degrees of freedom, ${\rm tr}_B\{\ldots\}$. In the basis of vibrational system eigenstates, $\{|v\rangle\}$, the system reduced density matrix, $\hat{\rho}_S(t)$, has elements

$$\rho_{vv}(t) = \langle v|\hat{\rho}_S(t)|v\rangle \quad , \quad \rho_{vv'}(t) = \langle v|\hat{\rho}_S(t)|v'\rangle \quad , \quad v \neq v' \quad , \tag{4.13}$$

which are known as vibrational populations, $\rho_{vv}(t)$, and vibrational coherences, $\rho_{vv'}(t)$, respectively.

4.3 The Hierarchical Effective Mode Representation

4.3.1 An Overview

The main issue with the bilinear system-bath Hamiltonian in Eq.(4.9) results from the strong exponential scaling of the bath Hilbert space due to the large number (N_B) of harmonic bath modes. This renders a numerical solution of system-bath TDSE (4.10) prohibitively expensive for initial system states, $|v_0\rangle$, with quantum numbers, $v_0 > 2$.

In order to mitigate this bath "*curse of dimensionality*", we here employ a *hierarchial effective mode* (HEM) representation of the system-bath Hamiltonian, following results obtained by Gindensperger, Cederbaum and co-workers[220, 221, 222] as well as Hughes, Burghardt and co-workers[223, 224, 225, 226, 227, 228, 229, 230]. Before turning to the details, we note that there are similar hierarchical approaches in surface and condensed matter physics.[231, 232, 233, 234, 235, 236]

The HEM representation of a bilinear system-bath Hamiltonian is obtained by a series of unitary transformations schematically depicted as

$$\hat{H}_S + \hat{H}_I + \hat{H}_B \overset{\underline{\underline{U}}^{(0)}}{\longrightarrow} \hat{H}_S + \hat{h}^{(1)}_{\rm eff} + \hat{H}^{(1)}_R \overset{\underline{\underline{U}}^{(1)}}{\longrightarrow} \ldots \overset{\underline{\underline{U}}^{(M-1)}}{\longrightarrow} \hat{H}_S + \sum_{m=1}^{M} \hat{h}^{(m)}_{\rm eff} + \hat{H}^{(M)}_R \quad , \tag{4.14}$$

mediated by M unitary transformation matrices, $\{\underline{\underline{U}}^{(0)}, \underline{\underline{U}}^{(1)}, \ldots, \underline{\underline{U}}^{(M-1)}\}$. The transformations iteratively generate, $M \ll N_B$, effective single-mode Hamiltonians, $\hat{h}^{(m)}_{\rm eff}$, accompanied by a $M^{\rm th}$-order residual-bath contribution, $\hat{H}^{(M)}_R$, respectively.

In Fig.4.2, the iterative transformation, Eq.(4.14), is depicted graphically: In the original bilinear system-bath Hamiltonian, Eq.(4.9), the bath modes are arranged in a star-like

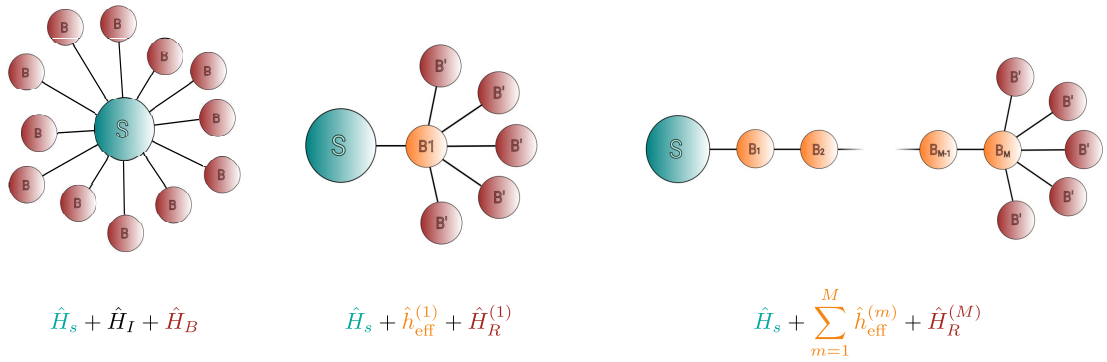

Figure 4.2: Pictorial representation of original bilinear system-bath Hamiltonian in Eq.(4.9) with a star-like configuration (left) and its transformation into chain-like structures within the HEM representation resulting in Hamiltonian Eq.(4.15) (right).

configuration around the central system, which resembles the bilinear coupling between individual (uncoupled) bath modes and the system mode, respectively. In contrast, for a M^{th}-order HEM representation, effective bath modes form a M-mode chain with next-neighbor interactions and a residual bath with $(N_B - M)$ non-interacting modes. The residual bath modes arrange in a star-like configuration "around" the M^{th}-effective mode, *i.e.*, interact bilinearly only with the last mode on the chain (note, they do not couple among each other). As indicated in the scheme (4.14), the corresponding bilinear HEM-Hamiltonian reads

$$\hat{H} = \hat{H}_S + \sum_{m=1}^{M} \hat{h}_{\text{eff}}^{(m)} + \hat{H}_R^{(M)} \quad , \tag{4.15}$$

with unaltered system Hamiltonian, $\hat{H}_S$, effective single-mode Hamiltonians, $\hat{h}_{\text{eff}}^{(m)}$ and residual bath Hamiltonian, $\hat{H}_R^{(M)}$, respectively. The first effective mode term, $\hat{h}_{\text{eff}}^{(1)}$, contains the unitarily transformed system-bath interaction and reads

$$\hat{h}_{\text{eff}}^{(1)} = \sum_{v>v'}^{N_S-1} q_{vv'}\, \bar{C}_0 \left(\hat{P}_{vv'}^{\dagger} + \hat{P}_{vv'}\right) \sqrt{\frac{\hbar}{2}} \left(\hat{B}_1^{\dagger} + \hat{B}_1\right) + \hbar\Omega_1 \left(\hat{B}_1^{\dagger}\hat{B}_1 + \frac{1}{2}\right) \quad , \tag{4.16}$$

with effective coupling coefficient, $\bar{C}_0$, effective bosonic phonon excitation and annihilation operators, $\hat{B}_1^{\dagger}$ and $\hat{B}_1$, and effective harmonic bath mode frequency, Ω_1. The remaining $(M-1)$-effective mode contributions are given by

$$\hat{h}_{\text{eff}}^{(m)} = \bar{C}_{m-1} \left(\hat{B}_{m-1}^{\dagger}\hat{B}_m + \hat{B}_{m-1}\hat{B}_m^{\dagger}\right) + \hbar\Omega_m \left(\hat{B}_m^{\dagger}\hat{B}_m + \frac{1}{2}\right) \quad , \tag{4.17}$$

with coupling coefficients, $\bar{C}_{m-1}$, and harmonic frequencies, Ω_m, for $2 \leq m \leq M$. Finally, the residual bath takes the form

$$\hat{H}_R^{(M)} = \sum_{j=M+1}^{N_B} d_{Mj} \left(\hat{B}_M^{\dagger}\hat{B}_j + \hat{B}_M\hat{B}_j^{\dagger}\right) + \sum_{j=M+1}^{N_B} \hbar\Omega_j \left(\hat{B}_j^{\dagger}\hat{B}_j + \frac{1}{2}\right), \tag{4.18}$$

with coupling coefficients, d_{Mj}, and frequencies, Ω_j, for $(N_B - M)$-residual effective modes. An explicit approach to construct the HEM-Hamiltonian in Eq.(4.15) will be presented in detail below.
Further, the HEM-Hamiltonian in Eq.(4.15) is unitarily equivalent to the system-bath Hamiltonian in Eq.(4.9). However, in contrast to the latter, N_B bath modes are now divided into a subset of M effective modes forming an M-member chain and the residual bath. The advantage of the HEM representation is, that the Hamiltonian Eq.(4.15) can be truncated at M^{th}-order by neglecting the residual part, $\hat{H}_R^{(M)}$. Despite the missing residual bath, a truncated HEM system-bath Hamiltonian reproduces the *exact* dynamics of a bilinear system-bath problem up to a finite time, which increases with the truncation order, M.[222] This property allows to systematically access the exact system-bath dynamics over finite time intervals of increasing length. In particular, vibrational relaxation processes as studied here can be fully captured by truncation orders significantly smaller than the original number of bath modes, $M \ll N_B$, as discussed below, which efficiently mitigates the bath scaling problem.

4.3.2 Derivation of 1st-Order HEM Hamiltonian

As a first step, we explicitly derive the 1st-order HEM-Hamiltonian with the transformed system-bath interaction in $\hat{h}_{\text{eff}}^{(1)}$ as given by Eq.(4.16). We start from the bilinear system-bath interaction in Eq.(4.9), which is rewritten as

$$\hat{H}_I = \sum_{v>v'}^{N_S-1} q_{vv'} \left(\hat{P}_{vv'}^\dagger + \hat{P}_{vv'} \right) \sqrt{\frac{\hbar}{2}} \sum_{k=1}^{N_B} c_k \left(\hat{b}_k^\dagger + \hat{b}_k \right) \quad , \tag{4.19}$$

$$= \sum_{v>v'}^{N_S-1} q_{vv'} \left(\hat{P}_{vv'}^\dagger + \hat{P}_{vv'} \right) \bar{C}_0 \sqrt{\frac{\hbar}{2}} \left(\hat{B}_1^\dagger + \hat{B}_1 \right) \quad , \tag{4.20}$$

with effective system-bath coupling constant

$$\bar{C}_0 = \sqrt{\sum_{k=1}^{N_B} c_k^2} \tag{4.21}$$

and effective mode creation and annihilation operators defined by

$$\hat{B}_1^{(\dagger)} = \sum_{k=1}^{N_B} \frac{c_k}{\bar{C}_0} \hat{b}_k^{(\dagger)} \equiv \sum_{k=1}^{N_B} t_{1k} \hat{b}_k^{(\dagger)} \quad . \tag{4.22}$$

The expansion coefficients, $\{t_{1k}\}$, form a normalized vector, $\underline{t}_1$ with normalization constant, $\bar{C}_0$. More generally, one obtains N_B-effective mode operators

$$\hat{B}_i^{(\dagger)} = \sum_{k=1}^{N_B} t_{ik} \hat{b}_k^{(\dagger)} \quad , \quad \sum_{k=1}^{N_B} t_{ik} t_{kj} = \delta_{ij} \quad , \tag{4.23}$$

where $\{t_{ik}\}$ are elements of an orthogonal transformation matrix, $\underline{\underline{T}}^{(0)}$, with first line given by t_{1k} in Eq.(4.22). From the inverse of Eq.(4.23), one obtains for $\hat{H}_B$

$$\hat{H}_B = \hbar\Omega_1 \left(\hat{B}_1^\dagger \hat{B}_1 + \frac{1}{2} \right) + \sum_{j=2}^{N_B} \hbar d_{1j} \left(\hat{B}_1^\dagger \hat{B}_j + \hat{B}_1 \hat{B}_j^\dagger \right) + \sum_{j=2}^{N_B} \hbar\Omega_j \left(\hat{B}_j^\dagger \hat{B}_j + \frac{1}{2} \right) + \sum_{i>j=2}^{N_B} \hbar d_{ij} \left(\hat{B}_i^\dagger \hat{B}_j + \hat{B}_i \hat{B}_j^\dagger \right) \quad . \quad (4.24)$$

The first term resembles the first effective mode, the second term couples the first effective mode to $(N_B - 1)$-"residual" interacting bath modes, which are given by terms three and four. Effective mode frequencies, Ω_i, and coupling coefficients, d_{ij}, read

$$\Omega_i = \sum_{k=1}^{N_B} \omega_k \, t_{ik}^2 \quad , \quad d_{ij} = \sum_{k=1}^{N_B} t_{ik} \, \omega_k \, t_{kj} \quad . \quad (4.25)$$

The 1$^{\text{st}}$-HEM representation is finally obtained by diagonalizing the residual mode bath. Hence, a second orthogonal transformation is introduced with

$$\hat{B}_1'^{(\dagger)} = \hat{B}_1^{(\dagger)} \quad , \hat{B}_i'^{(\dagger)} = \sum_{m=2}^{N_B} z_{im} \hat{B}_m^{(\dagger)} \quad , i \geq 2 \quad , \quad (4.26)$$

where $\{z_{im}\}$ are the elements of an orthogonal matrix, $\underline{\underline{Z}}^{(0)}$, respectively. Accordingly, $\hat{H}_B$ turns into

$$\hat{H}_B = \hbar\Omega_1 \left(\hat{B}_1^\dagger \hat{B}_1 + \frac{1}{2} \right) + \sum_{j=2}^{N_B} \hbar d'_{1j} \left(\hat{B}_1^\dagger \hat{B}'_j + \hat{B}_1 \hat{B}_j'^\dagger \right) + \sum_{j=2}^{N_B} \hbar\Omega'_j \left(\hat{B}_j'^\dagger \hat{B}'_j + \frac{1}{2} \right) \quad , \quad (4.27)$$

where the second and third terms resemble the first order residual bath with Hamiltonian

$$\hat{H}_R^{(1)} = \sum_{j=2}^{N_B} \hbar d_{1j} \left(\hat{B}_1^\dagger \hat{B}_j + \hat{B}_1 \hat{B}_j^\dagger \right) + \sum_{j=2}^{N_B} \hbar\Omega_j \left(\hat{B}_j^\dagger \hat{B}_j + \frac{1}{2} \right) \quad , \quad (4.28)$$

where we dropped the primes (*cf.* Eq.(4.18) with $M = 1$).

4.3.3 Derivation of M^{th}-Order HEM Hamiltonian

In the following, we introduce a numerically efficient approach to calculate all frequencies and coupling coefficients for a M^{th}-order HEM representation based on a set of orthogonal transformation matrices, $\left\{ \underline{\underline{U}}^{(m)} = \underline{\underline{Z}}^{(m)} \underline{\underline{T}}^{(m)} \right\}$, with $m = 0, 1, \ldots M-1$. In order to proceed, the N_B-mode harmonic bath Hamiltonian is rewritten as

$$\hat{H}_B = \underline{b}^\dagger \, \underline{\underline{H}}_B \, \underline{b} + \sum_{k=1}^{N_B} \frac{\hbar\omega_k}{2} \quad , \quad (4.29)$$

with diagonal Hessian

$$\underline{\underline{H}}_B = \mathrm{diag}(\omega_1, \omega_2, \ldots, \omega_{N_B}) \equiv \underline{\underline{H}}_R^{(0)} \quad , \tag{4.30}$$

which we denote as zeroth-order residual bath Hessian, $\underline{\underline{H}}_R^{(0)}$, in the following. The creation and annihilation operators are grouped in vectors

$$\underline{b} = (b_1, b_2, \ldots, b_{N_B})^{\mathrm{T}} , \quad \underline{b}^\dagger = (b_1^\dagger, b_2^\dagger, \ldots, b_{N_B}^\dagger) \quad , \tag{4.31}$$

where the superscript "T" denotes the vector transpose.

1st-Order Transformation

In the following, the general procedure is outlined by explicitly constructing the first-order HEM representation of the bath Hessian, $\underline{\underline{H}}_B^{(1)}$, which can be written as

$$\underline{\underline{H}}_B^{(1)} = \underline{\underline{U}}^{(0)} \, \underline{\underline{H}}_R^{(0)} \left(\underline{\underline{U}}^{(0)}\right)^T \quad . \tag{4.32}$$

with orthogonal transformation matrix

$$\underline{\underline{U}}^{(0)} = \underline{\underline{Z}}^{(0)} \, \underline{\underline{T}}^{(0)} \quad . \tag{4.33}$$

The first transformation step is mediated by $\underline{\underline{T}}^{(0)}$ (*cf.* Eq.(4.23)) and leads to

$$\underline{\underline{T}}^{(0)} \, \underline{\underline{H}}_R^{(0)} \left(\underline{\underline{T}}^{(0)}\right)^{\mathrm{T}} = \begin{pmatrix} \Omega_1 & \tilde{\underline{d}}^{\mathrm{T}} \\ \tilde{\underline{d}} & \underline{\underline{W}}_R^{(1)} \end{pmatrix} = \underline{\underline{W}}_B^{(0)} \quad , \tag{4.34}$$

with first effective mode harmonic frequency, Ω_1, and bilinear coupling coefficient vector, $\tilde{\underline{d}}$, which contains coupling coefficients between first effective and all remaining residual modes. Further, $\underline{\underline{W}}_R^{(1)}$ resembles the fully coupled first-order residual bath. In this work, the orthogonal transformation matrix, $\underline{\underline{T}}^{(0)}$, is constructed as *Householder* matrix

$$\underline{\underline{T}}^{(0)} = \underline{\underline{1}} - 2\, \underline{w} \otimes \underline{w} \quad , \quad \underline{\underline{T}}^{(0)} \left(\underline{\underline{T}}^{(0)}\right)^{\mathrm{T}} = 1 \quad , \tag{4.35}$$

with Kronecker product, $\otimes$, under the constraint that

$$\underline{t}_1 = (t_{11}, t_{12}, \ldots, t_{1N_B})^{\mathrm{T}} = \left(\frac{c_1}{\bar{C}_0}, \frac{c_2}{\bar{C}_0}, \ldots, \frac{c_{N_B}}{\bar{C}_0}\right)^{\mathrm{T}} \quad , \tag{4.36}$$

constitutes the first row, which is realized by determining vector elements of $\underline{w}$ as

$$w_1 = \sqrt{\frac{1 - t_{11}}{2}} \quad , \, w_j = -\frac{t_{1j}}{\sqrt{2(1 - t_{11})}} \quad , \tag{4.37}$$

with $j \geq 2$. The advantage of a *Householder* ansatz for $\underline{\underline{T}}^{(0)}$ is twofold: (i) The remaining $(N_B - 1)$-rows of $\underline{\underline{T}}^{(0)}$ are unambiguously determined by $\underline{t}_1$ and (ii) $\underline{\underline{T}}^{(0)}$ is orthogonal

by construction, which speeds up the numerical realization of the transformation approximately by a factor of five compared to standard Gram-Schmidt based orthogonalization schemes[222, 225].

In a second transformation step, $\underline{\underline{W}}_B^{(0)}$ in Eq.(4.34) is transformed to $\underline{\underline{H}}_B^{(1)}$ by

$$\underline{\underline{Z}}^{(0)} = \begin{pmatrix} 1 & \underline{0}^{\mathrm{T}} \\ \underline{0} & \underline{\underline{R}}^{(0)} \end{pmatrix} \quad , \quad \underline{\underline{Z}}^{(0)} \left(\underline{\underline{Z}}^{(0)}\right)^{\mathrm{T}} = 1 \quad , \tag{4.38}$$

where $\underline{\underline{R}}^{(0)}$ contains orthonormal eigenvectors of $\underline{\underline{W}}_R^{(1)}$, *i.e.*, diagonalizes the latter, such that

$$\underline{\underline{Z}}^{(0)} \underline{\underline{W}}_B^{(0)} \left(\underline{\underline{Z}}^{(0)}\right)^{\mathrm{T}} = \begin{pmatrix} \Omega_1 & \underline{d}^{\mathrm{T}} \\ \underline{d} & \underline{\underline{H}}_R^{(1)} \end{pmatrix} = \underline{\underline{H}}_B^{(1)} \quad . \tag{4.39}$$

The transformed vector $\underline{d}$ contains $(N_B - 1)$-coefficients coupling the first effective mode with frequency Ω_1 to the non-interacting, first-order residual bath with diagonal Hessian

$$\underline{\underline{H}}_R^{(1)} = \mathrm{diag}(\Omega_2, \Omega_3, \ldots, \Omega_{N_B}) = \underline{\underline{R}}^{(0)} \, \underline{\underline{W}}_R^{(1)} \left(\underline{\underline{R}}^{(0)}\right)^{\mathrm{T}} \quad , \tag{4.40}$$

as given in Eq.(4.28). In summary, we find for Eq.(4.32)

$$\underline{\underline{H}}_B^{(1)} = \underline{\underline{Z}}^{(0)} \, \underline{\underline{T}}^{(0)} \, \underline{\underline{H}}_R^{(0)} \, \left(\underline{\underline{T}}^{(0)}\right)^T \left(\underline{\underline{Z}}^{(0)}\right)^T = \begin{pmatrix} \Omega_1 & \underline{d}^{\mathrm{T}} \\ \underline{d} & \underline{\underline{H}}_R^{(1)} \end{pmatrix} \quad . \tag{4.41}$$

M^{th}-Order Transformation

The diagonal 1^{st}-order residual bath Hessian, $\underline{\underline{H}}_R^{(1)}$, resembles an equivalent starting point as $\underline{\underline{H}}_R^{(0)}$ before, however, now for a new orthogonal transformation mediated acting in the $(N_B - 1)$-dimensional residual mode subspace. In general, the M^{th}-order HEM representation is obtained iteratively via a series of orthogonal transformation of the $(m-1)^{\mathrm{th}}$-order residual bath Hessian

$$\underline{\underline{H}}_B^{(m)} = \underline{\underline{U}}^{(m-1)} \, \underline{\underline{H}}_R^{(m-1)} \, \left(\underline{\underline{U}}^{(m-1)}\right)^T \quad . \tag{4.42}$$

for $m = 1, 2, \ldots, M$ with

$$\underline{\underline{U}}^{(m-1)} = \underline{\underline{Z}}^{(m-1)} \, \underline{\underline{T}}^{(m-1)} \quad . \tag{4.43}$$

In every step, effective mode frequency Ω_m and the corresponding on-chain coupling coefficient C_{m-1} is obtained besides the residual bath parameters. Further, $\underline{\underline{T}}^{(m-1)}$ resembles a *Householder* matrix and $\underline{\underline{Z}}^{(m-1)}$ diagonalizes the $(m-1)^{\mathrm{th}}$-order residual bath, and both matrices are equivalently constructed as discussed above.

4.3.4 Properties of Truncated HEM Representation

The main advantage of the truncated M^{th}-order HEM representation, as noted above, manifests in its ability to exactly reproduce the time-evolution of the herein studied type of system-bath problems over time-intervals which increase with M. For the M^{th}-order truncated HEM system-bath Hamiltonian

$$\hat{H}^{(M)} = \hat{H}_S + \sum_{m=1}^{M} \hat{h}_{\text{eff}}^{(m)} \quad , \tag{4.44}$$

it is sufficient to exactly reproduce all moments, $C^{(k)}$, of the autocorrelation function, $C(t) = \langle \Psi_{\text{SB}}(0)|e^{-\mathrm{i}\,\hat{H}t/\hbar}|\Psi_{\text{SB}}(0)\rangle$, up to, $k \leq 2M+1$[222, 223, 224]

$$C(t) \approx \sum_{k=1}^{2M+1} \frac{(-\mathrm{i}\,t/\hbar)^k}{k!}\, C^{(k)} = \sum_{l=1}^{2M+1} \frac{(-\mathrm{i}\,t/\hbar)^l}{l!}\, \mathcal{C}^{(l)} \quad , \tag{4.45}$$

with, $\mathcal{C}^{(l)} = \langle \Psi_{\text{SB}}(0)| \left(\hat{H}^{(M)}\right)^l |\Psi_{\text{SB}}(0)\rangle$, respectively. As a (vibrational) relaxation process naturally occurs on a finite time scale, this aspect allows to drastically reduce the number of bath modes to be considered throughout the time-evolution.

4.4 Phonon-Driven Vibrational Multilevel Relaxation

4.4.1 Convergence of Truncated HEM Representation

We start our discussion by examining convergence properties of the HEM representation with respect to different truncation orders M and two different initial states, $|\Psi_{\text{SB}}(t_0)\rangle = |v_0\rangle\,|\underline{0}_B\rangle$, with $v_0 = 1, 2$, respectively. As $|\Psi_{\text{SB}}(t_0)\rangle$ is only an eigenstate to the zero-order Hamiltonian, $\hat{H}_0$, a non-trivial dynamics emerges due to energy exchange between initially excited system and bath. The time-evolution is studied by means of the ML-MCTDH method as implemented in the Heidelberg MCTDH package, version 8.6[84].
In Fig.4.3, system populations, $\rho_{vv}(t)$, are shown for initial system vibrational quantum numbers $v_0 = 1$ (left column) and $v_0 = 2$ (right column) for different HEM-truncation orders, $M = 10, 25, 40$ (top to bottom). The reference calculation, which reproduces the "exact" relaxation dynamics up to $t_f = 2000\,\text{fs}$, is obtained with a truncation order of $M = 60$ (*cf.* grey graphs in Fig.4.3). The relaxation process is characterized by an initial state decay up to 500 fs, followed by two damped recurrences at around 1000 and 1750 fs. A detailed discussion of the relaxation dynamics is given below. Here, we concentrate on the convergence properties of the HEM-representation.
For a truncation order of $M = 10$, the initial relaxation process is accurately described up to 500 fs for both initial states. With $M = 25$ effective modes, the onset of the recurrence at $t = 1000\,\text{fs}$ is captured and system populations diverge for both initial states around $t = 1100\,\text{fs}$. In order to fully capture recurrences details, the number of effective modes has to be increased up to $M = 40$, which indicates a nonlinear increase of the time-interval

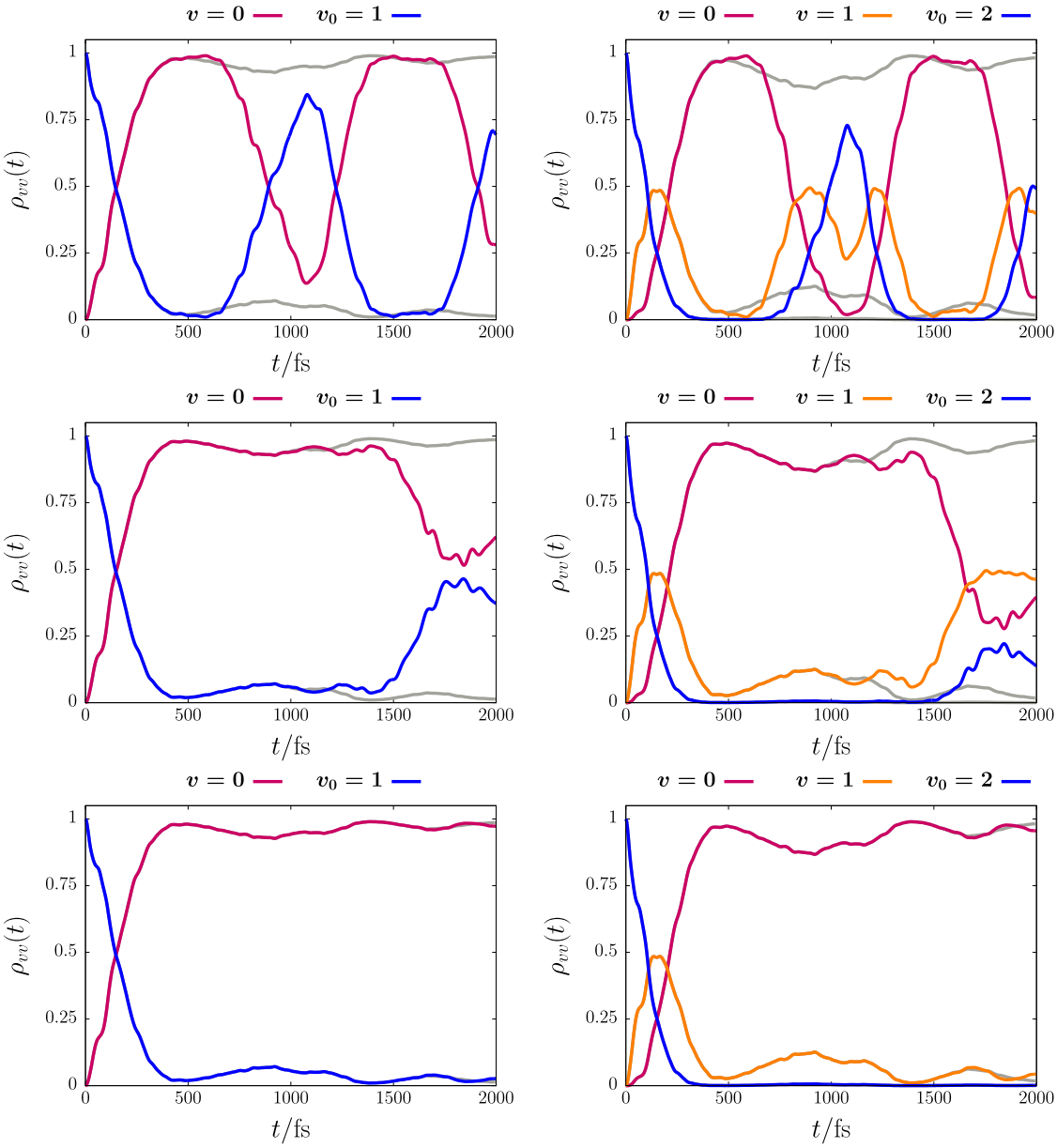

Figure 4.3: Time-evolution of vibrational populations, $\rho_{vv}(t)$, of adsorbate bending mode obtained with different HEM truncation orders, $M = 10$ (upper panels), $M = 25$ (middle panels), and $M = 40$ (lower panels), for two different initial system states, $v_0 = 1$ (left column) and $v_0 = 2$ (right column). The grey solid lines correspond to the "exact reference" with $M = 60$.

with the number of effective modes. The differences between dynamics with $M = 40$ and fully converged results ($M = 60$) are already rather small and slightly increase with the quantum number of the system initial state. Notably, we observe convergence to the exact result, independent of the initial system state, v_0. Increasing complexity and correlation

between system and bath manifests in an increase of required SPFs in the ML-MCTDH wave function to converge the natural populations to $\leq 10^{-4}$, respectively.

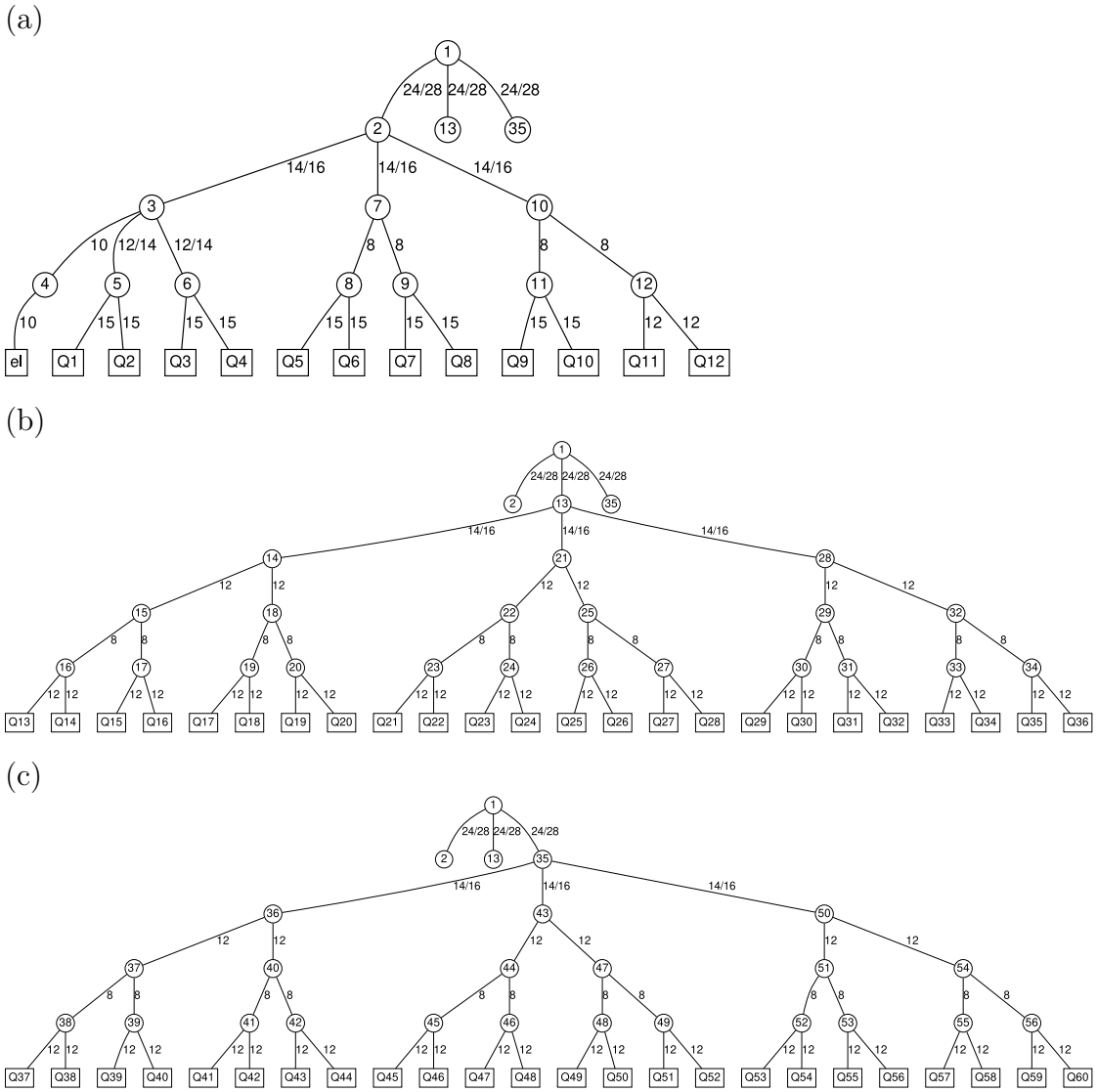

Figure 4.4: (a) First, (b) second and (c) third branch of the Multilayer-tree as employed for vibrational relaxation dynamics with initial system states, $|v_0\rangle$, for vibrational quantum numbers, $v_0 = 1$ to $v_0 = 5$. Numbers next to edges correspond to SPFs employed with smaller numbers for $v_0 = 1, \ldots, 4$ and higher numbers for $v_0 = 5$. Numbers at edges connecting to lowest layer correspond to primitive basis functions with sin-DVR for SQR effective bath modes and system eigenstates formally treated as "electronic states" in a non-adiabatic (ML)-MCTDH run.

In Fig.4.4, we show the ML-tree as considered in this chapter for a truncated HEM-Hamiltonian with $M = 60$ modes. Note, as we consider the system in eigenstate representa-

tion, the system states are treated formally equivalent to electronic states in non-adiabatic (ML)-MCTDH runs.

4.4.2 Truncated HEM-Bath Scaling and Dynamics

We discuss the reduced scaling of the truncated HEM bath compared to the full harmonic bath as well as properties and dynamics of selected effective bath modes. For an initial state, $|\Psi_{\mathrm{SB}}(t_0)\rangle = |v_0\rangle\,|\underline{0}_B\rangle$, the vibrational relaxation process can be depicted by a cascade of next-neighbor transitions between system eigenstates

$$|v_0\rangle \to |v_0-1\rangle \to \cdots \to |2\rangle \to |1\rangle \to |0\rangle \quad , \tag{4.46}$$

which are accompanied by single-phonon excitations of bath modes. Notably, overtone transitions as for example, $|v_0\rangle \to |v_0-2\rangle$, do not provide primary relaxation channels here because (i) our model phonon bath does not support appropriate frequencies for single-phonon processes and (ii) possible two-phonon processes are not dominant.[205]

Truncated HEM-Bath Scaling

Recently, it has been shown that the number of effective bath mode basis states, $n_B^{v_0}$, required to appropriately describe one-phonon induced relaxation processes scales polynomially with the number of bath modes N_B as[207]

$$n_B^{v_0} = \sum_{k=1}^{v_0} \frac{(N_B+k-1)!}{k!\,(N_B-1)!} \quad , v_0 = 1,2,\ldots \quad . \tag{4.47}$$

For a high dimensional bath, Eq.(4.47) behaves in leading order as

$$n_B^{v_0} \sim N_B^{v_0} \quad , N_B \,\text{large} \quad , \tag{4.48}$$

which renders a straightforward study of a vibrational relaxation process with $N_B = 2259$ bath modes and the Hamiltonian in Eq.(4.9) already for initial system states, $v_0 > 2$, prohibitively expensive for the "tier model" approach in Ref.[207]. In Fig.4.5, we show a comparison of vibrational populations obtained with both methods for $v_0 = 1, 2$, respectively, where very good agreement with some small deviations is observed. The latter are traced back to minor differences in linearization schemes employed to obtain the bilinear coupling coefficients, c_k.
Now, for the M^{th}-order truncated HEM representation, N_B in Eq.(4.47) is replaced by M and the leading order scaling in Eq.(4.48) reduces to $n_B^{v_0} \sim M_B^{v_0}$. Here, we find the relaxation dynamics for initial system states, $v_0 = 1, 2, \ldots, 5$, to be converged for a time-interval of $t_f = 2000\,\mathrm{fs}$ with only $M = 60$ effective modes, respectively. In contrast to the full bath with $N_B = 2259$ modes, this implies a significantly milder scaling of the truncated HEM basis size with $M^{v_0} \ll N_B^{v_0}$.

In general, the truncation order M of the HEM representation is assumed to depend on the natural time-scale of the process under study, the initial system state and the explicit nature

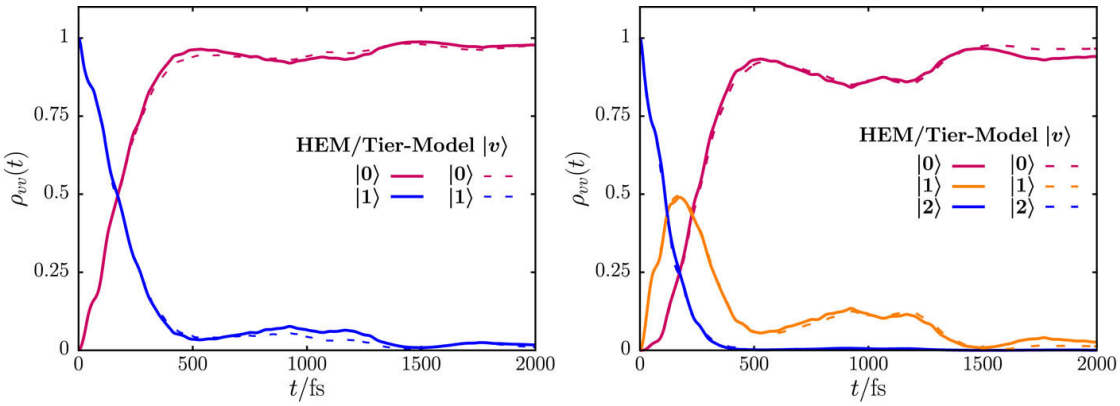

Figure 4.5: Vibrational population dynamics of adsorbate bending mode from truncated HEM-ML-MCTDH approach with $M = 60$ effective modes (bold lines) and Bixon-Jortner/"tier model" with 2259 bath modes (dashed lines) for system initial states, $v_0 = 1$ (left) and $v_0 = 2$ (right). For both methods, the full bilinear system-bath interaction Hamiltonian including post-RWA contributions was employed.

of bilinear system-bath couplings. Therefore, a truncation order of $M = 60$ as reported here is problem specific and does not provide a general result. Further, the independence of M with respect to the initial system state quantum number, v_0, as observed here has also to be assumed a non-general result. We finally note, that although the basis scaling issue can be efficiently mitigated via a truncated HEM representation, an efficient approach to the numerical solution of the system-bath TDSE (4.10) is still required.

Truncated HEM Properties and Dynamics

The properties of the truncated HEM-bath are determined by effective frequencies and couplings, which subsequently determine the excitation dynamics of effective modes. In Fig.(4.6), effective mode coupling parameters, $\bar{C}_i$, and frequencies, Ω_i, are shown for $M = 100$ effective modes. The coupling coefficients, which mediate the energy transfer between adjacent effective modes, are found to be non-uniformly distributed around a mean value of about $125\,\mathrm{cm}^{-1}$. The effective mode frequencies show a mean value of around $270\,\mathrm{cm}^{-1}$ for $M = 100$ modes. Interestingly, the effective system-bath coupling, $\bar{C}_0$, takes a value of $105\,\mathrm{cm}^{-1}$, which is a substantial fraction of the first effective mode frequency with $\Omega_1 = 205.4\,\mathrm{cm}^{-1}$. Hence, the system-bath coupling situation changes from weak for the "star"-type system-bath Hamiltonian to strong for the (truncated) HEM representation.

In order to gain some insights into the effective mode dynamics as initiated by the system vibrational relaxation, we a $M = 10$ truncated HEM representation and discuss selected energy expectation values as function of time. The chosen HEM-Hamiltonian is sufficient to exemplarily illustrate the main dynamical characteristics of effective modes over a time-interval of $t_f = 500\,\mathrm{fs}$ for an initial system state with $v_0 = 1$. In Fig.4.7(a), energy expectation values are shown for the system Hamiltonian, $\langle \hat{H}_S \rangle$, and the bare effective mode

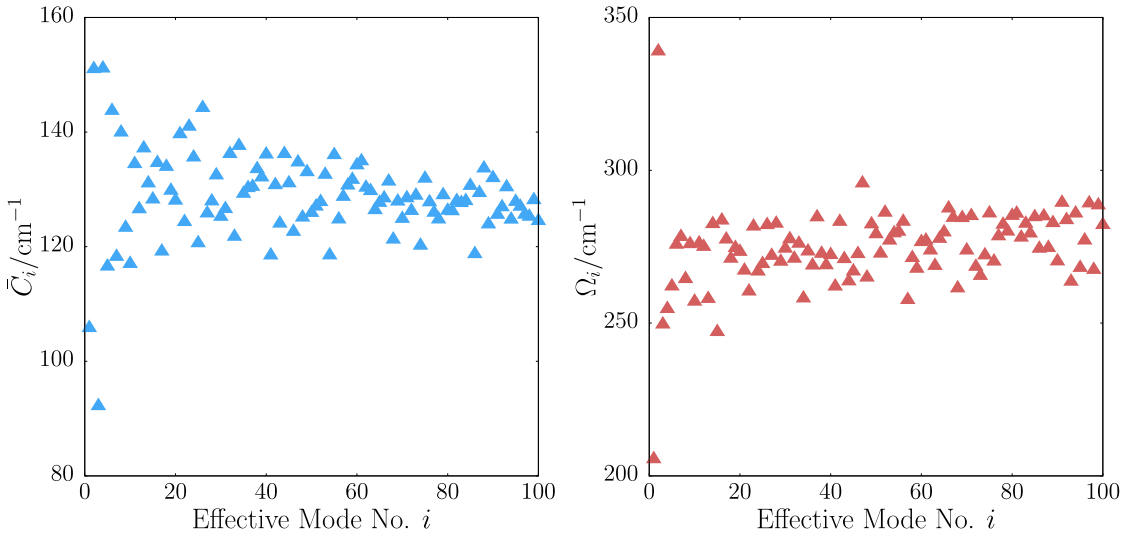

Figure 4.6: Effective coupling coefficients, $\bar{C}_i$, (left) and effective mode frequencies, Ω_i, (right) for $M = 100$ effective modes.

bath Hamiltonian, $\langle \hat{H}_B \rangle$, where the system ground state energy and the bath zero-point energy are chosen as reference. Further, the time-evolution of the interaction energy expectation value, $\langle \hat{H}_I \rangle$, which includes all next-neighbor contributions between adjacent modes along the chain, is shown. All three contributions sum to the total energy, $\langle \hat{H} \rangle$, which is conserved for the unitary dynamics of the system-bath TDSE. As time evolves, the vibrational relaxation process manifests as a decrease in system energy and an increase in both bath and interaction energies. Notably, the latter contributes significantly due to the enhanced coupling in the HEM representation. A particularly characteristic feature of $\langle \hat{H}_I \rangle$ are small oscillations at short times and values, $\langle \hat{H}_I \rangle < 0$, around $t = 20\,\mathrm{fs}$, which result from post-RWA, $\hat{P}^{\dagger}_{vv+1}\hat{B}^{\dagger}_1$ and $\hat{P}_{vv+1}\hat{B}_1$.

Turning to a more detailed perspective, we consider the time-evolution of bare effective mode energies in Fig.4.7(b) and (c). As energy is transferred from the system to the bath, effective modes are consecutively excited due to the chain character of the truncated HEM bath. Notably, the energies of individual modes show a complex time-evolution determined by a series of quantum beats and energy expectation values slightly out-of-phase. These signatures result from the interplay of unequal next-neighbor coupling coefficients and effective mode frequency related detunings. In general, the HEM bath dynamics is determined by non-resonant, next-neighbor energy transfer with rates governed by inter-mode coupling strengths.

The inter-mode interaction energies, as displayed in Fig.4.7(d), exhibit weaker signatures of quantum beats compared to the bare effective mode energies. The "S-B_1" contribution is particularly prominent as it is mostly negative for the studied time-interval, which relates to post-RWA effects showing small but non-negligible contributions up to 500 fs. Further, post-RWA interaction contributions are also responsible for population transfer to system states lying energetically above the initial system state, despite the overall relaxation process. We

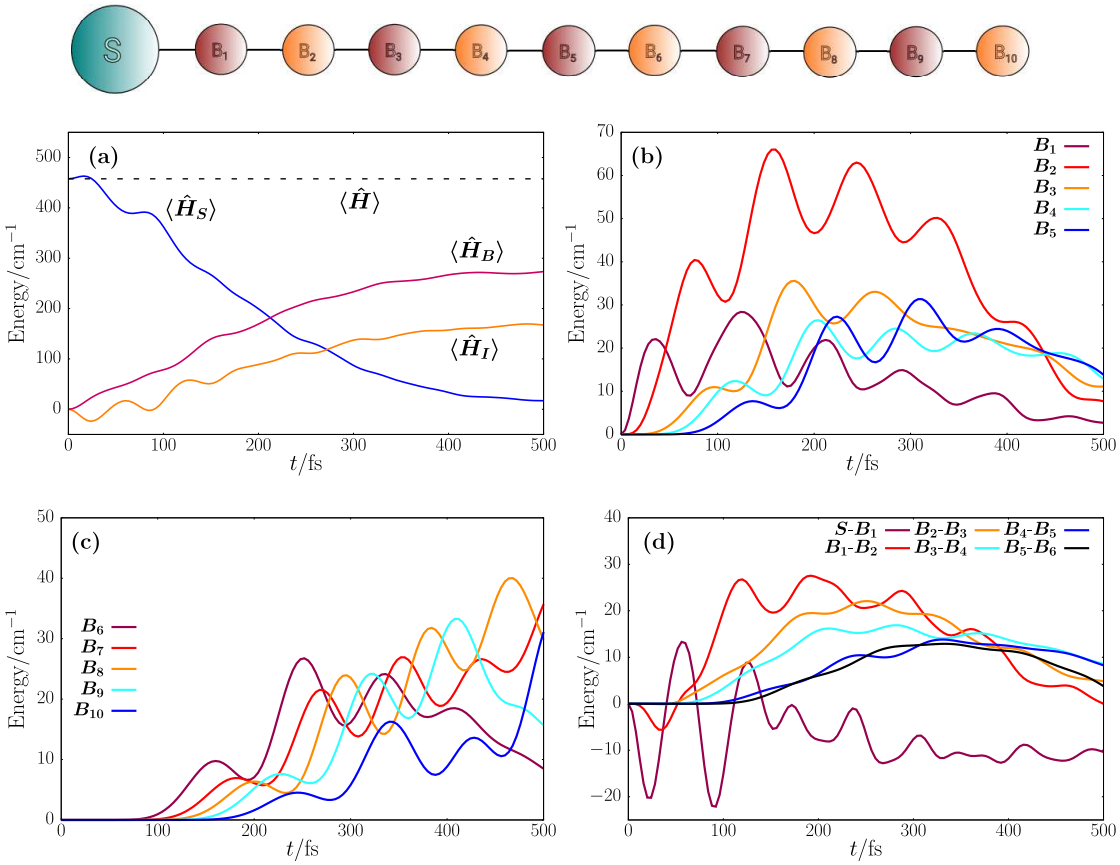

Figure 4.7: Time-dependent energy expectation values of a truncated HEM model with $M = 10$ effective modes and initial system quantum number, $v_0 = 1$. Corresponding HEM-Hamiltonian graphically illustrated on top of the figure. (a) Time evolution of system energy, $\langle \hat{H}_S \rangle$, bath energy, $\langle \hat{H}_B \rangle$, interaction energy, $\langle \hat{H}_I \rangle$, and total energy, $\langle \hat{H} \rangle$. (b) and (c), Time evolution of bare effective mode energy and (d) individual inter-mode coupling contributions.

finally note that for larger initial system vibrational quantum numbers, $v_0 > 1$, a similar dynamics is observed (not shown here), which differs only in the magnitude of expectation values as a result of higher amount of energy initial stored in the system mode.

4.4.3 One-Phonon-Driven Multilevel Relaxation

In the following, we systematically discuss the vibrational relaxation dynamics of an initially excited system D-Si-Si bending mode for initial vibrational quantum numbers, $v_0 = 1, 2, \ldots, 5$. We concentrate here on non-Markovian signatures in the full dynamics, which are to be contrasted by purley Markovian results below. Further, we provide a basis for discussing vibrational half-liftimes and possible scaling laws. The reduced system dynamics is obtained by numerically solving the full system-bath TDSE via the ML-MCTDH ap-

proach for a truncated HEM bath with $M = 60$ effective modes and a propagation time of $t_f = 2000\,\mathrm{fs}$, respectively.

Non-Markovian Vibrational Population Dynamics

In Fig.4.8(a)(-e), the time-evolution of the vibrational populations, $\rho_{vv}(t)$, is shown for different initial system states. The vibrational relaxation process follows the cascade (4.46) and the onset of the first prominent recurrence is observed at around 500 fs, independent of the initial system quantum number, v_0. Two damped recurrences in $\rho_{11}(t)$ and $\rho_{22}(t)$ are observed around 1000 fs and 1750 fs, which increase in magnitude with v_0, *i.e.*, population back-transfer from the bath to the system is more pronounced for energetically higher lying initial system states. The recurrences can be related to damped Rabi-type oscillations between the system and a few dominant bath modes due to a non-trivial bath vibrational density of states. Note that this argument holds only implicitly for the HEM representation, where a single effective mode is responsible for this "collective" effect.
Although vibrational relaxation is the dominant process here, we additionally observe non-zero population of system states lying energetically above the initial state, *i.e.*, processes following the scheme

$$\cdots \leftarrow |v_0 + 2\rangle \leftarrow |v_0 + 1\rangle \leftarrow |v_0\rangle \quad . \tag{4.49}$$

The latter result from post-RWA contributions in the system-bath Hamiltonian and in particular influence the initial decay of the excited system for short times up to 100 fs. Post-RWA effects manifest as damped low-amplitude oscillations in populations of states $|v_0 + 1\rangle$ and $|v_0 + 2\rangle$, which fully decay for longer times. From a numerical perspective, the inclusion of post-RWA effects does not substantially alter the truncated HEM bath basis scaling.

ML-MCTDH vs. multi-Davydov D2 Ansatz

An alternative, variational approach to the solution of the full system-bath TDSE is the coherent state based multi-Davydov-D2 (mD2) *ansatz*, which has been studied extensively in recent years.[237, 238, 239, 240, 241, 242, 243, 244, 245] Here, we compared the performance of combined HEM-mD2 and HEM-ML-MCTDH approaches to the adsorbate-surface model. The mD2-system-bath wave function is defined as[237]

$$|\Psi_{\mathrm{SB}}^{\mathrm{D2}}(t)\rangle = \sum_{j=1}^{K} \left(\sum_{v=0}^{N_S-1} A_{vj}(t)\,|v\rangle \right) |\boldsymbol{\alpha}_j(t)\rangle \quad , \tag{4.50}$$

with time-dependent coefficients, $A_{vj}(t)$, system eigenstates, $|v\rangle$, and M-dimensional effective mode coherent states, $|\boldsymbol{\alpha}_j(t)\rangle$, describing the bath. The parameter K is known as multiplicity and determines the convergence behavior of the mD2-ansatz, *i.e.*, in the "large K"-limit the exact system-bath wave function is recovered.[237] Further, details on mD2-theory, implementation and numerical details on regularization procedures as employed here can be found in Ref.[243].

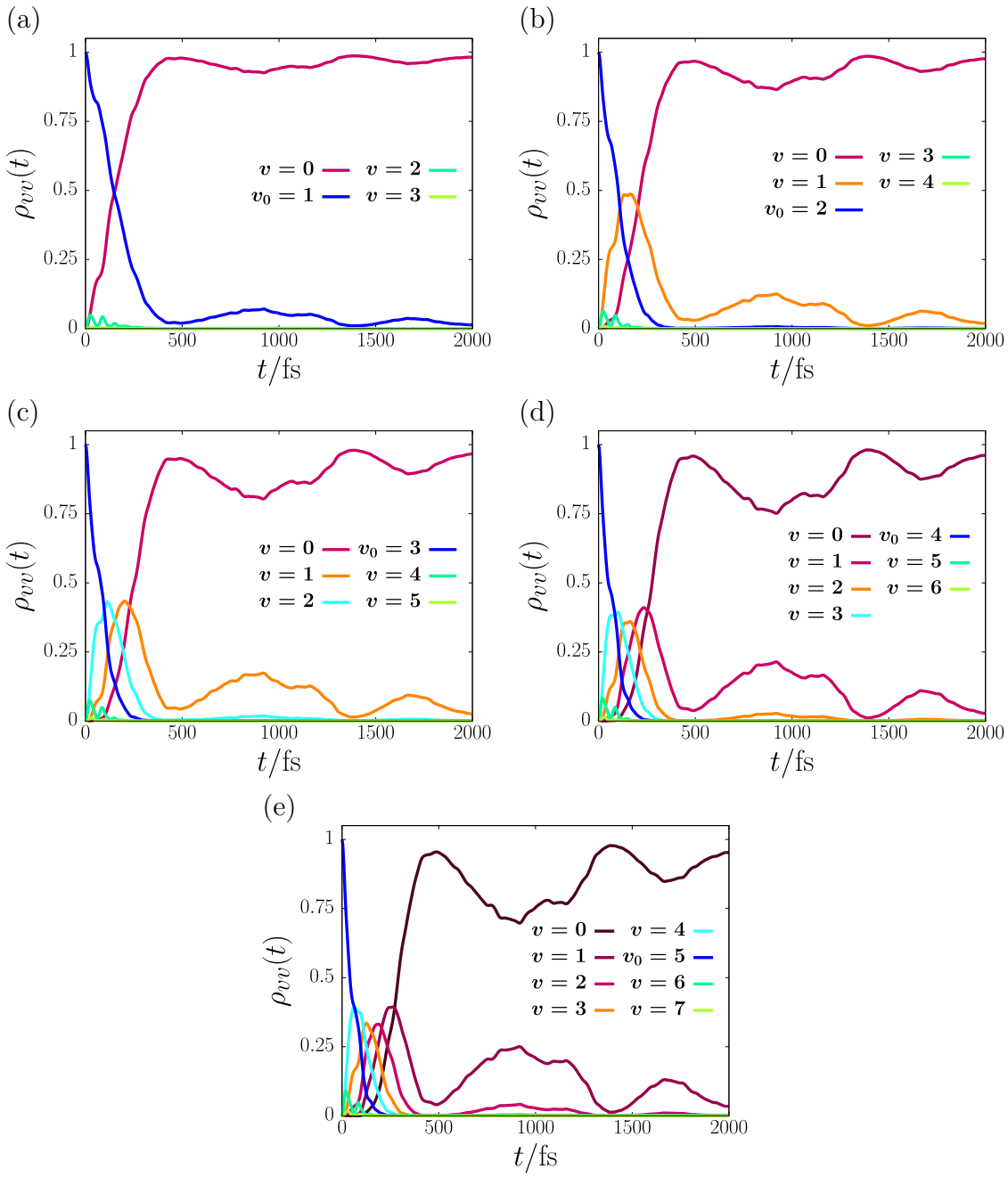

Figure 4.8: Time-evolution of reduced vibrational system populations, $\rho_{vv}(t)$, for initial vibrational system states, $|v_0\rangle$, with quantum numbers, $v_0 = 1, 2, \ldots, 5$, (a)-(e) as obtained from full system-bath TDSE with truncated HEM Hamiltonian for $M = 60$ effective modes.

In Fig.4.9, we show a comparison of results (HEM-mD2 vs. HEM-ML-MCTDH) for initial system quantum numbers, $v_0 = 3, 4, 5$, an effective mode chain with truncation order $M = 60$ and a multiplicity of $K = 30$ for $|\Psi_{\rm SB}^{\rm D_2}(t)\rangle$ in Eq.(4.50), respectively. Both methods give

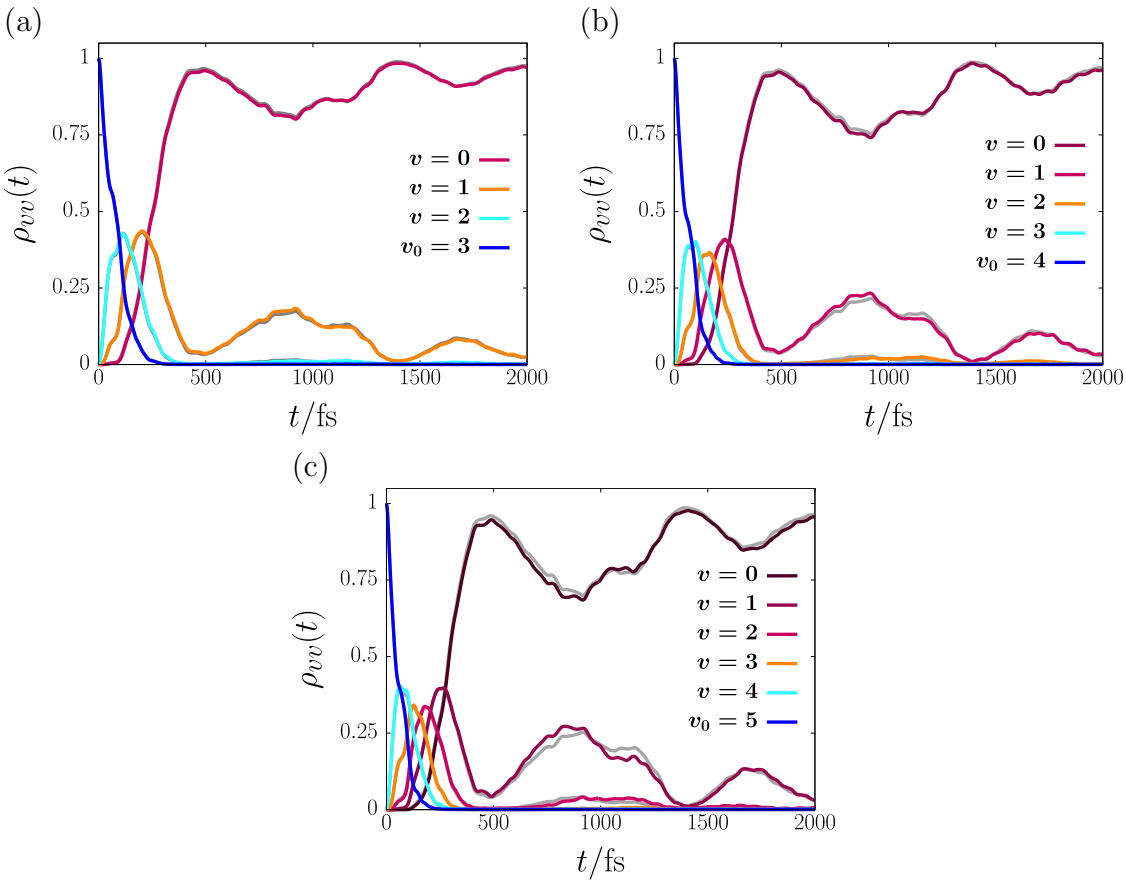

Figure 4.9: Reduced vibrational system population dynamics from multi-Davydov-D2 *ansatz* (colored) and ML-MCTDH approach (grey) for initial vibrational system states, $|v_0\rangle$, with quantum numbers (a) $v_0 = 3$, (b) $v_0 = 4$ and (c) $v_0 = 5$, obtained from full system-bath TDSE with truncated HEM Hamiltonian for $M = 60$ effective modes and mD2 multiplicity $K = 30$.

identical results (to within line thickness) for $t \leqslant 500\,\mathrm{fs}$, with slight deviations occurring later which increase with increasing v_0. As both methods are converged with respect to primitive basis/SPFs (ML-MCTDH) and multiplicity (mD2), we qualitatively attribute the deviations to differences in implementations and numerical details of the underlying equations of motion, but cannot give a precise reason at the present.
More generally, we find the mD2-*ansatz* (i) to follow a ratio, $K/M \ll 1$, *i.e.*, the multiplicity is significantly smaller than the number of effective modes (as in Ref.[241]), (ii) to show only weak dependence of multiplicity K on truncation order M, and (iii) to perform numerically faster than the HEM-ML-MCTDH approach by roughly a factor of three for the bilinear model system studied here. For the first and second aspect, we checked with $M = 100$ effective modes (not shown here) and observed converged results with $K = 30$ identically to the $M = 60$ scenario. Further, concerning computational time savings of the mD2-ansatz, we note that this is to be understood as a rough estimate, which points

at the capabilities of the mD2-ansatz to handle high-dimensional (bilinear) system-bath model problems. However, the herein employed ML-tree was not optimized with respect to computation time, *i.e.*, a rather strict convergence criterion with lowest natural population $\leq 10^{-4}$ for every node was considered, which might definitively be weakened.

In summary, we find the HEM-mD2 ansatz to constitute a promising approach to the study of high-dimensional model system-bath systems, which benefits from a comparatively fast performance and its "simplicity" in terms of a single convergence parameter given by the multiplicity, K. However, although the mD2 ansatz has been shown to have a favorable linear scaling of K up to 300 bath modes[240] (without HEM Hamiltonian), it remains to be seen how its performs for spin-boson models with several thousand harmonic bath modes, which has been successfully described by the ML-MCTDH approach[80] (also without HEM Hamiltonian). Another aspect concerns the study of anharmonic systems, whose description benefits from the high-flexibility of the (ML)-MCTDH ansatz but might be an interesting problem for the coherent state based mD2 ansatz.

Vibrational Coherence Dynamics

Additional insight into vibrational relaxation is obtained by analyzing vibrational coherences, $\rho_{vv+1}(t)$, which we consider for energetically adjacent system eigenstates. In Fig.4.10, we show the time evolution of the corresponding real part, $\mathrm{Re}[\rho_{vv+1}(t)]$, complementing vibrational population dynamics discussed in Fig.4.8. For all initial states, we observe small but non-zero oscillatory coherences emerging roughly after $t = 50\,\mathrm{fs}$, which increase in amplitude with time and are dominated by contributions $\rho_{01}(t)$ and $\rho_{12}(t)$, *i.e.*, involving the three lowest lying system vibrational states. The overall time-evolution is dominated by "beat"-like signatures, which parallel the population recurrence events, *i.e.*, where several system states contribute coherently to the full system-bath wave function. Note, as a recurrence event relates to a re-excitation of the system, the full wave function acquires a coherent contribution of several system states, which in turn manifests in enhanced coherence amplitudes Intestingly, coherences involving higher lying system states additionally play a role for increasing v_0, *i.e.*, $\rho_{23}(t)$ shows significant contributions for all v_0 and $\rho_{34}(t)$ contributes for $v_0 \geq 3$, respectively. For later times with $t > 1000\,\mathrm{fs}$, $\rho_{01}(t)$ and $\rho_{12}(t)$ oscillate in phase at the same frequency but different amplitudes. The oscillation period of about $T \approx 73\,\mathrm{fs}$ nicely reflects the energy difference between system states $|0\rangle$ and $|1\rangle$ or $|1\rangle$ and $|2\rangle$ as the system mode is only mildly anharmonic ($\omega_{10} \approx \omega_{21}$) with $T = 2\pi/\omega_{10} \sim 2\pi/\omega_{21}$, respectively.

Both, vibrational coherences and non-exponential decay of an initially pure system state are signatures of non-Markovian dynamics, which we will discuss in the following in greater detail. We finally note, that we did not discuss the full time-interval necessary for both recurrences and coherences to completely decay but concentrated exclusively on the main features of the relaxation dynamics at early times.

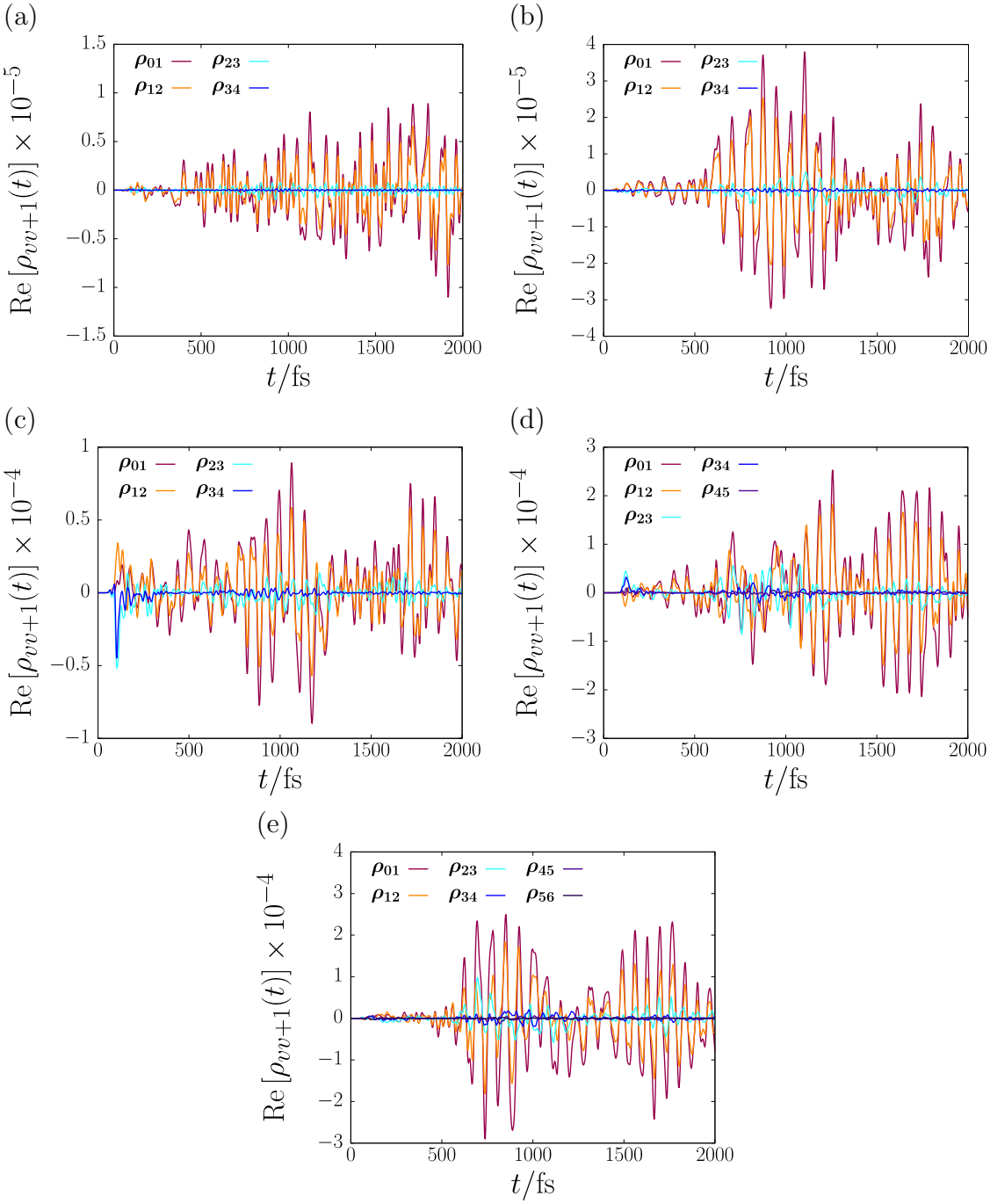

Figure 4.10: Time-evolution for real part of vibrational system coherences, $\mathrm{Re}[\rho_{vv+1}(t)]$, for energetically adjacent system eigenstates for initial vibrational system states, $|v_0\rangle$, with quantum numbers, $v_0 = 1, 2, \ldots, 5$, (a)-(e) obtained from full system-bath TDSE with truncated HEM Hamiltonian for $M = 60$ effective modes.

4.4.4 Markovian *vs.* Non-Markovian Relaxation Dynamics

We now turn to a detailed comparison of Markovian relaxation dynamics as governed by open-system Liouville-von Neumann equation in Lindblad form (*cf.* Sec.2.3.1) and the non-Markovian full system-bath dynamics. Non-Markovian signatures are discussed from four perspectives: (i) vibrational populations extracted from the Markovian reduced system density matrix, (ii) half-lifetimes (iii) purity and von Neumann-entropy, and (iv) the energy exchange of system and bath in terms of a system energy current.

Vibrational Population Dynamics

We first consider vibrational population dynamics with Markovian (bold lines) and non-Markovian (dashed lines) results shown in Fig.4.11. The "non-Markovian" vibrational populations are obtained with the truncated HEM representation in combination with the ML-MCTDH approach as discussed above. We observe two main differences in the Markovian regime: First, Markovian initial state populations, $\rho_{v_0v_0}(t)$, decay exponentially with time and, secondly, both no oscillatory fine-structure and no recurrences are observed in the Markovian limit. The latter two aspects relate to two approximate properties of the Lindblad-approach: (i) The bath is assumed to be infinitely large with a constant vibrational density of states and, (ii) the population transfer is exclusively unidirectional from system to bath.

Half-Lifetimes for Relaxation Process

Although the non-Markovian vibrational population decay is highly non-exponential, as observable from Fig.4.11, it turns out to be illustrative to define corresponding *non-Markovian* half-lifetimes, $\mathrm{T}_{1/2}^{(v_0)}$, after which the population of initial system state, $|v_0\rangle$, has dropped to 1/2. Further, we introduce a *Markovian* half-lifetime, $\mathcal{T}_{1/2}^{(v_0)}$, which is determined either by Fermi's Golden Rule (FGR) or equivalently by solving the LvN-equation in Lindblad form. From Tab.4.1 and Fig.4.12, we find non-Markovian half-lifetimes to range from $\mathrm{T}_{1/2}^{(v_0)} = 145\,\mathrm{fs}$ for $v_0 = 1$ to $\mathrm{T}_{1/2}^{(v_0)} = 41\,\mathrm{fs}$ for $v_0 = 5$. For low lying excited states with $v_0 = 1$ and $v_0 = 2$, we find these lifetimes to be in good agreement with results obtained by employing the "tier model" to solve the system-bath TDSE for D:Si(100)-(2×1) (*cf.* Fig.4.5).[207]
For a harmonic oscillator bilinearly coupled to a harmonic bath, it is well-known that Fermi's Golden Rule provides at $T = 0\,\mathrm{K}$ a strict selection rule, $\Delta v = -1$, as well as a half-lifetime scaling law[246]

$$T_{1/2}^{(v_0)} = \frac{T_{1/2}^{(1)}}{v_0} \quad . \tag{4.51}$$

This ideal scaling law is not well fulfilled for the "exact" HEM-ML-MCTDH solution of the system-bath TDSE, despite fitting trends. For example, we find Markovian $\mathcal{T}_{1/2}^{(5)} = 23\,\mathrm{fs}$ for $v_0 = 5$ following Eq.(4.51), which turns out to be $\mathrm{T}_{1/2}^{(v_0)} = 41\,\mathrm{fs}$ (non-Markovian) according to Tab.4.1 and Fig.4.12. Nevertheless, the ideal scaling law is well reproduced by the FGR half-lifetimes, $\ln(2)\,\gamma_v^{-1}$, where only for larger v_0 a small deviation from ideal scaling is seen

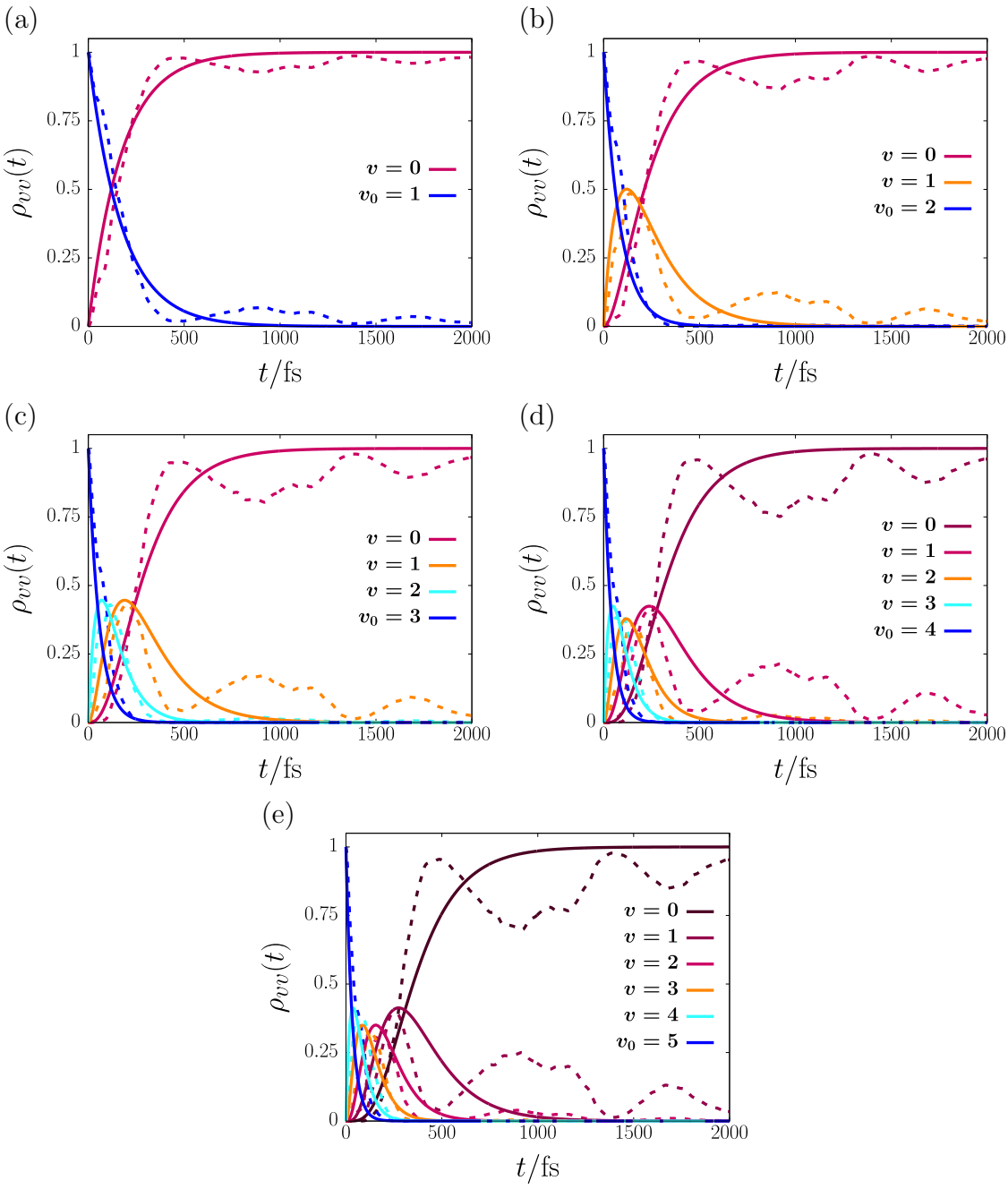

Figure 4.11: Markovian reduced vibrational system populations (bold) compared to non-Markovian populations (dashed) for, $v_0 = 1, 2, \ldots, 5$, (a)-(e) obtained from open-system Liouville-von Neumann equation in Lindblad form and full system-bath TDSE with truncated HEM Hamiltonian for $M = 60$ effective modes.

(note that the half-lifetime for $v_0 = 5$ should be 24 fs, not 23 fs), which resembles the weak anharmonicity of the system mode. Moreover, the "exact" non-Markovian half-lifetimes

Table 4.1: Initial state vibrational quantum numbers, v_0, energies difference initial system state/ground state energy, $(\varepsilon_{v_0} - \varepsilon_0)$, Fermi's Golden Rule (FGR) relaxation rates γ_v, FGR half-lifetimes $\ln(2)\,\gamma_v^{-1}$, half-lifetimes from HEM-ML-MCTDH solution of system-bath TDSE, $\mathrm{T}_{1/2}^{(v_0)}$, and half-lifetimes obtained from solving the Lindblad-LvN equation, $\mathcal{T}_{1/2}^{(v_0)}$.

v_0	$(\varepsilon_{v_0} - \varepsilon_0)/\mathrm{cm}^{-1}$	$\gamma_v/\mathrm{fs}^{-1}$	$\ln(2)\,\gamma_v^{-1}/\mathrm{fs}$	$\mathrm{T}_{1/2}^{(v_0)}/\mathrm{fs}$	$\mathcal{T}_{1/2}^{(v_0)}/\mathrm{fs}$
1	458	0.00578	120	145	120
2	917	0.01160	60	102	60
3	1379	0.01759	39	79	39
4	1842	0.02376	29	51	29
5	2308	0.03013	23	41	23

are additionally consistently larger than the FGR ones, which is in agreement with findings reported in Ref.[207]. Finally, we point at the absence of coherences in the Markovian framework as employed here. For pure initial states, $\rho_S(t_0) = |v_0\rangle\langle v_0|$, the decoherences are initially zero and stay zero throughout the time-evolution of the reduced system as population and coherence dynamics are strictly decoupled in the open-system Liouville-von Neumann-equation in Lindblad form. Hence, the emergence of vibrational coherences in the full dynamics additionally accounts for a non-Markovian signature opposed to a Markovian perspective based on the LvN-equation in Lindblad form.

Purity and von Neumann-Entropy

We now turn to reduced system properties to disucss non-Markovian signatures emerging as deviations from the Markovian dynamics. In particular, we discuss purity, $p_S(t)$, and von Neumann-entropy, $S_{\mathrm{vN}}(t)$, of the reduced system density matrix, $\hat{\rho}_S(t)$, as introduced in Eqs.(2.78) and (2.79) of Sec.2.3.1. In Fig.4.13, the time-evolution of $p_S(t)$ and $S_{\mathrm{vN}}(t)$ is shown for different initial system quantum numbers, v_0, and Markovian (dashed) and non-Markovian (bold) dynamics.
At $t = 0$, the system-bath wave function is in an uncorrelated product state, $|\Psi_{\mathrm{SB}}(0)\rangle = |v_0\rangle\,|\underline{0}_B\rangle$, such that $S_{\mathrm{vN}}(0) = 0$, which results in a pure reduced system state with $p_S(0) = 1$. As time evolves, the system is found to be in a mixed state due to finite system-bath entanglement, *i.e.*, the full system-bath wave function has a multiconfigurational character and cannot be represented by a single product state. Accordingly, we find $p_S(t) < 1$ and $S_{\mathrm{vN}}(t) > 0$ for $t > 0$, respectively. The Markovian dynamics qualitatively reproduce non-Markovian trends and display the mixed state character of the reduced system throughout the relaxation process. For small times, purity/von Neumann-entropy exhibits a minimum/maximum, which is gradually shifted to smaller times for increasing v_0. Further, the magnitude of both quantities increases with v_0. For times $t > 1500\,\mathrm{fs}$, both Markovian purity and von Neumann-entropy tend against their pure state limiting values as the Markovian relaxation process is complete, *i.e.*, the system is fully relaxed to

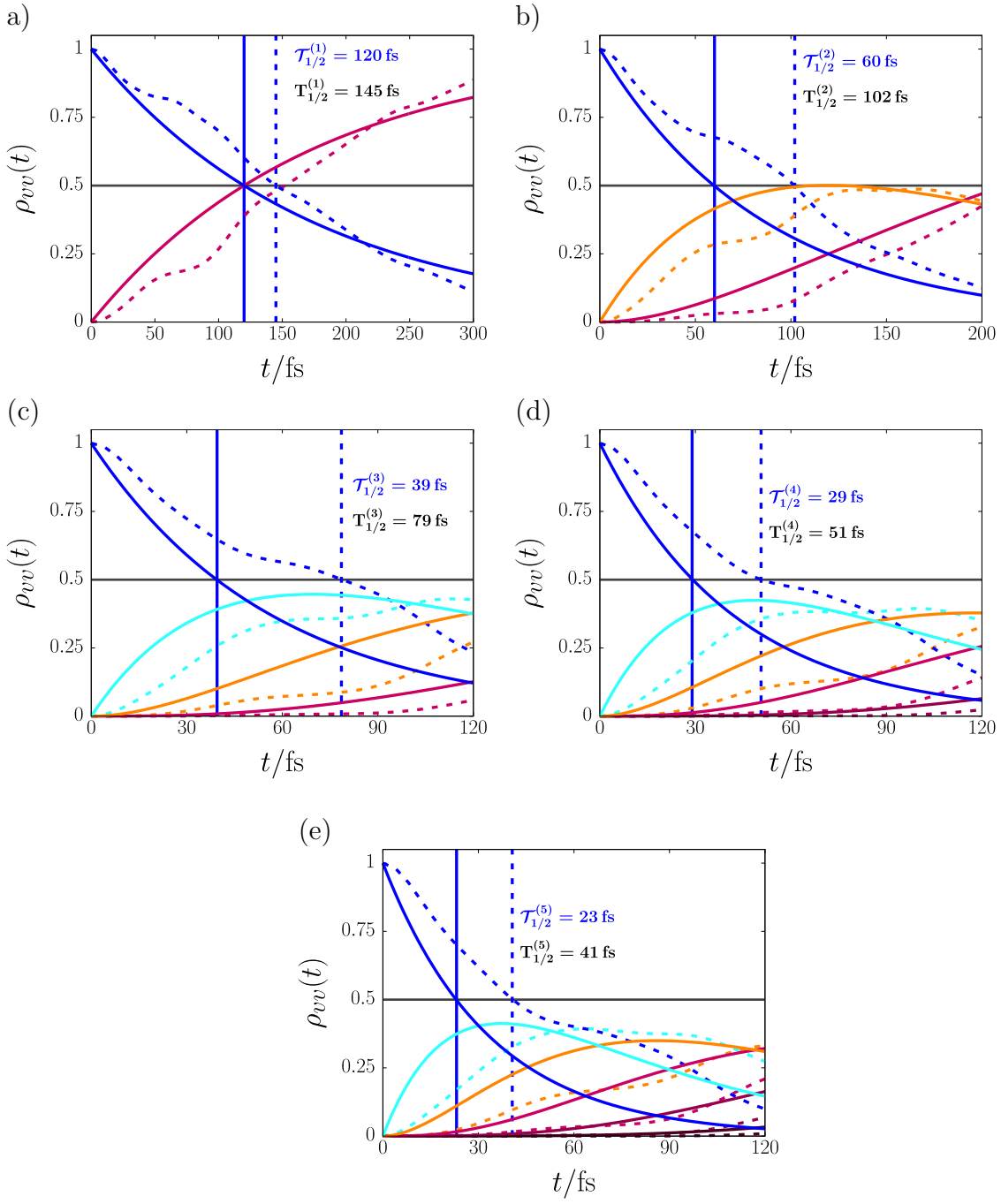

Figure 4.12: Initial relaxation dynamics of Markovian reduced vibrational system populations (bold) compared to non-Markovian populations (dashed) for, $v_0 = 1, 2, \ldots, 5$, (a)-(e) with Markovian, $\mathcal{T}_{1/2}^{(v_0)}$, and non-Markovian (truncated HEM representation) half-lifetimes, $\mathrm{T}_{1/2}^{(v_0)}$, in dependence of v_0.

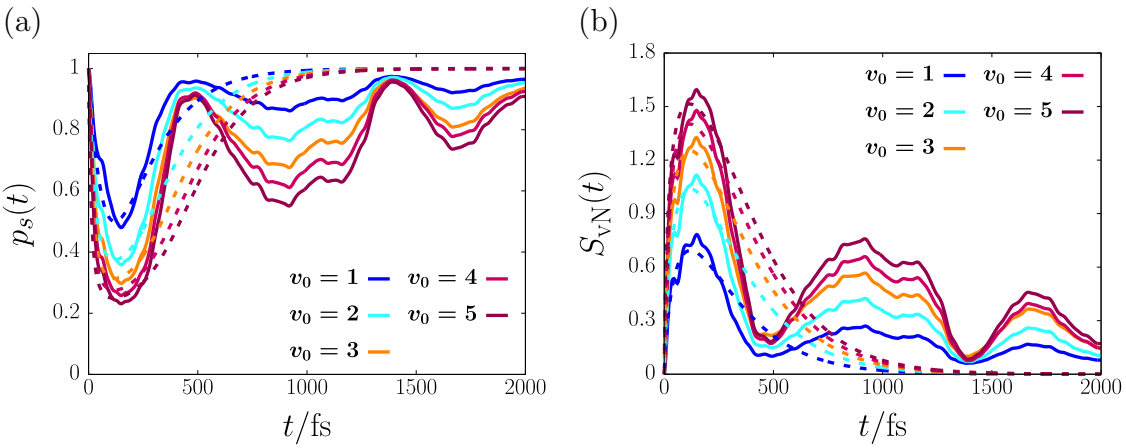

Figure 4.13: Time-evolution of purity, $p_S(t)$, (a) and von Neumann-entropy, $S_{\mathrm{vN}}(t)$, (b) for Markovian (dashed) and non-Markovian (bold) system reduced dynamics for different initial system quantum numbers, $v_0 = 1, 2, \ldots, 5$.

its ground state (*cf.* Fig.4.11). In passing, we note that an analytical expression for the von Neumann-entropy can be derived in the Lindblad framework for $v_0 = 1$, namely, $S_{\mathrm{vN}}(t) = k_B \left[\gamma_1 t \; e^{-\gamma_1 t} - (1 - e^{-\gamma_1 t}) \ln (1 - e^{-\gamma_1 t})\right]$.[246]
The non-Markovian dynamics deviate from the latter observations in two main aspects: Firstly, both purity and von Neumann-entropy capture the relaxation process as well as the recurrence events at later times, which are absent in the Markovian picture. Secondly, the non-Markovian reduced system stays in a mixed state due to finite system-bath entanglement for the time-interval studied here. This observation can be understood by remembering the non-zero vibrational coherences between low-lying system eigenstates as depicted in Fig.4.10. However, in the long-time limit a similar result as the Markovian one is to be expected, as the system ground state will be the dominant system contribution to the full system-bath wave function, while the bath resembles a correlated superposition state of excited bath modes.

System Energy Current

We finally turn to the energy exchange dynamics between system and bath, which we approach from the perspective of non-Markovian and Markovian system energy currents, $\mathcal{J}_S(t)$ and $\mathcal{J}_L(t)$, respectively. For the former, the general expression holds

$$\mathcal{J}_S(t) = \sum_{v=0}^{N_S-1} \varepsilon_v \frac{\partial \rho_{vv}(t)}{\partial t} \quad , \tag{4.52}$$

which turns for the LvN-equation in Lindblad form, Eq.(2.75), into

$$\mathcal{J}_L(t) = - \sum_{v=0}^{N_S-1} \gamma_v \, \Delta\varepsilon_v \, \rho_{vv}(t) \quad , \tag{4.53}$$

with energy difference, $\Delta\varepsilon_v = \varepsilon_v - \varepsilon_{v-1}$, and Fermi's golden rule relaxation rate, γ_v, for $|v\rangle \to |v-1\rangle$, respectively. Details on FGR rates, γ_v, and a derivation of the Markovian current, $\mathcal{J}_L(t)$, are provided in Appendix C.
The system energy current allows to quantify both magnitude and direction of bath-induced energy transfer. We briefly recall our convention, that $\mathcal{J}(t) < 0$ resembles energy transfer from system to bath ($S \to B$) and $\mathcal{J}(t) > 0$ relates to the reverse process ($S \leftarrow B$), respectively. Note that the expression $\mathcal{J}_S(t)$ in Eq.(4.52) is in principle generally applicable for both populations obtained from Markovian and non-Markovian approaches, however, we here restrict ourselves to the second case and accordingly refer to $\mathcal{J}_S(t)$ as "non-Markovian" current. In Fig.4.14, the time-evolution of both $\mathcal{J}_S(t)$ and $\mathcal{J}_L(t)$ (inset) are shown. At $t = 0$,

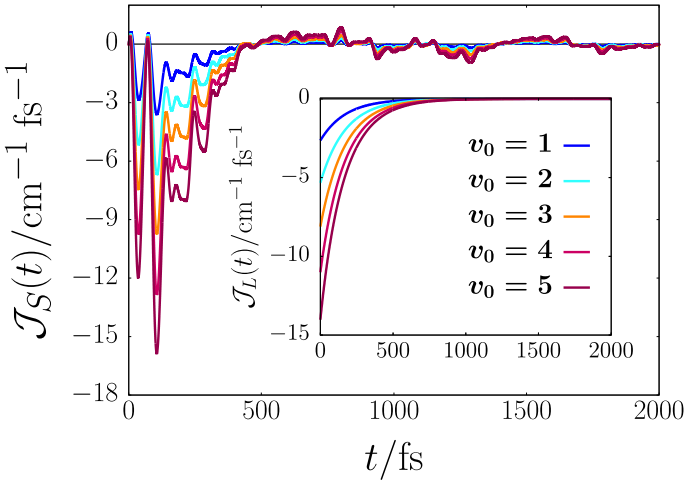

Figure 4.14: Time-evolution of non-Markovian $\mathcal{J}_S(t)$ and Markovian $\mathcal{J}_L(t)$ (inset) reduced system energy current for different initial system quantum numbers, $v_0 = 1, 2, \ldots, 5$.

the energy current is negative in both scenarios, which resembles the onset of the relaxation process with energy flow, $S \to B$. The amplitude of the currents differ significantly, *i.e.*, the Markovian one is larger, which directly reflects the exponential decay and subsequently shorter Markovian half-lifetimes. Further, the Markovian current tends monotonically to zero over a time interval of roughly 1500 fs, which resembles the completion of the Markovian relaxation process. For increasing v_0, the current amplitude naturally increases, which directly relates to the higher amount of energy initially stored in the system. Notably, $\mathcal{J}_L(t) \leq 0$ for all times, *i.e.*, the Markovian energy flow is exclusively unidirectional.
In contrast, the non-Markovian current exhibits an envelope taking a minimum around 100 fs and shows a rich structure dominated by oscillations, *i.e.*, system energy is released in a series of "bursts" to the bath with a maximum transfer rate reached around 100 fs. This behavior relates to the non-trivial character of the bath vibrational density of states. A second major difference to the Markovian limits relates to time-intervals where $\mathcal{J}_S(t) > 0$, *i.e.*, where the energy-flow is reversed, $S \leftarrow B$. This is the case for small times, where post-RWA effects play a role and for recurrence events, where the system is essentially re-exited by the bath. Interestingly, in the long-time limit the non-Markovian current exhibits

small amplitude oscillations around a mean value of zero. Equivalently as purity and von Neumann-entropy, the current amplitude increases with initial state quantum number v_0, respectively.

4.5 Summary and Outlook

We discussed the phonon-driven adsorbate relaxation dynamics for a bilinear system-bath Hamiltonian modeling a anharmonic adsorbate mode (system) coupled to a high dimensional phonon bath and the construction of a hierarchical effective mode (HEM) representation. We presented an efficient algorithm based on Householder matrices to numerically generate all relevant parameters of the HEM representation and combined the latter with the ML-MCTDH approach to numerically study phonon-driven vibrational adsorbate relaxation of a D-Si-Si bending mode due to vibration-phonon coupling at $T = 0\,\mathrm{K}$. The efficiency of the HEM model in combination with ML-MCTDH allowed us to study initial vibrational systems states up to $v_0 = 5$, avoiding thus the "curse of dimensionality" issue, which would otherwise make this problem with > 2000 bath modes intractable for a previously applied "tier model" approach, because the effort scales roughly as $\sim P^{v_0}$. Here, $P = N_B$ if no HEM representation is used, with $N_B > 2000$, and $P = M$ if the HEM representation is employed, with $M = 60$ effective modes. With this method, we found that the excited state lifetimes decay faster with increasing v_0, however, not according to an ideal scaling law, $T_{1/2}^{(v_0)} \propto v_0^{-1}$, despite the system being rather harmonic in our example. The vibrational density of states and the coupling functions, however, are non-trivial in our case. This in turn causes non-trivial behavior of state populations, $\rho_{vv}(t)$, including damped oscillations and recurrences. Further, with the "exact" system-bath dynamics for a non-trivial problem at hand, we were able to compare them to more approximate, reduced approaches in terms of Lindblad open-system density matrix theory. The Markovian approximation was tested in this way for a specific and realistic example. Non-Markovian signatures, *i.e.*, deviations from the Markovian dynamics, manifest in the "exact model" as oscillatory and non-smooth behavior of vibrational populations, purity of the reduced density matrix, the von Neumann-entropy and energy flow between system and bath. For the latter, one in fact finds some back-flow of energy from bath to system, in contrast to what Lindblad theory would predict. Further, the exact solution of the TDSE shows the occurrence of non-vanishing coherences, in contrast to the Lindblad model, for pure initial system states.

In conclusion, we have tested efficient numerical tools to study system-bath dynamics in non-trivial, realistic cases as they emerge, for example, in surface science. Possible next lines of research are to extend this work to finite temperature, to multi-dimensional (adsorbate) systems, more complicated system-bath couplings (including multi-phonon processes), and (adsorbate) systems or baths driven by external radiation.

Chapter 5

Thermofield-MCTDH for Non-Adiabatic Dynamics

5.1 Motivation

In the final chapter of this thesis, we consider the time-evolution of molecular quantum systems at finite temperature. Finite temperature constitutes an ubiquitous situation in chemical physics[53, 55] and naturally suffers from an enhanced scaling problem, which we here consider from the perspective of a density operator description. One class of non-stochastic approaches, which tries to directly tackle the full thermal dynamics, relies on mapping the density operator to a pure state defined on an enlarged Hilbert space, *i.e.*, the concept of purification[247, 248, 249] and the theoretical framework of thermofield dynamics (TFD)[250, 251, 252, 253, 254, 255]. The full "machinery" of wave function theory is then accessible for the solution of the Liouville-von Neumann equation for closed quantum systems, which is here formally equivalent to a Schrödinger-type equation. In the chemical physics community, especially TFD has been applied to both time-independent and time-dependent problems in recent years[256, 257, 258, 259, 260, 261, 262, 264, 265, 266, 263, 267, 268, 269, 270, 271, 272, 273, 274, 275, 276], where time-dependent scenarios were mainly approached by means of time-dependent matrix product states/tensor trains[258, 259, 260, 262, 263, 269, 270, 271, 273] to handle the severe scaling issues. In this thesis, we augment the set of time-dependent wave function/TFD approaches by formulating the MCTDH ansatz in the thermal quasi-particle representation of TFD. We apply our approach exemplarily to non-adiabatic dynamics and spectroscopy of the well studied pyrazine model at finite temperature.

Results discussed in this chapter are reproduced from "E.W. Fischer, P. Saalfrank. A thermofield-based multilayer multiconfigurational time-dependent Hartree approach to non-adiabatic quantum dynamics at finite temperature. *J. Chem. Phys.* **155**, 134109, (2021)."[277] with permission of AIP Publishing.

5.2 A Thermofield-based MCTDH Approach

We review the main concepts of thermofield dynamics and how it applies to the description of non-adiabatic dynamics in the framework of vibronic coupling Hamiltonians[4, 258], before combining it with the MCTDH ansatz.

5.2.1 Thermofield Dynamics

Basic Theory

In the symmetric formulation of TFD, a density operator $\hat{\rho}(t)$ is given by[250, 251]

$$\hat{\rho}(t) = \mathrm{tr}_{\tilde{\mathcal{H}}} \left\{ |\psi_\beta(t)\rangle \langle \psi_\beta(t)| \right\} \quad , \tag{5.1}$$

where $|\psi_\beta(t)\rangle$ is a normalized, time-dependent thermofield state, which explicitly depends on the inverse temperature, β, and is defined on a *thermal Fock space*[251]

$$\mathcal{H}_\beta = \mathcal{H} \otimes \tilde{\mathcal{H}} \quad . \tag{5.2}$$

The latter decomposes into the conventional "physical" Fock space, $\mathcal{H}$, and an exact copy denoted as "tilde" or "auxiliary" Fock space, $\tilde{\mathcal{H}}$, which provides an artificial thermal bath in TFD[254, 255]. The density operator $\hat{\rho}(t)$ in Eq.(5.1) is recovered from the thermofield state by exclusively tracing out the auxiliary DoF. Further, the time evolution of $|\psi_\beta(t)\rangle$ is governed by[251]

$$\frac{\partial}{\partial t} |\psi_\beta(t)\rangle = -\frac{\mathrm{i}}{\hbar} \left(\hat{H} - \tilde{H} \right) |\psi_\beta(t)\rangle \quad , |\psi_\beta(t_0)\rangle = |\psi_\beta\rangle \quad , \tag{5.3}$$

with initial state, $|\psi_\beta\rangle$, and Hermitian thermofield Hamiltonian, $\hat{H} - \tilde{H} = \bar{H}$, where $\tilde{H}$ is an exact copy of the physical Hamiltonian, $\hat{H}$, and acts exclusively on $\tilde{\mathcal{H}}$. The Schrödinger-like EoM (5.3) resembles the Liouville-von Neumann Eq.(2.69) on the thermal Fock space, $\mathcal{H}_\beta$, and is denoted as thermofield time-dependent Schrödinger equation (TF-TDSE), respectively.[254] Thermal ensemble averages in symmetric TFD take the form of conventional quantum mechanical expectation values with respect to time-dependent thermofield states[251]

$$\langle \hat{O} \rangle_\beta (t) = \langle \psi_\beta(t) | \hat{O} | \psi_\beta(t) \rangle \equiv \mathrm{tr}_{\mathcal{H}} \left\{ \hat{\rho}(t) \hat{O} \right\} \quad , \tag{5.4}$$

where $\hat{O}$ acts exclusively on the physical Fock space and the second equality holds due to the definition in Eq.(5.1). For systems in thermal equilibrium, the canonical ensemble average in TFD takes the form

$$\langle \hat{O} \rangle_\beta = \langle \underline{0}_\beta | \hat{O} | \underline{0}_\beta \rangle \quad , \tag{5.5}$$

with normalized thermal vacuum state[251]

$$|\underline{0}_\beta\rangle = \frac{e^{-\beta \hat{H}/2}}{\sqrt{Z_\beta}} \sum_{\underline{n}} |\underline{n}, \tilde{\underline{n}}\rangle \quad . \tag{5.6}$$

Here, $\underline{n} = (n_1, \ldots, n_f)$ is a multi-index for both the physical and auxiliary system with f-DoF and, $\{|\underline{n}, \underline{\tilde{n}}\rangle\}$, are basis states spanning the thermal Fock space, $\mathcal{H}_\beta$, respectively.

The symmetric formulation of TFD provides an alternative representation of quantum statistical dynamics in the language of wave function theory. Accordingly, powerful methods for the numerical solution of the conventional TDSE can directly be transferred to the TFD framework and applied to the propagation of a thermofield state evolving in time according to the TF-TDSE (5.3). This is particularly relevant as the "*curse of dimensionality*" is here severely enhanced due to the structure of $\mathcal{H}_\beta$ in Eq.(5.2), where the original physical problem is effectively doubled. In this thesis, we aim at tackling the enhanced scaling problem by extending the (multilayer) MCTDH approach to the TFD framework.

Non-Adiabatic Quantum Dynamics in TFD

We apply the formalism of TFD to non-adiabatic quantum dynamics at finite temperature, where we assume a temperature range, which is only sufficient to thermally excite vibrational degrees of freedom but not electronic DoF. Hence, we restrict the quantum statistical description to vibrational modes as the characteristic energy range of electronic excitations is assumed to be far larger than the thermal energy.[258, 259, 260]
For a vibronic problem involving M_e diabatic electronic states $\{|S_i\rangle\}$, the corresponding thermofield Hamiltonian reads[258]

$$\bar{H} = \sum_{i=1}^{M_e} \left(E_i + \hat{V}_{c,i} + \hat{H}_0 - \tilde{H}_0 \right) |S_i\rangle \langle S_i| + \sum_{i \neq j}^{M_e} \hat{V}_{ij} |S_i\rangle \langle S_j| \quad , \tag{5.7}$$

with electronic energies, E_i, diagonal inter-mode couplings, $\hat{V}_{c,i}$, and diabatic inter-state couplings, $\hat{V}_{ij}$, respectively. Here, only the normal-mode Hamiltonian, $\hat{H}_0$, is considered from the perspective of TFD[258] and augmented by its auxiliary counterpart, $\tilde{H}_0$, which leads to

$$\bar{H}_0 = \hat{H}_0 - \tilde{H}_0 = \sum_{k=1}^{f} \hbar\omega_k \left(\hat{a}_k^\dagger \hat{a}_k - \tilde{a}_k^\dagger \tilde{a}_k \right) \quad , \tag{5.8}$$

with physical, $\hat{a}_k^\dagger, \hat{a}_k$, and auxiliary normal mode operators, $\tilde{a}_k^\dagger, \tilde{a}_k$, for f vibrational degrees of freedom.[251] The latter operators satisfy the canonical bosonic commutation relations, where all commutators containing both physical and auxiliary operators vanish identically, and generate the basis states $|\underline{n}\rangle$ and $|\underline{\tilde{n}}\rangle$ in Eq.(5.6), respectively. Here, we assume $\bar{H}_0$ to be independent of the electronic state. A time-dependent, vibronic thermofield state in diabatic representation reads

$$|\Psi_\beta(t)\rangle = \sum_{i=1}^{M_e} |\psi_\beta^i(t)\rangle |S_i\rangle \quad , \tag{5.9}$$

with time-dependent, vibrational thermofield states, $|\psi_\beta^i(t)\rangle$, depending on the diabatic electronic state, $|S_i\rangle$. As initial state, we consider $|\Psi_\beta(t_0)\rangle = |\underline{0}_\beta\rangle |S_e\rangle$ for some fixed initial

state index, e, with normal mode thermal vacuum state

$$|\underline{0}_\beta\rangle = \frac{e^{-\beta\hat{H}_0/2}}{\sqrt{Z_\beta^0}} \sum_{\underline{n}} \prod_{k=1}^{f} \frac{\left(\hat{a}_k^\dagger\right)^{n_k}}{\sqrt{n_k!}} \frac{\left(\tilde{a}_k^\dagger\right)^{n_k}}{\sqrt{n_k!}} |\underline{0}, \underline{\tilde{0}}\rangle \quad , \tag{5.10}$$

multi-index, $\underline{n} = (n_1, \ldots, n_k, \ldots, n_f)$, physical normal mode Hamiltonian, $\hat{H}_0$, and corresponding normal mode partition function, Z_β^0, respectively.

5.2.2 Thermal Quasi-Particle MCTDH

The numerical solution of the TF-TDSE (5.3) suffers from two bottlenecks: Firstly, the ansatz for $|\Psi_\beta(t)\rangle$ in Eq.(5.9) scales strongly exponentially as $M_e M_v^{2f}$, with M_v vibrational basis function per normal-mode and, secondly, the complexity of the thermal vacuum state $|\underline{0}_\beta\rangle$, which contains strongly correlated pairs of physical and auxiliary states. In order to mitigate the complexity of $|\underline{0}_\beta\rangle$, we consider the *thermal quasi-particle* representation of TFD[251, 266], which additionally provides a natural starting point for the MCTDH ansatz.

The Thermal Quasi-Particle Representation

In the thermal quasi-particle (TQP) representation of TFD (TQP-TFD), one introduces TQP normal-mode operators $\hat{b}_k^\dagger, \hat{b}_k$ and $\tilde{b}_k^\dagger, \tilde{b}_k$, respectively. The operators, $\hat{b}_k$ and $\tilde{b}_k$, annihilate the corresponding thermal vacuum state identically

$$\hat{b}_k\, |0_\beta^{(k)}\rangle = \tilde{b}_k\, |0_\beta^{(k)}\rangle = 0 \quad , \tag{5.11}$$

and identify $|0_\beta^{(k)}\rangle$ as two-mode vacuum state for physical and auxiliary DoF.[251] The TQP operators are obtained from $\hat{a}_k^\dagger, \hat{a}_k$ and $\tilde{a}_k^\dagger, \tilde{a}_k$ by means of a unitary thermal Bogoliubov transformation (TBT)[251]

$$\hat{b}_k = \cosh\theta_k(\beta)\, \hat{a}_k - \sinh\theta_k(\beta)\, \tilde{a}_k^\dagger \quad , \tag{5.12}$$

$$\tilde{b}_k = \cosh\theta_k(\beta)\, \tilde{a}_k - \sinh\theta_k(\beta)\, \hat{a}_k^\dagger \quad , \tag{5.13}$$

with thermal mixing angles

$$\theta_k(\beta) = \operatorname{arctanh}\left(e^{-\beta\hbar\omega_k/2}\right) \quad , \tag{5.14}$$

which are determined by the harmonic frequency, ω_k, and the inverse temperature, β. The advantage of the TQP representation manifests in a Hartree product structure of the multi-mode thermal vacuum state, $|\underline{0}_\beta\rangle$, as given by

$$|\underline{0}_\beta\rangle = |0_\beta^{(1)}\rangle\, |0_\beta^{(2)}\rangle \ldots |0_\beta^{(f)}\rangle \quad , \tag{5.15}$$

where the highly correlated nature of Eq.(5.10) is now only of implicit nature. The simplicity of $|\underline{0}_\beta\rangle$ in Eq.(5.15), however, comes at the cost of a more complex TQP thermofield

Hamiltonian, $\bar{H}_\beta$, which now contains interaction terms coupling physical and auxiliary TQP modes. Further, an orthonormal basis of TQP number states $\{|\underline{n}_\beta^{(k)}\rangle\,, |\underline{\tilde{n}}_\beta^{(k)}\rangle\}$, which spans the k^{th}-mode's thermal Fock subspace, is generated by acting with $\hat{b}_k^\dagger$ and $\tilde{b}_k^\dagger$ on the vacuum state $|0_\beta^{(k)}\rangle$, respectively. Hence, in TQP representation, the TFD treatment of an f-dimensional vibrational problem at finite temperature turns into a $2f$-dimensional problem similar to the zero-temperature limit. We note, the temperature-dependence is still present in coupling terms of $\bar{H}_\beta$ as shown below. Finally, by employing the second quantization representation of the vibrational problem, we can now transfer the bosonic many-body formulation of the MCTDH method[89] to thermal quasi-particle TFD.

The MCTDH-TQP Ansatz

The MCTDH expansion of the vibronic thermofield state in Eq.(5.9), which we abbreviate in the following as MCTDH-TQP, is straightforwardly written as

$$|\Psi_\beta(t)\rangle = \sum_{i=1}^{M_e} \sum_{j_1,\dots,j_f}^{n_1,\dots,n_f} \sum_{i_1,\dots,i_f}^{m_1,\dots,m_f} A^{(1)}_{J,I,i}(t,\beta) \left(\prod_{\kappa,\tau=1}^{f} |\varphi_{j_\kappa}^{(1,\kappa)}(t,\beta)\rangle \; |\tilde{\varphi}_{i_\tau}^{(1,\tau)}(t,\beta)\rangle \right) |S_i\rangle \quad , \tag{5.16}$$

with multi-indices, $J = (j_1, \dots, j_f)$ and $I = (i_1, \dots, i_f)$, coefficients, $A^{(1)}_{J,I,i}(t,\beta)$, which depend on both time and inverse temperature, analogously to the orthonormal "thermal" SPFs, $|\varphi_{j_\kappa}^{(1,\kappa)}(t,\beta)\rangle$ and $|\tilde{\varphi}_{i_\tau}^{(1,\tau)}(t,\beta)\rangle$ (tSPFs). Physical tSPFs can subsequently be expanded in a primitive basis of TQP number states, $\{|n_\beta^{(l_\kappa)}\rangle\}$, as

$$|\varphi_{j_\kappa}^{(1,\kappa)}(t,\beta)\rangle = \sum_{l_\kappa=1}^{N_\kappa} B^{(\kappa)}_{j_\kappa l_\kappa}(t,\beta) \underbrace{\frac{\left(\hat{b}_\kappa^\dagger\right)^{n_{l_\kappa}}}{\sqrt{n_k!}} |0_\beta^{(k)}\rangle}_{=|n_\beta^{(l_\kappa)}\rangle} \quad , \tag{5.17}$$

and the expansion of auxiliary tSPFs, $|\tilde{\varphi}_{i_\tau}^{(1,\tau)}(t,\beta)\rangle$, follows analogously with respect to auxiliary TQP states, $|\tilde{n}_\beta^{(l_\tau)}\rangle$. The EoM are identical to standard MCTDH theory and follow from the Dirac-Frenkel variational principle

$$\langle \delta\Psi_\beta(t)| \mathrm{i}\hbar \frac{\partial}{\partial t} - \bar{H}_\beta |\Psi_\beta(t)\rangle = 0, \qquad \beta = \text{const.}, \tag{5.18}$$

for the thermofield state, $|\Psi_\beta(t)\rangle$, with TQP Hamiltonian, $\bar{H}_\beta$, at fixed inverse temperature, β. Further, the concepts of mode combination and multilayer extension of Eq.(5.16) apply directly as in case of the zero-temperature formalism. The construction of combined modes and in particular access to multilayer expansion provide the necessary numerical capabilities to solve the TF-TDSE. Mode combination and multilayer expansion are not restricted to a separation of physical and auxiliary DoF but allow for combined modes/ML-tree branches of mixed character. Besides the well-known advantages necessary for treating high-dimensional systems, the explicit combination of physical and auxiliary DoF turns out to be beneficial for treating the herein studied vibronic coupling Hamiltonians at elevated temperature as discussed below.

5.3 Thermal Effects on Ultrafast Relaxation of Pyrazine

We apply the MCTDH-TQP ansatz to examine temperature effects on the ultrafast non-adiabatic relaxation dynamics in the well-known pyrazine model[278, 279], which has previously been studied by the ρMCTDH(2) approach[105, 106] as introduced in Sec.2.3.2. In pyrazine, the electronically excited states $S_1(\pi, \pi^\star)$ and $S_2(n, \pi^\star)$ are subject to a conical intersection, providing an ultrafast internal conversion pathway. A minimal model of this process is given by a vibronic coupling model Hamiltonian in the two-dimensional S_1/S_2-subspace with four normal modes, $\mathcal{M}_4 = \{v_{6a}, v_{9a}, v_1, v_{10a}\}$, providing three tuning, $\mathcal{M}_t = \{v_{6a}, v_{9a}, v_1\}$, and a single coupling mode, v_{10a}, respectively. In an extended model, the remaining twenty normal modes of pyrazine are taken additionally into account. All calculations were performed with the Heidelberg MCTDH package, version 8.5.[84]
In the following, we introduce the TQP representation of the vibronic coupling Hamiltonian for pyrazine and the observables relevant for non-adiabatic dynamics.

5.3.1 Model Hamiltonian and Observables

TQP-Vibronic Coupling Hamiltonian for Pyrazine

In the thermal quasi-particle representation, the TFD vibronic coupling Hamiltonian for the 2-state-4-mode pyrazine model in Eq.(5.7) takes the form

$$\bar{H}_\beta = \sum_{i=1}^{2} \left(E_i + \bar{H}_\beta^{(0)} + \bar{H}_{\beta,i}^{(1)} + \bar{H}_{\beta,i}^{(2)} \right) |S_i\rangle \langle S_i| + \left(\hat{V}_\beta^{(1)} + \hat{V}_\beta^{(2)} \right) \sum_{i \neq j = 1}^{2} |S_i\rangle \langle S_j| \quad . \tag{5.19}$$

The first term resembles the diagonal terms with energies, $E_1 = -\Delta$ and $E_2 = +\Delta$, where, $2\Delta = E_2 - E_1$, is the energy difference between diabatic S_2- and S_1-potential energy surfaces evaluated at the ground state equilibrium position. Further, we have the normal mode TQP Hamiltonian, $\bar{H}_\beta^{(0)}$, linear and bilinear intra-state vibronic coupling terms, $\bar{H}_{\beta,i}^{(1)}$, and $\bar{H}_{\beta,i}^{(2)}$, as well as linear and quadratic vibronic coupling contributions, $\hat{V}_\beta^{(1)}$ and $\hat{V}_\beta^{(2)}$. Explicit expressions for the latter contributions are provided in Appendix D. In the following, we consider both the quadratic TQP-Hamiltonian in Eq.(5.19), and a simpler linear version, where terms $\bar{H}_{\beta,i}^{(2)}$ and $\hat{V}_{\beta,i}^{(2)}$ are neglected.
As noted above, an extended linear 2-state-24-mode model is also studied. The corresponding model Hamiltonian takes into account the remaining twenty normal modes of pyrazine in terms of a tuning mode bath and is given by

$$\bar{H}_\beta^{SB} = \sum_{i=1}^{2} \left(E_i + \bar{H}_\beta^{(0)} + \bar{H}_{\beta,i}^{(1)} + \hat{H}_{\beta,i}^{(SB)} + \bar{H}_\beta^{(B)} \right) |S_i\rangle \langle S_i| + \hat{V}_\beta^{(1)} \sum_{i \neq j = 1}^{2} |S_i\rangle \langle S_j| \quad , \tag{5.20}$$

with on-diagonal bilinear system-bath interaction, $\hat{H}_{\beta,i}^{(SB)}$, and bath Hamiltonian, $\bar{H}_\beta^{(B)}$ (*cf.* Appendix D for details). In the following, we refer to the TQP representation of the 2-state-4-mode pyrazine model as $(4+4)$D-model to explicitly indicate the doubling of the normal

mode DoF. Analogously, we denote the extended 2-state-24-mode model as $(24+24)$D-model.
Further, the initial vibronic thermofield states considered here are given by

$$|\Psi_\beta(t_0)\rangle = |S_2\rangle\,|\underline{0}_\beta\rangle \quad , \tag{5.21}$$

$$|\Psi_\beta(t_0)\rangle = |S_2\rangle\,|\underline{0}_\beta\rangle\,|\underline{0}_\beta^{(B)}\rangle \quad , \tag{5.22}$$

where an instantaneous excitation from the electronic ground state, $|S_2\rangle = \hat{\mu}\,|S_0\rangle$, as mediated by the electronic dipole operator, $\hat{\mu} = \mu_{20}\left(|S_0\rangle\,\langle S_2| + |S_2\rangle\,\langle S_0|\right)$ (with $\mu_{20} = 1$ in the following), is assumed. In Eq.(5.21), the thermal four-mode vacuum state reads

$$|\underline{0}_\beta\rangle = |0_\beta^{v10a}\rangle\,|0_\beta^{v6a}\rangle\,|0_\beta^{v9a}\rangle\,|0_\beta^{v1}\rangle \quad , \tag{5.23}$$

which resembles a Hartree-product of two-mode states for both identical physical and auxiliary DoF. For the extended pyrazine model with TFD-Hamiltonian Eq.(5.20), the initial state (*cf.* Eq.(5.22)) is augmented by a bath thermal vacuum state

$$|\underline{0}_\beta^{(B)}\rangle = \prod_{k=1}^{20} |0_\beta^{(b),k}\rangle \quad , \tag{5.24}$$

with two-bath-mode thermal vacuum states, $|0_\beta^{(b),k}\rangle$, respectively.

Observables in TQP-TFD

We now turn to the TQP-TFD expressions for observables considered here, which directly result from the definition in Eq.(5.4). The time-evolution of the electronic DoF is studied by means of electronic diabatic populations

$$P_\beta^{(S_i)}(t) = \langle\Psi_\beta(t)|\Big(|S_i\rangle\,\langle S_i|\Big)|\Psi_\beta(t)\rangle \quad , \quad i = 1,2 \quad . \tag{5.25}$$

The vibrational dynamics of both coupling and tuning modes is studied via time-dependent mean occupation numbers

$$\begin{aligned}\langle\hat{n}_k\rangle_\beta(t) = \cosh^2\theta_k\,\langle\hat{b}_k^\dagger\hat{b}_k\rangle_\beta(t) + \sinh^2\theta_k\,\langle\tilde{b}_k^\dagger\tilde{b}_k\rangle_\beta(t) \\ + \cosh\theta_k\sinh\theta_k\left(\langle\tilde{b}_k^\dagger\hat{b}_k^\dagger\rangle_\beta(t) + \langle\tilde{b}_k\hat{b}_k\rangle_\beta(t)\right) + \bar{n}_k(\beta) \quad ,\end{aligned} \tag{5.26}$$

with physical normal mode number operator, $\hat{n}_k$, and Bose-Einstein distribution, $\bar{n}_k(\beta) = \left(e^{\beta\hbar\omega_k}-1\right)^{-1}$, for the k^{th}-normal mode. Each vibrational mode is initially in a thermal equilibrium state, *i.e.*, $\langle\hat{n}_k\rangle_\beta(0) = \bar{n}_k(\beta)$. Further, we obtain linear absorption spectra at finite temperature as

$$\sigma_\beta(\omega) \propto \mathrm{Im}\int_0^\infty C_\beta(t)\,e^{\mathrm{i}\omega\,t}\,\mathrm{d}t \quad , \tag{5.27}$$

with thermal autocorrelation function

$$C_\beta(t) = \langle\Psi_\beta|e^{-\mathrm{i}\bar{H}_\beta\,t/\hbar}|\Psi_\beta\rangle = \mathrm{tr}\left\{\left(e^{\mathrm{i}\hat{H}\,t/\hbar}\hat{\mu}\,e^{-\mathrm{i}\hat{H}\,t/\hbar}\hat{\mu}\right)\hat{\rho}(t_0)\right\} \quad , \tag{5.28}$$

where, $|\Psi_\beta(t)\rangle = e^{-\mathrm{i}\bar{H}_\beta\,t/\hbar}\,|\Psi_\beta\rangle$, and, $\hat{\rho}(t_0) = \hat{\rho}_\beta^0\,|S_0\rangle\,\langle S_0|$, respectively. We note, this result resembles a special case of higher-order response functions recently derived in Ref.[270].

5.3.2 Multilayer Expansion of TQP-States

We begin our discussion by examining different multilayer expansions of TQP thermofield states for the linear and bilinear $(4+4)$D-models based on their numerical performance in terms of CPU time.

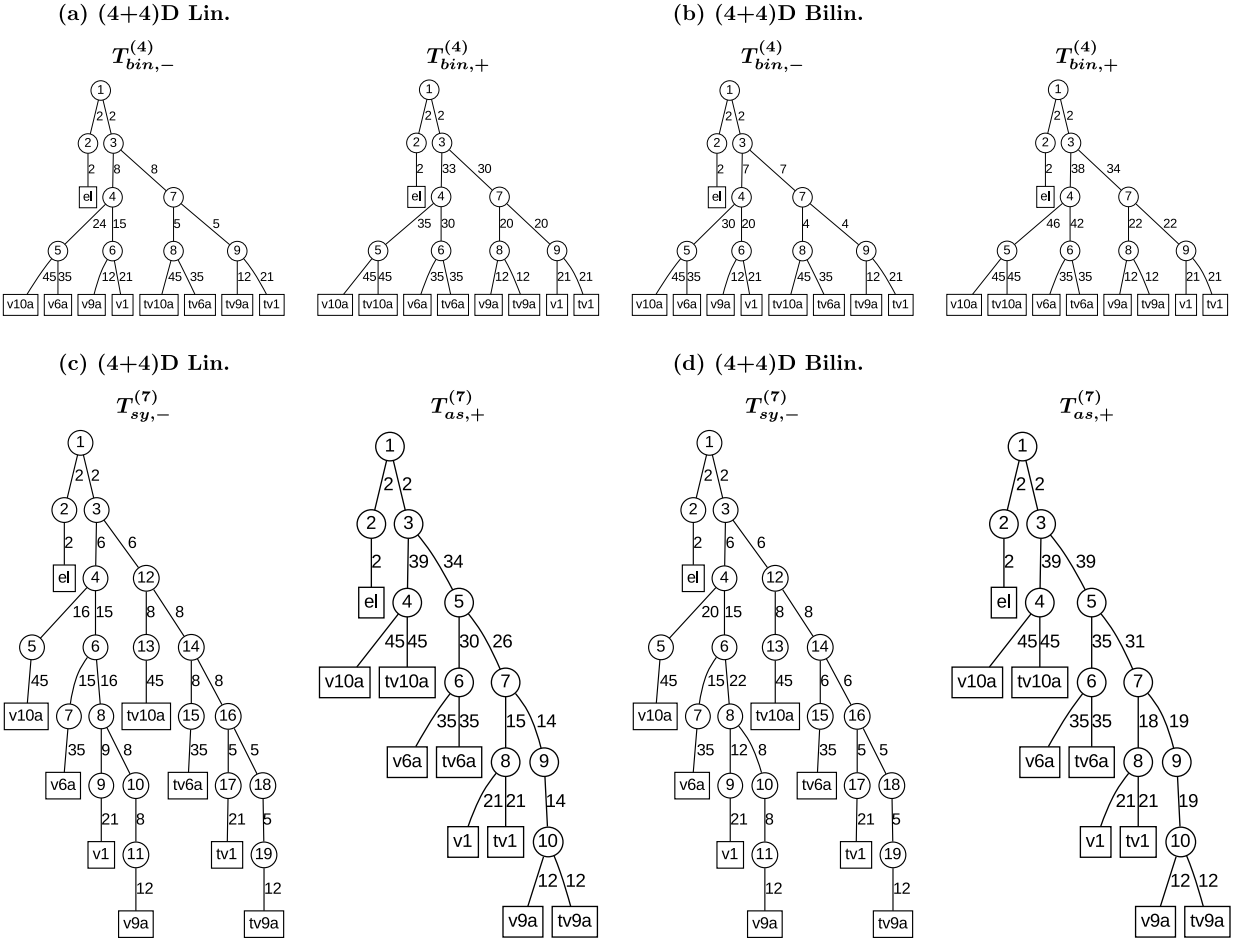

Figure 5.1: Multilayer trees for thermofield states of linear (lin.) and bilinear (bilin.) (4+4)D-pyrazine models with number of tSPFs given next to edges (at bottom layer, numbers correspond to primitive TQP number states). Physical primitive modes are specified as $\{v10a, v6a, v9a, v1\}$ and auxiliary primitive modes as $\{tv10a, tv6a, tv9a, tv1\}$. Top row: Symmetric binary 4-layer trees, $T^{(4)}_{bin}$, for (a) linear and (b) bilinear (4+4)D-model with low-temperature ($T^{(4)}_{bin,-}$) and high-temperature ($T^{(4)}_{bin,+}$) mode combination schemes. Bottom row: Symmetric, $T^{(7)}_{sy,-}$, and asymmetric, $T^{(7)}_{as,+}$, 7-layer trees for (c) linear and (d) bilinear (4+4)D-mode models with low-temperature (index "$-$") and high-temperature (index "$+$") mode combination schemes.

In Fig.5.1, we distinguish between binary symmetric trees with four layers, $T^{(4)}_{bin}$, and binary seven-layer trees in a symmetric, $T^{(7)}_{sy}$, and an asymmetric version, $T^{(7)}_{as}$, respectively.

The superscripts indicate the number of layers and the index refers to binary ("bin"), symmetric ("sy") or asymmetric ("as") ML-trees. Further, we distinguish a "low"- and "high"-temperature regime, where the former corresponds to T = 1-300 K and the latter to $T = 500\,\mathrm{K}$, which is a model-specific categorization and not a general statement. This distinction allows us to consider a low-temperature mode combination scheme with combined modes (v_{10a}, v_{6a}), (v_{9a}, v_1), (tv_{10a}, tv_{6a}), (tv_{9a}, tv_1), *i.e.*, physical and auxiliary DoF are fully separated, besides a high-temperature scheme with combined modes (v_{10a}, tv_{10a}), (v_{6a}, tv_{6a}), (v_1, tv_1), (v_{9a}, tv_{9a}), where physical modes are paired with their auxiliary counterparts. Further, for the low-temperature regime, which we indicate by a minus as index, we consider ML-trees, $T^{(4)}_{bin,-}$ and $T^{(7)}_{sy,-}$, and for the high-temperature regime, $T^{(4)}_{bin,+}$ and $T^{(7)}_{as,+}$, (additional plus as index), respectively. We note, all ML-trees considered here are identical for the linear and bilinear (4+4)D-models with respect to their topology, however, they differ in the numbers of tSPFs necessary to converge the calculations.

We propagate the initial vibronic thermofield state, $|\Psi_\beta\rangle = |S_2\rangle\,|\underline{0}_\beta\rangle$, up to $t_f = 150\,\mathrm{fs}$ and identify a propagation as converged, if the highest natural population $\leq 1.0 \times 10^{-3}$, respectively. As a reference, we consider a standard MCTDH expansion of the thermofield states with tree, $T^{(2)}_0$.

Table 5.1: CPU time (h:m) for linear (4+4)D-model Hamiltonian of pyrazine with different ML-tree topologies and propagation time, $t_f = 150\,\mathrm{fs}$ (Intel(R) Xeon(R) CPU E5-2650 v2 @ 2.60GHz, 126 GB RAM) at different temperatures.

Linear (4+4)D-Model

Temp.	$T^{(4)}_{bin,-}$	$T^{(4)}_{bin,+}$	$T^{(7)}_{sy,-}$	$T^{(7)}_{as,+}$	$T^{(2)}_0$
1 K	0:06	0:08	0:02	0:05	0:03
100 K	0:08	0:17	0:04	0:08	0:04
300 K	3:54	0:29	0:24	1:02	0:05
500 K	3:07	0:52	3:09	0:53	0:29

For both models and all ML-trees (*cf.* Tabs.5.1 and 5.2), we observe an increase in CPU time with increasing temperature, which directly relates to the increasing temperature-dependent interactions in the TQP-Hamiltonian (*cf.* Appendix D) and the related complexity of the propagated thermofield state. We observe the low- and high-temperature expansions (recall, $T = 500\,\mathrm{K}$ for the latter) to perform favorably in their respective regimes, which results in a CPU time reduction of factors $2 - 4$, depending on the ML-tree. In this context, we observe a more compact wave function representation for the high-temperature mode combination scheme in hand with an improved memory requirement for the high-temperature propagation runs. We note, however, that the interplay of different mode combination schemes and temperature effects is not yet fully understood besides those observations and requires further studies. Moreover, the seven-layer trees, $T^{(7)}_{sy,-}$ and $T^{(7)}_{as,+}$, surpass their four layer counterparts in terms of CPU times, which is particularly apparent for the bilinear

Table 5.2: CPU time (h:m) for bilinear (4+4)D-model Hamiltonian of pyrazine with different ML-tree topologies and propagation time, $t_f = 150\,\mathrm{fs}$ (Intel(R) Xeon(R) CPU E5-2650 v2 @ 2.60GHz, 126 GB RAM) at different temperatures.

Bilinear (4+4)D-Model

Temp.	$T^{(4)}_{bin,-}$	$T^{(4)}_{bin,+}$	$T^{(7)}_{sy,-}$	$T^{(7)}_{as,+}$	$T^{(2)}_{0}$
1 K	0:19	0:21	0:05	0:17	0:15
100 K	0:38	1:06	0:10	0:39	0:37
300 K	3:29	2:12	1:25	1:29	3:01
500 K	7:16	4:17	8:41	2:44	9:36

$(4 + 4)$D-model, while in the linear model a standard MCTDH expansion is numerically optimal.

The MCTDH-TQP ansatz is an alternative to the stochastic MCTDH[95, 96, 97] and density-operator based ρMCTDH[105, 106, 107] approaches to study finite temperatures. Stochastic approaches aim at converging thermal ensemble averages by sampling over independent trajectories, which initially require an imaginary-time propagation to prepare a proper initial state followed by a real-time propagation to capture the dynamics of the system. For an increasing number of DoF, the ML-MCTDH approach becomes mandatory and for higher temperatures, a growing number of realizations is required to converge a thermal ensemble average, which renders the stochastic approach numerically demanding. The MCTDH-TQP ansatz requires only a single run independent of temperature, but doubles the number of degrees of freedom. At the moment it remains an open question, which approach might be numerically favorable for a given problem at hand. Further, the ρMCTDH approach allows to propagate the density operator at different temperatures in a single propagation run, however, is currently restricted to small systems where it has been shown to be numerically efficient.[105] Here, the MCTDH-TQP approach can be favorable as it applies straightforwardly to large systems, based on the benefits of the multilayer format.

5.3.3 Finite Temperature Effects on Internal Conversion

We now turn to finite temperature effects on internal conversion dynamics in pyrazine and examine the time-evolution of diabatic electronic populations, $P^{(S_i)}_{\beta}(t)$ (*cf.* Eq.(5.25)), and vibrational mean occupation numbers, $\langle \hat{n}_k \rangle_\beta (t)$ (*cf.* Eq.(5.26)), respectively.
We first consider diabatic populations for linear and bilinear $(4 + 4)$D-models in Fig.5.2. There, we compare MCTDH-TQP and ρMCTDH results, where the latter were reproduced from Ref.[105]. Note, both methods are considered for the same temperatures. The MCTDH-TQP results have been obtained with the numerically most performant ML-trees discussed in the last section. In general, the internal conversion dynamics is qualitatively

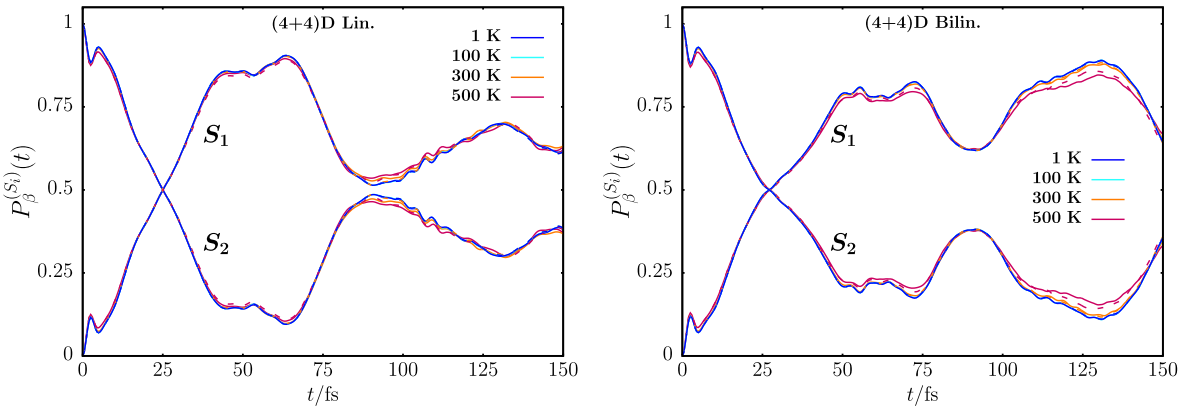

Figure 5.2: Time-evolution of diabatic electronic populations, $P_\beta^{(S_1)}(t)$ and $P_\beta^{(S_2)}(t)$, for electronic states, $|S_1\rangle$ and $|S_2\rangle$, at selected temperatures for linear (left) and bilinear (right) (4+4)D pyrazine models obtained with MCTDH-TQP approach in comparison to ρMCTDH results (dashed lines; same temperatures with color code as MCTDH-TQP) reproduced from Ref.[105].

characterized by an ultrafast initial decay of the S_2 excited state and a recurrence at around 100 fs. For the linear model, finite temperature effects manifest in a slightly faster initial relaxation and a mild damping of the recurrence. Although qualitatively identical, the effects in the linear model are smaller in magnitude compared to the bilinear (4+4)D-mode model. Our findings agree well with the ρMCTDH results at early times, however, showing a slightly less thermally damped recurrence at later times. One possible source for this deviation relates to the different representations of the Hamiltonian, *i.e.*, bosonic number states vs. DVR, employed in the two approaches.

Next, we discuss the vibrational dynamics in terms mean occupation numbers, $\langle \hat{n}_k \rangle_\beta(t)$, (*cf.* Fig.5.3). Here, the dynamics of the low-frequency tuning mode, $v6a$, and the coupling mode, $v10a$, can be distinguished from the high-frequency tuning modes ($v9a, v1$). The high-frequency modes show only small-amplitude Rabi-type oscillations over the studied time-interval and a very weak response to thermal effects, while modes $v6a$ and $v10a$ are irregularly excited. In particular, the low-frequency tuning mode, $v6a$, shows significant thermal excitations at $T = 500\,\mathrm{K}$ for long times in both the liner and bilinear modes. Notably, the thermal effects on the coupling mode, $v10a$, are more pronounced in the bilinear $(4+4)$D-model, due to the inter-mode coupling term $\hat{V}^{(2)}_{\beta,i}$, respectively.

Lastly, we consider the extended linear $(24+24)$D-model, where the effects of a bilinearly coupled twenty-mode bath on the inversion dynamics is taken into account. This model exceeds the actual capabilities of the ρMCTDH approach due to its enlarged vibrational space of 24 normal modes. The multilayer expansion of the underlying vibronic thermofield state is based on the binary four-layer tree, $T^{(4)}_{bin}$, which comprises the four-mode system and augmented by a five-layer sub-tree for the bath connected to node 3 in the original $T^{(4)}_{bin}$, respectively.

We employed the high-temperature mode combination scheme here for $T = 300\,\mathrm{K}$ and

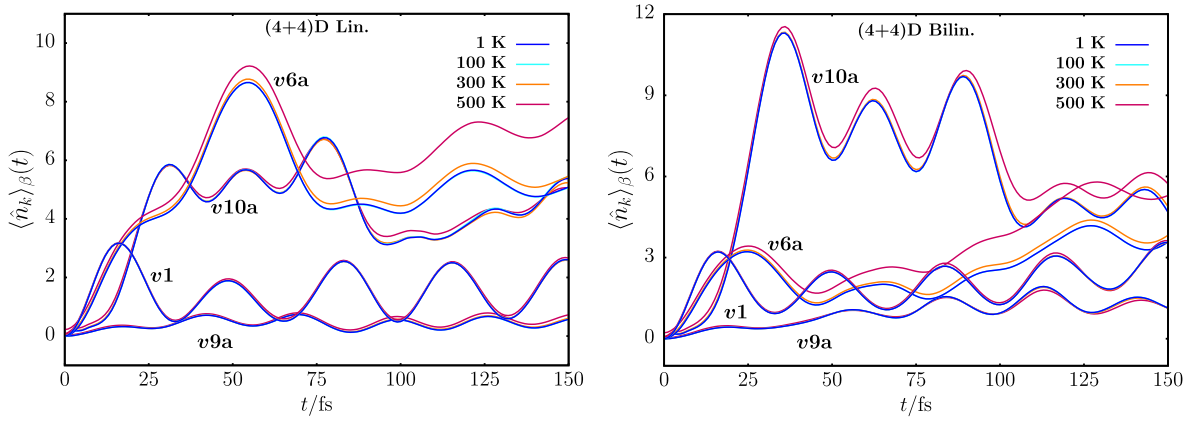

Figure 5.3: Time-evolution of the state averaged thermal mean occupation numbers, $\langle \hat{n}_k \rangle_\beta(t)$, of coupling mode, $v10a$, and tuning modesm $\{v6a, v9a, v1\}$, for the linear (left) and bilinear (right) (4+4)D pyrazine models obtained with MCTDH-TQP approach for selected temperatures.

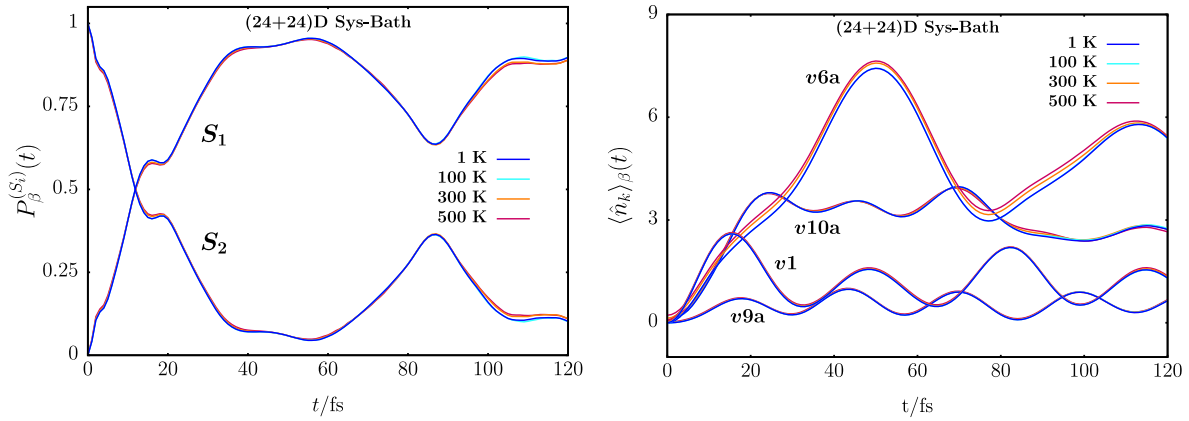

Figure 5.4: Time-evolution of diabatic electronic populations, $P_\beta^{(S_i)}(t)$ (left), and time-evolution of state-averaged thermal mean occupation numbers, $\langle \hat{n}_k \rangle_\beta(t)$ (right), obtained with MCTDH-TQP approach for linear (24+24)D system-bath pyrazine model at selected temperatures.

$T = 500\,\mathrm{K}$. On the left-hand side of Fig.5.4, we show the diabatic electronic populations, which are subject to a more pronounced population transfer from the S_2- to the S_1-state compared to the reduced $(4+4)$D-models. Thermal effects turn out to be rather small for the diabatic populations similar to the reduced four-mode scenario, which results from the relatively high harmonic frequencies of the normal modes compared to the thermal energy at selected temperatures. On the right-hand side of Fig.5.4, the vibrational mean occupation numbers are shown, which experience a similar dynamics as in the linear $(4+4)$D-model and only the low-frequency tuning mode, $v6a$, is subject to significant thermal excitations.

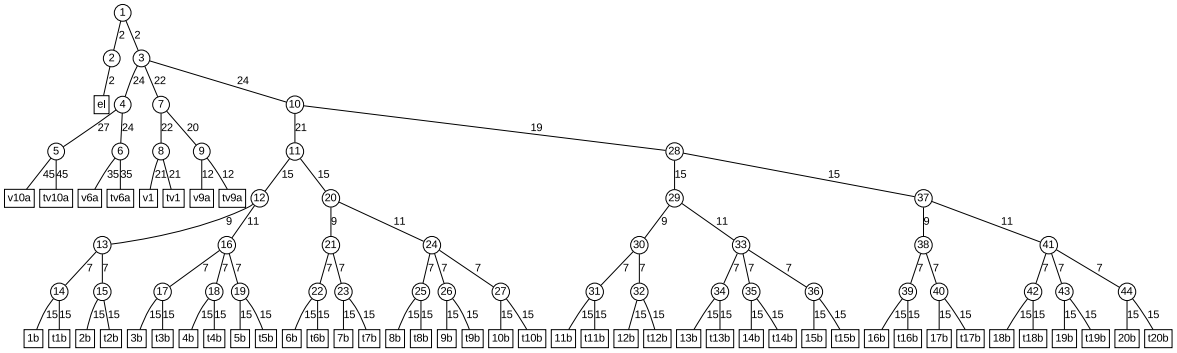

Figure 5.5: Exemplary ML-tree for a vibronic thermofield state of the linear (24+24)D pyrazine model.

5.3.4 Finite Temperature Effects on Vibronic Spectra

We finally consider the finite temperature effects on vibronic spectra of the pyrazine models as obtained from the thermal autocorrelation function, $C_\beta(t)$.

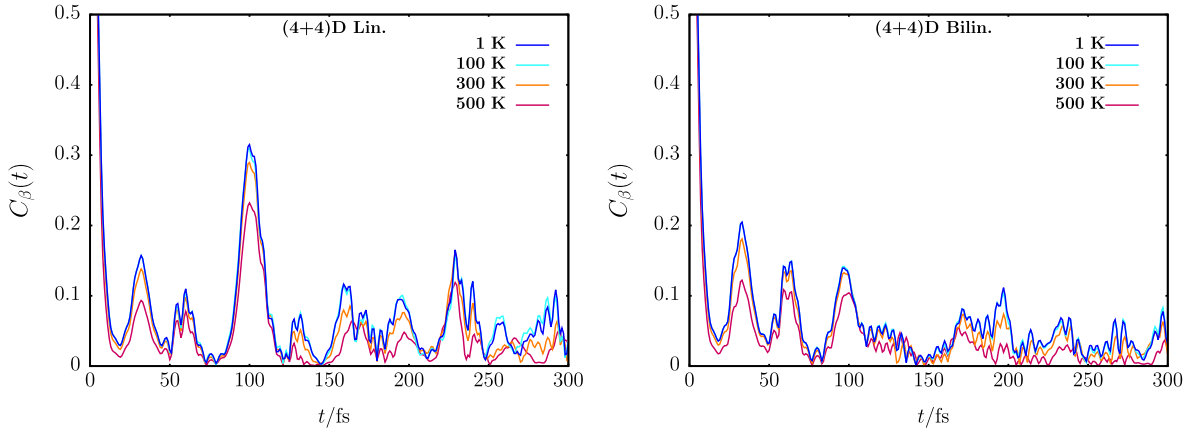

Figure 5.6: Time-evolution of the thermal autocorrelation function, $C_\beta(t)$, for linear (left) and bilinear (right) (4+4)D pyrazine models obtained with MCTDH-TQP approach at selected temperatures.

The time-evolution of the latter is shown for the linear and bilinear $(4+4)$D-models in Fig.5.6 and is dominated by an ultrafast initial decay up to 20 fs followed by a series of recurrences. Finite temperature effects manifest in a more pronounced initial decay and significantly damped recurrences at $T = 500$ K for both models. The corresponding linear absorption spectra, $\sigma_\beta(\omega)$, are shown in Fig.(5.7) for the linear and bilinear models. The presentation follows Ref.[278], where the origin of the energy axis resembles half the energy gap between the two diabatic surfaces and the spectra have been artificially broadened to account for the twenty residual modes in the $(4+4)$D-models. The low-intensity part of

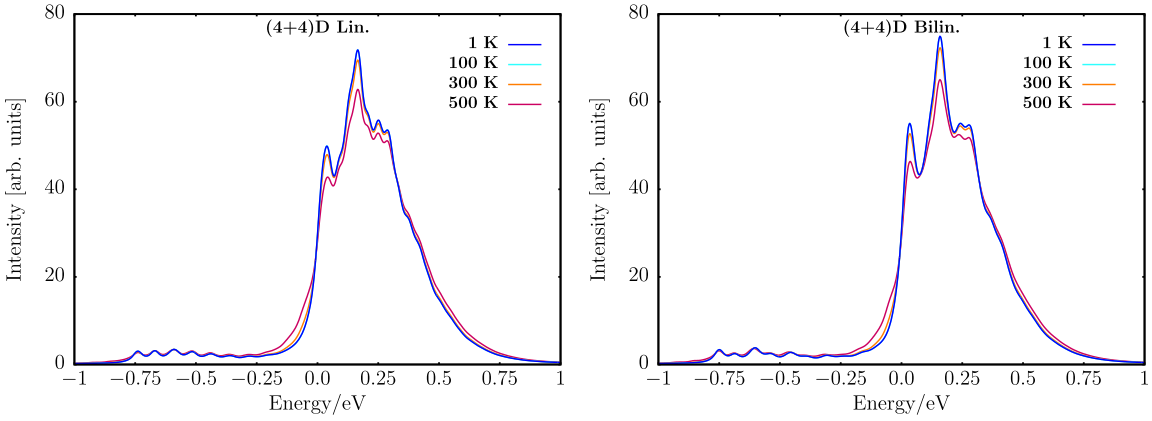

Figure 5.7: Temperature-dependent linear absorption spectra, $\sigma_\beta(\omega)$, calculated from TFD autocorrelation function, $C_\beta(t)$, obtained with MCTDH-TQP approach for linear (left) and bilinear (right) (4+4)D pyrazine models at selected temperatures.

the spectrum is located below the conical intersection between the S_1 and S_2 states, and dominated by a series of peaks referring to vibrational states, which exhibit only weak thermal effects. In contrast, the broad and intense peak lying energetically above the conical intersection, here positive energies, is subject to thermal broadening accompanied by an intensity reduction.
For the (24+24)D-model, we find the temperature effects in Fig.5.8 small as already seen in the last section (*cf.* Fig.5.4). The thermal autocorrelation function is subject to thermal damping, which are in particular dominant for the recurrence at around 100 fs. The

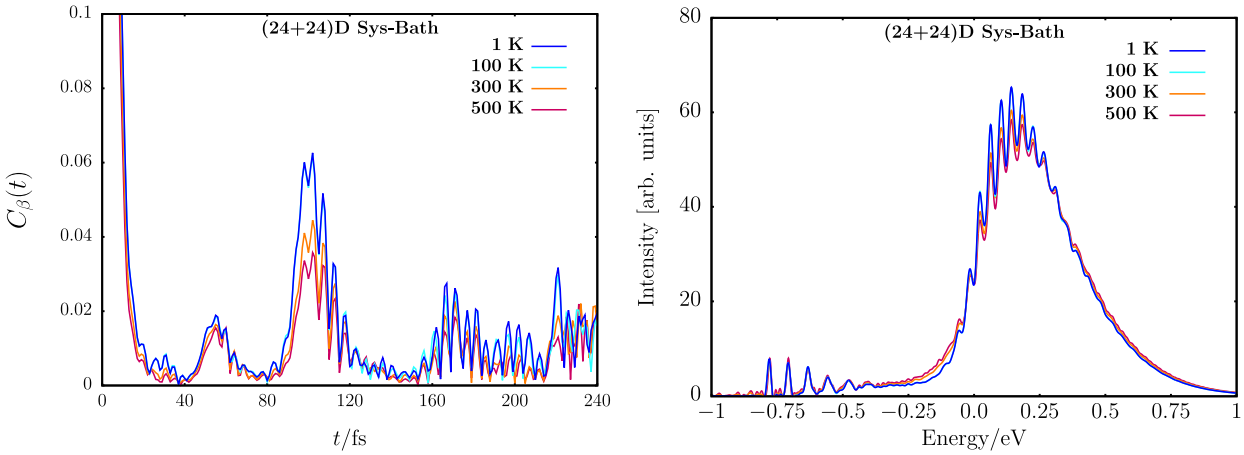

Figure 5.8: Time-evolution of thermal autocorrelation function, $C_\beta(t)$, (left) and corresponding temperature-dependent linear absorption spectra, $\sigma_\beta(\omega)$, (right) of linear (24+24)D system-bath pyrazine model for selected temperatures.

absorption spectrum is here broadened due to two effects: (i) the explicit inclusion of the

twenty-mode bath, which provides the dominant contribution and (ii) mild thermal effects accompanied by a slight intensity reduction.

5.4 Summary and Outlook

We introduced a thermofield-based formulation of the multilayer multiconfigurational time-dependent Hartree (ML-MCTDH) method for the treatment of non-adiabatic quantum dynamics at finite temperature. Our approach is based on the thermal quasi-particle (TQP) representation of symmetric thermofield dynamics (TFD), which provides a formulation of quantum statistical mechanics in the language of many-body theory. We introduced the ML-MCTDH approach for thermofield states by exploiting the formal equivalence of thermal quasi-particle TFD at fixed finite temperature and bosonic many-body theory at zero temperature with a doubled number of degrees of freedom. This equivalence allows for a transfer of bosonic many-body MCTDH, *i.e.*, MCTDH-SQR, to the thermal quasi-particle TFD framework. In particular, the thermal quasi-particle representation of TFD provides an appealing form of the multi-mode thermal vacuum state in terms of a Hartree product of single-mode thermal vacuum states, which constitutes an ideal initial state for the MCTDH method. From a practical point of view, the method presented here can be directly adapted via the ML-MCTDH-SQR method as implemented in the Heidelberg MCTDH package[84]. We applied our ansatz, abbreviated as MCTDH-TQP, to the well-studied two-state-four-mode vibronic coupling model of pyrazine and its two-state-24-mode extension, including an additional bilinearly coupled harmonic bath. From a computational point of view, the effect of temperature, which manifests as increased interactions in the TQP thermofield Hamiltonian, can be beneficially accounted for in the multilayer expansion of thermofield states by properly combining physical and auxiliary DoF. For the multilayer trees used in this work, it turned out to be computationally advantageous to fully separate physical and auxiliary DoF at "low" temperatures ($T = 1 - 300\,\mathrm{K}$) and combine two similar physical and auxiliary modes at "high" temperature ($T = 500\,\mathrm{K}$). We note, the distinction between "low" and "high" temperature is of course problem dependent. Further, we observed temperature effects to manifests as faster decay of electronic populations and autocorrelation function as well as thermal excitation of low frequency normal modes and thermal broadening in optical absorption spectra. Our approach allows to overcome the actual capabilities of the ρMCTDH ansatz, as shown for a linear two-state-24-mode system-bath model accessible via the ML-MCTDH-TQP approach.
A very promising route to future applications of the ML-MCTDH-TQP approach is provided by a recently formulated and refined dynamical spawning of single particle functions[280, 281], which opens the door to fully automatized convergence of SPFs. Furthermore, a comparison of the numerical performance of MCTDH-TQP with respect to stochastic and density operator approaches in the MCTDH framework as well as the numerical details of the high-temperature mode combination scheme is desirable. Finally, application to potentially laser-driven anharmonic vibrational problems featuring multiple low frequency modes or suited rotational (model) systems might benefit from the advantages of the thermofield dynamics approach.

Chapter 6

Summary & Conclusions

In this thesis, we numerically studied properties, dynamics and spectroscopy of selected molecular vibrational models interacting with complex vibrational environments from a quantum mechanical perspective. In particular, we studied vibrational polaritons in small molecules, phonon-driven vibrational adsorbate relaxation dynamics for a realistic adsorbate-surface model and introduced the thermofield formulation of the MCTDH method, which provides a non-stochastic approach to (non-adiabatic) quantum dynamics at finite temperature.

In Chapter 3, we studied rovibrational light-matter hybrid states in small molecules in the framework of non-relativistic cavity quantum electrodynamics as described by an effective rovibrational Pauli-Fierz Hamiltonian in length-gauge representation and long-wavelength approximation. Additionally, we considered the cavity Born-Oppenheimer approximation as well as neglected electron-photon correlation, which are reasonable approximations for infrared cavities. In the first part, we thoroughly discussed the non-trivial role of the dipole self-energy (DSE) for minimal models comprising a single molecular and a single cavity mode. The DSE manifest itself in three aspects: First, in absence of the DSE, the instability of the vibro-polaritonic ground state energy is found to result from a diverging bare light-matter interaction contribution, which is exactly canceled by the dipole self-energy. Second, classical dissociation and activation energies are independent of the light-matter interaction in the limit of vanishing electron-photon correlation on cavity potential energy surfaces (cPES) accounting for the DSE. As a consequence, we showed that no minimum energy path exists on a full cPES, which is lower in energy than its molecular counterpart on a corresponding conventional Born-Oppenheimer potential energy surface as obtained in the limit of vanishing light-matter interaction strength. Third, we discussed vibro-polaritonic infrared spectra and showed for a symmetric double-well model potential how symmetry properties of the system allow to distinguish between “dark” and “bright” vibro-polaritonic states. Both vibro-polaritonic excited states and infrared spectroscopic intensities are severely altered in absence of the DSE contribution.
In the second part, we considered a model for a freely rovibrating diatomic molecule, which interacts with two orthogonally polarized, degenerate cavity modes depending on its spatial orientation. By adiabatically separating low-energy rotational and high-energy vibro-

polaritonic degrees of freedom, we identified the formation of three-state vibro-polaritonic conical intersections (VPCI) between singly excited vibro-polaritonic states. The VPCI are located in a two-dimensional angular coordinate branching space and provide an effective transfer channel between different vibro-polaritonic states. Transfer dynamics manifest in a rich interference pattern in rotational densities, induced by the passage of rotational wave packets from different vibro-polaritonic surfaces. Spectroscopically, non-adiabatic cavity-induced effects result in a rich multi-peak progression in the spectral region of the upper vibro-polaritonic surface, which can be assigned to rovibratonal light-matter hybrid states containing contributions from all present degrees of freedom. Finally, spontaneous emission from cavity modes has been taken into account by means of a phenomenological non-Hermitian approach, which results in a strong intensity reduction of a purely photonic middle polariton peak and severe broadening of peaks in the rovibro-polaritonic progression.

The last part of Ch.3 was concerned with a cavity-altered thermal isomerization model in two dimensions. Here, we combined a harmonic analysis of extremal points on the cPES with full quantum rate theory based on cumulative reaction probabilities (CRP) and Eyring transition state theory to characterize the isomerization process in the light-matter hybrid system. Where CRP-based thermal rates account for the all quantum mechanical effects as tunneling besides anharmonicity of the cPES, Eyring thermal rates provide qualitatively correct results at ambient temperature, if light-matter interaction dependent zero-point energies are properly accounted for. We identified a reduction of thermal inversion rates as result of light-matter interaction, which we traced back to two quantum effects: First, the light-matter induced deformation of the cPES leads to a "valley-narrowing" effect at the cavity transition state, which significantly reduces the thermally accessible bound states. Second, a "barrier-broadening" effect was observed, which manifests itself in significantly attenuated tunneling rates at low temperatures. Further, we identified a dynamical resonance effect, which manifests itself in a localization of a reactant wave packet due to strong coherent energy transfer between a harmonized reactant mode and the cavity mode, if the latter is in resonance with the former.

In Chapter 4, we turned to a high-dimensional adsorbate-surface model problem and studied the phonon-induced vibrational relaxation dynamics of a single, mildly anharmonic D-Si-Si-bending mode coupled to more than 2000 harmonic surface (phonon) modes of a fully deuterium-covered, reconstructed silicon surface D:Si(100)-(2×1) at $T = 0\,\mathrm{K}$. In order to mitigate the "curse of dimensionality" induced by the high-dimensional phonon-bath Hilbert space, we combined a hierarchical effective mode (HEM) approach for the bilinear system-bath Hamiltonian with the multilayer-MCTDH method. For the HEM-approach, we introduced an efficient algorithm for the generation of effective mode coupling and frequency parameters, by employing beneficial properties of Householder matrices. The HEM approach allowed us to significantly reduce the full bath to $M = 60$ relevant effective modes, which were sufficient to fully account for the exact relaxation dynamics of the system mode on the relaxation time scale of $t_f = 2000\,\mathrm{fs}$. Notably, we found the number of effective modes to be independent of the initial systems states for examples studied herein with system quantum numbers, $v_0 \leq 5$. Further, we compared the performance of the HEM-ML-MCTDH approach with the recently introduced, coherent state based multi-Davydov

D2 (mD2) ansatz. We found the latter to be straightforwardly convergeable for the bilinear system-bath model by increasing the "multiplicity" (number) of multi-mode coherent states. Moreover, only a weak dependence of the multiplicity on the number of effective modes was observed and the mD2-ansatz showed a promising numerical performance with respect to computation time. Turning back to the properties of the system-bath model, we examined on non-Markovian signatures compared to results obtained from Markovian open system density matrix theory as described by a Liouville-von Neumann equation in Lindblad form. Here, we first addressed initial state half-lifetimes in presence of a non-trivial bath density-of-states. As a general trend, non-Markovian dynamics provide longer half-lifetimes compared to the Markovian limit, as in the latter the initial state population is subject to a fast exponential initial decay. Further, we observed the formation of small amplitude but clearly non-zero vibrational coherences in the non-Markovian scenario, when starting from a pure initial system state. As vibrational population and coherence dynamics is strictly decoupled in the Markovian limit as described by the Lindblad formalism, a pure initial state does not give rise to vibrational coherences here. Finally, we considered reduced system properties in terms of purity, von Neumann-entropy and a system energy current. The former two allowed us to access system-bath entanglement, which is on average qualitatively well described by the Lindblad approach. However, we found significant differences on short time scales, where the non-Markovian properties are characterized by a oscillatory fine structure, and in the "long-time limit" considered here, which is subject to weak but non-zero system-bath entanglement. Eventually, the system energy current allowed us to address both the rate of energy transfer as well as the transfer direction. In the non-Markovian scenario, we observed a non-monotonic energy transfer subject to regularly occurring energy back-transfer events leading to re-excitation of the system mode. In contrast, in the Markovian limit the current is exclusively unidirectional, *i.e.*, energy is only transferred from the system to the bath.

In the final Chapter 5, we approached the time-dependent description of quantum mechanical systems at finite temperature. By employing the theory of thermofield dynamics (TFD), we extended the powerful numerical machinery of the multilayer MCTDH approach to the finite temperature regime. We applied our MCTDH-TQP approach to the well-known vibronic coupling model of pyrazine, with molecular normal modes subject to thermal excitations. A beneficial theoretical framework was identified as the thermal quasi-particle representation of TFD, which allows to map a system with f vibrational modes at finite temperature to an artificially enlarged system of $2f$ interacting normal modes at vanishing temperature. We presented numerically advantageous topologies for multilayer representations of vibronic thermofield states ("ML-trees"), which are able to efficiently describe dynamics at both low and elevated temperatures. Further, we studied linear and bilinear variants of the 2-state-4-mode vibronic coupling model of pyrazine and examined the finite temperature effects on electronic, vibrational and spectroscopic properties. In particular, the numerical power of the ML-MCTDH-TQP approach allowed us to approach the 2-state-24-mode linear vibronic coupling model of pyrazine at selected temperatures, which overcomes the actual capabilities of the well-known direct propagation of the density matrix via the MCTDH ansatz (ρMCTDH) for closed systems.

Chapter 7

Publications

7.1 Non-Peer-Reviewed

9.) **Eric W. Fischer**, P. Saalfrank. Cavity-induced Non-Adiabatic Dynamics and Spectroscopy of Molecular Rovibrational Polaritons studied by Multi-Mode Quantum Models. arXiv:2205.00945, (2022). Under revision at *Journal of Chemical Physics*.

7.2 Peer-Reviewed

8.) **Eric W. Fischer**, Michael Werther, Foudhil Bouakline, Frank Grossmann, Peter Saalfrank. Non-Markovian Vibrational Relaxation Dynamics at Surfaces. *J. Chem. Phys.* **156**, 214702, (2022).

7.) **Eric W. Fischer**, Janet Anders, Peter Saalfrank. Cavity-Altered Thermal Isomerization Rates and Dynamical Resonant Localization in Vibropolaritonic Chemistry. *J. Chem. Phys.* **156**, 154305, (2022).

6.) **Eric W. Fischer**, Peter Saalfrank. A thermofield-based multilayer multiconfigurational time-dependent Hartree approach to non-adiabatic quantum dynamics at finite temperature. *J. Chem. Phys.* **155**, 134109, (2021).

5.) **Eric W. Fischer**, Peter Saalfrank. Ground state properties and infrared spectra of anharmonic vibrational polaritons of small molecules in cavities. *J. Chem. Phys.* **154**, 104311, (2021).

4.) **Eric W. Fischer**, Michael Werther, Foudhil Bouakline, Peter Saalfrank. A hierarchical effective mode approach to phonon-driven multilevel vibrational relaxation dynamics at surfaces. *J. Chem. Phys.* **153**, 064704, (2020).

3.) Foudhil Bouakline, **Eric W. Fischer**, Peter Saalfrank. A quantum-mechanical tier model for phonon-driven vibrational relaxation dynamics of adsorbates at surfaces. *J. Chem. Phys.* **150**, 244105, (2019).

7.3 Peer-Reviewed (Not Part of this Thesis)

2.) Phil Rosenow, Lars C. Bannow, **Eric W. Fischer**, Wolfgang Stolz, Kerstin Volz, Stephan W. Koch, Ralf Tonner. Ab initio calculations of the concentration dependent band gap reduction in dilute nitrides. *Phys. Rev. B* **97**, 075201, (2018).

1.) Lars C. Bannow, Phil Rosenow, Philipp Springer, **Eric W. Fischer**, Jörg Hader, Jerry V. Moloney, Ralf Tonner, Stephan W. Koch. An ab initio based approach to optical properties of semiconductor heterointerfaces. *Modelling Simul. Mater. Sci. Eng.* **25**, 065001, (2017).

Chapter 8

Appendix

A Details on Power-Zienau-Woolley Transformation

Here, we provide details on the Power-Zienau-Woolley Transformation as considered in Sec.2.2.2 of Ch.2. We recall that the quantized transvers vector potential in Eq.(2.28) is spatially uniform in the dipole/long-wavelength-approximation (*cf.* Eq.(2.31)), *i.e.*,

$$\underline{\hat{A}}(\underline{r}) \approx \underline{\hat{A}} = \sum_{\lambda=1}^{2}\sum_{k=1}^{N_c} \frac{\underline{e}_{\lambda k}}{\omega_k}\sqrt{\frac{\hbar\omega_k}{2\epsilon_0 V_c}}\left(\hat{a}_{\lambda k} + \hat{a}^\dagger_{\lambda k}\right) \quad . \tag{A.1}$$

The length-gauge representation of the Pauli-Fierz Hamiltonian is obtained as $\hat{\mathcal{U}}^\dagger \hat{H} \hat{\mathcal{U}}$ with molecular minimal coupling Hamiltonian, $\hat{H}$, in Eq.(2.27) and PZW transformation, $\hat{\mathcal{U}}$, as introduced in Eq.(2.34). In order to keep this appendix consistent, we restate here that the molecular potential, $V(\underline{r}, \underline{R})$ is invariant under the PZW-transformation as it commutes with both $\underline{d}$ and $\underline{A}$, respectively.

A.1 PZW-Transformation of Kinetic Energy Operators

We first consider the transformation of the kinetic energy terms (*cf.* Eq.(2.36)). We note, as the electronic and nuclear contribution in molecular dipole moment Eq.(2.35) commute, we can write $\hat{\mathcal{U}} = \hat{\mathcal{U}}_e \hat{\mathcal{U}}_n$, with electronic, $\hat{\mathcal{U}}_e$, and nuclear, $\hat{\mathcal{U}}_n$, PZW-contribution, respectively. Accordingly, we can consider the transformation of the two kinetic energy contributions individually, where we restrict ourselves here to the electronic part as the result is directly transferable to the nuclear contribution. Expanding the electronic KEO gives

$$\hat{\mathcal{U}}_e^\dagger \left(\sum_{i=1}^{N_e} \frac{\left(\hat{\underline{p}}_i + e\,\underline{\hat{A}}\right)^2}{2m_e} \right) \hat{\mathcal{U}}_e = \hat{\mathcal{U}}_e^\dagger \left(\sum_{i=1}^{N_e} \left(\frac{\hat{\underline{p}}_i^2}{2m_e} + \frac{e}{m_e}\hat{\underline{p}}_i \cdot \underline{\hat{A}} + \frac{e^2}{2m_e}\underline{\hat{A}}^2 \right) \right) \hat{\mathcal{U}}_e \quad , \tag{A.2}$$

where one directly observes the third term to be invariant under the PZW-transformation

$$\frac{e^2}{2m_e}\hat{\mathcal{U}}_e^\dagger \underline{\hat{A}}^2 \hat{\mathcal{U}}_e = \frac{e^2}{2m_e}\underline{\hat{A}}^2 \quad , \tag{A.3}$$

as both $\underline{\hat{A}}$ and $\underline{d}_e$ commute with $\underline{\hat{A}}^2$. Turning to the second term, linear in electronic momentum, and concentrating on the i^{th}-contribution, we employ the Baker-Campbell-Hausdorff (BCH) expansion and obtain

$$\frac{e}{m_e}\hat{\mathcal{U}}_e^\dagger\left(\underline{\hat{p}}_i\cdot\underline{\hat{A}}\right)\hat{\mathcal{U}}_e=\frac{e}{m_e}\left(\underline{\hat{p}}_i\cdot\underline{\hat{A}}-\frac{\mathrm{i}}{\hbar}\left[\underline{\hat{A}}\cdot\underline{d}_e,\underline{\hat{p}}_i\cdot\underline{\hat{A}}\right]+\dots\right)\quad , \tag{A.4}$$

where the commutator simplifies to

$$\left[\underline{\hat{A}}\cdot\underline{d}_e,\underline{\hat{p}}_i\cdot\underline{\hat{A}}\right]=\underline{\hat{A}}^2\left[\underline{d}_e,\underline{\hat{p}}_i\right]=-e\underline{\hat{A}}^2\sum_{j=1}^{N_e}\left[\underline{r}_j,\underline{\hat{p}}_i\right]=-e\,\underline{\hat{A}}^2\mathrm{i}\hbar\quad , \tag{A.5}$$

with, $\left[\underline{r}_j,\underline{\hat{p}}_i\right]=\mathrm{i}\hbar\delta_{ij}$, for the last equality. Notably, the result is independent of electronic momenta $\underline{p}_i$, such that the BCH expansion already truncates here as higher order nested commutators vanish identically, *e.g.*, $\left[\underline{\hat{A}}\cdot\underline{d}_e,\left[\underline{\hat{A}}\cdot\underline{d}_e,\underline{\hat{p}}_i\cdot\underline{\hat{A}}\right]\right]=0$. Hence, one finds for Eq.(A.4) with the result (A.5), that

$$\frac{e}{m_e}\hat{\mathcal{U}}_e^\dagger\left(\underline{\hat{p}}_i\cdot\underline{\hat{A}}\right)\hat{\mathcal{U}}_e=\frac{e}{m_e}\underline{\hat{p}}_i\cdot\underline{\hat{A}}-\frac{e^2}{m_e}\underline{\hat{A}}^2\quad . \tag{A.6}$$

Further, we consider the transformation of the bare electronic kinetic energy, which turns with the BCH expansion into

$$\frac{1}{2m_e}\hat{\mathcal{U}}_e^\dagger\,\underline{\hat{p}}_i^2\,\hat{\mathcal{U}}_e=\frac{1}{2m_e}\left(\underline{\hat{p}}_i^2-\frac{\mathrm{i}}{\hbar}\left[\underline{\hat{A}}\cdot\underline{d}_e,\underline{\hat{p}}_i^2\right]-\frac{1}{2\hbar^2}\left[\underline{\hat{A}}\cdot\underline{d}_e,\left[\underline{\hat{A}}\cdot\underline{d}_e,\underline{\hat{p}}_i^2\right]\right]\dots\right)\quad . \tag{A.7}$$

For the second term on the right-hand side, it holds that $\left[\underline{\hat{A}}\cdot\underline{d}_e,\underline{\hat{p}}_i^2\right]=\underline{\hat{A}}\cdot\left[\underline{d}_e,\underline{\hat{p}}_i^2\right]$, for which we employ the commutator identity

$$\left[\underline{d}_e,\underline{\hat{p}}_i^2\right]=\left[\underline{d}_e,\underline{\hat{p}}_i\right]\underline{\hat{p}}_i+\underline{\hat{p}}_i\left[\underline{d}_e,\underline{\hat{p}}_i\right]=-2\,e\,\mathrm{i}\hbar\,\underline{\hat{p}}_i\quad . \tag{A.8}$$

Here, we used, $\left[\underline{d}_e,\underline{\hat{p}}_i\right]=-e\,\mathrm{i}\hbar$, for the second equality as found in Eq.(A.5). Accordingly, the first-order term in Eq.(A.7) turns into

$$-\frac{\mathrm{i}}{2m_e\hbar}\underline{\hat{A}}\cdot\left[\underline{d}_e,\underline{\hat{p}}_i^2\right]=-\frac{e}{m_e}\underline{\hat{p}}_i\cdot\underline{\hat{A}}\quad . \tag{A.9}$$

With this result, we are now in the position to evaluate the nested, second-order commutator as

$$\left[\underline{\hat{A}}\cdot\underline{d}_e,\left[\underline{\hat{A}}\cdot\underline{d}_e,\underline{\hat{p}}_i^2\right]\right]=\underline{\hat{A}}^2\left[\underline{d}_e,\left[\underline{d}_e,\underline{\hat{p}}_i^2\right]\right]\quad , \tag{A.10}$$

$$=-2\,e\,\mathrm{i}\hbar\,\underline{\hat{A}}^2\left[\underline{d}_e,\underline{\hat{p}}_i\right]\quad , \tag{A.11}$$

$$=-2\,e^2\,\hbar^2\,\underline{\hat{A}}^2\quad . \tag{A.12}$$

As the second order commutator results in an expression independent of electronic momenta, the BCH-expansion truncates here. Hence, we obtain

$$-\frac{1}{4m_e\hbar^2}\left[\hat{\underline{A}}\cdot\underline{d}_e,\left[\hat{\underline{A}}\cdot\underline{d}_e,\hat{\underline{p}}_i^2\right]\right]=\frac{e^2}{2m_e}\,\hat{\underline{A}}^2 \quad , \tag{A.13}$$

and finally for the transformed bare electronic KEO

$$\frac{1}{2m_e}\hat{\mathcal{U}}_e^\dagger\,\hat{\underline{p}}_i^2\,\hat{\mathcal{U}}_e=\frac{\hat{\underline{p}}_i^2}{2m_e}-\frac{e}{m_e}\,\hat{\underline{p}}_i\cdot\hat{\underline{A}}+\frac{e^2}{2m_e}\,\hat{\underline{A}}^2 \quad . \tag{A.14}$$

By collecting expressions in Eqs.(A.3), (A.6) and (A.14),

$$\begin{aligned}
\frac{1}{2m_e}\hat{\mathcal{U}}_e^\dagger\,\hat{\underline{p}}_i^2\,\hat{\mathcal{U}}_e &= \frac{\hat{\underline{p}}_i^2}{2m_e}-\frac{e}{m_e}\,\hat{\underline{p}}_i\cdot\hat{\underline{A}}+\frac{e^2}{2m_e}\,\hat{\underline{A}}^2 \quad , \\
\frac{e}{m_e}\hat{\mathcal{U}}_e^\dagger\left(\hat{\underline{p}}_i\cdot\hat{\underline{A}}\right)\hat{\mathcal{U}}_e &= \frac{e}{m_e}\,\hat{\underline{p}}_i\cdot\hat{\underline{A}}-\frac{e^2}{m_e}\hat{\underline{A}}^2 \quad , \\
\frac{e^2}{2m_e}\hat{\mathcal{U}}_e^\dagger\hat{\underline{A}}^2\hat{\mathcal{U}}_e &= \frac{e^2}{2m_e}\hat{\underline{A}}^2 \quad ,
\end{aligned} \tag{A.15}$$

one finds, that

$$\hat{\mathcal{U}}_e^\dagger\left(\sum_{i=1}^{N_e}\frac{\left(\hat{\underline{p}}_i+e\,\hat{\underline{A}}\right)^2}{2m_e}\right)\hat{\mathcal{U}}_e=\sum_{i=1}^{N_e}\frac{\hat{\underline{p}}_i^2}{2m_e} \quad . \tag{A.16}$$

The same reasoning holds for the transformation of the nuclear contribution to the KEO in the minimal-coupling Pauli-Fierz Hamiltionian Eq.(2.27), which leads to Eq.(2.36).

A.2 PZW-Transformation of Cavity Mode Hamiltonian

We now consider the transformation properties of the cavity Hamiltonian, with

$$\hat{\mathcal{U}}^\dagger\hat{H}_C\hat{\mathcal{U}}=\sum_{\lambda,k}\hbar\omega_k\left(\hat{\mathcal{U}}^\dagger\hat{a}_{\lambda k}^\dagger\hat{a}_{\lambda k}\hat{\mathcal{U}}+\frac{1}{2}\right) \quad , \tag{A.17}$$

and as the PZW-transformation is unitary, it holds that

$$\hat{\mathcal{U}}^\dagger\hat{a}_{\lambda k}^\dagger\hat{a}_{\lambda k}\hat{\mathcal{U}}=\left(\hat{\mathcal{U}}^\dagger\hat{a}_{\lambda k}^\dagger\hat{\mathcal{U}}\right)\left(\hat{\mathcal{U}}^\dagger\hat{a}_{\lambda k}\hat{\mathcal{U}}\right) \quad . \tag{A.18}$$

For the first factor, we find with the BCH-expansion

$$\hat{\mathcal{U}}^\dagger\hat{a}_{\lambda k}^\dagger\hat{\mathcal{U}}=\hat{a}_{\lambda k}^\dagger-\frac{\mathrm{i}}{\hbar}\left[\underline{d}\cdot\underline{A},\hat{a}_{\lambda k}^\dagger\right]+\ldots \quad , \tag{A.19}$$

and obtain with $\left[\underline{d}\cdot\underline{A},\hat{a}^\dagger_{\lambda k}\right]=\underline{d}\cdot\left[\underline{A},\hat{a}^\dagger_{\lambda k}\right]$ and Eq.(A.1) for the commutator

$$\left[\underline{A},\hat{a}^\dagger_{\lambda k}\right]=\sum_{\lambda',k'}\frac{\underline{e}_{\lambda' k'}}{\omega'_k}\sqrt{\frac{\hbar\omega'_k}{2\epsilon_0 V_c}}\left(\left[\hat{a}_{\lambda' k'},\hat{a}^\dagger_{\lambda k}\right]+\left[\hat{a}^\dagger_{\lambda' k'},\hat{a}^\dagger_{\lambda k}\right]\right) \quad , \tag{A.20}$$

$$=\frac{\underline{e}_{\lambda k}}{\omega_k}\sqrt{\frac{\hbar\omega_k}{2\epsilon_0 V_c}} \quad , \tag{A.21}$$

where we used the canonical commutation relation Eq.(2.30) to obtain the second line. Hence, the BCH-expansion in Eq.(A.19) truncates at first order and we find for Eq.(A.19)

$$\hat{\mathcal{U}}^\dagger\hat{a}^\dagger_{\lambda k}\hat{\mathcal{U}}=\hat{a}^\dagger_{\lambda k}-\frac{\mathrm{i}}{\hbar\omega_k}\sqrt{\frac{\hbar\omega_k}{2\epsilon_0 V_c}}\left(\underline{e}_{\lambda k}\cdot\underline{d}\right) \quad , \tag{A.22}$$

and immediately as hermitian conjugate

$$\hat{\mathcal{U}}^\dagger\hat{a}_{\lambda k}\hat{\mathcal{U}}=\hat{a}_{\lambda k}+\frac{\mathrm{i}}{\hbar\omega_k}\sqrt{\frac{\hbar\omega_k}{2\epsilon_0 V_c}}\left(\underline{e}_{\lambda k}\cdot\underline{d}\right) \quad . \tag{A.23}$$

With Eq.(2.42), we accordingly have

$$\hat{\mathcal{U}}^\dagger\hat{H}_C\hat{\mathcal{U}}=\sum_{\lambda,k}\left[\hbar\omega_k\left(\hat{a}^\dagger_{\lambda k}-\frac{\mathrm{i}\,g_k}{\hbar\omega_k}\left(\underline{e}_{\lambda k}\cdot\underline{d}\right)\right)\left(\hat{a}_{\lambda k}+\frac{\mathrm{i}\,g_k}{\hbar\omega_k}\left(\underline{e}_{\lambda k}\cdot\underline{d}\right)\right)+\frac{\hbar\omega_k}{2}\right] \quad , \tag{A.24}$$

which reads after expansion

$$\hat{\mathcal{U}}^\dagger\hat{H}_C\hat{\mathcal{U}} \;=\; \sum_{\lambda,k}\left[\hbar\omega_k\left(\hat{a}^\dagger_{\lambda k}\hat{a}_{\lambda k}+\frac{1}{2}\right)+\mathrm{i}\,g_k\left(\underline{e}_{\lambda k}\cdot\underline{d}\right)\left(\hat{a}^\dagger_{\lambda k}-\hat{a}_{\lambda k}\right)+\frac{g_k^2}{\hbar\omega_k}\left(\underline{e}_{\lambda k}\cdot\underline{d}\right)^2\right] \quad . \tag{A.25}$$

The second term resembles the imaginary light-matter interaction, which can be written in terms of the quantized transvers component of the cavity electrical field in the dipole approximation, $\underline{\hat{E}}$, as

$$-\underline{d}\cdot\underline{\hat{E}}=-\underline{d}\cdot\underbrace{\left(\mathrm{i}\sum_{\lambda,k}\underline{e}_{\lambda k}\,g_k\left(\hat{a}_{\lambda k}-\hat{a}^\dagger_{\lambda k}\right)\right)}_{=\underline{\hat{E}}} \quad . \tag{A.26}$$

Finally, to obtain the expression in Eq.(2.37), one additionally considers the unitary rotation mediated by $\hat{S}$ in Eq.(2.39), which factorizes for every mode with, $\hat{S}_{\lambda k}=e^{\mathrm{i}\frac{\pi}{2}\hat{n}_{\lambda k}}$, where, $\hat{n}_{\lambda k}=\hat{a}^\dagger_{\lambda k}\hat{a}_{\lambda k}$, is a single cavity mode number operator. Further, we employ the BCH-expansion to obtain

$$\hat{S}^\dagger_{\lambda k}\hat{a}^\dagger_{\lambda k}\hat{S}_{\lambda k}=\hat{a}^\dagger_{\lambda k}-\left(\mathrm{i}\,\frac{\pi}{2}\right)\left[\hat{n}_{\lambda k},\hat{a}^\dagger_{\lambda k}\right]+\frac{1}{2!}\left(-\mathrm{i}\,\frac{\pi}{2}\right)^2\left[\hat{n}_{\lambda k},\left[\hat{n}_{\lambda k},\hat{a}^\dagger_{\lambda k}\right]\right]+\ldots \quad , \tag{A.27}$$

$$=\hat{a}^\dagger_{\lambda k}\left(1-\left(\mathrm{i}\,\frac{\pi}{2}\right)+\frac{1}{2!}\left(-\mathrm{i}\,\frac{\pi}{2}\right)^2+\ldots\right) \tag{A.28}$$

$$=\hat{a}^\dagger_{\lambda k}\,e^{-\mathrm{i}\frac{\pi}{2}} \quad . \tag{A.29}$$

Accordingly, we have

$$\hat{S}^{\dagger}_{\lambda k}\hat{a}^{\dagger}_{\lambda k}\hat{S}_{\lambda k} = -\mathrm{i}\,\hat{a}^{\dagger}_{\lambda k} \quad , \quad \hat{S}^{\dagger}_{\lambda k}\hat{a}_{\lambda k}\hat{S}_{\lambda k} = \mathrm{i}\,\hat{a}_{\lambda k} \quad . \tag{A.30}$$

The first and third term in Eq.(A.25) are invariant under this unitary transformation, whereas the second term turns into

$$\sum_{\lambda,k} \mathrm{i}\, g_k \Big(\underline{e}_{\lambda k} \cdot \underline{d} \Big) \Big(\hat{S}^{\dagger}_{\lambda k}\hat{a}^{\dagger}_{\lambda k}\hat{S}_{\lambda k} - \hat{S}^{\dagger}_{\lambda k}\hat{a}_{\lambda k}\hat{S}_{\lambda k} \Big) = \sum_{\lambda,k} g_k \Big(\underline{e}_{\lambda k} \cdot \underline{d} \Big) \Big(\hat{a}^{\dagger}_{\lambda k} + \hat{a}_{\lambda k} \Big) \quad , \tag{A.31}$$

as given in Eq.(2.37), respectively.

B Numerical Details on CRP-ABC

Here, we provide numerical details on the cumulative reaction probability with absorbing boundary conditions (CRP-ABC) approach as employed in Sec.3.4 of Ch.3. We consider a Colbert-Miller DVR[173] of the vibrational Pauli-Fierz Hamiltonian, $\hat{H}$, the corresponding Green's function, $\hat{G}$, and the complex absorbing potential, $\hat{\Gamma}$, in order to compute cumulative reaction probabilities, $N(E)$. For the cavity-altered ammonia inversion model, the matrix elements of the DVR-Hamiltonian read

$$\big(\underline{\underline{H}}\big)_{ii'jj'} = T^{m}_{ii'}\delta_{jj'} + T^{c}_{jj'}\delta_{ii'} + V(q_i, x_{cj})\,\delta_{ii'}\delta_{jj'} \quad , \tag{B.1}$$

with $i, i' = 1, \ldots, N_q$ and $j, j' = 1, \ldots, N_c$ for the molecular coordinate and cavity coordinate grid, respectively. Further, the KEO takes in the Colbert-Miller DVR the form[173]

$$T^{a}_{ii'} = \frac{\hbar^2}{2\Delta s_a^2}\,(-1)^{i-i'} \begin{cases} \dfrac{\pi^2}{3}, & i = i' \\ \dfrac{2}{(i-i')^2}, & i \neq i' \end{cases} \quad , \tag{B.2}$$

for coordinates, $s_a = (q, x_c)$. Each coordinate is discretized on an equidistant grid with $q_i = i\,\Delta q$, $x_{cj} = j\,\Delta x_c$ and $i, j = 0, \pm 1, \pm 2, \ldots, \pm\frac{N_s}{2}$, where $N_s = N_q, N_c$ is the number of DVR grid points for the respective DoF. For the cumulative reaction probability, $N(E, \eta)$, one has in DVR

$$N(E, \eta) = \mathrm{tr}\{\underline{\underline{\Gamma}}_R\,\underline{\underline{G}}\,\underline{\underline{\Gamma}}_P\,\underline{\underline{G}}^{\dagger}\} \quad , \tag{B.3}$$

with, $\underline{\underline{\Gamma}}_R$ and $\underline{\underline{\Gamma}}_P$, being matrix representations of reactant and product CAPs, while $\underline{\underline{G}}$ is the matrix representation of the Green's function, respectively. In particular, $\underline{\underline{\Gamma}}_R$ and $\underline{\underline{\Gamma}}_P$ are matrix representations of the reactant and product absorbers $\hat{\Gamma}_R$ and $\hat{\Gamma}_P$, which were introduced in Eq.((2.100)), with defined as

$$\hat{\Gamma}_P = \theta_P[f]\,\hat{\Gamma}\,, \quad \hat{\Gamma}_R = \theta_R[f]\,\hat{\Gamma} \quad , \tag{B.4}$$

where $\theta_P[f] = \theta[f(q, x_c)]$ is the Heaviside step function, such that $\theta_R[f] = (1 - \theta_P[f])$. The step function depends on a coordinate dependent function $f(q, x_c)$, which specifies a

separating surface between reactant and product regions on the cPES *via* the condition $f(q, x_c) = 0$[114]. The DVR of the absorbing potentials are given by

$$\Gamma^R_{ii'jj'} = \theta^R_{ii}\,\Gamma^m_{ii'}\,\delta_{jj'} + \theta^R_{ii}\,\Gamma^c_{jj'} \quad , \tag{B.5}$$

$$\Gamma^P_{ii'jj'} = \theta^P_{ii}\,\Gamma^m_{ii'}\,\delta_{jj'} + \theta^P_{ii}\,\Gamma^c_{jj'} \quad , \tag{B.6}$$

where we choose $f(q, x_c) = q$ and

$$\Gamma^m(q) = \frac{4\,k_0}{1 + \exp\left((q_m - q)/k_1\right)} + \frac{4\,k_0}{1 + \exp\left((q_m + q)/k_1\right)} \quad , \tag{B.7}$$

$$\Gamma^c(x_c) = \Gamma^c_0\,\frac{(x_c - x_{c0})^n}{(x_{cm} - x_{c0})^n} \quad . \tag{B.8}$$

The CAPs define two stripes along the q-coordinate, in which it increases from 0 in the interval $[q^i_0, q^+_0]$ in a smoothed-step like fashion to some finite value (k_0) at larger $|q|$. Additionally, the CAPs are turned on along x_c in a quartic-power fashion. After performing the trace, $N(E, \eta)$ can be written as

$$N(E, \eta) = \sum_{i=1}^{N}\sum_{j=1}^{N} \Gamma^R_{ii}\,|G_{ij}|^2\,\Gamma^P_{jj} \quad , \tag{B.9}$$

with $N = N_q\,N_c$, *i.e.*, only matrix elements, G_{ij}, coupling grid points in the reactant and product stripes contribute.

Convergence has been reached with parameters $k_0 = 0.08\,E_h$, $k_1 = 0.1\,a_0$, $q_m = 0.75\,a_0$ for Eq.(B.7) and $\Gamma^c_0 = 0.09\,E_h$, $n = 4$, $x_{c0} = 0.0\,\sqrt{m_e}\,a_0$, $x_{cm} = 200\,\sqrt{m_e}\,a_0$ for Eq.(B.8). The thermal rate constant, $k(T, \eta)$ as defined in Eq.(2.96), is numerically evaluated *via* the composite trapezoidal rule. An energy interval $[E_0, E_1]$ has been chosen with $E_0 = 0$ and $E_1 = 5\,E^a_{cl} = 10149\,\mathrm{cm}^{-1}$, and discretized via $N_e = 30$ equidistant grid points with spacing $\Delta E = E_1/N_e$. All numerical results for CRP and corresponding rates have been obtained by means of a private code based on the NumPy library, version 1.20, of Python version 3.8.

C Details on Relaxation Rates and Energy Current

C.1 Fermi's Golden Rule One-Phonon Relaxation Rates

Relaxation rates following Fermi's Golden Rule for one-phonon transitions in the open-system LvN-equation in Lindblad form (2.75) at $T = 0$ K are given by[205, 207]

$$\gamma_v = \pi\,|q_{vv-1}|^2 \sum_{k=1}^{N_B} \frac{c_k^2}{\omega_k}\,\delta(\Delta\varepsilon_{vv-1} - \hbar\omega_k) \quad , \tag{C.1}$$

with coupling coefficients, c_k, harmonic bath frequencies, ω_k, and vibrational transition matrix elements

$$q_{vv-1} = \langle v|q|v-1\rangle \quad . \tag{C.2}$$

The Dirac delta function, $\delta(\Delta\varepsilon_{vv-1}-\hbar\omega_k)$, depends on both the energy difference, $\Delta\varepsilon_{vv-1} = \varepsilon_v-\varepsilon_{v-1}$, between two system eigenstates $|v\rangle$ and $|v-1\rangle$ and the harmonic bath frequencies, ω_k. We approximate $\delta(\Delta\varepsilon_{vv-1}-\hbar\omega_k)$ by a Lorentzian

$$\delta(\Delta\varepsilon_{vv-1}-\hbar\omega_k) \approx \frac{1}{\pi}\frac{\sigma}{\sigma^2+(\Delta\varepsilon_{vv-1}-\hbar\omega_k)^2} \quad , \tag{C.3}$$

where we chose a finite width of, $\sigma = 10\,\mathrm{cm}^{-1}$, following Ref.[207]. Here, only next-neighbor transitions $v \to v-1$ are considered in the rate expressions, *i.e.*, overtone transitions, $v \to v-2, v-3\ldots$, are neglected. These overtone transition rates were found to be several orders of magnitude smaller than the fundamental transitions and were therefore neglected.

C.2 Derivations of the System Energy Current

We derive expressions of the system energy current for the full system-bath dynamics and the reduced Markovian dynamics described by the Liouville-von Neumann equation in Lindblad form.

Non-Markovian System Energy Current

The non-Markovian system energy current for the full system-bath quantum dynamics can be written, with the definition in Eq.(2.80), as

$$\mathcal{J}_S(t) = \frac{\partial}{\partial t}\mathrm{tr}_S\{\hat{\rho}_S(t)\hat{H}_S\} = \sum_{v=0}^{N_S-1}\varepsilon_v\frac{\partial\rho_{vv}(t)}{\partial t} \quad , \tag{C.4}$$

where the trace $\mathrm{tr}_S\{\ldots\}$ runs over the system energy eigenstates, $|v\rangle$, and we employed, $\hat{H}_S = \sum_v \varepsilon_v |v\rangle\langle v|$. Here, $\rho_{vv}(t)$ are vibrational populations for the full non-Markovian system-bath dynamics and ε_v are eigenenergies of the vibrational system, respectively. We note, Eq.(C.4) holds in principle for arbitrary populations obtained from both non-Markovian and Markovian approaches.

Markovian System Energy Current

The Markovian system energy current is derived from the Liouville-von Neumann equation in Lindblad form (2.75). We rewrite the latter in compact form as

$$\frac{\partial}{\partial t}\hat{\rho}_S(t) = \mathcal{L}\,\hat{\rho}_S(t) \quad , \tag{C.5}$$

with Lindblad-Liouvillian, $\mathcal{L} = \mathcal{L}_0 + \mathcal{L}_D$, comprising the unitary part $\mathcal{L}_0$ and $\mathcal{L}_D$ the dissipative part on the r.h.s of Eq.(C.5). Following the same argument as in the last section, we find

$$\mathcal{J}_L(t) = \frac{\partial}{\partial t}\mathrm{tr}_S\{\hat{\rho}_S(t)\hat{H}_S\} = \mathrm{tr}_S\{\frac{\partial}{\partial t}\hat{\rho}_S(t)\hat{H}_S\} \quad , \tag{C.6}$$

as $\hat{H}_S$ is not explicitly time-dependent. Accordingly, we have with Eq.(C.5)

$$\mathcal{J}_L(t) = \mathrm{tr}_S\{\hat{H}_S\,\mathcal{L}\,\hat{\rho}_S(t)\} \quad , \tag{C.7}$$

which turns with the explicit form of, $\mathcal{L}$, taking into account energy-conservation of the unitary part, into

$$\mathcal{J}_L(t) = \mathrm{tr}_S\{\hat{H}_S \sum_v \gamma_v \left(\hat{C}_v\hat{\rho}_S(t)\hat{C}_v^\dagger - \frac{1}{2}[\hat{C}_v^\dagger\hat{C}_v\ \hat{\rho}_S(t)]_+\right)\} \quad . \tag{C.8}$$

Expanding the latter equation gives

$$\mathcal{J}_L(t) = \sum_{v=1} \gamma_v\,\mathrm{tr}_S\{\hat{H}_S\,\hat{C}_v\hat{\rho}_S(t)\hat{C}_v^\dagger\} - \sum_{v=1}\frac{\gamma_v}{2}\,\mathrm{tr}_S\{\hat{H}_S\,\hat{C}_v^\dagger\hat{C}_v\,\hat{\rho}_S(t)\} - \sum_{v=1}\frac{\gamma_v}{2}\,\mathrm{tr}_S\{\hat{H}_S\,\hat{\rho}_S(t)\hat{C}_v^\dagger\hat{C}_v\} \quad , \tag{C.9}$$

which turns with $\hat{H}_S = \sum_v \varepsilon_v\,|v\rangle\,\langle v|$ after performing the traces into

$$\mathcal{J}_L(t) = \sum_{v=1}\gamma_v\,\varepsilon_{v-1}\,\rho_{vv}(t) - \sum_{v=1}\frac{\gamma_v}{2}\,\varepsilon_v\,\rho_{vv}(t) - \sum_{v=1}\frac{\gamma_v}{2}\,\varepsilon_v\,\rho_{vv}(t) \quad . \tag{C.10}$$

The desired result is finally obtained as

$$\mathcal{J}_L(t) = -\sum_{v=1}\gamma_v\,\Delta\varepsilon_v\,\rho_{vv}(t) \quad , \tag{C.11}$$

with, $\Delta\varepsilon_v = \varepsilon_v - \varepsilon_{v-1}$, and properties

$$\mathcal{J}_L(t) \leq 0,\ \forall t \geq 0 \quad , \quad \mathcal{J}_L(0) = -\gamma_{v_0}\,\Delta\varepsilon_{v_0} \quad . \tag{C.12}$$

In the "ideal scaling" case (linear oscillator bilinearly coupled to a harmonic bath), we have, $\gamma_{v_0} = \gamma_1 v_0$, and thus ($\rho_{v_0 v_0} = 1$), the initial energy current is, $\mathcal{J}_L(0) \propto v_0$.

D Details on TQP Vibronic Coupling Hamiltonian

Here, we provide explicit expressions for terms in TQP vibronic coupling Hamiltonians, Eq.(5.19) and Eq.(5.20), as discussed in Ch.5. The normal mode TQP Hamiltonian reads

$$\bar{H}_\beta^{(0)} = \sum_{k\in\mathcal{M}_4}\hbar\omega_k\left(\hat{b}_k^\dagger\hat{b}_k - \tilde{b}_k^\dagger\tilde{b}_k\right) \quad , \tag{D.1}$$

with normal mode frequencies, ω_k. The linear intra-state vibronic coupling term involving tuning modes is given by

$$\bar{H}_{\beta,i}^{(1)} = \sum_{k\in\mathcal{M}_t}\frac{a_k^{(i)}}{\sqrt{2}}\left(\cosh\theta_k\left(\hat{b}_k^\dagger + \hat{b}_k\right) + \sinh\theta_k\left(\tilde{b}_k^\dagger + \tilde{b}_k\right)\right) \quad , \tag{D.2}$$

with linear coupling coefficients, $a_k^{(i)}$. Further, the bilinear intra-state vibronic coupling contribution reads

$$\begin{aligned}\bar{H}^{(2)}_{\beta,i} = \sum_{k,k'\in\mathcal{M}_t} \frac{a^{(i)}_{kk'}}{2}\Big(&\cosh\theta_k\cosh\theta_{k'}\left(\hat{b}^\dagger_k+\hat{b}_k\right)\left(\hat{b}^\dagger_{k'}+\hat{b}_{k'}\right)\\ &+\cosh\theta_k\sinh\theta_{k'}\left(\hat{b}^\dagger_k+\hat{b}_k\right)\left(\tilde{b}^\dagger_{k'}+\tilde{b}_{k'}\right)\\ &+\sinh\theta_k\cosh\theta_{k'}\left(\tilde{b}^\dagger_k+\tilde{b}_k\right)\left(\hat{b}^\dagger_{k'}+\hat{b}_{k'}\right)\\ &+\sinh\theta_k\sinh\theta_{k'}\left(\tilde{b}^\dagger_k+\tilde{b}_k\right)\left(\tilde{b}^\dagger_{k'}+\tilde{b}_{k'}\right)\Big) \quad , \end{aligned} \tag{D.3}$$

with bilinear couplings, $a^{(i)}_{kk'}$, respectively. Notably, $\bar{H}^{(2)}_{\beta,i}$ couples physical and auxiliary DoF via the second and third terms. Next, the linear vibronic coupling contribution reads

$$\hat{V}^{(1)}_\beta = \frac{c_{10a}}{\sqrt{2}}\left(\cosh\theta_{10a}\left(\hat{b}^\dagger_{10a}+\hat{b}_{10a}\right)+\sinh\theta_{10a}\left(\tilde{b}^\dagger_{10a}+\tilde{b}_{10a}\right)\right) \tag{D.4}$$

and the quadratic vibronic coupling term is given by

$$\begin{aligned}\hat{V}^{(2)}_{\beta,i} = \sum_{k\in\mathcal{M}_t} \frac{c_{10a,k}}{2}\Big(&\cosh\theta_{10a}\cosh\theta_{k'}\left(\hat{b}^\dagger_{10a}+\hat{b}_{10a}\right)\left(\hat{b}^\dagger_{k'}+\hat{b}_{k'}\right)\\ &+\cosh\theta_{10a}\sinh\theta_{k'}\left(\hat{b}^\dagger_{10a}+\hat{b}_{10a}\right)\left(\tilde{b}^\dagger_{k'}+\tilde{b}_{k'}\right)\\ &+\sinh\theta_{10a}\cosh\theta_{k'}\left(\tilde{b}^\dagger_{10a}+\tilde{b}_{10a}\right)\left(\hat{b}^\dagger_{k'}+\hat{b}_{k'}\right)\\ &+\sinh\theta_{10a}\sinh\theta_{k'}\left(\tilde{b}^\dagger_{10a}+\tilde{b}_{10a}\right)\left(\tilde{b}^\dagger_{k'}+\tilde{b}_{k'}\right)\Big) \quad . \end{aligned} \tag{D.5}$$

Again, the quadratic contribution, $\hat{V}^{(2)}_{\beta,i}$, couples physical and auxiliary DoF of the coupling mode to the respective tuning mode DoF. All parameters $\Delta, \omega_k, a^{(i)}_k, a^{(i)}_{kk'}, c_{10a}$ and $c_{10a,k}$ in Eq.(5.19) have been taken from Ref.[279]. For the extended system-bath Hamiltonian in Eq.(5.20), the diagonal contribution is augmented by a bilinear system-bath interaction

$$\hat{H}^{(SB)}_{\beta,i} = \sum_{k=1}^{20}\frac{\kappa^{(i)}_k}{\sqrt{2}}\left(\cosh_{b,k}\left(\hat{b}^\dagger_{b,k}+\hat{b}_{b,k}\right)+\sinh_{b,k}\left(\tilde{b}^\dagger_{b,k}+\tilde{b}_{b,k}\right)\right) \quad , \tag{D.6}$$

with linear coupling coefficients, $\kappa^{(i)}_k$, as well as physical, $\hat{b}^\dagger_{b,k}$ and $\hat{b}_{b,k}$, and auxiliary, $\tilde{b}^\dagger_{b,k}$ and $\tilde{b}_{b,k}$, bath creation and annihilation operators, respectively. The corresponding twenty-mode TQP bath Hamiltonian reads

$$\bar{H}^{(B)}_\beta = \sum_{k=1}^{20}\hbar\omega_{b,k}\left(\hat{b}^\dagger_{b,k}\hat{b}_{b,k}-\tilde{b}^\dagger_{b,k}\tilde{b}_{b,k}\right) \quad , \tag{D.7}$$

with bath mode frequencies, $\omega_{b,k}$, respectively. The latter frequencies and linear coupling coefficients, $\kappa^{(i)}_k$, in $\hat{H}^{(SB)}_{\beta,i}$ haven been taken from Ref.[278].

E Abbreviations

KEO	Kinetic energy operator
TISE	Time-independent Schrödinger equation
PES	Potential energy surfaces
BOA	Born-Oppenheimer approximation
DoF	Degrees of freedom
FCI	Full configuration interaction
HF	Hartree-Fock
CI	Configuration interaction
CIS	Configuration interaction singles
CISD	Configuration interaction singles doubles
CC	Coupled cluster
CCS	Coupled cluster singles
CCSD	Coupled cluster singles doubles
CCSD(T)	Coupled cluster singles doubles with perturbative triples
DFT	Density functional theory
HK	Hohenberg-Kohn
HK-1	First Hohenberg-Kohn theorem
HK-2	Second Hohenberg-Kohn theorem
KS-DFT	Kohn-Sham density functional theory
LDA	Local density approximation
GGA	Generalized gradient approximation
PZW	Power-Zienau-Woolley
DSE	Dipole self-energy
cQED	Cavity quantum electrodynamics
VSC	Vibrational strong coupling
VUSC	Vibrational ultrastrong coupling
cBO	Cavity Born-Oppenheimer
cBOA	Cavity Born-Oppenheimer approximation
cPES	Cavity potential energy surface
QEDFT	Quantum electrodynamical density-functional theory
QED	Quantum electrodynamics
TDSE	Time-dependent Schrödinger equation
CoD	Curse of dimensionality
MCTDH	Multiconfigurational time-dependent Hartree
ML-MCTDH	Multilayer multiconfigurational time-dependent Hartree

LvN	Liouville-von Neumann
SPFs	Singe-particle functions
EoM	Equations of motion
DFVP	Dirac-Frenkel variational principle
DVR	discrete variable representation
SQR	second quantization representation
TTNS	Tree tensor network states
BIR	Block-improved relaxation
SPDOs	Single-particle density operators
CRP	Cumulative reaction probability
ABC	Absorbing boundary conditions
CAP	Complex absorbing potential
TST	Transition state theory
ESC	Electronic strong coupling
HO	Harmonic oscillator
IR	Infrared
VPCI	Vibro-polaritonic conical intersection
MEP	Minimum energy path
cMEP	Cavity minimum energy path
QM/MM	Quantum mechanics/molecular mechanics
RWA	Rotating wave approximation
HEM	Hierarchical effective mode
mD2	multi-Davydov D2
TFD	Thermofield dynamics
TF-TDSE	Thermofield time-dependent Schrödinger equation
TQP	Thermal quasi-particle
TBT	Thermal Bogoliubov transformation
tSPFs	Thermal singe-particle functions
BCH	Baker-Campbell-Hausdorff

Acknowledgements

Ich danke Prof. Dr. Peter Saalfrank, dass ich meine Doktorarbeit zu einem sehr spannenden und aktuellen Themengebiet in seiner Gruppe anfertigen durfte, sowie für die uneingeschränkte Freiheit und Unterstützung meiner Arbeitsweise und meines wissenschaftlichen Interesses. Ich danke Prof. Dr. Jean Christophe Tremblay, ohne den ich den Weg nach Potsdam vermutlich nicht gefunden hätte. Weiterhin danke ich Prof. Dr. Oriol Vendrell und Prof. Dr. Oliver Kühn für ihre Bereitschaft und ihr Interesse meine Dissertation zu begutachten.

Prof. Dr. Tillmann Klamroth danke ich für seinen uneingeschränkten technischen Support sowie für seine für alle meine Fragen immer offen stehenden Ohren. Weiterhin danke ich Prof. Dr. Hans-Dieter Meyer dafür meine Begeisterung für den MCTDH Ansatz geweckt zu haben sowie für jegliche Unterstützung zu diesem.

Als Teil des AKs Theoretische Chemie haben einige (ehemalige) Mitglieder auf ihre Art und Weise zu dieser Arbeit beigetragen, denen ich hier danken möchte. Dr. Giacomo Melani für seine uneingeschränkte Unterstützung und Motivation von Anfang an, für seine unnachahmlich offenherzige Art sowie für eine super Zeit zusammen mit Florian Bedurke in D.2.17. Dr. Foudhil Bouakline für viele Diskussionen, sein offenes Ohr sowie seine Hilfe zu allen möglichen wissenschaftlichen Fragen. Shreya Sinha für viele schöne Teestunden, Diskussionen und Blockkurse. Alkit Beqiraj für alle schönen Diskussionen über alles, beigelegte Dispute und Stunden beim JCF. Dr. David Picconi für seine Begeisterung und Hilfe zu G-MCTDH sowie Dr. Evgenii Titov für sehr hilfreiche Diskussionen. Ebenso danke ich insbesondere auch Kerstin Faustmann, Galina Jurchenko und Rainer Neumann, die in allen Belangen immer mit einer helfenden Hand zur Stelle sind.

Ich bin weiterhin sehr dankbar ein Mitglied der International Max-Planck Research School des Fritz-Haber Institutes gewesen sein zu dürfen und danke insbesondere Dr. Alex Paarmann, Ines Bressel sowie Bettina Menzel für ihren Einsatz, ihre Unterstützung und anregende Seminare, sowie Manya Hettwer für ihre große Hilfe bei der Organisation von Konferenzreisen.

Meinen Kooperationspartnern Prof. Dr. Frank Grossmann und Dr. Michael Werther danke ich für eine sehr lehrreiche und produktive Zusammenarbeit sowie einen sehr schönen Besuch in Dresden.

Weiterhin danke ich Stefan Foss und Anja Tschiersch für viele schöne Kaffee-/JCF- und

Handballstunden, Simona Riedel für die super Korrektur dieser Arbeit sowie Floyd Hagin und allen Unihandballer:innen für eine sehr spassige Zeit. Ebenso danke ich allen Aktiven beim JCF Potsdam für viele schöne Treffen und Aktionen.
Ein großer Dank geht an Mathias Pfriender, der für mich zur richtigen Zeit am richtigen Ort ein fantastischer Chemielehrer war.
Zuletzt möchte ich meiner Familie besonderen Dank aussprechen. Zunächst meinen Eltern und Großeltern, die mit ihrer Neugierde und Begeisterung für alles was "vor dem Küchenfenster" geschieht sowie ihrer uneingeschränkten Unterstützung und Offenheit für alles was ich interessant finde auf ihre Art und Weise maßgeblich zur Existenz dieser Arbeit beigetragen haben. Meinem Bruder dafür, dass er in jeder Lebenslage da ist und immer ein offenes Ohr hat. Sabine für jegliche Unterstützung, konstruktive Kritik an dieser Arbeit und alles was es außerhalb der Wissenschaft gibt.

Bibliography

[1] M. Born, K. Huang. *The Dynamical Theory of Crystal Lattices*. Oxford University Press, London, (1954).

[2] L. S. Cederbaum; *Born-Oppenheimer Approximation and Beyond* in *Conical Intersections: Electronic Structure, Dynamics & Spectroscopy* edited by W. Domcke, D. R. Yarkony, K. Köppel, World Scientific, (2004).

[3] H. Köppel; *Diabatic Representation: Methods for the Construction of Diabatic Electronic States* in *Conical Intersections: Electronic Structure, Dynamics & Spectroscopy* edited by W. Domcke, D. R. Yarkony, K. Köppel, World Scientific, (2004).

[4] H. Köppel, W Domcke, L. S. Cederbaum; *The Multi-Mode Vibronic-Coupling Approach* in *Conical Intersections: Electronic Structure, Dynamics & Spectroscopy* edited by W. Domcke, D. R. Yarkony, K. Köppel, World Scientific, (2004).

[5] M. Born, R. Oppenheimer. Zur Quantentheorie der Molekeln. *Ann. d. Phys.* **84**, 30, (1927).

[6] C. J. Ballhausen, A. E. Hansen. Electronic spectra. *Ann. Rev. Phys. Chem.* **23**, 15, (1972).

[7] A. Szabo, N. S. Ostlund. *Modern Quantum Chemistry: Introduction to Advanced Electronic Structure Theory*. Dover Publications, Inc., Mineola, New York, (1996).

[8] T. Helgaker, P. Jørgensen, J. Olsen. *Molecular Electronic-Structure Theory*. Wiley VCH, Weinheim, (2012).

[9] K. Raghavachari, G. W. Trucks, J. A. Pople, M. Head-Gordon. A fifth-order perturbation comparison of electron correlation theories. *Chem. Phys. Lett.* **157**, 479, (1989).

[10] W. Koch, M. C. Holthausen. *A Chemist's Guide to Density Functional Theory*. Wiley VCH, Weinheim, (2001).

[11] A. D. Becke. Density-functional thermochemistry. III. The role of exact exchange. *J. Chem. Phys.* **98**, 5648, (1993).

[12] D. P. Craig, T. Thirunamachandran. *Molecular Quantum Electrodynamics: An Introduction to Radiation Molecule Interactions*, Dover Publications, Inc., Mineola, New York, (1984).

[13] J. Flick, M. Ruggenthaler, H. Appel, A. Rubio. Atoms and molecules in cavities, from weak to strong coupling in quantum-electrodynamics (QED) chemistry. *Proc Natl Acad Sci* **114**, 3026, (2017).

[14] M. Ruggenthaler, J. Flick, C. Pellegrini, H. Appel, I. V. Tokatly, A. Rubio. Quantum-electrodynamical density-functional theory: Bridging quantum optics and electronic-structure theory. *Phys. Rev. A* **90**, 012508, (2014).

[15] C. Schäfer, M. Ruggenthaler, A. Rubio Ab initio nonrelativistic quantum electrodynamics: Bridging quantum chemistry and quantum optics from weak to strong coupling. *Phys. Rev. A* **98**, 043801, (2018).

[16] P.W. Mionni. *An Introduction to Quantum Optics and Quantum Fluctuations*. Oxford University Press, Oxford, (2019).

[17] I. V. Tokatly. Time-dependent density functional theory for many-electron systems interacting with cavity photons. *Phys. Rev. Lett.* **110**, 233001, (2013).

[18] J. Flick, M. Ruggenthaler, H. Appel, A. Rubio. Kohn–Sham approach to quantum electrodynamical density-functional theory: Exact time-dependent effective potentials in real space. *Proc Natl Acad Sci* **112**, 15285, (2015).

[19] C. Pellegrini, J. Flick, I. V. Tokatly, H. Appel, A. Rubio. Optimized Effective Potential for Quantum Electrodynamical Time-Dependent Density Functional Theory. *Phys. Rev. Lett.* **115**, 093001, (2015).

[20] E. A. Power, S. Zienau. Coulomb gauge in non-relativistic quantum electro-dynamics and the shape of spectral lines. *Phil. Trans. R. Soc. Lond. A* **251**, 427, (1959).

[21] R. G. Woolley. Molecular quantum electrodynamics. *Prog. R. Soc. Lond. A* **321**, 557, (1971).

[22] M. Babiker, E. A. Power, T. Thirunamachandran. On a generalization of the Power–Zienau–Woolley transformation in quantum electrodynamics and atomic field equations. *Proc. R. Soc. Lond. A* **338**, 235, (1974).

[23] R. G. Woolley. Power-Zienau-Woolley representations of nonrelativistic QED for atoms and molecules. *Phys. Rev. Res.* **2**, 043835, (2020).

[24] A. Mandal, T. D. Krauss, P. Huo. Polariton-mediated electron transfer via cavity quantum electrodynamics. *J. Chem. Phys. B* **124**, 6321, (2020).

[25] J. Feist, A. I. Fernández-Domínguez, F. J. García-Vidal. Macroscopic QED for quantum nanophotonics: emitter-centered modes as a minimal basis for multiemitter problems. *Nanophotonics* **10**, 477, (2020).

[26] V. Rokaj, D. M. Welakuh, M. Ruggenthaler, A. Rubio. Light–matter interaction in the long-wavelength limit: no ground-state without dipole self-energy. *J. Phys. B: At. Mol. Opt. Phys.* **51**, 034005, (2018).

[27] C. Schäfer, M. Ruggenthaler, V. Rokaj, A. Rubio. Relevance of the quadratic diamagnetic and self-polarization terms in cavity quantum electrodynamics. *ACS Photonics* **7**, 975, (2020).

[28] J. Flick, H. Appel, M. Ruggenthaler, A. Rubio. Cavity Born–Oppenheimer Approximation for Correlated Electron–Nuclear-Photon Systems. *J. Chem. Theory Comput* **13**, 1616, (2017).

[29] E. Jaynes, F. W.Cummings. 63, Comparison of quantum and semiclassical radiation theories with application to the beam maser. *Proc. IEEE* **51**, 89, (1963).

[30] M. Tavis, F. W. Cummings. Exact Solution for an N-Molecule—Radiation-Field Hamiltonian *Phys. Rev.* **170**, 379, (1968).

[31] M. Tavis, F. W. Cummings. Approximate Solutions for an N-Molecule-Radiation-Field Hamiltonian. *Phys. Rev.* **188**, 692, (1969).

[32] A. F. Kockum, A. Miranowicz, S. De Liberato, S. Savasta, F. Nori. Ultrastrong coupling between light and matter. *Nat. Rev. Phys.* **1**, 19, (2019).

[33] D. De Bernardis, P. Pilar, T. Jaako, S. De Liberato, P. Rabl. Breakdown of gauge invariance in ultrastrong-coupling cavity QED. *Phys. Rev. A* **98**, 053819, (2018).

[34] A. Stokes, A. Nazir. Gauge ambiguities imply Jaynes–Cummings physics remains valid in ultrastrong coupling QED. *Nat. Commun.* **10**, 499, (2019).

[35] O. Di Stefano, A. Settineri, V. Macrí, Luigi Garziano, Roberto Stassi, Salvatore Savasta, Franco Nori. Resolution of gauge ambiguities in ultrastrong-coupling cavity Quantum electrodynamics. *Nat. Phys.*, **15**, 803, (2019).

[36] M. A. D. Taylor, A. Manda, W. Zhou, P. Huo. Resolution of gauge ambiguities in molecular cavity quantum electrodynamics. *Phys. Rev. Lett.* **125**, 123602, (2020).

[37] A.Stokes, A.Nazir. Gauge non-invariance due to material truncation in ultrastrong-coupling QED. arXiv:2005.06499, (2020).

[38] A. Vukics, G. Kónya, P.Domokos. The gauge-invariant Lagrangian, the Power–Zienau–Woolley picture, and the choices of field momenta in nonrelativistic quantum electrodynamics. *Sci. Rep.* **11**, 16337, (2021).

[39] M.A.D. Taylor, A. Mandal, P. Huo. Resolving ambiguities of the mode truncation in cavity quantum electrodynamics. *Opt. Lett.* **47**, 1446, (2022).

[40] M. Ruggenthaler, F. Mackenroth, D. Bauer. Time-dependent Kohn-Sham approach to quantum electrodynamics. *Phys. Rev. A* **84**, 042107, (2011).

[41] U. Mordovina, C. Bungey, H. Appel, P. J. Knowles, A. Rubio, F. R. Manby. Polaritonic Coupled-Cluster Theory. *Phys. Rev. Res.* **2**, 023262, (2020).

[42] T. S. Haugland, E. Ronca, E. F. Kjønstad, A. Rubio, H. Koch. Coupled Cluster Theory for Molecular Polaritons: Changing Ground and Excited States. *Phys. Rev. X* **10**, 041043, (2020).

[43] T. S. Haugland, C. Schäfer, E. Ronca, A. Rubio, H. Koch. Intermolecular interactions in optical cavities: An *ab initio* QED study. *J. Chem. Phys.* **154**, 094113, (2021).

[44] A. E. DePrince III. Cavity-Modulated Ionization Potentials and Electron Affinities from Quantum Electrodynamics Coupled-Cluster Theory. *J. Chem. Phys.* **154**, 094112, (2021).

[45] F. Pavŏsević, J. Flick. Polaritonic Unitary Coupled Cluster for Quantum Computations. *J. Phys. Chem. Lett.* **12**, 9100, (2021).

[46] M. D. Liebenthal, N. Vu,A. E. DePrince III. Equation-of-motion Cavity Quantum Electrodynamics Coupled-cluster Theory for Electron Attachment. *J. Chem. Phys.* **156**, 054105, (2022).

[47] R.R. Riso, T.S. Haugland, E. Ronca, H. Koch. Molecular orbital theory in cavity QED environments. *Nat. Commun.* **13**, 1368, (2022).

[48] F. Pavŏsević, S. Hammes-Schiffer, A. Rubio, J. Flick. Cavity-Modulated Proton Transfer Reactions. *J. Am. Chem. Soc.* **11**, 144, (2022).

[49] F. Hernández, F. Herrera. Multi-level quantum Rabi model for anharmonic vibrational polaritons. *J. Chem. Phys.* **151**, 144116, (2019).

[50] J. Flick, D. M. Welakuh, M. Ruggenthaler, H. Appel, A. Rubio. Light–matter response in nonrelativistic quantum electrodynamics. *ACS Photonics* **6**, 2757, (2019).

[51] R. Orus. A Practical Introduction to Tensor Networks: Matrix Product States and Projected Entangled Pair States. *Ann. Phys.* **349**, 117, (2014).

[52] H. Larsson. Computing vibrational eigenstates with tree tensor network states (TTNS). *J. Chem. Phys.* **151**, 204102, (2019).

[53] H. P. Breuer, F. Petruccione. *The Theory of Open Quantum Systems*. Oxford University Press, (2007).

[54] K. Blum. *Density Matrix Theory and Applications*. Springer, Berlin, Heidelberg, (2012).

[55] A. Nitzan. *Chemical Dynamics in Condensed Phases: Relaxation, Transfer, and Reactions in Condensed Molecular Systems*. (Oxford University Press, 2014).

[56] G. Lindblad. On the generators of quantum dynamical semigroups. *Commun. Math. Phys.* **48**, 119, (1976).

[57] V. Gorini, A. Kossakowski, E. C. G. Sudarshan. Completely positive dynamical semigroups of N-level systems. *J. Math. Phys.* **17**, 821, (1976).

[58] K. A. Velizhanin, H. Wang, M. Thoss. Heat transport through model molecular junctions: A multilayer multiconfiguration time-dependent Hartree approac. *Chem. Phys. Lett.* **460**, 325, (2008).

[59] H.-D. Meyer, U. Manthe, L. S. Cederbaum. The multi-configurational time-dependent Hartree approach. *Chem. Phys. Lett.* **165**, 73, (1990).

[60] U. Manthe, H.-D. Meyer, L. S. Cederbaum. Wave-packet dynamics within the multiconfiguration Hartree framework: General aspects and application to NOCl. *J. Chem. Phys.* **97**, 3199, (1992).

[61] M. H. Beck, A. Jäckle, G. A. Worth, H.-D. Meyer. The multiconfiguration time-dependent Hartree (MCTDH) method: a highly efficient algorithm for propagating wavepackets. *Phys. Rep.* **324**, 1, (2000).

[62] *Multidimensional Quantum Dynamics: MCTDH Theory and Applications*, edited by H.-D. Meyer, F. Gatti and G. A. Worth (Wiley VCH, Weinheim, 2009).

[63] H.-D. Meyer. Studying molecular quantumdynamics with themulticonfigurationtime-dependent Hartree method. *WIREs Comput. Mol. Sci.* **2**, 351, (2012).

[64] U. Manthe. The multi-configurational time-dependent Hartree approach revisited. *J. Chem. Phys.* **142**, 244109, (2015).

[65] F. Gatti, B. Lasorne, H.-D. Meyer, A. Nauts. *Applications of Quantum Dynamics in Chemistry*, Springer International Publishing AG, (2017).

[66] K. Balzer, Z. Li, O. Vendrell, M. Eckstein. Multiconfiguration time-dependent Hartree impurity solver for nonequilibrium dynamical mean-field theory. *Phys. Rev. B* **91**, 045136, (2015).

[67] T. G. Kolda, B. W. Bader. Tensor Decompositions and Applications. *SIAM Rev.* **51**, 455, (2009).

[68] H. Wang, M. Thoss. Multilayer formulation of the multiconfiguration time-dependent Hartree theory. *J. Chem. Phys.* **119**, 1289, (2003).

[69] U. Manthe. A multilayer multiconfigurational time-dependent Hartree approach for quantum dynamics on general potential energy surfaces. *J. Chem. Phys* **128**, 164116, (2008).

[70] U. Manthe. Layered discrete variable representations and their application within the multiconfigurational time-dependent Hartree approach. *J. Chem. Phys.* **130**, 054109, (2009).

[71] O. Vendrell, H.-D. Meyer. Multilayer multiconfiguration time-dependent Hartree method: Implementation and applications to a Henon–Heiles Hamiltonian and to pyrazine. *J. Chem. Phys* **134**, 044135, (2011).

[72] H. Wang. Multilayer multiconfiguration time-dependent Hartree theory. *J. Phys. Chem. A* **119**, 7951, (2015).

[73] M. Thoss, H. Wang. Quantum dynamical simulation of ultrafast molecular processes in the condensed phase. *Chem. Phys.* **322**, 210 (2006).

[74] H. Wang, M. Thoss. Quantum-mechanical evaluation of the Boltzmann operator in correlation functions for large molecular systems: A multilayer multiconfiguration time-dependent Hartree approach. *J. Chem. Phys.* **124**, 034114, (2006).

[75] H. Wang, D. E. Skinner, M. Thoss. Calculation of reactive flux correlation functions for systems in a condensed phase environment: A multilayer multiconfiguration time-dependent Hartree approach. *J. Chem. Phys.* **125**, 174502, (2006).

[76] H. Wang, M. Thoss. Quantum dynamical simulation of electron-transfer reactions in an anharmonic environment. *J. Phys. Chem. A* **111**, 10369, (2007).

[77] I. R. Craig, M. Thoss, H. Wang. Proton transfer reactions in model condensed-phase environments: Accurate quantum dynamics using the multilayer multiconfiguration time-dependent Hartree approach. *J. Chem. Phys.* **127**, 144503, (2007).

[78] M. Thoss, I. Kondov, H. Wang. Correlated electron-nuclear dynamics in ultrafast photoinduced electron-transfer reactions at dye-semiconductor interfaces. *Phys. Rev. B* **76**, 153331, (2007).

[79] I. Kondov, M. Thoss, H. Wang. Quantum dynamics of photoinduced electron transfer reactions in dye-semiconductor systems: Description and application to coumarin 343-TiO_2. *J. Phys. Chem. C* **111**, 11970, (2007).

[80] H. Wang, M. Thoss. From coherent motion to localization: dynamics of the spin-boson model at zero temperature. *New J. Phys.* **10**, 115005, (2008).

[81] H. Wang, M. Thoss. From coherent motion to localization: II. Dynamics of the spin-boson model with sub-Ohmic spectral density at zero temperature. *Chem. Phys.* **370**, 78, (2010).

[82] H. Wang, M. Thoss. Numerically exact, time-dependent study of correlated electron transport in model molecular junctions. *J. Chem. Phys.* **138**, 134704, (2013).

[83] H. Wang, M. Thoss. A multilayer multiconfiguration time-dependent Hartree study of the nonequilibrium Anderson impurity model at zero temperature. *Chem. Phys.* **509**, 13, (2018).

[84] G. A. Worth, M. H. Beck, A. Jäckle, and H.-D. Meyer, The MCTDH Package, Version 8.2, 2000; H.-D. Meyer, Version 8.3, 2002; Version 8.4, 2007; O. Vendrell and H.-D. Meyer, Version 8.5, 2013. Version 8.5 contains the ML-MCTDH algorithm. See http://mctdh.uni-hd.de.

[85] J. Zanghellini, M. Kitzler, C. Fabian, T. Brabec, A. Scrinzi. An MCTDHF approach to multielectron dynamics in laser fields. *Laser Phys.* **13**, 1064, (2003).

[86] T. Kato, H. Kono. Time-dependent multiconfiguration theory for electronic dynamics of molecules in an intense laser field. *Chem. Phys. Lett.* **392**, 533, (2004).

[87] M. Nest, T. Klamroth, P. Saalfrank. The multiconfiguration time-dependent Hartree–Fock method for quantum chemical calculations. *J. Chem. Phys.* **122**, 124102, (2005).

[88] O. E. Alon, A. I. Streltsov, L. S. Cederbaum. Multiconfigurational time-dependent Hartree method for bosons: Many-body dynamics of bosonic systems. *Phys. Rev. A* **77**, 033613, (2008).

[89] H. Wang, M. Thoss. Numerically exact quantum dynamics for indistinguishable particles: The multilayer multiconfiguration time-dependent Hartree theory in second quantization representation. *J. Chem. Phys.* **131**, 024114, (2009).

[90] L. Cao, S. Krönke, O. Vendrell, P. Schmelcher. The multi-layer multi-configuration time-dependent Hartree method for bosons: Theory, implementation, and applications. *J. Chem. Phys.* **139**, 134103, (2013).

[91] S. Krönke, L. Cao, O. Vendrell, P. Schmelcher. Non-equilibrium quantum dynamics of ultra-cold atomic mixtures: the multi-layer multi-configuration time-dependent Hartree method for bosons. *New J. Phys.* **15**, 063018, (2013).

[92] U. Manthe, T. Weike. On the multi-layer multi-configurational time-dependent Hartree approach for bosons and fermions. *J. Chem. Phys.* **146**, 064117, (2017).

[93] T. Weike, U. Manthe. The multi-configurational time-dependent Hartree approach in optimized second quantization: Imaginary time propagation and particle number conservation. *J. Chem. Phys.* **152**, 034101, (2020).

[94] T. Weike, U. Manthe. The multi-configurational time-dependent Hartree approach in optimized second quantization: thermal ensembles and statistical sampling. *Chem. Phys.* **555**, 111413, (2021).

[95] F. Matzkies, U. Manthe. Accurate reaction rate calculations including internal and rotational motion: A statistical multi-configurational time-dependent Hartree approach. *J. Chem. Phys.* **110**, 88, (1999).

[96] U. Manthe, F. Huarte-Larrañaga. Partition functions for reaction rate calculations: statistical sampling and MCTDH propagation. *Chem. Phys. Lett.* **349**, 321, (2001).

[97] M. Nest, R. Kosloff. Quantum dynamical treatment of inelastic scattering of atoms at a surface at finite temperature: The random phase thermal wave function approach. *J. Chem. Phys.* **127**, 134711, (2007).

[98] F. Lüder, M. Nest, P. Saalfrank. Temperature effects for vibrational relaxation of hydrogen adsorbed on Si(100): a stochastic multiconfigurational time-dependent Hartree (MCTDH) study. *Theor. Chem. Acc.* **127**, 183, (2010).

[99] U. Lorenz, P. Saalfrank. Comparing thermal wave function methods for multiconfiguration time-dependent Hartree simulations. *J. Chem. Phys.* **140**, 044106, (2014).

[100] P. A. M. Dirac. Note on Exchange Phenomena in the Thomas Atom. *Proc. Camb. Philos. Soc.* **26**, 376, (1930).

[101] J. Frenkel. *Wave Mechanics; Advanced General Theory*, Clarendon Press, Oxford, (1934).

[102] R. Kosloff, H. Tal-Ezer. A direct relaxation method for calculating eigenfunctions and eigenvalues of the Schrödinger equation on a grid. *Chem. Phys. Lett.* **127**, 223, (1986).

[103] H.-D. Meyer, F. Le Quéré, C. Léonard, F. Gatti. Calculation and selective population of vibrational levels with the Multiconfiguration Time-Dependent Hartree (MCTDH) algorithm. *Chem. Phys.* **329**, 179, (2006).

[104] L. J. Doriol, F. Gatti, C. Iung, H.-D. Meyer. Computation of vibrational energy levels and eigenstates of fluoroform using the multiconfiguration time-dependent Hartree method. *J. Chem. Phys.* **129**, 224109, (2008).

[105] A. Raab, I. Burghardt, H.-D. Meyer. The multiconfiguration time-dependent Hartree method generalized to the propagation of density operators. *J. Chem. Phys.* **111**, 8759, (1999).

[106] A. Raab, H.-D. Meyer. A numerical study on the performance of the multiconfiguration time-dependent Hartree method for density operators. *J. Chem. Phys.* **112**, 10718, (2000).

[107] A. Raab, H.-D. Meyer. Multiconfigurational expansions of density operators: equations of motion and their properties. *Theor. Chem. Acc.* **104**, 358, (2000).

[108] H. D. Meyer, G. A. Worth. Quantum molecular dynamics: propagating wavepackets and density operators using the multiconfiguration time-dependent Hartree method. *Theor. Chem. Acc.* **109**, 251, (2003).

[109] D. Picconi, I. Burghardt. Open system dynamics using Gaussian-based multiconfigurational time-dependent Hartree wavefunctions: Application to environment-modulated tunneling. *J. Chem. Phys.* **150**, 224106, (2019).

[110] C. Cattarius, H.-D. Meyer. Multidimensional density operator propagations in open systems: Model studies on vibrational relaxations and surface sticking processes. *J. Chem. Phys.* **121**, 9283, (2004).

[111] B. Brüggemann, P. Persson, H.-D. Meyer, V. May. Frequency dispersed transient absorption spectra of dissolved perylene: A case study using the density matrix version of the MCTDH method. *Chem. Phys.* **347**, 152, (2008).

[112] W. H. Miller. Semiclassical limit of quantum mechanical transition state theory for nonseparable systems. *J. Chem. Phys.* **62**, 1899, (1975).

[113] W. H. Miller, S. D. Schwartz, J. W. Tromp. Quantum mechanical rate constants for bimolecular reactions. *J. Chem. Phys.* **79**, 4889, (1983).

[114] T. Seideman, W.H. Miller. Calculation of the cumulative reaction probability via a discrete variable representation with absorbing boundary conditions. *J. Chem. Phys.* **96**, 4412, (1992).

[115] T. Seideman, W.H. Miller. Quantum mechanical reaction probabilities via a discrete variable representation-absorbing boundary condition Green's function. *J. Chem. Phys.* **97**, 2499, (1992).

[116] H. Eyring. The activated complex and the absolute rate of chemical reactions. *Chem. Rev.* **17**, 65, (1935).

[117] R. Levine. *Molecular Reaction Dynamics*. Cambridge University Press, (2005).

[118] C. Rietze, E. Titov, S. Lindner, P. Saalfrank. Thermal isomerization of azobenzenes: on the performance of Eyring transition state theory. *J. Phys.: Condens. Matter* **29**, 314002, (2017).

[119] T. Schwartz, J.A. Hutchison, C. Genet, T.W. Ebbesen. Reversible Switching of Ultrastrong Light-Molecule Coupling. *Phys. Rev. Lett.* **106**, 196405, (2011).

[120] J. A. Hutchison, T. Schwartz, C. Genet, E. Devaux, T. W. Ebbesen. Modifying Chemical Landscapes by Coupling to Vacuum Fields. *Angew. Chem. Int.* **51**, 1592, (2012).

[121] A. Thomas, J. George, A. Shalabney, M. Dryzhakov, S. J. Varma, J. Moran, T. Chervy, X. Zhong, E. Devaux, C. Genet, J. A. Hutchison, T. W. Ebbesen. Ground-State Chemical Reactivity under Vibrational Coupling to the Vacuum Electromagnetic Field. *Angew. Chem. Int. Ed.* **55**, 11462, (2016).

[122] A. Thomas, L. Lethuillier-Karl, K. Nagarajan, R. M. A. Vergauwe, J. George, T. Chervy, A. Shalabney, E. Devaux, C. Genet, J. Moran, T. W. Ebbesen. Tilting a ground-state reactivity landscape by vibrational strong coupling. *Science* **363**, 615, (2019).

[123] A. Shalabney, J. George, J. A. Hutchison, G. Pupillo, C. Genet, T.W. Ebbesen. Coherent coupling of molecular resonators with a microcavity mode. *Nat. Commun.* **6**, 5981, (2015).

[124] J. George, A. Shalabney, J. A. Hutchison, C. Genet, T.W. Ebbesen. Liquid-Phase Vibrational Strong Coupling. *J. Phys. Chem. Lett.* **6**, 1027, (2015).

[125] J. George, T. Chervy, A. Shalabney, E. Devaux, H.Hiura, C. Genet, T.W. Ebbesen. Multiple Rabi Splittings under Ultrastrong Vibrational Coupling. *Phys. Rev. Lett.* **117**, 153601, (2016).

[126] T. W. Ebbesen. Hybrid Light–Matter States in a Molecular and Material Science Perspective. *Acc. Chem. Res.* **49**, 2403, (2016).

[127] J. Feist, J. Galego, F.J. Garcia-Vidal. Polaritonic Chemistry with Organic Molecules. *ACS Photonics* **5**, 205, (2018).

[128] F. J. Garcia-Vidal, C. Ciuti, T.W. Ebbesen. Manipulating Matter by Strong Coupling to Vacuum Fields. *Science* **373**, eabd0336, (2021).

[129] J. Galego, J.F. Garcia-Vidal, J. Feist. Cavity-Induced Modifications of Molecular Structure in the Strong-Coupling Regime. *Phys. Rev. X* **5**, 041022, (2015).

[130] F. Herrera, F.C. Spano. Cavity-Controlled Chemistry in Molecular Ensembles. *Phys. Rev. Lett.* **116**, 238301, (2016).

[131] J. Galego, J.F. Garcia-Vidal, J. Feist. Suppressing Photochemical Reactions with Quantized Light Fields. *Nat. Commun.* **7**, 13841, (2016).

[132] M. Kowalewski, K. Bennett, S. Mukamel. Cavity Femtochemistry: Manipulating Nonadiabatic Dynamics at Avoided Crossings. *J. Phys. Chem. Lett.* **7**, 2050, (2016).

[133] J. Galego, J.F. Garcia-Vidal, J. Feist. Many-Molecule Reaction Triggered by a Single Photon in Polaritonic Chemistry. *Phys. Rev. Lett.* **119**, 136001, (2017).

[134] J. Fregoni, G. Granucci, E. Coccia, M. Persico, S. Corni. Manipulating Azobenzene Photoisomerization through Strong Light-Molecule Coupling. *Nat. Commun.* **9**, 4688, (2018).

[135] J. F. Triana, D. Peláez, J. L. Sanz-Vicario. Entangled photonic-nuclear molecular dynamics of LiF in quantum optical cavities. *J. Phys. Chem. A* **122**, 2266, (2018).

[136] O. Vendrell. Coherent dynamics in cavity femtochemistry: Application of the multi-configuration time-dependent Hartree method. *Chem. Phys.* **509**, 55, (2018).

[137] O. Vendrell. Collective Jahn-Teller interactions through light-matter coupling in a cavity. *Phys. Rev. Lett.* **121**, 253001, (2018).

[138] A. Mandal, P. Huo. Investigating new reactivities enabled by polariton photochemistry. *J. Phys. Chem. Lett.* **10**, 5519, (2019).

[139] C. Schäfer, M. Ruggenthaler, H. Appel, A. Rubio. Modification of excitation and charge transfer in cavity quantum-electrodynamical chemistry. *PNAS* **116**, 4883, (2019).

[140] I. Ulusoy, J. A. Gomez, O. Vendrell. Modifying the nonradiative decay dynamics through conical intersections via collective coupling to a cavity mode. *J. Phys. Chem. A* **123**, 8832, (2019).

[141] A. Semenov, A. Nitzan. Electron transfer in confined electromagnetic fields. *J. Chem. Phys.* **150**, 174122, (2019).

[142] P. Antoniou, F. Suchanek, J.F. Varner, J.J. Foley. Role of Cavity Losses on Nonadiabatic Couplings and Dynamics in Polaritonic Chemistry. *J. Phys. Chem. Lett.* **11**, 9063, (2020).

[143] J. Fregoni, G. Granucci, M. Persico, S. Corni. Strong Coupling with Light Enhances the Photoisomerization Quantum Yield of Azobenzene. *Chem.* **6**, 250, (2020).

[144] S. Felicetti, J. Fregoni, T. Schnappinger, S. Reiter, R. de Vivie-Riedle, J. Feist. Photoprotecting Uracil by Coupling with Lossy Nanocavities. *J. Phys. Chem. Lett.* **11**, 8810, (2020).

[145] I. Ulusoy, O. Vendrell. Dynamics and spectroscopy of molecular ensembles in a lossy microcavity. *J. Chem. Phys.* **153**, 044108, (2020).

[146] I. Ulusoy, J. A. Gomez, O. Vendrell. Many-photon excitation of organic molecules in a cavity—Superradiance as a measure of coherence. *J. Chem. Phys.* **153**, 244107, (2020).

[147] K. Nagarajan, A. Thomas, T.W. Ebbesen. Chemistry under Vibrational Strong Coupling. *J. Am. Chem. Soc.* **143**, 16877, (2021).

[148] D.S. Wang, S.F. Yelin. A Roadmap Toward the Theory of Vibrational Polariton Chemistry. *ACS Photonics* **8**, 2818, (2021).

[149] T.E. Li, B. Cui, J.E. Subotnik, A. Nitzan. Molecular Polaritonics: Chemical Dynamics Under Strong Light–Matter Coupling. *Ann. Rev. Phys. Chem.* **73**, 3.1, (2022).

[150] A.D. Dunkelberger, B.S. Simpkins, I. Vurgaftman, J.C. Owrutsky. Vibration-Cavity Polariton Chemistry and Dynamics. *Ann. Rev. Phys. Chem.* **73**, 19.1, (2022).

[151] J. Fregoni, F.J. Garcia-Vidal, J. Feist. Theoretical Challenges in Polaritonic Chemistry. *ACS Photonics* **9**, 1069, (2022).

[152] E.W. Fischer, P. Saalfrank. Ground state properties and infrared spectra of anharmonic vibrational polaritons of small molecules in cavities. *J. Chem. Phys.* **154**, 104311, (2021).

[153] J.F. Triana, F.J.Hernández, F. Herrera. The shape of the electric dipole function determines the sub-picosecond dynamics of anharmonic vibrational polaritons. *J. Chem. Phys.* **152**, 234111, (2020).

[154] A. Caldeira, A. Leggett. Path integral approach to quantum Brownian motion. *Physica A* **121**, 587, (1983).

[155] A. Caldeira, A. Leggett. Quantum tunnelling in a dissipative system. *Ann. Phys.* **149**, 374, (1983).

[156] Gaussian 16, Revision C.01, M. J. Frisch, G. W. Trucks, H. B. Schlegel, G. E. Scuseria, M. A. Robb, J. R. Cheeseman, G. Scalmani, V. Barone, G. A. Petersson, H. Nakatsuji, X. Li, M. Caricato, A. V. Marenich, J. Bloino, B. G. Janesko, R. Gomperts, B. Mennucci, H. P. Hratchian, J. V. Ortiz, A. F. Izmaylov, J. L. Sonnenberg, D. Williams-Young, F. Ding, F. Lipparini, F. Egidi, J. Goings, B. Peng, A. Petrone, T. Henderson, D. Ranasinghe, V. G. Zakrzewski, J. Gao, N. Rega, G. Zheng, W. Liang, M. Hada, M. Ehara, K. Toyota, R. Fukuda, J. Hasegawa, M. Ishida, T. Nakajima, Y. Honda, O. Kitao, H. Nakai, T. Vreven, K. Throssell, J. A. Montgomery, Jr., J. E. Peralta, F. Ogliaro, M. J. Bearpark, J. J. Heyd, E. N. Brothers, K. N. Kudin, V. N. Staroverov, T. A. Keith, R. Kobayashi, J. Normand, K. Raghavachari, A. P. Rendell, J. C. Burant, S. S. Iyengar, J. Tomasi, M. Cossi, J. M. Millam, M. Klene, C. Adamo, R. Cammi, J. W. Ochterski, R. L. Martin, K. Morokuma, O. Farkas, J. B. Foresman, and D. J. Fox, Gaussian, Inc., Wallingford CT, 2016.

[157] M. S. Arruda, F. V. Prudente, A. M. Maniero. Full configuration interaction determination of potential energy curve for LiH molecule using cc-pVXZ (X=D,T and Q) basis sets. *Rev. Mex. Fis. S* **56**, 51, (2010).

[158] M. V. Korolkov, G. K. Paramonov, B. Schmidt. State-selective control for vibrational excitation and dissociation of diatomic molecules with shaped ultrashort infrared laser pulses. *J. Chem. Phys.* **105**, 1862, (1996).

[159] G. K. Paramonov, P. Saalfrank. Time-evolution operator method for non-Markovian density matrix propagation in time and space representation: Application to laser association of OH in an environment. *Phys. Rev. A* **79**, 013415, (2009).

[160] V. Spirko. Vibrational anharmonicity and the inversion potential function of NH_3. *J. Mol. Spectrosc.* **101**, 30, (1983).

[161] *CRC Handbook of Chemistry and Physics*, edited by D. R. Lide (CRC Press/Taylor & Francis, Boca Raton, Fl, 2009).

[162] M. F. Mannig. Energy Levels of a Symmetrical Double Minima Problem with Applications to the NH_3 and ND_3 Molecules. *J. Chem. Phys.* **3**, 136, (1935).

[163] P. Saalfrank, S. Holloway, G. R. Darling. Theory of laser-induced desorption of ammonia from Cu(111): State-resolved dynamics, isotope effects, and selective surface photochemistry. *J. Chem. Phys.* **103**, 6720, (1995).

[164] R. Marquardt, M. Quack, I. Thanopulos, D. Luckhaus. A global electric dipole function of ammonia and isotopomers in the electronic ground state. *J. Chem. Phys.* **119**, 10724, (2003).

[165] J. Bonini, J. Flick. Ab initio linear-response approach to vibro-polaritons in the cavity Born-Oppenheimer approximation. *J. Chem. Theory Comput.* **18**, 2764, (2022).

[166] E.J. Heller. The semiclassical way to molecular spectroscopy. *Acc. Chem. Res.* **14**, 368, (1981).

[167] J. Flick, P. Narang. Cavity-Correlated Electron-Nuclear Dynamics from First Principles. *Phys. Rev. Lett.* **121**, 113002, (2018).

[168] D. Sidler, M. Ruggenthaler, H. Appel, A. Rubio. Chemistry in quantum cavities: Exact results, the impact of thermal velocities, and modified dissociation. *J. Phys. Chem. Lett.* **11**, 7525, (2020).

[169] M.H. Farag, A. Mandal, P. Huo. Polariton induced conical intersection and berry phase. *Phys. Chem. Chem. Phys.* **23**, 16868, (2021).

[170] T. Szidarovszky, Péter Badankó, Gábor J Halász, Ágnes Vibók. Nonadiabatic phenomena in molecular vibrational polaritons. *J. Chem. Phys.* **154**, 064305, (2021).

[171] E.W. Fischer, P. Saalfrank. Cavity-induced Non-Adiabatic Dynamics and Spectroscopy of Molecular Rovibrational Polaritons studied by Multi-Mode Quantum Models. arXiv:2205.00945, (2022).

[172] D. H. Rank, A. G. St Pierre, T. A. Wiggins. Rotational and vibration constants of CO. *J. Mol. Spec.* **18**, 418, (1965).

[173] D.T. Colbert, W.H. Miller. A novel discrete variable representation for quantum mechanical reactive scattering via the S-matrix Kohn method. *J. Chem. Phys.* **96**, 1982, (1992).

[174] N. Mina-Camilde , Carlos Manzanares I., J. F. Caballero. Molecular Constants of Carbon Monoxide at $v = 0, 1, 2$, and 3: A Vibrational Spectroscopy Experiment in Physical Chemistry. *J. Chem. Educ.* **73**, 804, (1996).

[175] C. Hua-Jun, W. Jie, L. Hao, C. Xin-Lu. Electric dipole moment function and line intensities for the ground state of carbon monoxide. *Chin. Phys. B* **24**, 083102, (2015).

[176] G. Scuseria, M. D. Miller. The dipole moment of carbon monoxide. *J. Chem. Phys.* **94**, 6660, (1991).

[177] S. Matsika, D. R. Yarkony. Beyond Two-State Conical Intersections. Three-State Conical Intersections in Low Symmetry Molecules: the Allyl Radical. *J. Am. Chem. Soc.* **125**, 10672, (2003).

[178] S. Matsika. Three-state conical intersections in nucleic acid bases. *J. Phys. Chem. A* **109**, 7538, (2005).

[179] J. D. Coe, T. J. Martinez. Competitive decay at two-and three-state conical intersections in excited-state intramolecular proton transfer. *J. Am. Chem. Soc.* **127**, 4560, (2005).

[180] S. Matsika. "*Three-State Intersections*" in *Conical Intersections: Theory, Computation and Experiment* by W. Domcke, D. R. Yarkony, H. Köppel; Advanced Series in Physical Chemistry. 17. World Scientific. (2011).

[181] L. A. Martinez-Martinez, R. F. Ribeiro, J. Campos-González-Angulo, J. Yuen-Zhou. Can ultrastrong coupling change ground-state chemical reactions? *ACS Photonics* **5**, 167, (2018).

[182] L. Lacombe, N.M. Hofmann, N.T. Maitra. Exact potential energy surface for molecules in cavities. *Phys. Rev. Lett.* **123**, 083201, (2019).

[183] J. A. Campos-Gonzalez-Angulo, R. F. Ribeiro, J. Yuen-Zhou. Resonant catalysis of thermally activated chemical reactions with vibrational polaritons. *Nat. Commun.* **10**, 4685, (2019).

[184] J. Galego, C. Climent, F. J. Garcia-Vidal, J. Feist. Cavity Casimir-Polder forces and their effects in ground-state chemical reactivity. *Phys. Rev. X* **9**, 021057, (2019).

[185] J. A. Campos-Gonzalez-Angulo, J. Yuen-Zhou. Polaritonic normal modes in transition state theory. *J. Chem. Phys.* **152**, 161101, (2020).

[186] V. P. Zhdanov. Vacuum field in a cavity, light-mediated vibrational coupling, and chemical reactivity. *Chem. Phys.* **535**, 110767, (2020).

[187] T.E. Li, H.T. Chen, A. Nitzan, J.E. Subotnik. Quasiclassical modeling of cavity quantum electrodynamics. *Phys. Rev. A* **101**, 033831, (2020).

[188] T. E. Li, J. E. Subotnik, A. Nitzan. On the origin of ground-state vacuum-field catalysis: Equilibrium consideration. *J. Chem. Phys.* **152**, 234107, (2020).

[189] T. E. Li, J. E. Subotnik, A. Nitzan. Cavity molecular dynamics simulations of liquid water under vibrational ultrastrong coupling. *PNAS* **117**, 18324, (2020).

[190] T. E. Li, A. Nitzan, J. E. Subotnik. Cavity molecular dynamics simulations of vibrational polariton-enhanced molecular nonlinear absorption. *J. Chem. Phys.* **154**, 094124, (2021).

[191] T. E. Li, A. Nitzan, J. E. Subotnik. Collective vibrational strong coupling effects on molecular vibrational relaxation and energy transfer: Numerical insights via cavity molecular dynamics simulations. *Angew. Chem.* **133**, 2, (2021).

[192] T. E. Li, A. Nitzan, J. E. Subotnik. Energy-efficient pathway for selectively exciting solute molecules to high vibrational states via solvent vibration-polariton pumping. arXiv:2104.15121, (2021).

[193] M. Du, J. A. Campos-Gonzalez-Angulo, J. Yuen-Zhou. Nonequilibrium effects of cavity leakage and vibrational dissipation in thermally activated polariton chemistry. *J. Chem. Phys.* **154**, 084108, (2021).

[194] X. Li, A. Mandal, P. Huo. Cavity frequency-dependent theory for vibrational polariton chemistry. *Nat. Commun* **12**, 1, (2021).

[195] X. Li, P. Huo. Investigating Tunneling-Controlled Chemical Reactions through Ab Initio Ring Polymer Molecular Dynamics. *J. Phys. Chem. Lett.* **12**, 5030, (2021).

[196] X. Li, A. Mandal, P. Huo. Theory of mode-selective chemistry through polaritonic vibrational strong coupling. *J. Phys. Chem. Lett.* **12**, 6974, (2021).

[197] P.-Y. Yang, J. Cao. Quantum effects in chemical reactions under polaritonic vibrational strong coupling. *J. Phys. Chem. Lett.* **12**, 9531, (2021).

[198] A. Mandal, P. Huo. Theory of vibrational polariton chemistry in the collective coupling regime. *J. Chem. Phys.* **156**, 014101, (2022).

[199] C. Schäfer, J. Flick, E. Ronca, P. Narang, A. Rubio. Shining Light on the Microscopic Resonant Mechanism Responsible for Cavity-Mediated Chemical Reactivity. arXiv:2104.12429v4, (2022).

[200] E.W. Fischer, J. Anders, P. Saalfrank. Cavity-Altered Thermal Isomerization Rates and Dynamical Resonant Localization in Vibropolaritonic Chemistry. *J. Chem. Phys.* **156**, 154305, (2022).

[201] X. Zhu, K. C. Thompson, T. J. Martinez; *J. Chem. Phys.* **150**, 164103, (2019).

[202] J. Lather, P. Bhatt, A. Thomas, T. W. Ebbesen, J. George. Cavity Catalysis by Cooperative Vibrational Strong Coupling of Reactant and Solvent Molecules. *Angew. Chem.* **131**, 10745, (2019).

[203] I. Andrianov, P. Saalfrank. Vibrational relaxation rates for H on a Si(100) : (2×1) surface: a two-dimensional model. *Chem. Phys. Lett.* **350**, 191, (2001).

[204] I. Andrianov, P. Saalfrank. Theoretical study of vibration-phonon coupling of H adsorbed on a Si(100) surface. *J. Chem. Phys.* **124**, 034710, (2006).

[205] U. Lorenz, P. Saalfrank. A novel system-bath Hamiltonian for vibration-phonon coupling: Formulation, and application to the relaxation of Si–H and Si–D bending modes of H/D:Si(100)-(2×1). *Chem. Phys.* **482**, 69, (2017).

[206] F. Bouakline, U. Lorenz, G. Melani, G. K. Paramonov, P. Saalfrank. Isotopic effects in vibrational relaxation dynamics of H on a Si(100) surface. *J. Chem. Phys.* **147**, 144703, (2017).

[207] F. Bouakline, E. W. Fischer, P. Saalfrank. A quantum-mechanical tier model for phonon-driven vibrational relaxation dynamics of adsorbates at surfaces. *J. Chem. Phys.* **150**, 244105, (2019).

[208] P. Guyot-Sionnest, P. Lin, E. Miller. Vibrational dynamics of the Si–H stretching modes of the Si(100)/H:2×1 surface. *J. Chem. Phys.* **102**, 4269, (1995).

[209] Y. Huang, C. T. Rettner, D. J. Auerbach, A. M. Wodtke. Vibrational Promotion of Electron Transfer. *Science* **290**, 111, (2000).

[210] G.-J. Kroes, C. Díaz. Quantum and classical dynamics of reactive scattering of H_2 from metal surfaces. *Chem. Soc. Rev.* **45**, 3658, (2016).

[211] H. Guo, P. Saalfrank, T. Seideman. Theory of photoinduced surface reactions of admolecules. *Prog. Surf. Sci.* **62**, 239, (1999).

[212] P. Kratzer. Reaction dynamics of atomic hydrogen with the hydrogenated Si(001) (2×1) surface. *J. Chem. Phys.* **106**, 6752, (1997).

[213] T. -C. Shen, C. Wang, G. Abeln, J. Tucker, J. Lyding, P. Avouris, R. Walkup. Atomic-scale desorption through electronic and vibrational excitation mechanisms. *Science* **268**, 1590, (1995).

[214] M. Jech, A.-M. El-Sayed, S. Tyaginov, D. Waldhör, F. Bouakline, P. Saalfrank, D. Jabs, Ch. Jungemann, M. Waltl, T. Grasser. Quantum Chemistry Treatment of Silicon-Hydrogen Bond Rupture by Nonequilibrium Carriers in Semiconductor Devices. *Phys. Rev. Appl.* **16**, 014026, (2021).

[215] P. Saalfrank. Quantum Dynamical Approach to Ultrafast Molecular Desorption from Surfaces. *Chem. Rev.* **106**, 4116, (2006).

[216] S. Sakong, P. Kratzer, X. Han, T. Balgar, E. Hasselbrink. Isotope effects in the vibrational lifetime of hydrogen on germanium(100): Theory and experiment. *J. Chem. Phys.* **131**, 124502, (2009).

[217] H. Arnolds. Vibrational dynamics of adsorbates – Quo vadis? *Prog. Surf. Sci.* **86**, 1, (2011).

[218] E.W. Fischer, M. Werther, F. Bouakline, P. Saalfrank. A hierarchical effective mode approach to phonon-driven multilevel vibrational relaxation dynamics at surfaces. *J. Chem. Phys.* **153**, 064704, (2020).

[219] E.W. Fischer, M. Werther, F. Bouakline, F. Grossmann, P. Saalfrank. Non-Markovian Vibrational Relaxation Dynamics at Surfaces. *J. Chem. Phys.* **156**, 214702, (2022).

[220] E. Gindensperger, I. Burghardt, L. S. Cederbaum. Short-time dynamics through conical intersections in macrosystems. I. Theory: Effective-mode formulation. *J. Chem. Phys.* **124**, 144103, (2006).

[221] E. Gindensperger, H. Köppel, L. S. Cederbaum. Hierarchy of effective modes for the dynamics through conical intersections in macrosystems. *J. Chem. Phys.* **126**, 034106, (2007).

[222] E. Gindensperger, L. S. Cederbaum. Quantum dynamics in macrosystems with several coupled electronic states: Hierarchy of effective Hamiltonians. *J. Chem. Phys.* **127**, 124107, (2007).

[223] H. Tamura, E. R. Bittner, I. Burghardt. Nonadiabatic quantum dynamics based on a hierarchical electron-phonon model: Exciton dissociation in semiconducting polymers. *J. Chem. Phys.* **127**, 034706, (2007).

[224] H. Tamura, J. G. S. Ramon, E. R. Bittner, I. Burghardt. Phonon-Driven Ultrafast Exciton Dissociation at Donor-Acceptor Polymer Heterojunctions. *Phys. Rev. Lett.* **100**, 107402, (2008).

[225] K. H. Hughes, C. D. Christ, I. Burghardt. Effective-mode representation of non-Markovian dynamics: A hierarchical approximation of the spectral density. I. Application to single surface dynamics. *J. Chem. Phys.* **131**, 024109, (2009).

[226] K. H. Hughes, C. D. Christ, I. Burghardt. Effective-mode representation of non-Markovian dynamics: A hierarchical approximation of the spectral density. II. Application to environment-induced nonadiabatic dynamics. *J. Chem. Phys.* **131**, 124108, (2009).

[227] I. Burghardt, R. Martinazzo, K. H. Hughes. Non-Markovian reduced dynamics based upon a hierarchical effective-mode representation. *J. Chem. Phys.* **137**, 144107, (2012).

[228] M. Bonfanti, G. F. Tantardini, K. H. Hughes, R. Martinazzo, I. Burghardt. Compact MCTDH Wave Functions for High-Dimensional System-Bath Quantum Dynamics. *J. Phys. Chem. A* **116**, 11406, (2012).

[229] W. Popp, M. Polkehn, K. H. Hughes, R. Martinazzo, I. Burghardt. Vibronic coupling models for donor-acceptor aggregates using an effective-mode scheme: Application to mixed Frenkel and charge-transfer excitons in oligothiophene aggregates. *J. Chem. Phys.* **150**, 244114, (2019).

[230] W. Popp, M. Polkehn, R. Binder, I. Burghardt. Coherent Charge Transfer Exciton Formation in Regioregular P3HT: A Quantum Dynamical Study. *J. Phys. Chem. Lett.* **10**, 3326, (2019).

[231] R. Baer, R. Kosloff. Quantum dissipative dynamics of adsorbates near metal surfaces: A surrogate Hamiltonian theory applied to hydrogen on nickel. *J. Chem. Phys.* **106**, 8862, (1997).

[232] R. Bulla, N. H. Tong, M. Vojta. Numerical Renormalization Group for Bosonic Systems and Application to the Sub-Ohmic Spin-Boson Model.*Phys. Rev. Lett.* **91**, 170601, (2003).

[233] M. Vojta, N. H. Tong, R. Bulla. Quantum Phase Transitions in the Sub-Ohmic Spin-Boson Model: Failure of the Quantum-Classical Mapping. *Phys. Rev. Lett.* **94**, 070604, (2005).

[234] R. Bulla, H.-J. Lee, N.-H. Tong, M. Vojta. Numerical renormalization group for quantum impurities in a bosonic bath. *Phys. Rev. B* **71**, 045122, (2005).

[235] A. W. Chin, Á. Rivas, S. F. Huelga, M. B. Plenio. Exact mapping between system-reservoir quantum models and semi-infinite discrete chains using orthogonal polynomials. *J. Math. Phys.* **51**, 092109, (2010).

[236] J. Prior, A. W. Chin, S. F. Huelga, M. B. Plenio. Efficient Simulation of Strong System-Environment Interactions. *Phys. Rev. Lett.* **105**, 050404, (2010).

[237] N. Zhou, Z. Huang, J. Zhu, V. Chernyak, Y. Zhao. Polaron dynamics with a multitude of Davydov D2 trial states. *J. Chem. Phys.* **143**, 014113, (2015).

[238] L. Wang , L. Chen, N. Zhou, Y. Zhao. Variational dynamics of the sub-Ohmic spin-boson model on the basis of multiple Davydov D1 states. *J. Chem. Phys.* **144**, 024101, (2016).

[239] Z. Huang, L. Wang, C. Wu, L. Chen, F. Grossmann, Y. Zhao. Polaron dynamics with off-diagonal coupling: beyond the Ehrenfest approximation. *Phys. Chem. Chem. Phys.* **19**, 1655, (2017).

[240] Y. Fujihashi, L. Wang, Y. Zhao. Direct evaluation of boson dynamics via finite-temperature time-dependent variation with multiple Davydov states. *J. Chem. Phys.* **147**, 234107, (2017).

[241] R. Hartmann, M. Werther, F. Grossmann, W. T. Strunz. Exact open quantum system dynamics: Optimal frequency vs. time representation of bath correlations. *J.Chem. Phys.* **150**, 234105, (2019).

[242] L. Chen, M. F. Gelin, W. Domcke. Multimode quantum dynamics with multiple Davydov D2 trial states: Application to a 24-dimensional conical intersection model. *J. Chem. Phys.* **150**, 024101, (2019).

[243] M. Werther, F. Grossmann. Apoptosis of moving nonorthogonal basis functions in many-particle quantum dynamics. *Phys. Rev. B* **101**, 174315, (2020).

[244] M. Werther. *The multi Davydov-Ansatz: apoptosis of moving Gaussian basis functions with applications to open quantum system dynamics*. Dissertation, Technische Universität Dresden, Germany, (2020).

[245] Y. Zhao, K. Sun, L. Cheng, M. Gelin. The hierarchy of Davydov's Ansätze and its applications. *WIREs Comput Mol Sci.* **e1589**, (2021).

[246] F. Bouakline, F. Lüder, R. Martinazzo, P. Saalfrank. Reduced and Exact Quantum Dynamics of the Vibrational Relaxation of a Molecular System Interacting with a Finite-Dimensional Bath. *J. Phys. Chem. A* **116**, 11118, (2012).

[247] M. Zwolak, G. Vidal. Mixed-State Dynamics in One-Dimensional Quantum Lattice Systems: A Time-Dependent Superoperator Renormalization Algorithm. *Phys. Rev. Lett.* **93**, 207205, (2004).

[248] F. Verstraete, J. J. Garcia-Ripoll, J. I. Cirac. Matrix Product Density Operators: Simulation of Finite-Temperature and Dissipative Systems. *Phys. Rev. Lett.* **93**, 207204, (2004).

[249] A. E. Feiguin, S. R. White. Finite-temperature density matrix renormalization using an enlarged Hilbert space. *Phys. Rev. B* **72**, 220401, (2005).

[250] Y. Takahashi, H. Umezawa. Thermo Field Dynamics. *Collect. Phenom.* **2**, 55, (1975).

[251] Y. Takahashi, H. Umezawa. Thermo Field Dynamics. *Int. J. Mod. Phys. B* **10**, 1755, (1996).

[252] H. Umezawa, H. Matsumoto, M. Tachiki. *Thermofield Dynamics and Condensed States*. North-Holland, Amsterdam, (1982).

[253] H. Umezawa. *Advanced Field Theory*. American Institute of Physics, New York, (1993).

[254] F. C. Khanna, A. P. C. Malbouisson, J. M. C. Malbouisson, A. E. Santana. *Thermal Quantum Field Theory: Algebraic Aspects and Applications*. World Scientific, Singapore, (2009).

[255] M. Blasone, P. Jizba, G. Vitiello. *Quantum Field Theory and its Macroscopic Manifestations: Boson Condensation, Ordered Patterns and Topological Defects*. Imperial College Press, Singapore, (2011).

[256] G. Ritschel, D. Suess, S. Möbius, W. T. Strunz, A. Eisfeld. Non-Markovian Quantum State Diffusion for temperature-dependent linear spectra of light harvesting aggregates. *J. Chem. Phys.* **142**, 034115, (2015).

[257] C. S. Reddy, M. D. Prasad. Finite temperature vibronic spectra of harmonic surfaces: a time-dependent coupled cluster approach. *Mol. Phys.* **113**, 3023, (2015).

[258] R. Borrelli, M. F. Gelin. Quantum electron-vibrational dynamics at finite temperature: Thermo field dynamics approach. *J. Chem. Phys.* **145**, 224101, (2016).

[259] R. Borrelli, M. F. Gelin. Simulation of Quantum Dynamics of Excitonic Systems at Finite Temperature: an efficient method based on Thermo Field Dynamics. *Sci. Rep.* **7**, 1, (2017).

[260] M. F. Gelin, R. Borrelli. Thermal Schrödinger equation: efficient tool for simulation of many-body quantum dynamics at finite temperature. *Ann. Phys.* **529**, 1700200, (2017).

[261] L. Wang, Y. Fujihashi, L. Chen, Y. Zhao. Finite-temperature time-dependent variation with multiple Davydov states. *J. Chem. Phys.* **146**, 124127, (2017).

[262] R. Borrelli. Theoretical study of charge-transfer processes at finite temperature using a novel thermal Schrödinger equation. *Chem. Phys.* **515**, 236, (2018).

[263] R. Borrelli. Density matrix dynamics in twin-formulation: An efficient methodology based on tensor-train representation of reduced equations of motion. *J. Chem. Phys.* **150**, 234102, (2019).

[264] G. Harsha, T. M. Henderson, G. E. Scuseria. Thermofield theory for finite-temperature quantum chemistry. *J. Chem. Phys.* **150**, 154109, (2019).

[265] G. Harsha, T. M. Henderson, G. E. Scuseria. Thermofield Theory for Finite-Temperature Coupled Cluster. *J. Chem. Theory Comput.* **15**, 6127, (2019).

[266] P. Shushkov, T. F. Miller III. Real-time density-matrix coupled-cluster approach for closed and open systems at finite temperature. *J. Chem. Phys.* **151**, 134107, (2019).

[267] T. Begušić, J. Vaníček. On-the-fly ab initio semiclassical evaluation of vibronic spectra at finite temperature. *J. Chem. Phys.* **153**, 024105, (2020).

[268] T. Begušić, J. Vaníček. Finite-Temperature, Anharmonicity, and Duschinsky Effects on the Two-Dimensional Electronic Spectra from Ab Initio Thermo-Field Gaussian Wavepacket Dynamics. *J. Phys. Chem. Lett.* **12**, 2997, (2021).

[269] R. Borrelli, M. F. Gelin. Finite-Temperature, Anharmonicity, and Duschinsky Effects on the Two-Dimensional Electronic Spectra from Ab Initio Thermo-Field Gaussian Wavepacket Dynamics. *WIREs Comput Mol Sci.* **1539**, (2021).

[270] M. F. Gelin, R. Borrelli. Simulation of Nonlinear Femtosecond Signals at Finite Temperature via a Thermo Field Dynamics-Tensor Train Method: General Theory and Application to Time- and Frequency-Resolved Fluorescence of the Fenna–Matthews–Olson Complex. *J. Chem. Theory Comput.* **17**, 4316, (2021).

[271] L. Chen, R. Borrelli, D. V. Shalashilin, Y. Zhao, M. F. Gelin. Simulation of Time- and Frequency-Resolved Four-Wave-Mixing Signals at Finite Temperatures: A Thermo-Field Dynamics Approach. *J. Chem. Theory Comput.* **17**, 4359, (2021).

[272] D. Brey, W. Popp, P. Budakoti, G. D'Avino, I. Burghardt. Quantum Dynamics of Electron–Hole Separation in Stacked Perylene Diimide-Based Self-Assembled Nanostructures. *J. Phys. Chem. C* **45**, 125, (2021).

[273] R. Borrelli, S. Dolgov. Expanding the Range of Hierarchical Equations of Motion by Tensor-Train Implementation. *J. Phys. Chem. B* **125**, 5397, (2021).

[274] G. Harsha, Y. Xu, T. M. Henderson, G. E. Scuseria. Thermal coupled cluster theory for SU(2) systems. *Phys. Rev. B* **105**, 045125, (2022).

[275] K. Polley, R. F. Loringa. Two-dimensional vibronic spectroscopy with semiclassical thermofield dynamics. *J. Chem. Phys.* **156**, 124108, (2022).

[276] J. Zeng, Y. Yao. Variational Squeezed Davydov Ansatz for Realistic Chemical Systems with Nonlinear Vibronic Coupling. *J. Chem. Theory Comput.* **18**, 1255, (2022).

[277] E.W. Fischer, P. Saalfrank. A thermofield-based multilayer multiconfigurational time-dependent Hartree approach to non-adiabatic quantum dynamics at finite temperature. *J. Chem. Phys.* **155**, 134109, (2021).

[278] G. Worth, H.-D. Meyer, L. S. Cederbaum Relaxation of a system with a conical intersection coupled to a bath: A benchmark 24-dimensional wave packet study treating the environment explicitly. *J. Chem. Phys.* **109**, 3518, (1998).

[279] A. Raab, G. Worth, H.-D. Meyer, L. S. Cederbaum. Molecular dynamics of pyrazine after excitation to the electronic state using a realistic 24-mode model Hamiltonian. *J. Chem. Phys.* **110**, 936, (1999).

[280] D. Mendive-Tapia, T. Firmino, H.-D. Meyer, F. Gatti. Towards a systematic convergence of Multi-Layer (ML) Multi-Configuration Time-Dependent Hartree nuclear wavefunctions: The ML-spawning algorithm. *Chem. Phys.* **482**, 113, (2017).

[281] D. Mendive-Tapia, H.-D. Meyer. Regularizing the MCTDH equations of motion through an optimal choice on-the-fly (i.e., spawning) of unoccupied single-particle functions. *J. Chem. Phys.* **153**, 234114, (2020).

Erklärung

Hiermit versichere ich, dass die vorliegende Arbeit an keiner anderen Hochschule eingereicht sowie selbstständig und ausschließlich mit den angegebenen Quellen angefertig worden ist.

Potsdam, Juni 2022